BRNO UNIVERSITY OF TECHNOLOGY
VYSOKÉ UČENÍ TECHNICKÉ V BRNĚ

FACULTY OF CIVIL ENGINEERING
FAKULTA STAVEBNÍ

INSTITUTE OF STRUCTURAL MECHANICS
ÚSTAV STAVEBNÍ MECHANIKY

ANALYSIS OF MIXED MODE I/II FAILURE OF SELECTED STRUCTURAL CONCRETE GRADES
ANALÝZA KOMBINOVANÉHO MÓDU I/II NAMÁHANÍ VYBRANÝCH TŘÍD BETONU

DOCTORAL THESIS
DISERTAČNÍ PRÁCE

AUTHOR — Ing. Petr Miarka
AUTOR PRÁCE

SUPERVISOR — doc. Ing. STANISLAV SEITL, Ph.D.
VEDOUCÍ PRÁCE

BRNO 2021

ABSTRACT

The presented thesis is devoted to the experimental and numerical analysis of concrete fracture under the mixed-mode I/II load. This phenomenon was analysed on various concrete grades and types which are used in the fabrication of precast concrete structural elements. Subsequently, the Brazilian disc test with central specimen was used in experimental and numerical parts.

The numerical part employs both linear elastic fracture mechanics (LEFM) approach and non-linear material model to assess the concrete fracture and failure under the mixed mode I/II load. The LEFM part is dedicated to evaluation the geometry functions and higher order terms of the Williams' expansion, while the non-linear analysis is dedicated to crack initiation and propagation throughout the specimen using the concrete damage plasticity model.

The experimental part is dedicated to the analysis of the mixed mode-mode I/II fracture resistance by the generalised tangential stress (GMTS) criterion with focus set on the governing role of the critical distance r_C. Furthermore, the experimental part validates the applicability of the Williams' expansion on the concrete. For this, experimentally measured displacements by digital image correlation technique were used to calculate the Williams's expansion terms. Lastly, the thesis deals with the influence of the aggressive environment on the material's fracture toughness and on the fracture resistance under the mixed mode I/II has been studied.

KEYWORDS

Brazilian Disc, Linear Elastic Fracture Mechanics, Mixed Mode I/II, Concrete, DIC

ABSTRAKT

Předkládaná disertační práce je zaměřená na experimentální a numerickou analýzu poškození betonu vlivem kombinovaného módu namáhaní I/II. Tento typ poškození je studován na různých třídách a typech betonu, které se běžně používají při výrobě prefabrikovaných dílců. Pro tuto analýzu, jak experimentální, tak i numerickou, bylo použito těleso tvaru brazilského disku s centrálním zářezem.

V numerické části je použito obou současných přístupů teorie lineární elastické lomové mechaniky (LEFM) a také nelineární analýzy pro popis iniciace a šíření trhliny v betonovém tělese zatíženého kombinovaným módem I/II. Teorie LEFM je použito ke stanovení tvarových funkcí a také vyšších členů Williamova rozvoje pro popis napětí před čelem trhliny. Zatímco nelineární model je zaměřen na iniciaci a propagaci trhliny celým průřezem tělesa za použití materiálového modelu „Concrete Damage Plasticity“.

Experimentální část je věnovaná analýze lomové odolnosti betonu v kombinovaném módu zatížení I/II pomocí obecného kritéria tangenciálního napětí (GMTS) se zaměřením především na efekt parametru kritické vzdálenosti r_C. Dále pak experimentální část validuje použití Williamsovy řady na betonu. K tomuto je použito experimentálně zachycené pole posunutí metodou digitální korelace obrazu, které sloužilo jako vstupy k výpočtu členů Williamsovy řady. Poslední část je pak věnovaná vlivu agresivního prostředí na hodnoty lomové houževnatosti a také lomové odolnosti v kombinovaném módu I/II zatížení.

KLÍČOVÁ SLOVA

Brazilský disk, lomová mechanika, kombinovaný mód I/II, beton, MTS, GMTS, DIC

BIBLIOGRAFICKÁ CITACE

Ing. Petr Miarka *Analysis of Mixed Mode I/II Failure of Selected Structural Concrete Grades.* Brno, 2021. 151 s., 17 s. příl. Disertační práce. Vysoké učení technické v Brně, Fakulta stavební, Ústav stavební mechaniky. Vedoucí práce doc. Ing. Stanislav Seitl, Ph.D.

PROHLÁŠENÍ

Prohlašuji, že jsem disertační práci s názvem "*Analysis of Mixed Mode I/II Failure of Selected Structural Concrete Grades*" zpracoval samostatně a že jsem uvedl všechny použité informační zdroje.

V Brně dne 25. 2. 2021

Ing. Petr Miarka
autor práce

PROHLÁŠENÍ O SHODĚ LISTINNÉ A ELEKTRONICKÉ FORMY ZÁVĚREČNÉ PRÁCE

Prohlašuji, že elektronická forma odevzdané disertační práce s názvem „*Analysis of Mixed Mode I/II Failure of Selected Structural Concrete Grades*“ je shodná s odevzdanou listinnou formou.

V Brně dne 25. 2. 2021

Ing. Petr Miarka
autor práce

Acknowledgment

The completion of this work would not be possible without the support that I was receiving from many individuals, to whom I would like to express my gratitude.

I would like to appreciate the supervision of my work by doc. Ing. Stanislav Seitl, Ph.D. I am grateful that he gave me enough freedom to pursuit my own ideas and, at the same time, provided intense and enthusiastic guidance.

In the very same manner, my gratitude goes to prof. Wouter De Corte Ph.D., who found my interest in study of materials and in FEM modelling. He provided me with his unique critical thinking of my work whenever my ideas turned out to be questionable.

Apart from these gentlemen I must cordially express my gratitude to the colleagues, researchers and friends I was able to closely collaborate with or I could have a fruitful discussion with them over my work. Namely Josef Květoň, Jan Mašek, Lukáš Novák from Institute of Structural Mechanics FCE BUT whom made my Ph.D study unforgettable experience, Jan Klusák from Institute of Physics of Materials Czech Academy of Sciences who has been very helpful over the years spent at IPM, Vlastimil Bílek from the Faculty of Civil Engineering of Technical University of Ostrava who is able to develop any concrete mixture and also to colleagues from Ghent University – Arne Jansseune, Kizzy Van Meirvenne, Gieljan Vantyghen, Veerle Boel and Hanne Glass whom made my stay in Gent more than enjoyable.

In addition to my colleagues I need to express my gratitude to my oldest friends Martin and Lucka, whom encourage me over past years and to my biggest fan Verča together with Tomáš and Lucie, whom shared my joy and sometimes disappointment over my life and research decisions.

Finally and most importantly, I take this opportunity to express the deepest gratitude to my sister, parents, grandparents and to my girlfriend Barča. Their unconditional love and support helped me in times of self-doubt and allowed me to share my joy of my success. Without their care and support, my life would not be that simple.

The results presented in this work were achieved thanks to financial support of:

- **Brno PhD Talent** project Funded by the Brno City Municipality.
- Czech Science Foundation under the projects n.o. **GA18-12289Y** and **GA16-18702S**.
- Ministry of Education, Sports and Youth of under Specific University Research projects: **FAST-J-18-5164**, **FAST-S-18-5614**, **FAST-J-19-5783**, **FAST-S-19-5896**, **FAST-J-20-6341** and **FAST-S-20-6278**.
- Ministry of Industry and Trade under the project: **CZ.01.1.02/0.0/0.0/15_019/0004505 - KONANOS**.
- National Sustainability Programme I project: "**AdMaS UP** – Advanced Materials, Structures and Technologies" (**No. LO1408**) supported by the Ministry of Education, Youth and Sports of the Czech Republic and Brno University of Technology
- The mobility projects funded by the Ministry of Education, Youth and Sports of the Czech Republic with registration n.o. **8J18AT009** and **8J20AT013**.
- **IPMINFRA LM2015069** and **CEITEC 2020 LQ1601** funded by the Ministry of Education, Youth and Sports of the Czech Republic.

Thank you!

Table of Content

List of Figures

List of Tables

Chapter I
Introduction and problem statement

1. Introduction

The last two decades have witnessed a considerable progress towards the design, construction and maintenance of concrete structures which concerned both economic and environmental impacts of these structures on the environment to be built in. These two primary demands can be met by the development and eventual use of a material which exhibits higher mechanical performance and simultaneously has a lower environmental impact. The use of high-strength concrete (HSC) [1] allows for a material reduction in the structure's cross-sectional dimensions, while high-performance concrete (HPC) [2, 3] exhibits higher long-term performance and durability of the structure. The structures (e.g. bridges or beams) to be built from such materials can benefit from a greater span length, a shallow beam cross-section and an extended service lifetime.

The modern HPC and HSC mixtures used in the construction consume less natural resources, i.e. raw materials for cement production, aggregates, water, and their mixture typically contains less cement (lower CO_2 emission) [4, 5], while the mechanical and/or durability performance is enhanced. This results in a reduction of the production cost (subtle structural element) and CO_2 emissions (lower cement content). This reduction of natural resources is done by composing a concrete mixture which contains mineral admixtures, i.e. supplementary cementitious materials (SCM) like silica fume [6], ground granulated blast furnace slag [7], fly ash, or it can include natural pozzolans, e.g. pumice [8], metakaolin or zeolite [9] etc.

Regarding the strict CO_2 emission requirements, the concrete technology developed completely new cement free materials due to new sustainable binders. These cement free materials replaced cement by an alkali activated binder. Thus, the concrete made with such binder is called an alkali-activated concrete (AAC) [10, 11] or sometimes referred as geopolymers. In this case the grains hold together by reaction alkali-activators NaOH or KOH [12], which activate the precursors. The precursors can be, e.g. grinded and quenched blast furnace slags [10], various slags from ferrous and non-ferrous metallurgy [10], Fe-rich clays [13], ground coal bottom ash [14] and kaolin [15].

On the other hand, subtle structures made of the new materials drew attention to a comprehensive structural analysis, which resulted in the use of advanced material models as implemented in the finite element method (FEM) software. This overcame a traditional, sometimes empirical design methods mentioned in the standards [16, 17] or in recommendations [18], due to the lack of knowledge of the material's or structural response and may not be sufficient to provide an effective structural design.

Standard tests performed before the start of the numerical modelling provide information about the material's mechanical behaviour such as the compressive f_c or the tensile f_t strength, the Young's modulus E and the bulk density ρ. Advanced material behaviour can be described using fracture mechanical parameters (FMP) such as the fracture toughness K_{IC}, the fracture energy G_f, and the crack mouth opening displacement (*CMOD*) or the crack mouth opening sliding (*CMOS*). The fracture energy G_f is considered as an important material parameter, which depends on the aggregate size and the quality of the concrete [19, 20], although no definite test shape or procedure is agreed upon regarding a geometrically independent value [21, 22]. A verification of such a set of input data is usually conducted with the inverse analysis [23], with an example of such application to the fracture energy to be found in [24]. Thorough knowledge of this behaviour is required as it is the most important parameter in the post peak behaviour of the material in tension

as it is closely related to crack initiation; it also determines the durability within the structure's lifetime.

Due to the structural geometry, the loading conditions or the construction technology, concrete structures and their structural elements are typically subjected to a combination of bending and shear loads. The fracture process in such structural elements can be divided into actions from tensile loads (mode I), shear loads (mode II) or any combination of tensile and shear loads (mixed mode I/II).

Typically, tensile mode I crack opening and propagation are studied, while shear mode II is normally neglected in most research works. Even a simply supported beam with distributed load (see Figure 1(a)) carries such a combination of mode I and mode II load. If the stress distribution is plotted in principal stresses, one can find the location of the highest tensile mode I stresses and highest mode II shear stresses, which produce the main failure mechanism (transverse tension) of concrete structures. The highest normal mode I stress are located in the mid span of the beam, while the highest shear mode II stresses are located above support. These points attract most attention in the design process of the concrete beam.

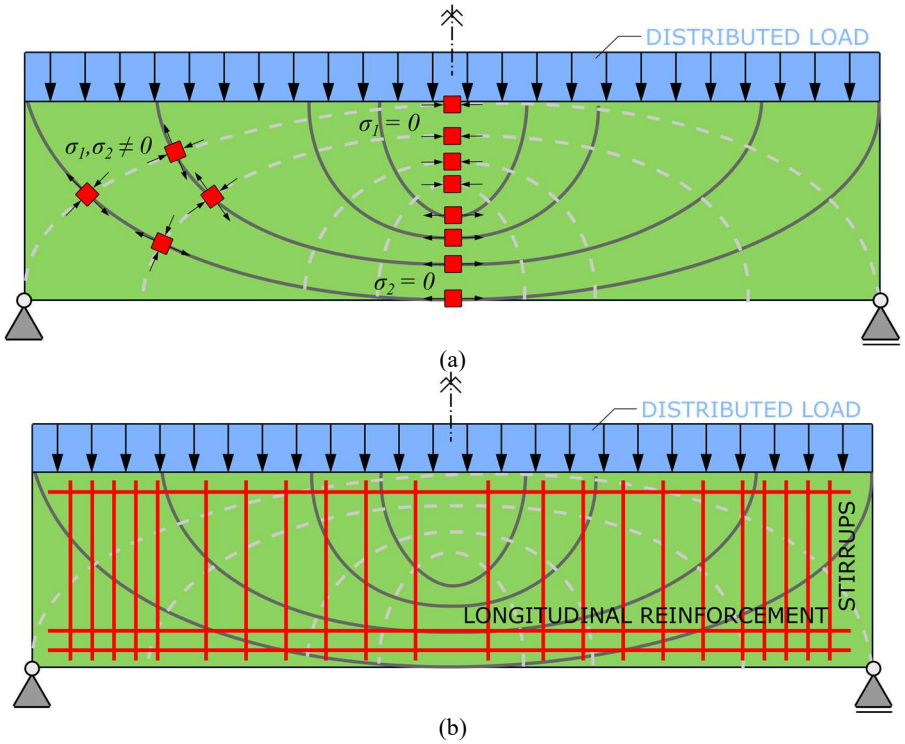

Figure 1: Principal stress σ_1 and σ_2 trajectories on the simply supported beam with a distributed load (a) and designed steel reinforcement (b).

Nevertheless, there is a location with a combination of tensile and shear stress which produces mixed mode I/II crack initiation. This fact is unintentionally omitted in studies, and in practice this weakest material point is strengthened using shear reinforcement – stirrups [16] (see Figure 1(b)). However, static or cyclic load [25, 26] can lead to micro-cracks in the concrete cover layer which propagate and increase in size until final failure occurs [27, 28]. This often leads to reinforcement exposure, and thus to the reduction of the total service lifetime [29-31]. Comprehensive numerical and experimental studies of combined tensile and shear failure of structural beam elements can be found in [32-35] or for slabs in [36, 37].

Despite the improved strength and performance, the HPC concrete is prone to forming micro-cracks, which propagate and increase in size throughout the cover layer. This leads to a significant durability issue as the steel reinforcement is exposed to weather conditions [29, 38-42]. Moreover, these weather conditions are often highly aggressive (de-icing salts or a marine environment) and

assist to accelerate the steel reinforcement corrosion which results into the structure's premature degradation [43, 44]. Typically, an aggressive environment exhibits the presence of chloride ions [44-46]. A large number of studies from multiple research fields have been devoted to this phenomenon, e.g. modeling of damage induced by chloride penetration [47-51], long-term concrete penetration resistance [52-55], or evaluation of the chloride penetration depth based on colorimetric methods [56-59]. Consequently, these studies resulted in the formulation of standards and proposed the methodology of assessing the level of chloride contamination in a concrete structure, e.g. Nordtest [60, 61], American Association of State and Highway Transportation [62, 63] or ASTM standard [64]. Moreover, knowing the relationship between the level of fracture and the rate of chloride penetration can significantly improve the accuracy and reliability of life estimation models [65].

Typically, the fracture mechanical parameters are evaluated from recommendations, where the specimens are prismatic plates, beams or cubes with rectangular/square cross-section e.g. the compact tension (CT) test [66], the three-point or the four-point bending (3PB, 4PB) test [67, 68] (Figure 2(a)) or the wedge splitting test (WST) [69-72] (Figure 2(b)). These tests provide information about the fracture behaviour under the tensile mode I. Information about shear mode II is provided by tests such as the eccentric asymmetric four-point bending test (EA4PBT) [73-75] (Figure 2(c)) or the double-edge notched specimen test (DENS) [76, 77] (Figure 2(d)). Finally, the mixed mode I/II fracture of concrete was studied in [78-80] by using several tests methods. Recently Lin et al. [81] investigated mixed mode I/II fracture failure of concrete through digital image correlation and later in [82] by acoustic emission. Lastly, Wei et al. [83, 84] showed accurate numerical results of crack propagation by combining fracture mechanical criteria and a single constitutive material model.

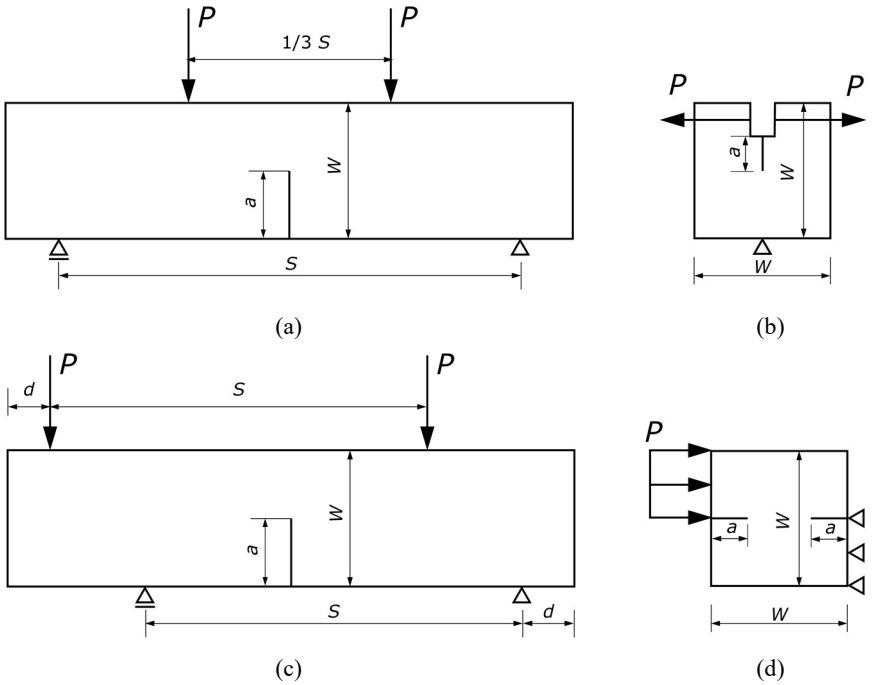

Figure 2: Comparison of test specimens for fracture mechanical tests – for mode I: four-point bending test (a) and wedge splitting test (b), for mode II: eccentric asymmetric four-point bending test (c) and double-edge notched specimen (d).

All of these tests can be used in the design of new structures as samples can be cast together with the structure in any shape and size. In contrast, for a structure to be renovated, a core has to be drilled, which removes a cylindrical material sample from the investigated structure. Reshaping a cylindrical sample into a prism is ineffective and expensive. Therefore, to avoid additional

unnecessary expenses, a fracture mechanical test should be performed on a specimen made directly from the core drill sample.

The Brazilian disc test with central notch (BDCN) [85-91] (Figure 3(a)) or semi-circular bend (SCB) test [92-97] (Figure 3(b)) suggest such an application and provide information about tensile mode I, combination of tensile and shear mixed mode I/II and pure shear mode II crack initiation conditions. The investigation of the mixed mode I/II is done by inclining the initial notch against the load position. This allows the fracture mechanical test to be performed under relatively simple experimental conditions using a standard compressive testing apparatus with sufficient load capacity.

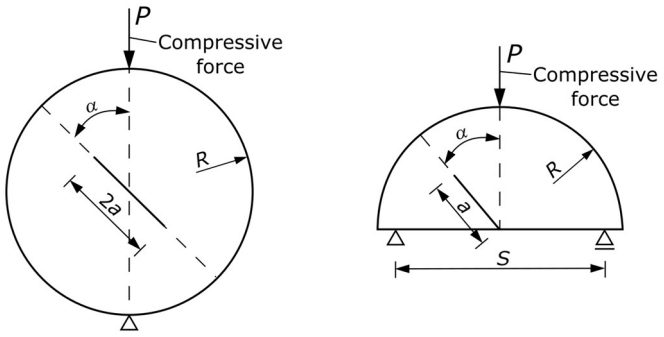

(a) (b)

Figure 3: Comparison of two fracture mechanical test made form core-drill sample – Brazilian disc with central notch (a) and semi-circular bend test (b).

The mixed-mode I/II fracture condition is achieved, in both of these specimens, by inclining the initial notch against the loading position. This fact reduces demands on the experiments, as a common testing apparatus with sufficient load capacity can be used. On the other hand, the preparation of the notches is more labour intensive and requires a skilled worked compared to traditional prismatic specimens.

2. Problem Statement

Concrete material is profoundly used in almost every civil engineering structures, which are part of the important infrastructure, already built or to be built. Technological progress and increasing ambitious, sometimes critical, requirements on the new structure have launched a complete change in the concrete technology and construction. Such requirements can be split into two main branches.

The first demand concerns environmental impacts with increased awareness of the CO_2 emissions reduction of whole cement industry. Consequently, the focus was placed on various mitigation strategies, which include variety of approaches e.g. fuel substitution, use of alternative raw materials, and use of material substitutes [5]. The other demand reflects both a need to repair current infrastructure, e.g. roads, bridges, buildings, where old system have lost its functionally and a need to build new infrastructure to expand current system. This aims to reduce structure's and maintenance costs over the designed structure's lifetime. Cost reduction potential is expected not only from the more environmental cement production but also from more efficient use of cement in concrete and in its application in construction industry. This implies the need for corresponding standards and quality measures to safeguard the concrete construction along the structure's life [4].

Such demands have gradually led to the development of new concrete mixtures with improved mechanical properties and structural response. However, the main failure of concrete structure is due to development of micro-cracks which are progressively increasing in size over the time and result in the major macro-crack. This process affects the structure's durability and reduces the

structure's life. Hence, the analysis of the crack initiation and propagation in concrete material is at most interest to reduce the additional cost or worse the structure demolition.

These cracks can initiate due to several reasons but mainly from the action of external loads i.e. static or cyclic. Static loads are present during whole structural activity and usually lead to single damage initiation, while the cyclic loads repeat themselves, which can result in the longer damage initiation process. Typically, it takes years for damage to be spotted and located on the structure. Both loading types lead to the crack initiation, which are results of excessive tension, shear or combination of both stress types present in the structure [98]. From the linear elastic fracture mechanics (LEFM) viewpoint, this process is called mixed mode I/II crack initiation and it can consider actions from both static and fatigue loads.

Recent studies investigating the fracture resistance under the mixed mode I/II based on a specimen with a circular geometry have used various fracture mechanical criteria and are not limited to concrete (e.g. rock, mortar, PMMA). All these criteria are based on the prediction of the crack initiation angle, i.e. they investigate only the onset of fracture under the mixed mode I/II and do not provide any information on crack propagation in the whole ligament area. Nevertheless, they predict the onset of fracture with good agreement to experimental measurements. In this thesis a generalized maximum tangential stress (GMTS) criterion will be used. The GMTS was recently validated in works by Hou et al. who presented accurate results on mortar and concrete [99] and by Seitl et al. on concrete C 50/60 [100].

Experimental verification of the analytical formulas mentioned in fracture mechanical handbooks, which are then used as an inputs to the fracture mechanical criteria, can be done by employing the digital image correlation (DIC) method [87, 103]. The DIC technique captures deformations fields of the specimen that arise due to the applied load during experimental testing. Such displacement fields captured in the close vicinity of the crack tip measured under the various mixed-mode I/II loading conditions is used to calculate fracture mechanical parameters.

Recent numerical and experimental studies place focus on the mixed mode I/II crack initiation as investigated by advanced and yet computationally demanding models. Another approach to investigate mixed mode I/II crack initiation is by employing the LEFM's fracture criteria. The application of fracture criteria shows both good agreement in prediction of material's failure and low computational demands. However, the literature only provides information about the crack initiation direction i.e. the onset of fracture and do not deal with the fracture process throughout the specimen.

The above-mentioned research objectives and standards mostly focus on the crack initiation and crack path prediction. However, the structure is exposed to combination of environmental and physical loads within the structure lifetime. The study presented by Veselý et al. [101, 102] investigated the dependence of crack growth with respect to ability of concrete to resist chloride ingress. However, the research of the actual effect of soluble chlorides on the crack development is unique, especially considering mixed mode I/II loading conditions. Therefore, the relationship between the FMPs of the cement-based composite/concrete and its resistance to chloride penetration is a very interesting problem to investigate together with the influence of the chloride penetration depth on the load bearing capacity of the cross-section. Thus, it is of the most interest to investigate the influence of the aggressive chloride environment on the fracture toughness and fracture resistance under the mixed mode I/II loading conditions.

This lack of knowledge of the material fracture resistance to the mixed-mode I/II has led to the present study.

3. Goals

3.1 General

Given the fact that the mixed mode I/II is present in many types of structures, including cyclically loaded ones a good knowledge and understanding of the static and fatigue crack initiation under the mixed mode I/II is crucial.

In order to achieve a correct and reliable application of the mixed mode I/II fracture resistance, this work aims to give better insight into crack initiation and failure mechanism of the mixed mode I/II load, which has been studied numerically and verified experimentally.

The main objectives of the presented thesis are:

a) Deepen the understanding of mixed mode I/II crack initiation conditions for concrete materials.
b) To analyse and validate the use of analytical formulas by employment of the digital image correlation technique.
c) Deepen the knowledge of governing role of the critical distance r_C on the mixed-mode I/II crack initiation process.
d) To establish the connection among the experimental results and the numerical simulation throughout appropriate material model.
e) To study the influence of the aggressive environment on the fracture resistance of under the mixed mode I/II load.
f) To verify applicability of the higher order terms of the Williams's expansion on the concrete materials.
g) Analyse the stress and strain fields by non-linear numerical analysis in order to give insights to crack initiation conditions under the mixed mode I/II.

3.2 Methods

Experimental research is carried out, considering various types of concrete mixtures, e.g. C50/60, two kinds of HPC, AAC and HSC. These mixtures were compared to the commonly used C 50/60 concrete grade in the fabrication of the precast concrete structural elements. Firstly, the mechanical tests were carried out to determinate the material's performance. Furthermore, comprehensive numerical simulation by finite elements models was carried out to analyse the crack initiation and failure mechanism under the mixed mode I/II load and to obtain analytical formulas for the used geometry. For this, two different software was used i.e. ANSYS and Abaqus, nonetheless the obtained results were not compared in between due to the licence agreement. Afterwards, these concrete mixtures were tested to obtain mixed mode I/II fracture resistance curves. In addition to this, the HPC mixture was studied by the digital image correlation technique to verify the analytical formulas given by the literature and to analyse the failure mechanism of the mixed mode I/II loading. Lastly the HPC mixture has been exposed to the aggressive environment to study the influence of aggressive environment on the FMPs.

This experimental research and mixture development were done in close cooperation with the ŽPSV s.r.o. company, Institute of Physics of Materials of the Czech Academy of the Sciences, Department of Building Materials and Diagnostics of Structures of the Faculty of Civil Engineering of Technical University of Ostrava, Department of Structural Engineering and Building Materials at Ghent University and Department of Civil and Materials Engineering at University of Malaga.

4. Contents

With the intention of a clear and concise setting out of the main concerns exposed, this thesis consists of six main chapters which analyse the mixed mode I/II fracture of concrete or concrete like materials by various analytical, numerical and experimental methods, since the mixed mode I/II fracture and crack initiation is often omitted in the structure's design process.

After a general introduction of linear elastic fracture mechanics in failure assessment, **Chapter II** introduces the Williams' expansion used for description of stress and displacement fields for cracked body together with the over-deterministic method used for determination of its higher order terms. Afterwards the fracture mechanism of concrete is described together with prosed models, both simplified and non-linear models, which take into account concrete specific behaviour. Lastly, the material model, concrete damage plasticity, as implemented in finite element software Abaqus is presented, which was used in the non-linear analysis.

Chapter III lists the studied concrete mixtures composition and gives an overview of measured mechanical properties. Furthermore, the applied test procedures and corresponding specimens are described. Additionally, the digital image correlation technique is introduced as it was used for the evaluation of Williams's expansion coefficients. The Chapter III concludes with the introduction on the chloride penetration depth measurement and presents the experimental details of the aggressive environment.

Chapter IV deals with the numerical modelling of the mixed-mode I/II fracture by employing both linear elastic fracture mechanics and non-linear material model. The geometry, boundary conditions are introduced and described for botch modelling approaches. The non-linear analysis is extended by the model calibration by means of the material model's parameters. Afterwards the numerical results are discussed and present for both parts. The numerical research is using the measured material's characteristic from Chapter III as input parameters.

In **Chapter V** experimental results found on the geometries and material as presented in Chapter III are shown and discussed. The main focus was set to analyse the fracture resistance under the mixed mode I/II loading conditions and to compare evaluated fracture resistance curves for each material between each other. The validation of the applicability of the Williams' expansion on the concrete specimen is done by employing the digital image correlation technique. Lastly, the study of influence of the aggressive environment on the fracture resistance under the mixed mode I/II and its results are presented here.

Final conclusions and concluding remarks are drawn regarding the conducted fracture mechanical study on the mixed mode I/II failure in **Chapter VI**. The proposal for future work is given here as well.

Chapter II
Theoretical Background

Concrete cracking is a very complex mechanism, which is substantially different from the cracking behaviour of the other materials used in civil engineering industry. Over the last few decades, suitable fracture mechanical models, together with test configuration have been established to determinate the fracture mechanical parameters of concrete, which belongs to quasi-brittle materials. This chapter gives a brief history of the fundamental concepts of fracture mechanics in general and the specific concrete fracture. Special attention is paid to the description of the stress and displacement fields in cracked body under the mixed mode I/II loading, together with typical aspects of strain softening, bridging stresses and fracture energy, which are found in literature. Finally, an overview of material models suitable for non-linear numerical analysis are presented together with Concrete Damaged Plasticity material model and its input parameters.

1. Linear Elastic Fracture Mechanics

The fundamental concepts of fracture mechanics have been established in 1920 by Griffith [104], in which Griffith prosed hypothesis of the unstable crack propagation based on the first law of thermodynamics. This hypothesis is based on the elliptical hole/crack concept, which was published by Inglis in 1913 [105]. Griffith established an energy-based relationship between applied stress and crack length: when the strain-energy change, which results from an increment of crack growth, is sufficient to overcome the surface energy of the material a flaw becomes unstable and thus the fracture failure occurs. This hypothesis correctly predicted failure, if applied to glass specimen. If applied to other material, like to ductile metals, Griffith's approach has some shortcomings. Therefore, Irwin [106] developed a modified version of the Griffith's energy-based approach. Irwin in his modifications used Westergaard's approach, which showed that the stresses and displacements near the crack tip can be described by a single constant, related to the energy release rate, which is now called the stress intensity factor (SIF). During the same period of time, Williams [107] and [108] applied a somewhat different technique to derive crack tip solutions with results essentially identical to Irwin's results. These concepts of fracture mechanics that were derived prior to 1960 are applicable only to materials that obey Hooke's law, with some corrections for small-scale plasticity. These analyses are restricted to structures whose global behaviour is linear elastic, therefore this research field is call linear elastic fracture mechanics shortly - LEFM.

During relatively short period of time 1960-1961, several researchers turned their attention to the crack-tip plasticity. The corrections were made to the yielding at the crack tip including Irwin [109], which is relatively simple extension of the LEFM concept. While Dugdale [110] and Barenblatt [111] have developed somewhat more complex models. First application of the fracture mechanics to concrete was done by Kaplan in 1961 [112]. Another milestone in researching the flaws and material failure was done by Rice in 1968 [113], who developed characterization of the nonlinear material behaviour ahead of the crack tip. Rice idealized the plastic deformation as nonlinear elastic, which generalize the energy release to the nonlinear materials. He showed that this generalization of energy release rate can be expressed as a line integral, which he called the *J*-integral, evaluated along the contour around the crack. That same year, the Hutchinson [114] and Rice and Rosengren [115] showed that the *J*-integral can be viewed as a nonlinear stress intensity parameter as well as an energy release rate. This method is now known as a HRR solution.

This thesis, in most of its parts, deals with the LEFM concept and uses the solution prosed by Williams [107]. The LEFM is study using methods of the linear elastic stress analysis in the close vicinity of the crack tip in homogeneous isotropic cracked material, under which a crack or crack-like flaw will extend. The literature dedicated to LEFM recognize three basic modes of the crack opening [116-118]. These crack opening modes are showed in Figure 4.

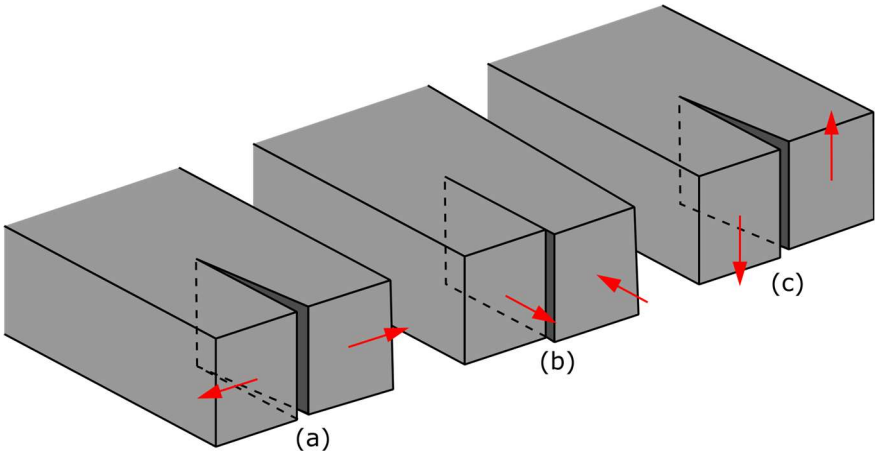

Figure 4: Basic crack opening modes recognized by LEFM – (a) -Mode I, the tensile opening mode, (b) – Mode II, the in-plane shear mode and (c) – Mode III, the out-plane shear mode.

Mode I, the opening mode is when the opposing crack faces/surfaces move directly apart due to tensile load, Figure 4(a). Mode II, so-called the in-plane shear, is present when the crack faces/surfaces move over each other perpendicular to the crack front, Figure 4(b). The Mode III, so-called the out-plane shear is present when the crack surfaces move over from each other parallel to the crack front, Figure 4(c). Any combination of such a loading mode is called mixed mode loading conditions. Further in this thesis the crack analysis is limited to the two-dimensional (2D) problem with focus set to analyse the combination of tensile mode I and shear mode II i.e. the mixed mode I/II loading conditions.

1.1 Stress Fields for Mixed mode I/II

The abovementioned LEFM concept derived by Williams uses, in most of the applications, the stress field in the close vicinity of the crack tip described by Williams' expansion (WE) [107]. This expansion is an infinite power series originally derived for a homogenous elastic isotropic cracked body, which can be described by a following Airy's stress function:

$$\phi(r,\theta) = \sum_{n=0}^{\infty} r^{\lambda_n+1} F_n(\theta), \tag{2.1}$$

where $F_n(\theta)$ are the corresponding eigenfunctions, which have following form:

$$F_n(\theta) = A_n \sin(\lambda_n + 1)\,\theta + B_n \cos(\lambda_n + 1)\,\theta + C_n \sin(\lambda_n - 1)\,\theta + D_n \cos(\lambda_n - 1)\,\theta, \tag{2.2}$$

where A_n, B_n, C_n, D_n, are unknown constants to be determined, which have to satisfy traction free boundary condition along the crack surface for $\theta = \pm\,\pi$ i.e. $\sigma_{\theta\theta}(0) = \sigma_{\theta\theta}(2\pi) = 0$ and $\sigma_{r\theta}(0) = \sigma_{r\theta}(2\pi) = 0$, and λ_n are the eigenvalues and the roots of eigenvalues are:

$$\lambda_n = \frac{n}{2}, n = 0, \pm1, \pm2, \ldots \tag{2.3}$$

The negative values of λ_n would give rise to infinite displacements at the crack tip, which is not physically permissible, and a zero λ_n ($n = 0$) leads to physically impermissible unbounded strain energy in a small disc area around the crack tip, hence those values are excluded [117]. Hence,

the only positive eigenvalues are kept. For the detailed derivation of the WE for all three loading modes author recommends Chapter 3 from the literature [118].

After receiving solution and some mathematical manipulation the WE can be rewritten into stress tensor form, which accuracy depends on the number of terms used and known stress function. The stress tensor using in Cartesian coordinates for mode I and mode II described by WE have a following form:

$$\begin{Bmatrix}\sigma_{xx}\\ \sigma_{yy}\\ \sigma_{xy}\end{Bmatrix} = \sum_{n=1}^{\infty}\frac{n}{2}A_n r^{\left(\frac{n}{2}-1\right)}\begin{Bmatrix}\left(2+\frac{n}{2}+(-1)^n\right)cos\left(\frac{n}{2}-1\right)\theta-\left(\frac{n}{2}-1\right)cos\left(\frac{n}{2}-3\right)\theta\\ \left(2-\frac{n}{2}-(-1)^n\right)cos\left(\frac{n}{2}-1\right)\theta+\left(\frac{n}{2}-1\right)cos\left(\frac{n}{2}-3\right)\theta\\ \left(\frac{n}{2}-1\right)sin\left(\frac{n}{2}-3\right)\theta-\left(\frac{n}{2}+(-1)^n\right)sin\left(\frac{n}{2}-1\right)\theta\end{Bmatrix}$$
$$-\sum_{m=1}^{\infty}\frac{m}{2}B_n r^{\left(\frac{m}{2}-1\right)}\begin{Bmatrix}\left(2+\frac{m}{2}-(-1)^m\right)sin\left(\frac{m}{2}-1\right)\theta-\left(\frac{m}{2}-1\right)sin\left(\frac{m}{2}-3\right)\theta\\ \left(2-\frac{m}{2}+(-1)^m\right)sin\left(\frac{m}{2}-1\right)\theta+\left(\frac{m}{2}-1\right)sin\left(\frac{m}{2}-3\right)\theta\\ -\left(\frac{m}{2}-1\right)cos\left(\frac{m}{2}-3\right)\theta+\left(\frac{m}{2}-(-1)^m\right)cos\left(\frac{m}{2}-1\right)\theta\end{Bmatrix}, \quad (2.4)$$

where r and θ are the polar coordinates, n, m are the orders of the term in the WE infinite power series, coefficient A_n corresponds to mode I and coefficient B_m corresponds to mode II. The coefficient of the first singular term for $n = 1$, i.e. A_1, is related to the stress intensity factor (SIF) for mode I, and the second coefficient A_2 corresponds to the distance-independent term called T-stress. For mode II the first singular term for $m = 1$, i.e. B_1, is related to the SIF for mode II. These engineering terms can be calculated as follows:

$$K_I = \sqrt{2\pi}A_1, T = 4A_2, K_{II} = -\sqrt{2\pi}B_1. \quad (2.5)$$

Using Eq. (2.5) a stress tensor from Eq. (2.4) can be rewritten into a simplified two-parameter form:

$$\sigma_{i,j} = \frac{K_I}{\sqrt{2\pi r}}f_{i,j}^{I}(\theta) + \frac{K_{II}}{\sqrt{2\pi r}}f_{i,j}^{II}(\theta) + T + O_{i,j}(r,\theta) \quad (2.6)$$

where σ_{ij} represents the stress tensor components, K_I, K_{II} are the SIFs for mode I and mode II, respectively, $f_{i,j}^{I}(\theta)$, $f_{i,j}^{II}(\theta)$, are known shape functions for mode I and mode II (with origin at the crack tip; crack faces lie along the (x-axis) and $O_{i,j}$ are the higher order (HO) terms. The Cartesian coordinate system formulation for the stress tensor used in Eq. (2.4) is shown in Figure 5(a), while the same stress tensor in polar coordinates is shown in Figure 5(b).

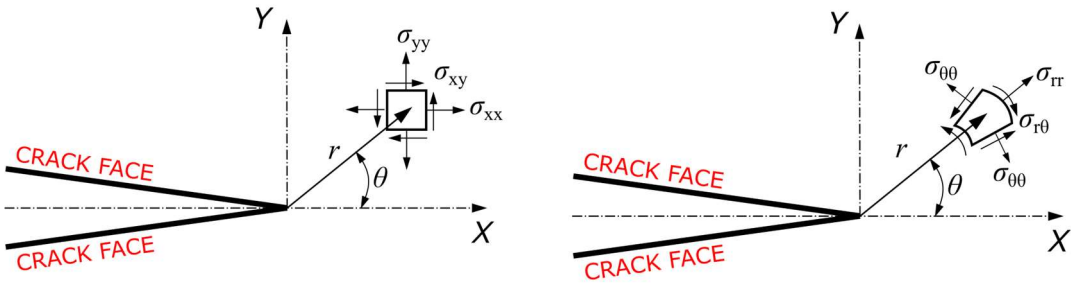

Figure 5: Stress tensor components in the Cartesian coordinate system (a) and in the polar coordinate system (b) with the origin at the crack tip.

Further in this thesis, for the description of the stress fields around the crack tip a polar coordinate system is used. For this a stress tensor component using SIFs and T-stress can be expressed in following form:

$$\sigma_{rr} = \frac{K_I}{\sqrt{2\pi r}} cos\left(\frac{\theta}{2}\right)\left[1 + sin^2\left(\frac{\theta}{2}\right)\right] + \frac{K_{II}}{\sqrt{2\pi r}} sin\left(\frac{\theta}{2}\right)\left[1 + 3sin^2\left(\frac{\theta}{2}\right)\right] + Tcos^2\theta + O\left(r^{\frac{1}{2}}\right), \quad (2.7)$$

$$\sigma_{\theta\theta} = \frac{K_I}{\sqrt{2\pi r}} cos\left(\frac{\theta}{2}\right)\left[cos^2\left(\frac{\theta}{2}\right)\right] - \frac{K_{II}}{\sqrt{2\pi r}} sin\left(\frac{\theta}{2}\right)\left[3cos^2\left(\frac{\theta}{2}\right)\right] + Tsin^2\theta + O\left(r^{1/2}\right), \quad (2.8)$$

$$\tau_{r\theta} = \frac{K_I}{\sqrt{2\pi r}} cos\left(\frac{\theta}{2}\right) sin\left(\frac{\theta}{2}\right) + \frac{K_{II}}{\sqrt{2\pi r}} cos\left(\frac{\theta}{2}\right)\left[1 - 3sin^2\left(\frac{\theta}{2}\right)\right] + Tsin^2\theta + O\left(r^{1/2}\right). \quad (2.9)$$

The stress field in the polar coordinates can be obtained from stress tensor written in Cartesian coordinate system by using coordinate system transformation. Transformation from Cartesian to polar coordinates is done by following expressions:

$$\sigma_{rr} = \sigma_{xx}cos^2\theta + \sigma_{yy}sin^2\theta + 2\sigma_{xy}\sin\theta\cos\theta, \quad (2.10)$$

$$\sigma_{\theta\theta} = \sigma_{xx}sin^2\theta + \sigma_{yy}cos^2\theta - 2\sigma_{xy}\sin\theta\cos\theta, \quad (2.11)$$

$$\sigma_{r\theta} = \left(\sigma_{yy} - \sigma_{xx}\right)\sin\theta\cos\theta + \sigma_{xy}(cos^2\theta - sin^2\theta). \quad (2.12)$$

The transformation from polar coordinate system to Cartesian coordinate system is done by Eq. (2.13)-(2.15):

$$\sigma_{xx} = \sigma_{rr}cos^2\theta + \sigma_{\theta\theta}sin^2\theta + 2\sigma_{r\theta}\sin 2\theta, \quad (2.13)$$

$$\sigma_{yy} = \sigma_{rr}sin^2\theta + \sigma_{\theta\theta}cos^2\theta - \sigma_{r\theta}\sin 2\theta, \quad (2.14)$$

$$\sigma_{xy} = (\sigma_{rr} - \sigma_{\theta\theta})\sin\theta\cos\theta + \sigma_{r\theta}(\cos 2\theta), \quad (2.15)$$

1.1.1 Fracture Toughness

In material science, if the stress intensity factor approach is used, the fracture toughness K_{IC} is the critical stress intensity factor of a cracked body/component. Thus, stress intensity factor K_I can be analytically calculated from:

$$K_I = \sigma\sqrt{\pi a}Y_I, \quad (2.16)$$

where σ is the applied stress, a is the crack length and Y_I is the geometry function dependent on the shape of the test specimen.

Material's failure occurs when $K_I \geq K_{IC}$, K_I is driving force and K_{IC} is a measure of material resistance. This happens when, the maximum applied force or sometimes called critical force P_C remotely produces the critical stress σ_C in Eq. (2.16), which caused sudden specimen's/structure failure.

In the Irwin's approach to energy release rate G, the relationship between K_I and G is defined as the rate of change in potential energy with the crack area for a linear elastic material. Then this relationship is given:

$$G = \frac{{K_I}^2}{E} \Leftrightarrow K_I = \sqrt{GE}, \quad (2.17)$$

where E is the material's Young's modulus of elasticity. Thus, the fracture toughness can be expressed by both $K_{IC} \geq G_{IC}$. Similarly, to this the stress intensity factor and fracture toughness is applicable for other two loading modes i.e. in plane shear mode II and out-plane shear mode III (as presented in Figure 4(b) and (c)).

Fracture toughness K_{IC} is considered to be size-independent material property used as a fracture parameter. The fracture toughness is used to analyse the brittle fracture of glass, rocks, polymers and ceramics. Another application is found in the fatigue crack propagation, analysed by Paris-Erdogan power law [119], as it denotes the value, for which crack propagation suddenly becomes rapid and unlimited. In addition to this, fracture toughness is used in the analysis of the mixed

mode I/II fracture resistance by employing various criteria. Most of these criteria consider the failure, which is mainly in mode I. Thus, the fracture toughness K_{IC} plays a key role in such analysis.

1.1.2 T-stress

The elastic 2D *T*-stress or the first non-singular stress term of the WE ($n = 2$), has been used as a measure of constraint, which acts parallel to the crack line. The sign and magnitude of the *T*-stress has a great effect on the size and shape of the crack tip plastic zone for mode I loading. Specimens with a negative *T*-stress have lower constraint compared with those having a positive *T*-stress. This effect of constraint level on the shape and size of the plastic zone is presented in Figure 6.

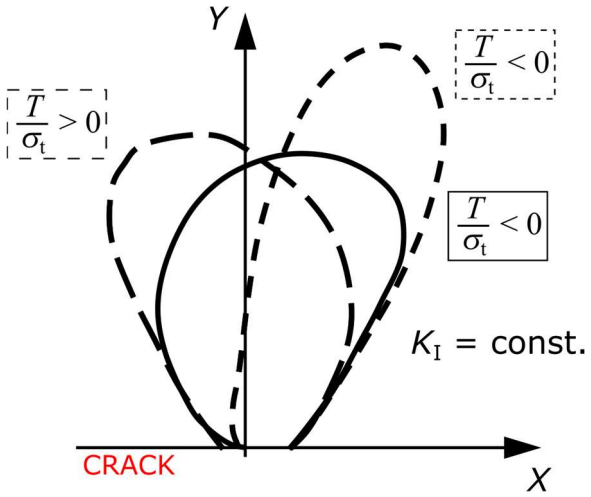

Figure 6: Influence of the *T*-stress on the shape and size of the plastic zone ahead of crack tip and its close vicinity adopted from [120].

From Figure 6, it can be observed, that if the *T*-stress > 0 MPa, the shape of the plastic zone works to slow down the crack propagation, while the size and shape of the plastic zone for values of *T*-stress < 0 MPa tends to increase the crack propagation [120]. In practical testing it is recommended to use test configuration, for which *T*-stress has value 0 MPa for early stages of the crack initiation and propagation. These different values of *T*-stress change the crack initiation direction and crack path direction. The influence of the constraint effect has been showed experimentally on the fatigue crack propagation experiments performed by Hutař et al. [121, 122] and recently by Miarka et al. [123]. For more details of the *T*-stress effects on the crack tip stress fields, author recommends the Gupta's review article [124].

Elastic *T*-stress can be calculated by using Kfouri's method [125] based on the path independent interaction integral, or directly from the stresses ahead of crack tip by using direct extrapolation method. The direct extrapolation method was proposed by Yang [126] calculates *T*-stress at a polar angle $\theta = 0°$ as:

$$T = \lim_{r \to 0} (\sigma_{xx} - \sigma_{yy}). \tag{2.18}$$

Another method to obtain value of the elastic *T*-stress is by analytical formulas, which can be found in works/handbooks made by Leevers and Radon [127], Knésl and Bednář [128], and Fett [129]. All of these authors proposed the following relation between the biaxiality parameter β, mode I stress intensity factor K_I, *T*-stress T and crack length a:

$$T = \frac{\beta K_I}{\sqrt{\pi a}}, \tag{2.19}$$

where β is the biaxiality parameter, K_I is the stress intensity factor for mode I and a is the crack length.

With a recent development and implementation of the *T*-stress calculation routines to FEM software, development of advanced fracture criteria for mixed mode I/II fracture arose and have been used in practice. The traditional and advanced fracture criteria are briefly discussed in section 1.3 of this thesis.

For the fast and sufficiently accurate calculation of the SIF and *T*-stress, an interaction integral [125] (which is a derivation of the *J*-integral [113]) was used in this thesis. The interaction integral *I*-integral is implemented in the employed FEM software ANSYS. This calculation uses a path-independent integral around the notch at various radial distances, which can be used for 2D or 3D analysis.

The interaction integral has the following form:

$$I = \frac{2}{E^*}(K_1 K_1^{aux} + K_2 K_2^{aux}) + \frac{1}{\mu} K_3 K_3^{aux}, \tag{2.20}$$

where K_i is the stress intensity factor for mode I, II and III, K_i^{aux} is the auxiliary stress intensity factor for mode I, II and III, E^* is the Young's modulus for plane strain $E/(1-\nu^2)$, ν is the Poisson's ratio and μ is the shear modulus. For a 2D problem the SIF for mode III K_3 is equal to 0. The *T*-stress is then calculated using the following equation:

$$T = \frac{E}{(1-\upsilon^2)}\left\{\frac{I}{f} + \upsilon\varepsilon_{33}\right\}, \tag{2.21}$$

where *I* is the interaction integral from Eq. (2.20), *f* is the line load applied along the crack front (typically $f = 1$) and ε_{33} is the extensional strain at the crack front in the direction tangential to the crack front.

1.2 Displacements Fields for Mixed Mode I/II

As with the stresses, the displacement field for mixed mode I/II load conditions around the crack tip can be expressed using the WE [130]. The displacement in the direction of *x*-axis *u* is expressed as:

$$\begin{aligned} u = &\sum_{n=0}^{N} \frac{A_n}{2\mu} r^{\frac{n}{2}} \left\{\left(\kappa + \frac{n}{2} + (-1)^n\right) cos\frac{n}{2}\theta - \frac{n}{2} cos\left(\frac{n}{2} - 2\right)\theta\right\} \\ &+ \sum_{m=0}^{M} \frac{B_m}{2\mu} r^{\frac{m}{2}} \left\{\left(-\kappa - \frac{m}{2} + (-1)^m\right) sin\frac{m}{2}\theta + \frac{m}{2} sin\left(\frac{m}{2} - 2\right)\theta\right\}, \end{aligned} \tag{2.22}$$

while the displacement in the direction of *y*-axis *v* is expressed as:

$$\begin{aligned} v = &\sum_{n=0}^{N} \frac{A_n}{2\mu} r^{\frac{n}{2}} \left\{\left(\kappa - \frac{n}{2} - (-1)^n\right) sin\frac{n}{2}\theta - \frac{n}{2} sin\left(\frac{n}{2} - 2\right)\theta\right\} \\ &+ \sum_{m=0}^{M} \frac{B_m}{2\mu} r^{\frac{m}{2}} \left\{\left(\kappa - \frac{m}{2} + (-1)^m\right) cos\frac{m}{2}\theta + \frac{m}{2} cos\left(\frac{m}{2} - 2\right)\theta\right\}, \end{aligned} \tag{2.23}$$

where *u* and *v* are the displacement vector components in the *x* and *y* direction, μ is the shear modulus, which can be expressed as $E/2(1 + \nu)$, κ is Kolosov's constant for plane strain $3 - 4\nu$ and for plane stress $(3 - \nu)/(1 + \nu)$ conditions, and *E* and ν are the Young's modulus and the Poisson's ratio, respectively.

For an easier orientation, the Eqs. (2.22) - (2.23) can be simplified as:

$$u = f_0 A_0 + \sum_{n=1}^{N} A_n f_n^I(r,\theta) + \sum_{m=0}^{M} B_m f_m^{II}(r,\theta), \tag{2.24}$$

$$v = g_0 B_0 + \sum_{n=0}^{N} A_n g_n^I(r,\theta) + \sum_{m=1}^{M} B_m g_m^{II}(r,\theta)\,, \tag{2.25}$$

where $f_n^I(r,\theta)$ and $g_n^I(r,\theta)$ are known geometry functions for mode I and $f_n^{II}(r,\theta)$ and $g_n^{II}(r,\theta)$ are known geometry functions for mode II in polar coordinates.

The rigid body rotation and translation of the crack tip is shown in Figure 7.

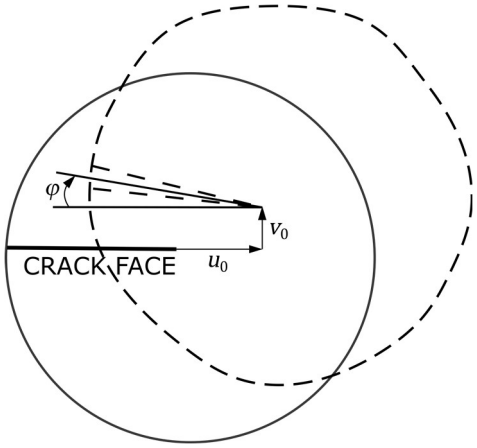

Figure 7: Rigid body translation at the crack tip and rigid body rotation with respect to the crack tip [130].

The terms f_0A_0 and g_0B_0 from Eqs. (2.24) and (2.25) are the displacements corresponding to $n = 0$ and are directly related to the rigid body translation of the crack tip. Such displacement components can be written as:

$$u_0 = f_0 A_0 = \frac{\kappa+1}{2\mu} A_0, \tag{2.26}$$

$$v = g_0 B_0 = \frac{\kappa+1}{2\mu} B_0. \tag{2.27}$$

These displacement u_0 and v_0 are independent of the position of the points and can be taken as the rigid body translation of the crack tip. In addition, the displacement components corresponding to the second term of mode II expansion are:

$$u = -\frac{\kappa+1}{2\mu} B_2 r \sin\theta = -\frac{\kappa+1}{2\mu} B_2 y = \varphi y, \tag{2.28}$$

$$v = \frac{\kappa+1}{2\mu} B_2 r \cos\theta = -\frac{\kappa+1}{2\mu} B_2 x = \varphi x, \tag{2.29}$$

where x and y are the Cartesian coordinates. The term B_2 is directly related to the rigid body rotation of the crack with respect to the crack tip as $\varphi = -(\kappa + 1)B_2/2\mu$. Therefore, the rigid body translation of the crack depends on the coefficients A_0 and B_0 and the rigid body rotation with respect to the crack tip depends on B_2. The magnitude of the rigid body rotation of the crack, denoted by φ, is equal to the angle between original direction of the crack and the bisector of crack faces after the structural deformation.

1.3 Mixed Mode I/II Fracture criteria

In the engineering practice the structure or its components are very often loaded with multiple types of loads which produce the mixed mode I/II fracture. Knowledge of the direction of the crack initiation can help to extend the structure's life and reduce structure's sudden failures. Subsequently, the crack will initiate under the mixed mode I/II condition, however later in the crack propagation process, it will turn into direction where the mode I prevail [131].

Usually the mixed mode I/II fracture analysis is done by employing various fracture criteria. Traditional criteria are e.g. maximum tangential stress (MTS) criterion postulated by Erdogan and Sih in 1963 [132] and strain energy density (SED) criterion postulated by Sih in 1974 [133, 134]. Both criteria use in the mixed mode I/II fracture analysis only SIFs for mode I and mode II. Consequently, the computational demands are low as the solution is simple linear or quadratic equation.

The recent development of fracture analysis of mixed mode I/II loading conditions lead to postulate advanced fracture criteria e.g. generalized strain energy density (GSED) criterion [135, 136], averaged strain energy density (ASED) criterion [137-139], extended maximum tangential strain (EMTSN) criterion [140-142] and generalized maximum tangential stress (GMTS) criterion [143, 144]. These recent fracture criteria are using SIFs as well as the traditional ones together with additional parameters. These parameters are the *T*-stress (i.e. the second term of the WE) or more WE terms and the critical distance r_C. Employment of additional parameters leads to more computationally demanded procedures, which are mainly solved numerically.

Further in this thesis the GMTS is applied to the mixed-mode I/II fracture analysis. The GMTS is comprehensively described and discussed in the following subsection, is used to predict mixed mode I/II fracture. The difference between the MTS and GMTS is showed, together with another approach to the MTS criterion. In addition, a GSED criterion is described as well as it uses the *T*-stress to determinate the mixed-mode I/II failure.

1.3.1 Generalised Maximum Tangential Criterion

The GMTS criterion is extension of the traditional MTS criterion. The GMTS, uses the tangential stress $\sigma_{\theta\theta}$ as presented in Eq. (2.8) on p. 12. The $\sigma_{\theta\theta}$ is expressed by using first two engineering terms presented in Eq. (2.5) on p. 11 i.e. K_I and T for mode I and K_{II} for mode II.

The maximum value is found by search for function maximum and by complying to the conditions, then crack initiation direction θ_0 can be obtained from conditions when:

$$\frac{\partial \sigma_{\theta\theta}}{\partial \theta}|_{\theta=\theta_0} = 0 \text{ and } \frac{\partial^2 \sigma_{\theta\theta}}{\partial^2 \theta} < 0. \tag{2.30}$$

This modifies Eq. (2.8) on p. 12 to following form of MTS criterion:

$$[K_I sin\theta_0 + K_{II}(3cos\theta_0 - 1)] = 0 \tag{2.31}$$

or in GMTS form:

$$[K_I sin\theta_0 + K_{II}(3cos\theta_0 - 1)] - \frac{16T}{3}\sqrt{2\pi r_c} cos\theta_0 sin\frac{\theta_0}{2} = 0. \tag{2.32}$$

The main difference between Eq. (2.31) and Eq. (2.32) is that the crack initiation angle θ_0 of the maximum tangential stress $\sigma_{\theta\theta}$ for any combination of modes I and II depends on K_I, K_{II}, T and on the critical distance r_C. Please note, if the critical distance $r_C = 0$, the GMTS expression simplified itself to MTS expression as presented in Eq. (2.31). The angle θ_0 determined from Eq. (2.32) is then used to predict the direction of the mixed mode I/II fracture.

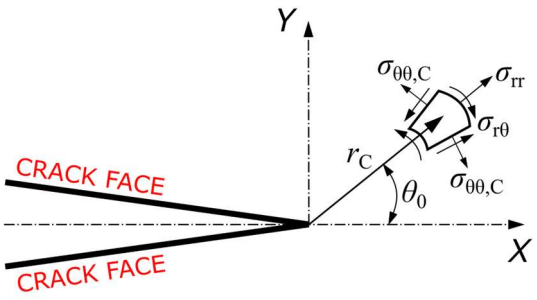

Figure 8: Stress tensor in polar coordinates with a critical distance r_C, onset of fracture θ_0 and critical tangential stress $\sigma_{\theta\theta,C}$ with the origin at the crack tip.

According to GMTS criterion for mixed mode I/II, the brittle fracture occurs radially from the crack in the direction of the maximum tangential stress θ_0. The crack initiate when along the θ_0 and critical distance r_C the maximum tangential stress $\sigma_{\theta\theta}$ reaches its critical value $\sigma_{\theta\theta,C}$ (See Figure 8). The brittle fracture occurs when $K_I = K_{IC}$, $K_{II} = 0$. and $\theta_0 = 0°$, this assumption simplifies Eq. (2.8) on p. 12 to:

$$\sqrt{2\pi r_C}\sigma_{\theta\theta,C} = K_{IC}, \tag{2.33}$$

where K_{IC} is the fracture toughness for mode I.

The brittle fracture can be obtained by substituting the fracture toughness K_{IC} and found crack initiation direction θ_0 into Eq. (2.8). This will lead to:

$$K_{Ic} = cos\frac{\theta_0}{2}\left[K_I cos^2\frac{\theta_0}{2} - \frac{3}{2}K_{II}sin\theta_0\right] + \sqrt{2\pi r_c}Tsin^2\theta_0. \tag{2.34}$$

Such Eq. (2.34) can be used for the calculation of fracture initiation for pure mode I, pure mode II and mixed mode I/II.

In addition to above-mentioned the MTS and GMTS two more criteria are presented. First one is the analytical maximum average tangential stress (MATS) criterion postulated by Matvienko in 2012 [145], which uses first two terms and second one semi-analytical MATS postulated by Klusák [146], which uses numerically generated tangential stress $\sigma_{\theta\theta}$ with infinite number of WE terms. Both criteria can be express as:

$$\bar{\sigma}_{\theta\theta} = \frac{1}{d_{avg}}\int_0^{d_{avg}} \sigma_{\theta\theta}(r)dr, \tag{2.35}$$

where d_{avg} is the length over which is the tangential stress $\sigma_{\theta\theta}$ averaged. In case of Matvienko's approach to MATS, the tangential stress $\sigma_{\theta\theta}$ is expressed from Eq. (2.8) on p. 12 and then analytically operated. In case of Klusák's approach, the tangential stress $\sigma_{\theta\theta}$ generated from FEM solution is averaged radially in distance d for each polar angle θ. In addition to this, Klusák's approach can be simply applied on the wedge notch types and on the bi-material's interfaces. In both cases the conditions from Eq. (2.30) have to be fulfilled.

1.3.2 Generalised Strain Energy Density Criterion

The generalised strain energy density (GSED) criterion [135] is hereunder introduced as it can be directly compared to the GMTS criterion. In comparison to the GMTS criterion, the GESD criterion is based on the idea that a crack growth will take place in the direction where the strain energy reaches its minimum.

The strain energy density function dW/dV stored in an element dV for 2D solution can be written as:

$$\frac{dW}{dV} = \frac{1}{2\mu}\left[\frac{\kappa+1}{8}(\sigma_{rr}+\sigma_{\theta\theta})^2 - \sigma_{rr}\sigma_{\theta\theta} + \sigma_{r\theta}^2\right] = 0, \tag{2.36}$$

where, μ is the shear modulus $\mu=E/(2(1+\nu))$ and κ is the Kollosov's constant. The strain energy density (SED) factor, S, which represents the elastic energy field in the vicinity of the crack tip is defined as:

$$S = r\frac{dW}{dV} > 0. \tag{2.37}$$

This minimum can be obtained from the conditions:

$$\frac{\partial S}{\partial \theta}|_{\theta=\theta_0} = 0 \text{ and } \frac{\partial^2 S}{\partial^2 \theta} > 0. \tag{2.38}$$

By replacing the stress components from Eqs. (2.8)-(2.10) on p. 12 into Eq. (2.37) and by applying the conditions stated in Eq. (2.38) one may derive the crack initiation direction θ_0:

$$\begin{aligned} C_1K_I^2 + C_2K_{II}^2 + C_3K_IK_{II} + C_4\left(\beta^{SE}\alpha^{SE}K_{eff}\right)K_I + C_5\left(\beta^{SE}\alpha^{SE}K_{eff}\right)K_{II} \\ + C_6\left(\beta^{SE}\alpha^{SE}K_{eff}\right)^2 = 0 \end{aligned} \tag{2.39}$$

in which

$$C_1 = \frac{1}{16\pi G}\sin\theta_0\,(2\cos\theta_0 - \kappa + 1) \tag{2.40}$$

$$C_2 = \frac{-1}{16\pi G}\sin\theta_0\,(6\cos\theta_0 - \kappa + 1) \tag{2.41}$$

$$C_3 = \frac{1}{8\pi G}(2\cos(2\theta_0) - (\kappa-1)\cos\theta_0) \tag{2.42}$$

$$C_4 = \frac{-1}{16\pi G}\sin\frac{\theta_0}{2}\left(5(\cos(2\theta_0) + \cos\theta_0) + (\kappa+1)\right) \tag{2.43}$$

$$C_5 = \frac{-1}{16\pi G}\cos\frac{\theta_0}{2}\left(5(\cos(2\theta_0) - \cos\theta_0) + (\kappa+3)\right) \tag{2.44}$$

$$C_6 = 0 \tag{2.45}$$

The dimensionless parameters β^{SE} is the dimensionless parameter as defined in (2.19) on p. 13. The parameters α^{SE} and effective SIF K_{eff} are defined as:

$$\alpha^{SE} = \sqrt{\frac{2r_C}{a}} \tag{2.46}$$

$$K_{eff} = \sqrt{K_I^2 + K_{II}^2} \tag{2.47}$$

Similarly to GMTS, the GSED criterion depends on the SIFs for modes I and II, T-stress and material constants ν and critical distance r_C. Please note, that the traditional SED criterion can be obtain from Eq. (2.39) when the parameter β^{SE} is equal to 0. According to the GSED criterion brittle fracture occurs when the SED factor S reaches its critical value S_{cr}. The critical SED factor S_{cr} has direct relation to the fracture toughness K_{IC} for mode I which can be expressed as:

$$S_{cr} = \frac{1}{8\pi\mu}(\kappa-1)K_{IC}^2. \tag{2.48}$$

The above-mentioned analytical approach to the solution of GSED is obtain numerically by using, e.g. Newton's iterative method, which is highly time consuming. This again suggest the use of averaged strain energy density (ASED) criterion proposed by Klusák [147]. Klusák's approach for ASED is similar to the MATS and again uses the SED numerically generated, which is then averaged over the distance d_{avg}. ASED criterion is obtain from the averaging conditions:

$$\bar{\Sigma} = \frac{1}{d_{avg}} \int_0^{d_{avg}} \Sigma(r) dr, \tag{2.49}$$

where $\Sigma = S$ is the numerically obtained strain energy density. The Eq. (2.49) searches for minimum of S/Σ by averaging the numerically generated S/Σ over the radial distance d for each polar angle θ.

The author believes in proper introduction of the SED criteria as it can be an alternative to the MTS or GMTS criterion. Nevertheless, this thesis is limited to the use of MTS and GMTS criteria due to the fact, that the concrete's main failure mechanism is in the direction of high tensile stresses and higher computational demands compared to the GMTS criterion.

1.3.3 Critical Distance

It is recognized that plastic deformation will occur at the crack tip or in its close vicinity as a result of the high stresses that are generated by the sharp stress concentration. To estimate the extent of this plastic deformation, Irwin equated the yield strength to the *Y*-direction stress along the *X*-axis and solved it for the radius. The radius value determined was the distance along the *X*-axis where the stress perpendicular to the crack direction would equal the yield strength; thus, Irwin [109] found that the extent of plastic deformation. This extent of the plastic zone is now commonly referred as critical distance r_C.

The fundamental approach to acquire the values of material's critical distance can be evaluated by substituting material's fracture toughness from Eq. (2.17) on p. 12 into tangential stress $\sigma_{\theta\theta}$ from Eq. (2.8) on p. 12 or its critical value $\sigma_{\theta\theta,C}$ from Eq. (2.33) on p. 17 and considering various boundary conditions, this will lead to following formulas:

$$r_c = \frac{1}{2\pi}\left(\frac{K_{IC}}{\sigma_t}\right)^2 \text{ – plane stress,} \tag{2.50}$$

$$r_c = \frac{1}{6\pi}\left(\frac{K_{IC}}{\sigma_t}\right)^2 \text{ – plane strain.} \tag{2.51}$$

In Eqs. (2.50) and (2.51) K_{IC} is the fracture toughness for mode I and σ_t is the tensile strength or sometimes referred as f_t in application to concrete materials.

In case of the brittle fracture, the critical distance r_C interprets the location where the stress reached its critical value which will result into material's failure. Moreover, if two materials with the same value of fracture toughness K_{IC} and tensile strength σ_t are compared, both r_C are the same. However in the case, when both materials will have a different value of e.g. tensile strength σ_t, the critical distance will extend and the location of failure will vary for both materials. This representation of material's critical distance r_C in terms of tangential stress $\sigma_{\theta\theta}$ and the influence on its critical value $\sigma_{\theta\theta,C}$ is showed in Figure 9.

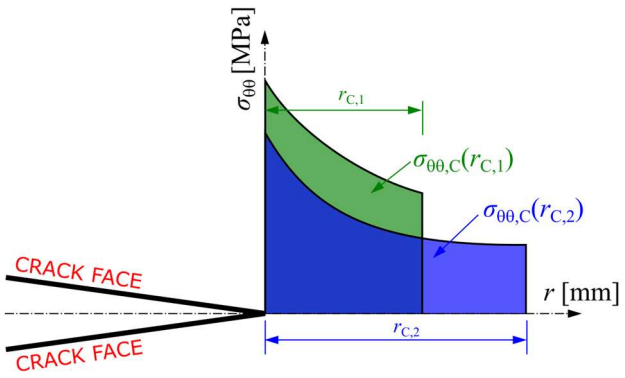

Figure 9: Graphical representation of the material's critical distance r_C.

In concrete materials, the above-mentioned plastic zone is virtually small or not present at all. However, there exists another non-linear zone ahead of the crack which is greater in size, so called fracture process zone (FPZ). The characteristic length l_{ch} in concrete fracture substitutes the role of material's critical distance r_C. Here in this subsection, the FPZ is only briefly introduced and more details of its properties and its formation are stated in following section 2 of this thesis.

Hillerborg [148] in his work pioneered the calculation of the characteristic length l_{ch} by following equation:

$$l_{ch} = \frac{E G_F}{{f_t}^2}, \tag{2.52}$$

where E is the Young's modulus, f_t is the tensile strength and G_F is size independent fracture energy.

Bažant and Planas [149] presented another relation for the FPZ length based on the energy balance in the crack tip as:

$$r_C = \frac{m+1}{\pi}\left(\frac{K_{IC}}{f_t}\right)^2 = \frac{m+1}{\pi} l_{ch}, \tag{2.53}$$

where m is the power of polynomial approximation function which represents bridging stress in FPZ. If the bridging stress ahead of the crack tip is linear respective to the crack tip-opening displacement (*CTOD*), r_C equals to:

$$r_C = \frac{2}{\pi}\left(\frac{K_{IC}}{f_t}\right)^2 = \frac{2}{\pi} l_{ch}. \tag{2.54}$$

The validity of Eq. (2.54) was experimentally demonstrated by Ayatollahi and Aliha in [150] for ceramic materials. Moreover, they found out, that the critical distance is approximately 100 times greater than the average grain size.

Karihalloo in his work [151] also assumed that the bridging stress in the FPZ can be expressed a series of function of *CTOD*. Karihaloo proposed following formulation, by considering only first term of expansion, of critical distance r_C:

$$r_C = \frac{3}{8}\frac{E w_c}{f_t}, \tag{2.55}$$

where w_C is the critical *CTOD* value which can be expressed as the function of the fracture energy G_F or fracture toughness K_{IC}.

All of these methods for estimation of material's critical distance r_C use fracture toughness related to the first term of the WE, i.e. A_{1C} or in engineering form of K_{IC}. Ayatollahi and Akbardoost [152] have recently postulated the method to determinate the critical distance r_C by using the third term of WE A_{3C}. Moreover, they showed its size independency for concrete material. The critical distance r_C for 3PB test geometry using the A_1 and A_3 terms can be express as:

$$r_C = \left[\frac{f_t\sqrt{2\pi} \pm \sqrt{2\pi f_t^2 - 12\frac{A_3^*}{A_1^*}\frac{K_{IC}^2}{W}}}{6\frac{A_3^*}{A_1^*}\frac{K_{IC}}{W}} \right]^2, \tag{2.56}$$

where A_1^* and A_3^* are dimensionless parameters related to the A_1 and A_3 term dependent on the specimen's geometry and W is the specific dimension.

The fracture toughness K_{IC} (A_{1C}) is dominant in close vicinity of the crack tip, while the higher order terms are dominant further from the crack tip. Thus, this approach postulated by Ayatollahi and Akbardoost [152] might be advantageous especially for the concrete materials for which this non-linear zone ahead of crack tip is large.

1.4 Over-deterministic Method

To evaluate the SIFs and T-stress derived from the Williams' expansion, the over-deterministic method (ODM) proposed by Ayatollahi and Nejati [130] can be used. This is an improvement of the general method proposed by Sanford and Dally [153], which also determines SIFs and far field stress from displacement, however does not account for higher order terms of the WE.

$$\begin{bmatrix} u_1 \\ u_2 \\ \vdots \\ u_k \\ \\ v_1 \\ v_2 \\ \vdots \\ v_k \end{bmatrix} = \begin{bmatrix} f_1^I(r_1,\theta_1) \cdots f_N^I(r_1,\theta_1) f_1^{II}(r_1,\theta_1) f_3^{II}(r_1,\theta_1) \cdots f_M^{II}(r_1,\theta_1) f_0 0 f_2^{II}(r_1,\theta_1) \\ f_2^I(r_2,\theta_2) \cdots f_N^I(r_2,\theta_2) f_1^{II}(r_2,\theta_2) f_3^{II}(r_2,\theta_2) \cdots f_M^{II}(r_2,\theta_2) f_0 0 f_2^{II}(r_2,\theta_2) \\ \vdots \quad \vdots \quad \vdots \quad \vdots \quad \vdots \quad \vdots \quad \vdots \quad \vdots \\ f_1^I(r_k,\theta_k) \ldots f_N^I(r_k,\theta_k) f_1^{II}(r_1,\theta_1) f_3^{II}(r_k,\theta_k) \ldots f_M^{II}(r_k,\theta_k) f_0 0 f_2^{II}(r_k,\theta_k) \\ g_1^I(r_1,\theta_1) \cdots g_N^I(r_1,\theta_1) g_1^{II}(r_1,\theta_1) g_3^{II}(r_1,\theta_1) \cdots g_M^{II}(r_1,\theta_1) 0 g_0 g_2^{II}(r_1,\theta_1) \\ g_2^I(r_2,\theta_2) \cdots g_N^I(r_2,\theta_2) g_1^{II}(r_2,\theta_2) g_3^{II}(r_2,\theta_2) \cdots g_M^{II}(r_2,\theta_2) 0 g_0 g_2^{II}(r_2,\theta_2) \\ \vdots \quad \vdots \quad \vdots \quad \vdots \quad \vdots \quad \vdots \quad \vdots \quad \vdots \\ g_1^I(r_k,\theta_k) \ldots g f_N^I(r_k,\theta_k) g_1^{II}(r_1,\theta_1) g_3^{II}(r_k,\theta_k) \ldots g_M^{II}(r_k,\theta_k) 0 g_0 g_2^{II}(r_k,\theta_k) \end{bmatrix} \begin{bmatrix} A_1 \\ \vdots \\ A_N \\ B_1 \\ B_3 \\ \vdots \\ B_M \\ A_0 \\ B_0 \\ B_2 \end{bmatrix} \tag{2.57}$$

The current implementation of ODM generated reliable results previously in [123] applied to mode I displacements. The ODM utilizes k numbers of horizontal u and vertical v displacements of the displacement fields. Using Eqs. (2.22) and (2.23) on p. 14, where the unknowns are only N numbers of A_n coefficients and M numbers of B_n coefficients, an over-determined system of equations can be formed as:

$$[U]_{2k+1} = [C]_{2k\times(N+M+2)}[X]_{(N+M+2)}, \tag{2.58}$$

where $[U]$ contains the displacements u and v, $[C]$ contains the values of shape functions $f_I(r,\theta)$ and $g_I(r,\theta)$ for mode I and shape functions $f_{II}(r,\theta)$ and $g_{II}(r,\theta)$ for mode II, $[X]$ are the unknown WE coefficients and N and M are the demanded number of evaluated WE coefficients. In order to have a more accurate solution independent of the selected nodes, the number of nodes is chosen to be more than the number required to solve the set of equations (i.e. 2k > N+M+2). This assumption leads to the solution by the least-square method in a vector form expressed as:

$$\begin{aligned} [C]^T[U] &= [C]^T[C][X], \\ [X] &= ([C]^T[C])^{-1}[C]^T[U]. \end{aligned} \tag{2.59}$$

This method can be applied on both experimental measured and on the numerically generated displacements fields. On the other hand, if the WE coefficients are known prior to experimental measurement, one can easily generate the displacements *u* and *v* in front of crack tip. Moreover, the validation of the applicability of LEFM can be made between the experimentally captured displacements by the digital image correlation (DIC) technique and the numerically generated displacements by FEM software. This process is schematically showed in Figure 10.

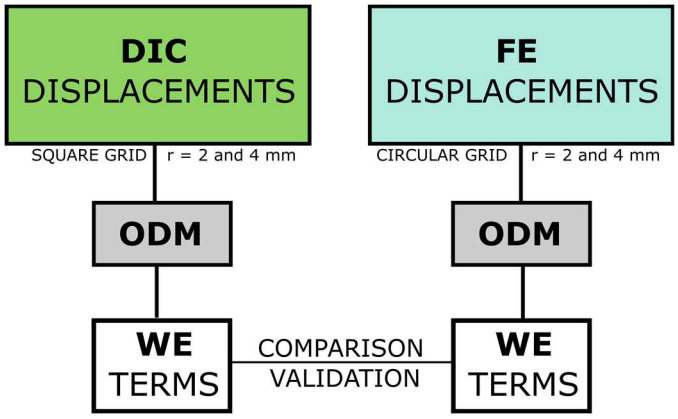

Figure 10: Comparison of ODM process for the experimentally measured DIC and numerically generated FE displacements.

After obtaining demanded WE terms from the ODM solution, it is recommended to validate the results with the analytical formulas found in the literature e.g. Tada [154]. If the geometry does not allow for analytical solution, the calculated WE terms have to be used to estimate stress fields around the crack tip and then compared to the numerical FEM solution.

2. Concrete Fracture

Concrete is composite material composed of fine and coarse aggregates bounded together with a cement matrix that hardens over time. Thus, fracture of concrete is highly complex process that still poses challenge in composing experimental setup, numerical modelling, and concrete technology. Microstructure of concrete is highly heterogenous due to presence of flaws, such as pores, inclusions, and micro-cracks. These micro-cracks are locations, which can promote debonding of aggregate particles from the cement matrix. Further coalescence of these microscopic cracks due to external loading inevitably leads to observable macro-cracking. The cracks are not only affecting the aesthetic look and durability, but possibly jeopardizing the structural stability, as well. However, concrete cracking is inherent to the material and it does not necessarily result in structural failure; stabilized cracks are not dangerous [20]. It is important to fully understand the material's fracture and failure behaviour in order to make correct judgment of this.

To introduce main differences in the fracture process of concrete material, it is most explanatory to compare concrete to other materials in form of material's response to the actions of external tensile load. This comparison is usually expressed by the applied load versus produced deformation (P-δ) diagram. Concrete's response to the load, so-called quasi-brittle, is compared between brittle (glass) and ductile (steel) materials. When the tensile strength σ_t of a material is reach, cracking will occur. However, the ductile material, exhibits yielding plateau in the (P-δ) diagram (see curve (c) in Figure 11) which prolongs the structure's failure. This plateau is a result of plasticizing micro-structure ahead of the crack tip. On the other hand, the brittle material does not show any of this yielding plateau and the failure is achieved immediately after reaching its tensile strength σ_t due to lack of existence of the plastic zone ahead of the crack tip (see curve (a) in Figure 11). However, the quasi-brittle material in same situation evinces softening behaviour, which gradually lowers the tensile stress in the P-δ diagram (see curve (b) in Figure 11). This comparison of different material types and resulting material's response to the tensile load is presented in Figure 11.

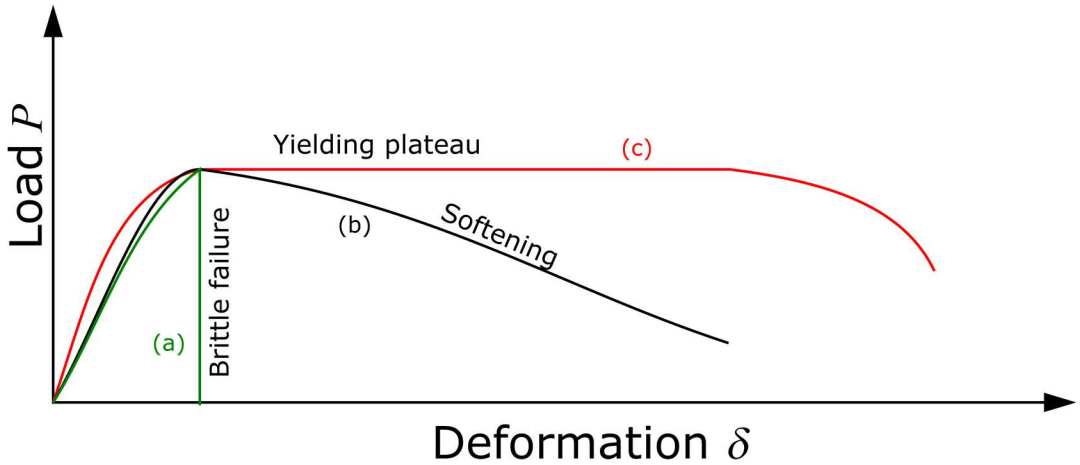

Figure 11: Load-deformation P-δ diagram of (a) - brittle, (b) - quasi-brittle and (c) - ductile material adopted from [20]

The region in which the quasi-brittle material undergoes softening damage (tearing), featured by progressive micro-cracking, is called the fracture process zone (FPZ). This softening, in the FPZ is result from the micro-cracking of concrete material. The presence of FPZ is the main reason for the deviation of the concrete behaviour from the LEFM prediction. The FPZ is formed, when micro-cracks are propagating and later coalescing into observable macro-crack. In this zone, due to the existence of micro-cracks concrete material progressively softens [20]. This above-referred phenomenon of response to tensile load can be examined in more detail if the crack tip situation

is shown. The detail of the size and formation of various nonlinear zones ahead of crack tip due to actions of external tensile loads for different materials is presented in Figure 12.

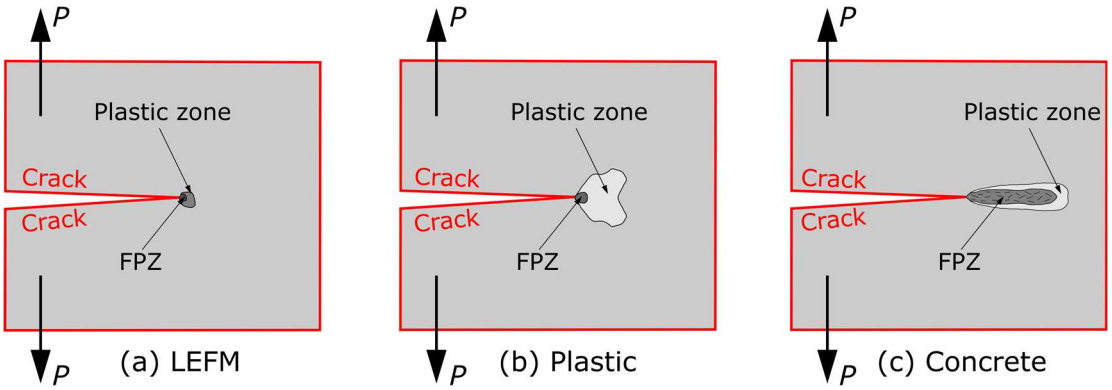

Figure 12: Comparison of the size and shape of the fracture process zone ahead of the crack tip of various materials (a) – linear fracture, (b) – plastic and (c) - concrete [20, 155].

The brittle material, possesses both FPZ and plastic zone, however their size is virtually small (practically absent) and have no influence on extending the structure's life after reaching the ultimate load P_C or tensile strength σ_t (See Figure 12(a)). Ductile material, such as steel, possesses small FPZ which is surrounded by much larger nonlinear plastic zone. This plastic zone extends the structure life from the immediate failure. The difference in size of FPZ and plastic zone is showed in Figure 12(b). Whereas the quasi-brittle material has the FPZ of great size, due to nonexistence of the plastic flow since concrete in tension is not capable of plastic deformation, which practically occupies the entire space ahead of crack tip with nonlinear deformation [20, 155].

This FPZ is known to be property of all quasi-brittle materials, which are mainly heterogenous materials consisting of brittle constituents and inhomogeneities not negligible to the structure's size. These materials include concrete, as the archetypical case, fibre-reinforced concrete, shale and various rocks, fibre-polymer composites, coarse-grained or toughened ceramics, refractories, bone, cartilage, dentine, dental cements, biological shells, many biomaterials, stiff soils, silt, grouted soils, sea ice, consolidated snow, cold asphalt concrete, coal, various printed materials, rigid foams, wood, paper, carton, etc., and all brittle materials on the micrometre scale [156].

Generally, this FPZ can be defined as the zone where flaws become active due to the fact that the tensile strength is reached. So the FPZ is actually a bridging zone between a macro-crack and the uncracked region of a cracked element/body. Outside the FPZ concrete behaves as nearly elastic [157, 158]. Furthermore, the length of this FPZ in concrete structures is not constant, but related to the maximum aggregate size D_{max} a typical value is roughly $12D_{max}$ [155]. This means that, depending on the structural size, the FPZ may encompass the whole cross-section [157]. This influence of the aggregate size on the length of the FPZ was experimentally studied by Mihashi [159] with the acoustic emission (AE) technique.

Furthermore, the development in of the FPZ in concrete is changing over the P-δ process. The concrete material is progressively softening in this zone due to micro-cracking. This can be schematically explained by Figure 13. It is appropriate to highlight significant features of this zone. The linear-elastic behaviour to the tensile load is until the point A is reached. The region between point A and point B exhibits the pre-peak nonlinearity, in which the FPZ is formed. In between the points B and C, the after peak softening is reached as a result of fully formed FPZ and micro-cracking. The tail of softening diagram C-D is on the other hand result of aggregate interlock and other frictional effects. At this stage the macro crack is fully developed.

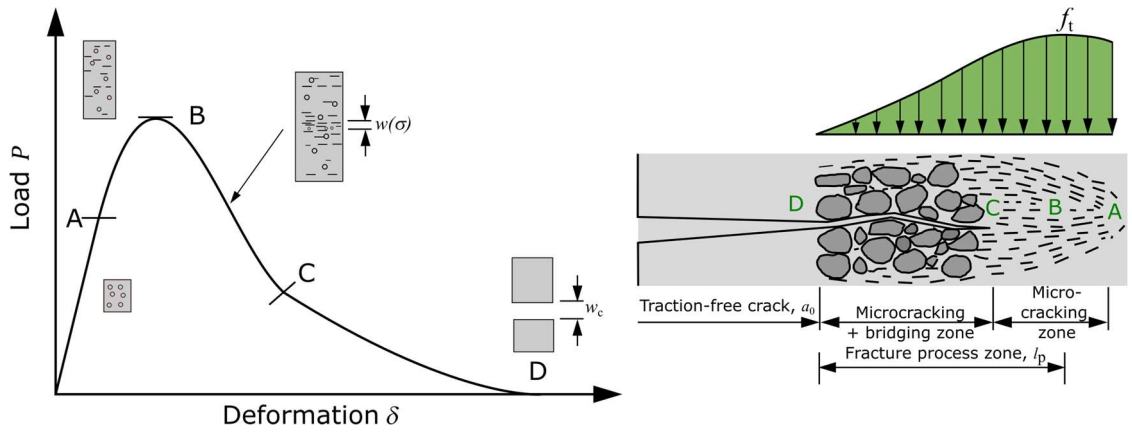

(a) (b)

Figure 13: Typical P-δ response of a pre-cracked concrete specimen (a), and the fracture process zone ahead of the real traction-free crack (b). Note that the FPZ extends only over the tension softening region (BCD) and it may be surrounded by a nonlinear (but not a softening) region, e.g. the region AB adopted from [20].

The fracture front has been experimentally observed by Mindess [160]. From measurements of tensile strain fields by Moire interferometry presented by Cedolin [161], it appears that the fracture front a zone of micro-cracks has width about the aggregate size. From microscopic observations show that the larger, micro-cracks are not spread over a band of a large width but are concentrated essentially on a line. This line along which the micro-cracks are scattered is not straight but in the most case it is highly tortuous (Figure 13(b)).

However, cracks generally propagate in a direction perpendicular to the maximum tensile stress σ_t and in heterogeneous materials, such as concrete, they tend to follow the weakest path. On the other hand, when a crack starts to propagate in matrix and then encounters a tougher aggregate particle, the crack is arrested and/or branched. Thus the crack path is deflected and a larger surface area is created which results into a higher load and energy needed for crack to continue its propagation [162]. This formation of FPZ and some different situations during concrete crack propagation are schematically represented in Figure 14.

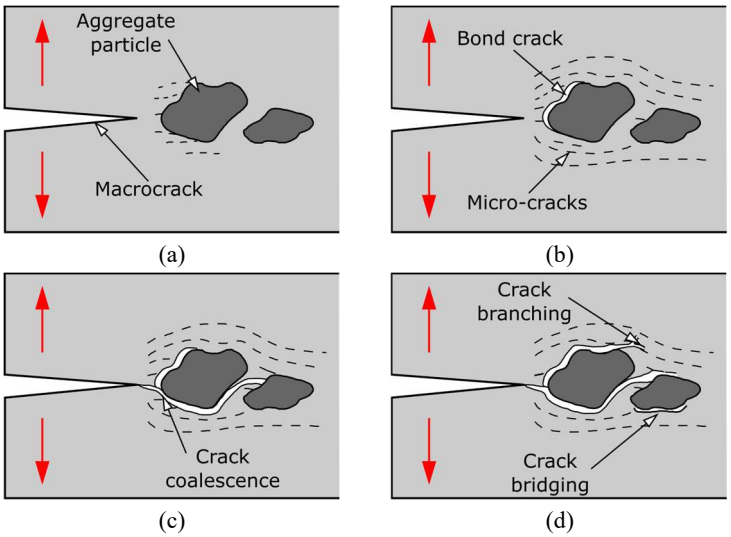

Figure 14: Development of FPZ – (a) micro-cracking at aggregate due to presence of macro-crack, (b) – debonding and micro-cracking, (c) – coalescence of deboned crack with macro-crack, and micro-cracking, (d) – crack bridging, debonding crack branching and micro-cracking. Adopted from [20].

Furthermore, when new crack surfaces are formed, they may still be in contact by the aggregate bridging mechanism, thus creating the ability to sustain some normal tensile stress along the FPZ [20]. These so-called cohesive stresses represent the forces transmitted across a developing crack

due to wedging and pull-out of aggregates fragments [157] and they are assumed to be a monotonically decreasing function of the crack opening displacement in the FPZ [158].

It should be realized that the boundary of the FPZ should not be defined as the boundary of visible micro-cracks but as the boundary of the strain-softening region, i.e., the region in which the maximum stress decreases with increasing maximum strain. Since the strain-softening is caused not just by micro-cracking but also by unobservable bond ruptures and sub-microscopic flaws, the FPZ is probably much wider (as well as longer) than the region of visible micro-cracks. Measurements of Cedolin et al. [161] appear to support this view. Nonetheless, the question of the actual shape of the micro-crack zone is unimportant for the macroscopic continuum modelling.

2.1 Size-Effect

Another important property of concrete fracture which should be considered in practice is the size-effect. The size of the specimen was studied by Bažant in [163] and in [149] which resulted into formulation of the size-effect law (SEL). A large amount of research has been dedicated to this phenomenon – for a comprehensive overview, the author would like to refer to Bažant [164] and [165]. Here it will be briefly introduced as it is considered important concrete property.

The size-effect, mostly related to a certain material property, is the change of that property when the size of the structure increases [166]. The most important size-effect for structural engineers is the one related to the maximum load a structural element can withstand. For concrete structures, there is inevitably a large gap between the scales of large structures (e.g. dams or bridges) and of laboratory tests [164]. For instance, the flexural strength of a concrete beam decreases as the beam's depth increases [162] or in small specimens where the FPZ cannot develop to its full length, the energy consumed by fracture is less than in a large specimen [67]. Generally, the SEL is defined through comparison of geometrically similar structures of different sizes, and is conveniently characterized in terms of the nominal stress σ_N at the ultimate load. The basic scaling laws are power laws in terms of the characteristic structural size D, for which the definition is arbitrary (e.g. the beam depth, the beam span, a diagonal dimension…).

According to the classical theories, based on strength criteria, concrete failure exhibits no size-effect and all geometrically similar structures fail at the same nominal stress (σ_N is constant). This is illustrated by the horizontal dashed line in Figure 15, in which σ_N is plotted against the structure's size D in double logarithmic coordinates. On the other hand, if the failure asses by LEFM theory, an inclined dashed line with slope -1/2 appears in Figure 15 with a rather strong size-effect. However, the concrete structures showing the SEL a transitional behaviour, described by the solid curve. This curve is product of concrete (quasi-brittle material), incapable of purely plastic deformations and possessing a FPZ which size is not negligible compared to the structure size. In fact, the concept of quasi-brittleness is relative. If the size of a quasi-brittle structure becomes sufficiently large compared to the material inhomogeneities, the structure becomes perfectly brittle and follows LEFM principles [165].

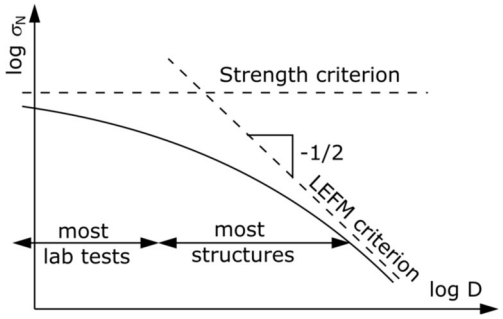

Figure 15: Size-effect of concrete for geometrically similar structures of different sizes.

Apart from the size-effect on the strength, there is also a size-effect on the shape of the post-peak descending load-deflection curve. This is comprehensively described in the following section as it is also affecting the value of fracture energy G_F. In addition to this, there exists variation on size-effect e.g. recently reported width effect by Carloni et. al [167, 168].

2.2 Fracture Energy

Typically, the FMPs of concrete are evaluated from the recommended geometry of the three-point bending (3PB) test with straight-through notch in the mid span of the specimen [67] (see Figure 16(a)). This experimental set-up, which provides stable and reliable results, is well acknowledged among researchers [169-171]. On the other hand, there is no agreement among researchers on the definite specimen's geometry and cross-section shape which could provide the independent value of the fracture energy G_F [22, 172-174].

In this section, an author's interesting contribution to the measurement of FMPs on non-traditional notch type is briefly presented. Recently, Miarka et al [175] validated the use of the chevron-notched three-point bending (CN3PB) test [176-178](see Figure 16(b)) for the experimental evaluation of the specific fracture energy G_f. Experimental bending test set-ups with specimens possessing a cross-section with chevron notch have been introduced and standardized since the 1960's [64, 179]. This experimental set-up is used to evaluate fracture toughness of various materials e.g. ceramics [180], brittle metals like bearing steel [181] or aluminium alloys [182].

The main advantage of this test set-up is that no sharp pre-crack has to be introduced because a sharp crack is formed during loading at the beginning of the test [183]. Furthermore, no crack length measurement is required, and a stable crack growth from the notch tip prior to the final fracture load can be reached due to the geometry of the notch [184, 185].

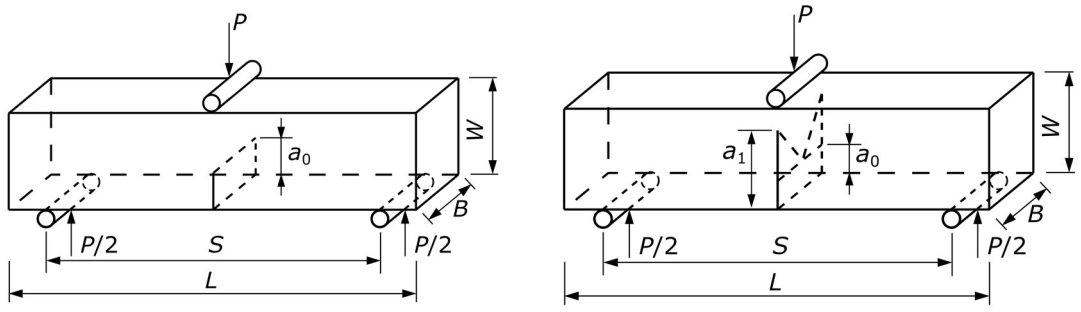

Figure 16: Sketches of 3PB specimen with straight-through notch (a) and 3PB specimen with chevron notch (b).

Generally, the notches can have various endings, which are shown in Figure 17. The straight-through notch is sawed by a single cut going through the whole thickness of the specimen. The relative crack length is then expressed by dimensionless parameter $\alpha_0 = a_0/W$, where W is the specimen's height and a_0 is the initial notch length (see Figure 17(a)). However, in case of the chevron notch, there can be two types of notches, i.e. sharp or blunt chevron notch. To produce such kind of a notch, two or more cuts are necessary. In case of the sharp notch, the relative crack length is expressed by two parameters α_0 and α_1. The parameter α_0 expresses the position of the sharp end of the chevron notch in the centre of the cross-section, while the α_1 denotes the notch length at the edge of the specimen (see Figure 17(b)). Similarly, to the straight-through notch type, the α_0 and α_1 are expressed as a_0/W and a_1/W respectively. In case of the blunt chevron notch, the parameter b_1 is additionally introduced, which defines the blunt end from the edge of the cross-section. This parameter is needed to precisely define the blunt chevron notch position (see Figure 17(c)).

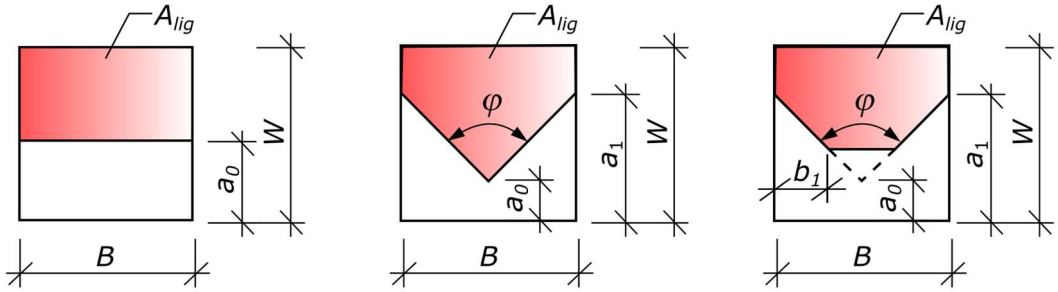

(a) (b) (c)

Figure 17: Comparison of ligament area A_{lig} of straight-through notch (a), chevron notch with constant angle (b) and chevron notch with constant angle with blunt ending (c).

The unnotched cross-section area ahead of the notch as shown in Figure 17 is so-called ligament area A_{lig}. Specimens with the same initiation length a_0 of the chevron notch have a smaller ligament area A_{lig} compared to the standard specimens with the straight-through notch, therefore more specific fracture energy is needed in the fracture process in case of the straight through notch.

Suppose that the crack growth is stable, and the work done by external load is spent entirely in crack propagation. Based on the Griffith energy balance criterion [104], crack growth in an elastic body in the state of equilibrium is a natural process of energy transfer between the strain energy of the body and the fracture energy required for creating a new crack surface, so that a state of minimum potential energy is achieved for the system at a given load level. Thus for an elastic brittle material the fracture energy G_F is identical and equal to the toughness G_C. Therefore, one should get the same result, from which the fracture toughness K_{IC} using the Eq. (2.17) can be calculated. The reason for the variability of G_F with specimen size and for its significant departure from G_C has to do with the violation of the two-basic assumption of the LEFM theory. The LEFM theory assumes that the work done by the external load goes solely into stable crack extension, and that the energy required for the latter is independent of specimen geometry and loading conditions [20].

For quasi-brittle material (i.e. concrete), the work is consumed in breaking the unnotched part of the beam's cross-section to create new surfaces. In the load-displacement (P-δ) relations (See Figure 18), the area enclosed by the response curve represents the work done by the external load to produce fracture of the specimen/beam.

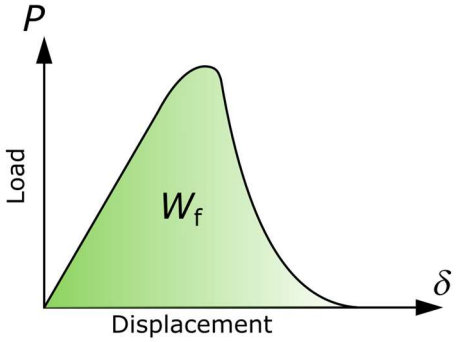

Figure 18: Work of fracture [67].

According to the RILEM method [67] for 3PB test on notched specimens, the specific work of the external force (fracture value) W_f, is obtained from the complete load – displacement (P-δ) diagram as follows:

$$W_f = \int P(\delta) d\delta. \tag{2.60}$$

The value of the specific fracture energy G_f (energy needed to create a crack of unit area) can be expressed as:

$$G_f = \frac{W_f}{A_{lig}}, \tag{2.61}$$

where W_f is the work of fracture calculated from Eq. (2.60) and A_{lig} is the ligament area.

Hu and Wittmann [186, 187] introduced the boundary effect method (BEM), which considers the influence of the free boundary of the uncracked ligament. Based on their findings, it is possible to obtain size-independent specific fracture energy G_f of concrete based on the experimental measurements on the specimens with various notch lengths. Taking the BEM into account, the size-independent fracture energy can be evaluated as:

$$G_f(\alpha) = \frac{1}{W - a_0} \int_0^{W-a_0} g_f(x) dx, \tag{2.62}$$

where G_f is the average size independent fracture energy, and g_f is the local fracture energy which depends on the distance x along the uncracked ligament length.

Later, Karihaloo et al. [22, 188] discussed influence of various notch depths on the evaluation of the size-independent fracture energy G_F. For this, a substitution of the complex function used for the description of local fracture energy g_f by bilinear approximation was done. The bilinear expression is described as follows:

$$G_f(\alpha_0) = \begin{cases} G_F \left[1 - \frac{1}{2} \frac{\lambda}{1 - \alpha_0}\right]; & 1 - \alpha_0 > \lambda \\ G_F \frac{1}{2} \frac{1 - \alpha_0}{\lambda}; & 1 - \alpha_0 \leq \lambda \end{cases}, \tag{2.63}$$

where G_f is the size-dependent fracture energy, α_0 is the relative notch length and λ is the parameter of the transition point expressed as $\lambda = l_t/W$, where l_t is the transition zone length. Eq. (2.63) then leads into a solving equation with two unknowns, G_F and l_t. The simplified boundary effect method (SBEM) and the transition zone length was experimentally verified by Muralidhara et al. [189], showing reliable results.

Miarka et al. [175] verified the applicability of the CN3PB test on the evaluation of the FMPs of concrete or concrete-like materials. For this, experiments were prepared, in which the 3PB test and CN3PB test specimens had the same ligament area A_{lig}. This assumption provided easy quantification of the influence of the notch type on the values of fracture load P_{max}, fracture toughness K_{IC}, work of fracture W_f and, most importantly, on the values of specific fracture energy G_f of studied material. Moreover, the experiments were designed with specimens which had various notch geometry, they had similar dimensions, i.e. thickness, height and span. The value of G_F was evaluated from experimental load-displacement (P-δ) diagrams and by employing the above-mentioned SBEM.

2.3 Models for Predicting Concrete Failure

This sub-section is dedicated to various approaches on predicting concrete failure due to crack initiation under the tensile loads. First two are dedicated to establishing value of the concrete's fracture toughness K_{IC}, other two are briefly introduced and compared between each other as they are both dealing with non-linear modelling of such phenomenon and the last one is described in more details as it used later in the non-linear analysis.

2.3.1 The Two Parameter Fracture Model

The two-parameter fracture model for concrete proposed by Jenq and Shah in 1985 [190] transfers the effect of pre-peak nonlinear behaviour of the concrete structure into the elastic equivalent structure. This is done on the assumption that the onset of fracture in concrete can be predicted based on knowledge of fracture toughness K_{IC} and related crack tip opening displacement $CTOD_C$. Moreover, the sharp notch of a length a_0, which originated from nonlinear behaviour, is transformed into effective crack $a_e > a_0$ of the equivalent elastic structure, which is calculated from the unloading compliance C_u. Model's principle is shown in Figure 19.

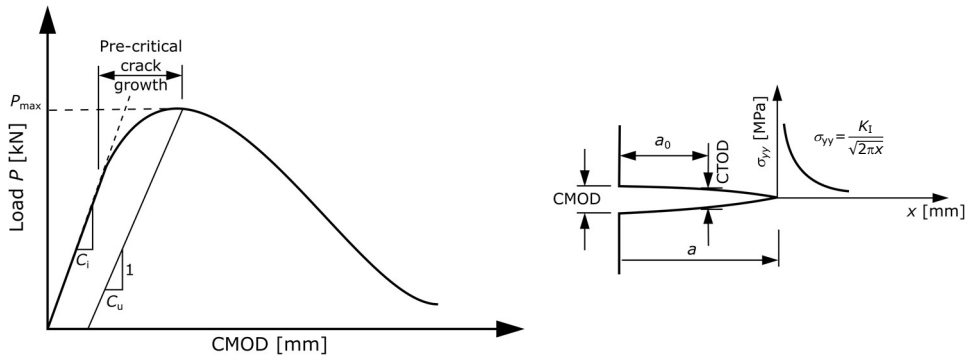

Figure 19: A typical *P-CMOD* diagram (a) showing the initial compliance C_i and unloading compliance C_u and (b) crack tip situation.

The parameters for the load level of $P = P_{max}$ correspond to $K_I = K_{IC}$, $CTOD = CTOD_C$ and $a = a_e$. The K_{IC} and $CTOD_C$ are independent on the specimen's size. The parameter a_e depends on the specimen's size, however if the specimens size increase to the "infinity" the parameter a_e will tend to approach crack length of a_0. Thus, this model correctly predicts the linear elastic fracture behaviour.

The main shortcoming of this model is that it predicts the failure only for the load level of P_{max}, beyond that point the model is not able to correctly predict the typical softening branch of *P-CMOD* diagram.

2.3.2 The Effective Crack Model

Another approach to concrete fracture was proposed by Nallathambi and Karihallo in 1990 [19], the effective crack model, is based on similar principle as the two-parameter model. Difference is in the calculation of the effective crack a_e. In this case it is done from the secant stiffness of the *P-CMOD* or *P-*δ diagram.

The secant stiffness E_{sec} is calculated from the *P-*δ diagram as a connection between origin point P_0 and P_{max}. The secant stiffness E is then used in the calculation of the stress σ_N ahead of crack tip. Furthermore, these parameters are used to calculate the effective crack length a_e, which is then used for the calculation of the effective fracture toughness K_{IC}^{eff}. The calculation of the effective fracture toughness K_{IC}^{eff} is done by substituting crack length a by effective crack length a_e in Eq. (2.16) on p. 12.

This approach again cannot predict the post-peak softening behaviour and have same proper related to the infinite specimen size, for which the effective crack length a_e tends to approach initial crack a. Please note, that the relation postulated by Nallathambi an Karihaloo can be used only for 3PB test geometry.

2.3.3 Fictious Crack Model

The fictious crack model (FCM) for the concrete fracture was proposed by Hillerborg in 1976 [191]. It is considered to be the first nonlinear material model used in theory of concrete fracture. It includes the tension softening fracture process within the fracture process zone through the

fictious crack, whose faces are affected by closing stresses. The term "fictious" is used here as the crack cannot be continuous with full separation of its faces.

These closing stresses are not constant over the length of the FPZ, they increase from zero value at the pre-existing traction-free macro-crack to the full uniaxial tensile strength f_t at the tip of the fictious crack. The crack is extended by the value of l_{ch}, i.e. characteristic length of FPZ from Eq. (2.52) on p. 20. The stress-strain relation used by Hillerborg is shown in Figure 20.

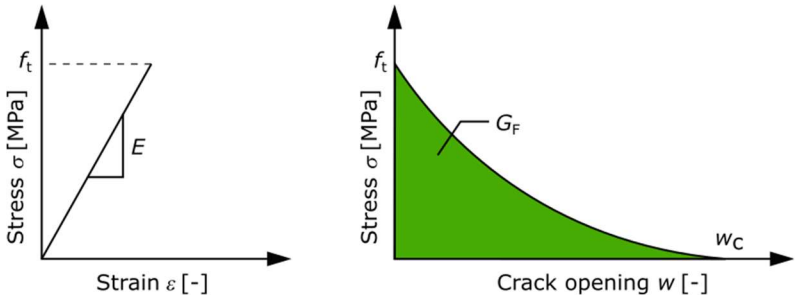

Figure 20: Stress-strain relation of Hillerborg's fictious crack model (a) – linear elastic material ahead of the fictitious crack tip and (b) – softening material withing the fracture process zone.

This model includes the fracture energy G_F as an area under the softening curve (see Figure 20(b)), which is one of two material parameters describing the concrete fracture as the brittle parameters i.e. K_{IC} or G_C do not describe the material's behaviour properly. The second one is the stress-displacement relation $\sigma(w)$ in the softening zone. Knowing this relation, the fracture energy G_F can be calculated as:

$$G_F = \int_{f_t}^{0} w(\sigma)\, d\sigma = \int_{0}^{w_c} \sigma(w)\, dw, \tag{2.64}$$

where the f_t is uniaxial tensile strength and w_c is the critical crack tip opening displacement of the pre-existing macro-crack at which the whole crack ($a_0 + l_{ch}$) begins to grow.

It is obvious, that the fracture energy G_F depends on the function of the softening branch. Literature offers various functions $\sigma(w)$ for softening branch approximations, e.g. linear proposed by Petersson [192], exponential proposed by Hoordijk [193] and bi-linear as implemented in recommendations [18, 67]. The other shortcoming of this model is to properly obtain the value of w_c, as the existing macro-crack is never sharp.

2.3.4 Crack Band Model

The micro-cracking and bridging stresses in the FPZ are not continuous and mainly it does not develop in narrow discrete region in line with the traction-free crack as the FCM suggests. Thus, crack band model (CBM) was developed by Bažant and Oh in 1983 [194], which considers micro-crack to be smeared over a band of width h (see Figure 21(a)) initially parallel to the opening stress σ_{yy}.

Again, the softening curve can be approximated by many simple functions as in the case of FCM. The fracture energy G_F is now:

$$G_F = h \int_{0}^{\varepsilon_c} \sigma_{yy}(\varepsilon)\, d\varepsilon, \tag{2.65}$$

where ε_c corresponds to the critical crack tip opening displacement of fictious crack model ($\varepsilon_c = w_c/h$). The band width h can be related to the gage length or to the element size in numerical analysis and it is recommended to be of $h = 3g$, where g is maximum aggregate size [194].

The CBM uses stress-strain $\sigma(\varepsilon)$, i.e. a decreasing stress with increasing inelastic deformation, while in case of FCM $\sigma(w)$ relation is used. Nonetheless, this strain is now related to the inelastic

deformation w and fracture energy G_F which results to the ultimate strain at complete rupture ε_c is now related to w_c. The stress-strain $\sigma(\varepsilon)$ softening relation is showed in Figure 21(b).

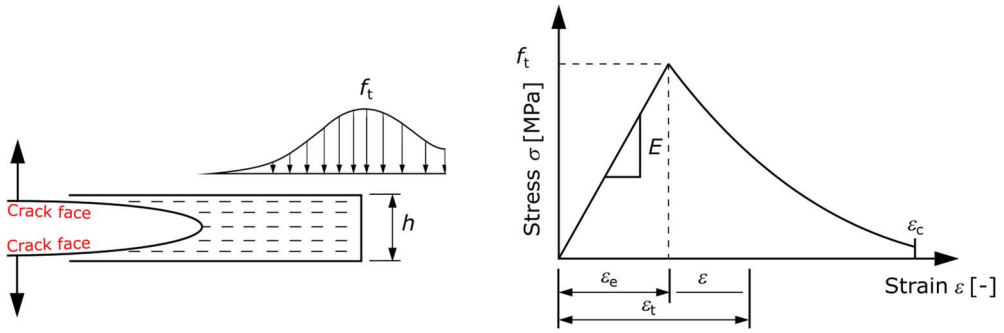

(a) (b)

Figure 21: Micro-cracking measured over a band width h (a) and the inelastic deformations in the FPZ with strain-softening curve.

Moreover, the CBM incorporates the shear retention factor ω and the damage parameters d. The shear retention factor allows for the crack face roughness due to aggregate interlock. The damage parameter allows for the stiffness reduction in the loading and loading process. It takes value of 0 corresponding to no damage and 1 which represents complete rupture.

2.3.5 Material model - Concrete Damaged Plasticity Model in Abaqus

In this subsection, the adopted concrete damaged plasticity (CDP) material model is briefly introduced. The CDP material model, as implemented in FE software Abaqus [195], is presented below. The model's yield function was proposed by Lubliner [196] and later modified by Lee and Fenves [197] to account for the different strength evolution in tension and compression. The yield function in terms of effective stresses has the following form:

$$F = \frac{1}{1-\alpha^{CDP}}\left(\bar{q} - 3\alpha^{CDP}\bar{p} + \beta^{CDP}(\tilde{\varepsilon}^{pl})\langle\bar{\hat{\sigma}}_{max}\rangle - \gamma^{CDP}\langle-\bar{\hat{\sigma}}_{max}\rangle\right), \tag{2.66}$$

where $\bar{p}$ is the hydrostatic pressure, $\bar{q}$ is the von Misses equivalent effective stress, $\bar{\hat{\sigma}}_{max}$ is the maximum principal effective stress, α^{CPD}, β^{CPD} are constitutive parameters describing the flow of the yield function and γ^{CPD} is the parameter related to the shape of the yield function. Parameters α^{CDP}, β^{CDP}, and γ^{CDP} are expressed by Eqs. (2.67) to (2.69).

$$\alpha^{CDP} = \frac{(\sigma_{b0}/\sigma_{c0}) - 1}{2(\sigma_{b0}/\sigma_{c0}) - 1}; 0 \le \alpha^{CDP} \le 0.5, \tag{2.67}$$

where σ_{b0} is the biaxial compressive strength and σ_{c0} is the uniaxial compressive strength.

$$\beta^{CDP} = \frac{\sigma_c(\varepsilon_c^{pl})}{\sigma_t(\varepsilon_t^{pl})}(1-\alpha^{CDP}) - (1+\alpha^{CDP}), \tag{2.68}$$

where $\sigma_c(\varepsilon_c^{pl})$ and $\sigma_c(\varepsilon_t^{pl})$ are the effective cohesion stresses for compression and tension, respectively.

The shape of the yield surface is expressed as:

$$\gamma^{CDP} = \frac{3(1-K_c)}{2K_c - 1}. \tag{2.69}$$

In this, K_c is the ratio of the tensile to the compressive meridian and defines the shape of the yield surface in the deviatory plane in Figure 22(a). Typically, K_c = 2/3 corresponds to the Rankine formulation and 1 to the Drucker–Prager criterion. In biaxial compression, where $\bar{\hat{\sigma}}_{max}$ = 0, the parameter β^{CDP} is not active, and only the parameter α^{CDP} is being used. Parameter γ^{CDP} is active when the $\bar{\hat{\sigma}}_{max} < 0$, which occurs in triaxial compression. The concrete damaged plasticity model

uses the flow potential function $G(\sigma)$, which is a non-associated Drucker–Prager hyperbolic function and is defined by Eq. (2.70).

$$G(\sigma) = \sqrt{(\varepsilon_{CDP}\sigma_{t0}\tan\psi)^2 + \bar{q}^2} - \bar{p}\tan\psi, \tag{2.70}$$

where ε_{CDP} is the eccentricity and ψ is the dilation angle.

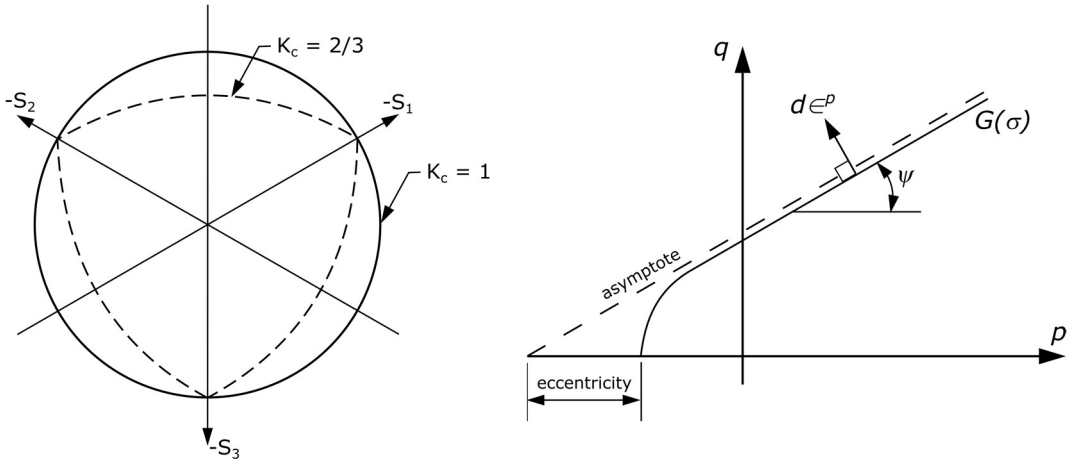

(a) (b)

Figure 22: Yield surfaces in the deviatory plane - (a) and schematic of the plastic flow potential with dilation angle ψ and eccentricity in the meridian plane (b).

The CDP constitutive input parameters, which define the plasticity, are shown in Table 1. These plasticity parameters were comprehensively studied by [198, 199] and showed accurate results, moreover they have been calibrated prior to numerical study (See Chapter IV Section 3.2 Material Model Calibration). Therefore, they have been adapted for this study i.e. values are artificial and not based on experimental measurement.

Table 1: Input constitutive material parameters for CDP model.

Dilatation angle ψ [°]	Eccentricity ε [-]	σ_{b0}/σ_{c0} [-]	K_c [-]	Viscosity parameter η [-]
36	0.1	1.16	0.666	0

The CDP material model assumes that the uniaxial tensile and compressive response of concrete is characterized by damaged plasticity, which is defined by the damage parameter d_{tot} and is used in the model according to Eq. (2.71).

$$\sigma = (1 - d_{tot})\bar{\sigma} = (1 - d_{tot})E_0(\varepsilon - \varepsilon^{pl}), \tag{2.71}$$

The damage parameter d_{tot} is defined in terms of compression and tension d_c and d_t, respectively by:

$$(1 - d_{tot}) = (1 - s_t d_c)(1 - s_c d_t), \tag{2.72}$$

where s_t and s_c describe the tensile and compressive stiffness recovery. The damage parameters for compression d_c and tension d_t can be calculated according to Eq. (2.73) and Eq. (2.74), respectively

$$d_c = 1 - \frac{\sigma_c}{E_o\left(\varepsilon_c - \varepsilon_c^{pl}\right)}, \tag{2.73}$$

where E_0 is the Young's modulus, σ_c is the compressive stress, ε_c is the compressive strain and ε_c^{pl} is the compressive plastic strain.

$$d_t = 1 - \frac{\sigma_t}{E_o\left(\varepsilon_t - \varepsilon_t^{pl}\right)}, \tag{2.74}$$

where E_0 is the Young's modulus, σ_t is the tensile stress, ε_t is tensile strain and ε_t^{pl} tensile plastic strain.

In the CDP material model a visco-plastic regularization can be introduced according to Duvuant-Lions [200] generalized formulation. By introducing a viscosity parameter η the plastic strain tensor is upgraded, and the damage uses additional relaxation time. The visco-plastic strain rate regularization is described in Eq. (2.75).

$$\varepsilon_v^{pl} = \frac{1}{\eta}\left(\varepsilon^{pl} - \varepsilon_v^{pl}\right), \tag{2.75}$$

Similarly to the strain definition, a stiffness degradation variable for the visco-plasticity d_v is defined as:

$$d_v = \frac{1}{\eta}(d_{tot} - d_v), \tag{2.76}$$

The stress-strain relation of the visco-plastic model is given as:

$$\sigma = (1 - d_v)E_0\left(\varepsilon - \varepsilon_v^{pl}\right). \tag{2.77}$$

However, this regularization technique has some limitations, which can be overcome by using the non-local approach [201-204] e.g. the integral non-local approach proposed by Pijaudier-Cabot [205] or the gradient approach proposed by Peerlings [206]. Nevertheless, the visco-plastic regularization is a common technique used in modelling of the softening materials studied by a static/implicit or even by explicit analysis, which can help to overcome common convergence problems.

Chapter III
Materials and Methods

In order to investigate the mixed-mode I/II crack initiation, propagation and fracture resistance of concrete, several different types and grades of concrete mixture were composed. Each studied concrete mixture and its composition together with mechanical properties are comprehensively introduced and discussed. In this chapter, the used specimens along with the experimental setup are precisely described. Furthermore, a basic principle of modern experimental technique of digital image correlation method is introduced. Lastly, the aggressive environmental conditions and its experimental measurement are presented to provide basic information of used material.

1. Concrete Mixtures

Hereunder, the mixture composition of each studied concrete material is presented. The mixture composition was in direct cooperation with the concrete precast plant at ŽPSV s.r.o. company. Presented mixtures are used in the prefabrication of the concrete structural elements e.g. bridge beams, floor panels and the railway sleepers. The intent of investigation of more than one mixture is to improve its mechanical and mainly fracture mechanical properties, while reducing the cement content. Furthermore, the measured material's mechanical properties according to European standards are presented.

1.1 Concrete C50/60

The C 50/60 concrete type was selected to be reference mixture as it is typically used for the pre-stressed precast elements which are produced nowadays. C 50/60 shows variety in structural applications because of its high compressive and tensile strength. Usually, concrete with a compressive strength higher than 60 MPa and water to cement w/c ratio lower than 0.42 can be considered as a high-performance concrete (HPC) [3]. However, this term of HPC will not be used for this mixture.

Figure 23: Fresh C 50/60 mixture poured into moulds.

The C 50/60 concrete contains 450 kg of CEM I 42.5 R, the water to cement ratio w/c is 0.40. Fine aggregate was natural sand 0/4 mm and crushed aggregate 4/8 mm and 8/16 mm from high quality granite was used as well as drinking water. The concrete was mixed in a volume of 1 m^3 and poured immediately into moulds, see Figure 23. A polycarboxylates-based superplasticizer was used to reach good workability. The slump of this mixture was 540 mm in accordance with

[207] and can be classified as class F4. The fresh C 50/60 mixture in moulds is presented in Figure 23.

The mechanical properties were measured in accordance with European standards at 28 days age. The measured mechanical propertied together with bulk density are presented in Table 2.

Table 2: Mechanical properties with standard deviation of used C 50/60 concrete at 28 days age.

Compressive cube strength $f_{c,cube}$ [MPa]	85.8 ± 2.9
Compressive cylindrical strength $f_{c,cyl}$ [MPa]	72.8 ± 2.5
Flexural strength f_t [MPa]	18.5 ±1.0
Indirect tensile strength f_t [MPa]	5.52 ± 0.31
Young's Modulus E [GPa]	38.3 ± 0.3
Bulk density ρ [kg/m^3]	2390 ± 27.32

From both the presented compressive strengths $f_{c,cube}$ and $f_{c,cyl}$ this concrete mixture could fit into the C 70/85 group. These high strengths and Young's modulus are result of high w/c ratio as it allows full hydration of cement grains. However, the manufacturer uses C 50/60 grade, therefore, for consistency reasons, the C 50/60 marking will be kept.

Moreover, this mixture of C 50/60 concrete was frequently used in production of precast elements as it showed constant mechanical results. Thus this concrete will be taken as reference mixture in the comparison with other studied concrete mixtures.

1.2 High-strength Concrete

High-strength concrete (HSC) was designed in close cooperation with a concrete precast plant, in order to improve mechanical performance of C 50/60 as presented in [208] and to reduce the production costs. For this binder, Portland cement CEM I 42.5 R, was used together with three mineral admixtures. Moreover, binder consist 80 % of CEM I 42.5 R, 7.5 % of granulated blast furnace slag (GBFS), 2 % of limestone and 10 % of metakaolin Metaver. Water/binder ratio was 0.2. The aggregates were composed from natural sand 0/4 mm and crushed high quality granite with a size of 4/8 mm (the maximum aggregate size is 8 mm). A polycarboxylate based superplasticizer Glenium 300 was selected based on its great compatibility with cement and to reach good workability of the mixture. The concrete was mixed in volume of 1 m^3 and poured immediately into moulds. The material composition per m^3 is showed in Table 3.

Table 3: Material composition of studied HSC per m^3.

	CEM I 42.5R	GBFS	Limestone	Metakaolin Metaver	Superplasticizer (Glenium 300)	Water	Sand 0/4	Crushed aggregates 4/8
[kg]	650	60	15	75	17	165	400	600

Prepared samples were carefully covered with a PE-foil, which helped to prevent excessive moisture exchange with the environment, as the specimens were stored outside of the laboratory environment (precast concrete plant), with a temperature ≈ 5 - 25ºC for a period of 28 days. The measured mechanical properties of studied HSC were in accordance to the European standards at the 28 days age and the measured mechanical properties are presented in Table 4.

Table 4: Mechanical properties of studied HSC mixture.

Compressive strength at 1 day $f_{c,cube}$ [MPa]	65.2
Compressive strength at 28 days $f_{c,cube}$ [MPa]	106.2
Compressive cylindrical strength $f_{c,cyl}$ [MPa]	94.1
Indirect tensile strength - cube f_{ct} [MPa]	7.4
Young's modulus - cube E_{cube} [GPa]	41
Young's modulus - cylinder E_{cyl} [GPa]	-
Bulk density ρ [kg/m^3]	2350

The cubes were tested in the age of 1 and 28 days to see the strength development over the time. As it can be seen from Table 4, the intent to design mixture with higher mechanical performance compared to the C 50/60 concrete was fully met. Consequently, the HSC mixture shows high early strength of more than 65 MPa, which already fits in the group of C 50/60 grade.

The HSC's material structure as well as its typical granite aggregate, is presented in Figure 24 together with the cylindrical samples drilled out of the beam after the test.

(a) (b)

Figure 24: Example of HSC's structure (a) and core-drill samples (b).

1.3 High-performance Concrete Batch A

High-performance concrete (HPC) was designed in close cooperation with a concrete precast plant, in order to improve mechanical performance of C 50/60 as presented in [208] and to reduce the production costs. For this binder, Portland cement CEM I 42.5 R, was used together with three mineral admixtures. Moreover, binder consist 79 % of CEM I 42.5 R, 5.5% of granulated blast furnace slag (GBFS), 4% of limestone and 11.5 % of metakaolin Metaver. Water/binder ratio was 0.23. The aggregates were composed from natural sand 0/4 mm and crushed high quality granite with a size of 4/8 mm and 8/16 mm (the maximum aggregate size is 16 mm). A polycarboxylate based superplasticizer Glenium 300 was selected based on its compatibility with cement and to reach good workability of the mixture. The concrete was mixed in volume of 1 m^3 and poured immediately into moulds. The material composition per m^3 is showed in Table 5.

Table 5: Material composition of studied HPC per m^3.

	CEM I 42.5R	GBFS	Limestone	Metakaolin Metaver	Superplasticizer (Glenium 300)	Water	Sand 0/4	Crushed aggregates 4/8	Crushed aggregates 8/16
[kg]	575	40	30	80	20	165	590	185	725

Prepared samples were carefully covered with a PE-foil, which helped to prevent excessive moisture exchange with the environment, as the specimens were stored outside of the laboratory environment (precast concrete plant), with a temperature ≈ 5 - 25°C for a period of 28 days. The measured mechanical properties of studied HPC were in accordance to the European standards at the 28 days age and the measured mechanical properties are presented in Table 6.

Table 6: Mechanical properties of studied HPC mixture.

Compressive strength at 1 day $f_{c,cube}$ [MPa]	51.1
Compressive strength at 28 days $f_{c,cube}$ [MPa]	100.5
Compressive cylindrical strength $f_{c,cyl}$ [MPa]	94.1
Indirect tensile strength - cube f_{ct} [MPa]	5.4
Young's modulus - cube E_{cube} [GPa]	42.1
Young's modulus - cylinder E_{cyl} [GPa]	40.6
Bulk density ρ [kg/m^3]	2342

The cubes were tested in the age of 1 and 28 days to see the strength development over the time. As it can be seen from Table 6, the intent to design mixture with higher mechanical performance compared to the C 50/60 concrete was again fully met.

The HPC's material structure as well as typical granite aggregate of size 8/16, is presented in Figure 25 together with the cylindrical samples drilled out of the beam after the test.

(a) (b)

Figure 25: Example of HPC's structure (a) and core-drill samples (b).

1.4 Alkali-Activated Concrete

Alkali-activated concrete (AAC) [10, 209] was designed based on the formerly performed tests, see [210, 211]. The mixture composition was designed according to [212]. The traditional binder, Portland cement, was fully substituted by the granulated blast furnace slag (GBFS) [2]. The dry mass of the activator was 8 % and the water to slag ratio was 0.45. Sodium water glass and potassium hydroxide were combined to reduce efflorescence of an appropriate silicate modulus of the activator (M_s = 0.67 or mass ratio (K_2O + Na_2O) / SiO_2 is 60/40). This composition of the activator is convenient in terms of both setting and strengths. A naphthalene-based plasticizer was also used for a better workability of the mixture. Natural aggregates were used with a maximum size of 8/16 mm. The slump of this mixture was 600 mm. The material composition per m^3 is showed in Table 7.

Table 7: Material composition of used AAC per m^3.

	GBFS	Na-WG M_s = 2.0	50 % solution of KOH	Water	PSN-plasticizer	Sand 0/4	Crushed aggregates 4/8	Crushed aggregates 8/16
[kg]	450	45	34	159	10	855	385	400

Again, this mixture was poured into the moulds immediately after mixing. Afterwards, the specimens were carefully covered with a PE-foil, which helped to prevent moisture exchange with the environment, because the specimens were stored outside of the laboratory environment (precast concrete plant), with a temperature ≈ 5 - 25°C for a period of 28 days.

The AAC's binding paste has typical white colour comparison to the other tested concrete types. This is due to complete substitution of the Portland cement, which has its typical grey/dark grey colour. An example of the material's structure and core-drill samples drilled out of beam after the test are shown in Figure 26.

(a) (b)

Figure 26: Example of AAC's structure (a) and core-drill samples (b).

The AAC material was tested at various ages to cover the strength development. To test the mechanical properties, 150 mm cubes, and 150 mm diameter with 300 mm height cylinders were prepared - see Table 2. In total, three specimens were used to determine the mechanical properties addressed in Table 8. The measured mechanical properties of the AAC show a relatively low early strength [213, 214], which increases over time and ultimately reaches relatively high values, more than 60 MPa (see Table 8). Compared to the ordinary Portland cement-based concrete of a similar strength, this AAC mixture shows a significantly lower value of modulus of elasticity – see also [24].

Table 8: The compressive strength f_c at different concrete ages and the Young's modulus E of Alkali-activated concrete mixture.

f_c – 24 h - cubes 150 mm [MPa]	8.8 ± 0.3
f_c – 14 d - cubes 150 mm [MPa]	53.4 ± 1.2
f_c – 28 d - cubes 150 mm [MPa]	62.0 ± 1.5
f_c – 28 d - cylinders 150 × 300 mm [MPa]	48.0 ± 3.4
f_{ct} – 28 d - cubes 150 mm [MPa]	3.4 ± 0.2
f_{ct} – 28 d splitting cylinders 150 × 300 mm [MPa]	3.2 ± 0.2
E_{stat} – 28 d - cylinders 150 × 300 mm [GPa]	26.3 ± 1.1
E_{dyn} – 28 d – cylinders 150 × 300 mm [GPa]	29.6 ± 3.3
Bulk density ρ [kg/m^3]	2210 ± 3.3

The AAC's material mechanical performance is lower compared to C 50/60 mixture, however this mixture with its parameters belongs to the grade of C 50/60, while the C 50/60 mixture fits more into grade of C 70/85. Therefore the designed AAC mixture could be used as a replacement in the production of precast concrete elements of the C 50/60 mixture made with traditional Portland cement binder.

1.5 High performance Concrete Batch B – Chloride

Another HPC was designed to analyse the material's resistance to chloride ingress. For this a binder, Portland cement CEM I 42.5 R, was used together with one mineral admixtures. Moreover, binder consist 88 % of CEM I 42.5 R and 12 % of metakaolin Metaver. Water/binder ratio was 0.25. The aggregates were composed from natural sand 0/4 mm and crushed high quality granite with a size of 4/8 mm and 8/16 mm (the maximum aggregate size is 16 mm). A polycarboxylate based superplasticizer was selected based on its compatibility with cement and to reach good workability of the mixture. The concrete was mixed in volume of 1 m^3 and poured immediately into moulds. The material composition per m^3 is showed in Table 9.

Table 9: Material composition of studied High-performance concrete per m^3.

	CEM I 42.5R	Metakaolin Metaver	Superplasticizer	Water	Sand 0/4	Crushed aggregates 4/8	Crushed aggregates 8/16
[kg]	575	80	20	165	680	200	810

Prepared samples were carefully covered with a PE-foil, which helped to prevent excessive moisture exchange with the environment, as the specimens were stored outside of the laboratory environment (precast concrete plant), with a temperature ≈ 5 - 25°C for a period of 28 days.

The measured mechanical properties of studied HPC were in accordance to the European standards at the 28 days age and the measured mechanical properties are presented in Table 10.

Table 10: Mechanical properties of studied HPC mixture.

Compressive strength at 1 day $f_{c,cube}$ [MPa]	30.2
Compressive strength at 28 days $f_{c,cube}$ [MPa]	102.0
Indirect tensile strength - cube f_{ct} [MPa]	5.8
Young's modulus - cube E_{cube} [GPa]	42.1
Young's modulus - cylinder E_{cyl} [GPa]	39.5
Bulk density ρ [kg/m^3]	2395 ± 11.3

The cubes were tested in the age of 1 and 28 days to see the strength development over the time. As it can be seen from Table 10, the intent to design mixture with higher mechanical performance compared to the C 50/60 concrete was again fully met.

2. Specimens

Underneath both Brazilian disc (BD) and Brazilian disc with central notch (BDCN) specimens are described. These specimens have been mostly used in this study to determinate indirect tensile strength f_t and fracture toughness K_{IC} for mode I and K_{IIC} for mode II.

2.1 Brazilian Disc

The Brazilian disc (BD) is widely used to determinate the indirect or transverse tensile strength f_t of rocks [85]. In addition, it can be used on concrete, PMMA and asphalts mixtures. The dimensions and typical boundary conditions during the test are shown Figure 27.

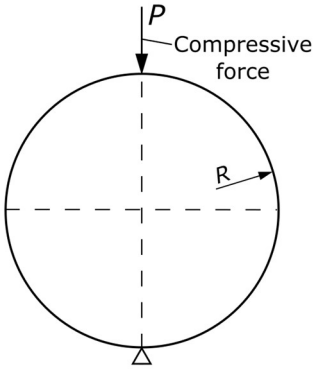

Figure 27: Dimensions and boundary conditions of Brazilian disc specimen.

The indirect tensile strength f_t can be evaluated for the BD specimen by the following equation:

$$f_t = \frac{P}{\pi RB}, \tag{3.1}$$

where P is the applied compressive load, R is the disc's radius and B is the specimen's thickness.

The BD's failure occurs in centre of the disc in the location of the maximum tensile stress. Measured indirect tensile strength f_t is used to determinate material's critical distance r_C as it is evaluated from circular geometry which reduce the error produced by different geometries.

2.2 Brazilian Disc with a Central Notch

A Brazilian Disc with a Central Notch (BDCN) was selected as a main geometry to investigate the mixed mode I/II fracture resistance. The BDCN specimen was used due to the simplicity of specimen preparation, the relatively simple experimental setup and the possibility of mixed mode I/II loading. This mixed mode I/II loading is achieved by inclining the initial notch to the loading point by the angle α. A geometry and boundary conditions of the BDCN specimen is presented in Figure 28.

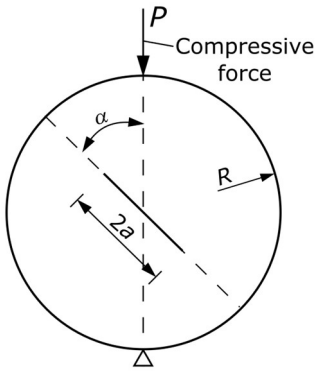

Figure 28: Dimensions and boundary conditions of a Brazilian disc with a central notch specimen.

The BDCN specimen is prepared by cuts of the cylindrical samples. The cylindrical sample can be obtained from core drill (real structure prior to renovation) or from mixture cast to moulds (new mixture development). In this study the BDCN specimens have been made from moulded samples with dimension of 150 × 300 mm (height × diameter). Actual, experimental setup for the BDCN specimen is showed in Figure 29

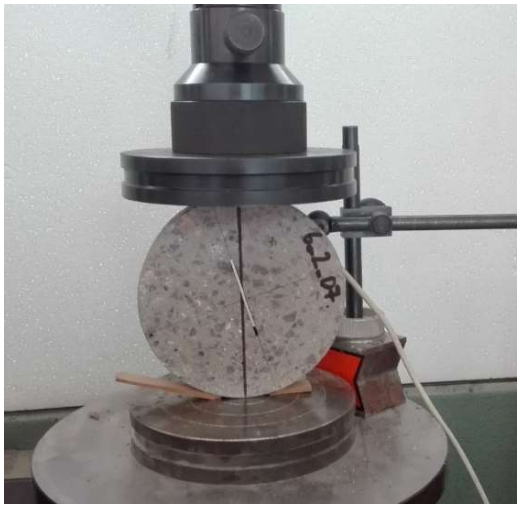

Figure 29: Experimental set-up of BDCN specimen (a/R = 0.4 α = 20°).

The notch in the BDCN specimen has length of 2a and the relative notch length ration is then expressed as a/R and thus the notched specimen is used in the evaluation of FMPs of concrete materials. Such notch can possess various notch types' endings, i.e. straight through notch, sharp chevron notch and round chevron notch. In this study, a straight through notch Figure 30(a) will be used as it provides direct location of the crack initiation. For this a water jet cutter has been used in order to provide straight notch ends and to reduce labour costs. All of these notch types are shown in Figure 30.

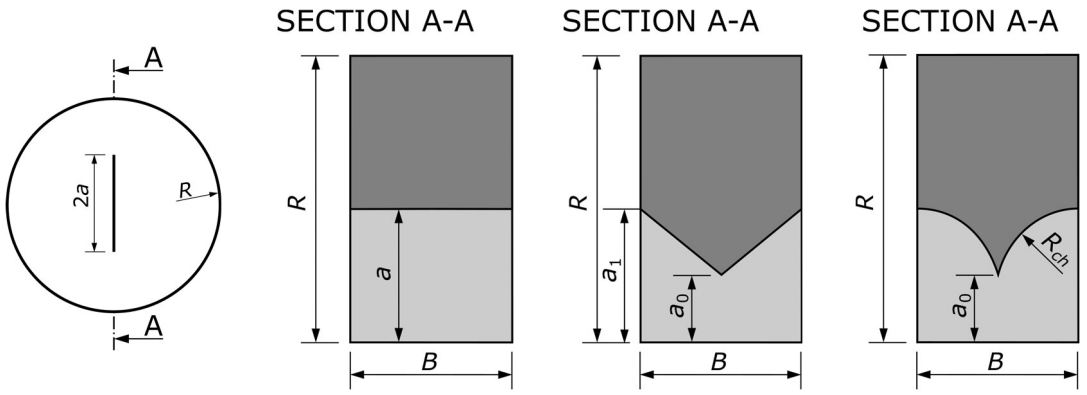

Figure 30: Comparison of notch ends for BDCN specimen showed on ½ cross-section.

The chevron notch is widely used for testing and evaluation of FMPs of rocks on various geometry shapes e.g. cracked chevron notched Brazilian disc (CCNBD) [89, 215, 216]. Both chevron notches presented in Figure 30(c) and Figure 30(d) are labour intensive as two or more cuts are necessary to provide chevron notch into the BDCN geometry and usually resulted in bad execution of the notch ends.

Further in the analysis of the mixed mode I/II fracture resistance the SIFs will be determined on the BDCN geometry. The SIFs for mode I and mode II are calculated using Eqs. (3.2) and (3.3) according to the handbook by Tada & Paris [154] and by the literature Ayatollahi [144, 217] and by Seitl et al [208].

$$K_I = \frac{P\sqrt{a}}{RB\sqrt{\pi}} \frac{1}{\sqrt{1-\frac{a}{R}}} Y_I(a/R, \alpha), \tag{3.2}$$

$$K_{II} = \frac{P\sqrt{a}}{RB\sqrt{\pi}} \frac{1}{\sqrt{1-\frac{a}{R}}} Y_{II}(a/R, \alpha), \tag{3.3}$$

where P is the applied compressive load, R is the specimen radius, a is the crack length, α is the notch inclination angle, B is the thickness of the specimen and Y_I and Y_{II} are the shape functions for mode I and mode II, respectively.

Please note that the measured dimensions used in Eqs. (3.2) and (3.3) for all studied materials are showed in Appendix A of this thesis. General dimensions were radius R o 150 mm, relative notch ration a/R of 0.4 and thickness B of approximately 28 mm.

As above-mentioned the biaxiality parameter β (Eq. (2.19) on p. 13) for the calculation T-stress can be used for test specimen which has $K_I > 0$ in whole test range. However, in case of the BDCN specimen, the K_I value is for some notch inclination angles α equal to zero, which leads to infinite values of parameter β. For this reason, it is recommended that another method to be used, i.e. the direct extrapolation method proposed by Yang [126], or using procedure as implemented in FEM software which allows directly to obtain the T-stress value by Eq. (2.20) on p. 14.

Using the analytical formulas for calculation of the SIFs for mode I, mode II and for T-stress and estimating value of material's fracture toughness K_{IC} one can applied the GMTS criterion to the BDCN geometry. The mixed mode I/II fracture resistance is usually expressed in the relative coordinates for mode I as ratio of K_I/K_{IC} and for mode II as ratio of K_{II}/K_{IC}.

The fracture resistance is then expressed by substituting these assumptions to the Eq. (2.34) on p. 17. The fracture resistance curve for mode I is then obtained from:

$$\frac{K_{IC}}{K_I} = cos\frac{\theta_0}{2}\left[cos^2\frac{\theta_0}{2} - \frac{3}{2}\frac{K_{II}}{K_I}sin\theta_0\right] + \sqrt{2\pi r_C}\frac{T}{K_I}sin^2\theta_0, \tag{3.4}$$

and for mode II:

$$\frac{K_{IC}}{K_{II}} = cos\frac{\theta_0}{2}\left[\frac{K_I}{K_{II}}cos^2\frac{\theta_0}{2} - \frac{3}{2}sin\theta_0\right] + \sqrt{2\pi r_C}\frac{T}{K_{II}}sin^2\theta_0, \tag{3.5}$$

Both Eq. (3.4) and Eq. (3.5) show noticeable dependency of whole GMTS criterion on the second term of the WE and on the critical distance r_C. Thus, the estimation of proper value of the critical distance r_C in this case is crucial. The literature offers various options for the calculation of r_C however, this this will limit to itself to calculate r_C based on the Eqs. (2.50) or (2.51) on p. 19.

3. Digital Image Correlation Technique

The digital image correlation (DIC) technique is a full-field optical technique used for displacement measurements in structural or mechanical components. It works analysing a sequence of images of the analysed component from an initial state (undeformed) to a final state (deformed). This technique can be implemented both in 2D (in-plane) and 3D (in and out-of-plane).

In this work, 2D DIC is implemented since the displacement fields are obtained on a plane specimen. Its implementation comprises the following steps according to [218]: 1) specimen and experimental equipment preparations, 2) acquisition of a sequence of images and 3) processing of the acquired images and displacements. The specimen surface must have a random grey intensity distribution (a random speckle pattern), which deforms together with the specimen. The speckle pattern can be the natural texture of the specimen surface or artificially made by spraying a random black speckle over a white background applied on the specimen surface. The camera must be placed with its optical axis perpendicular to the specimen surface in order to avoid inaccurate two-dimensional measurements. After preparing the specimen and assembling the set-up, a sequence of images is acquired from an initial or reference state (undeformed state) until a final state (deformed state).

The DIC technique was used to investigate the crack tip behaviour of the BDCN specimen for various crack lengths and various inclination angles α. DIC provides full-field displacement information by comparing images taken before and after straining the specimen body [219]. Each image is divided into smaller regions, or 'interrogation windows'. The cross-correlation product is used to measure the similarity between the interrogation windows before and after straining the body for the purposes of the study:

$$c(u,v) = \sum_{x=-\frac{N}{2}}^{x=\frac{N}{2}}\sum_{y=-\frac{N}{2}}^{y=\frac{N}{2}} I_A(x,y)\cdot I_B(x+u, y+v), \tag{3.6}$$

where c is the cross-correlation product, which is a function of u and v, these being the displacement vectors joining the centres of the two regions of interest along directions x and y, respectively; I_A and I_B are the intensity distribution of the two digital images before and after straining the sample, respectively; and N is the number of interrogation windows into which the digital images were divided. The maximum value of the cross-correlation product (Eq. (3.6)) is the probable displacement vector for the centre of each interrogation window in I_A.

The DIC principle is schematically explained in Figure 32. Once the sequence of images has been acquired, its processing is performed. The basic principle of 2D DIC consists on tracking the displacement of points in two recorded images before and after deformation. To compute the

displacements at a certain point P, a square reference subset centred at point P from the reference image is chosen and used to track its corresponding location in the deformed image. To implement 2D DIC, it is necessary to define the region of interest (ROI) in the reference image. This ROI is divided into evenly spaced squares called facets. The displacements are computed at the centre of each facet to obtain full-field deformation. To evaluate the degree of similarity between the reference and the deformed facet, a correlation criterion must be defined. The most commonly employed correlation criteria are cross-correlation (CC) and sum-squared difference correlation (SSD). Further information about these correlation criteria can be found in reference [219].

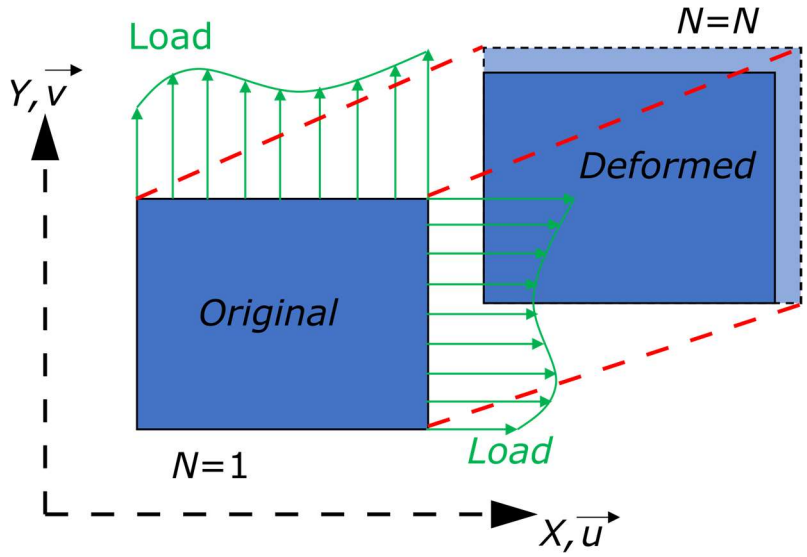

Figure 31: Principle of the digital image correlation (DIC) technique.

3.1.1 Specimens and Test Setup for DIC

In this subsection, the equipment used for testing and the experimental methods are described. The material used in the DIC study was HPC Batch A. The actual measured dimensions of D, B and $2a$ are presented in Table 11, which are based on the dimensions of the BDCN specimen presented in Figure 33. The measured geometry is average value from three measurements.

Table 11: Measured dimensions of the used BDCN specimens.

Specimen	α [°]	D [mm]	B [mm]	$2a$ [mm]	a/R [-]
HPC_4_3_2	5	149.18	30.65	40.46	0.271
HPC_4_3_3	10	149.23	30.47	40.08	0.269
HPC_4_3_4	27.7	149.21	31.50	40.41	0.271
HPC_6_3_1	0	149.18	30.56	60.59	0.406
HPC_6_3_2	5	149.23	30.48	60.21	0.403
HPC_6_3_3	15	149.17	30.56	60.29	0.404

Relative notch ratio $a/R = 0.267$ with marked notch inclination angles are presented in Figure 32.

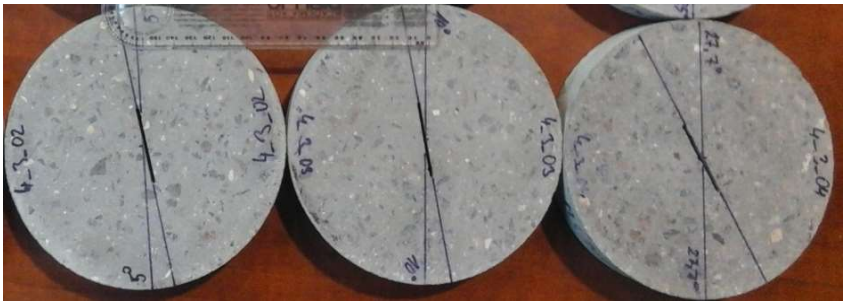

Figure 32: BDCN specimens with marked notch inclination angles with relative notch lengths a/R of 0.267.

DIC requires the surface to have a random pattern so that each interrogation window is unique in each image and can be easily located in the same image after it has undergone some deformation or rigid body movement. Thus, the pattern with a random grey intensity distribution was obtained by spray painting the surface with black and white speckles. An 8-bit 2048 × 2048 pixel CCD camera (Gazelle GZL-CL-41C6M) with a maximum image acquisition rate of 150 frames per second was used for taking images, and recommendations from previous analyses were followed [222]. The experimental setup was similar to the one used previously [223]. Sprayed BDCN specimen used in the DIC analysis and mounted in the testing rig is presented in Figure 33.

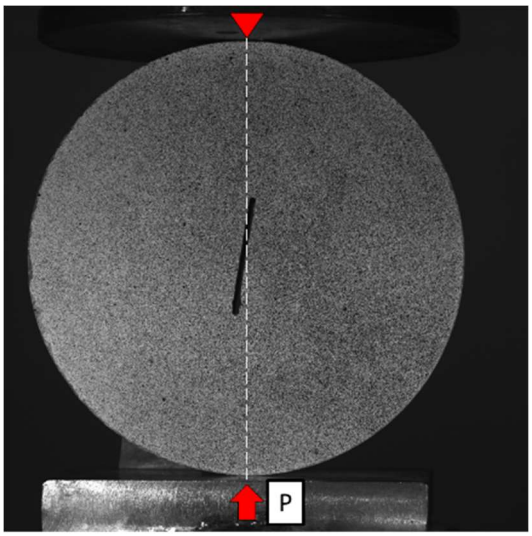

Figure 33: Experimental setup for a BDCN specimen with a treated surface for DIC measurement.

The experimental testing was performed using an MTS servo-hydraulic rig with a maximum capacity of 100 kN and a vertical displacement speed of 0.01 mm/s (similar to one presented in Figure 29). The DIC experimental setup was equipped with a 4.1 MPx CCD camera coupled with a Schneider lens, which provided a field of view (FOV) of 181.24 × 181.24 mm^2. Two light sources were used to ensure good homogeneous light conditions for the DIC technique. The digital images were processed by VIC 2D V6 software in order to obtain a displacement field [224]. Used experimental setup is presented in Figure 34.

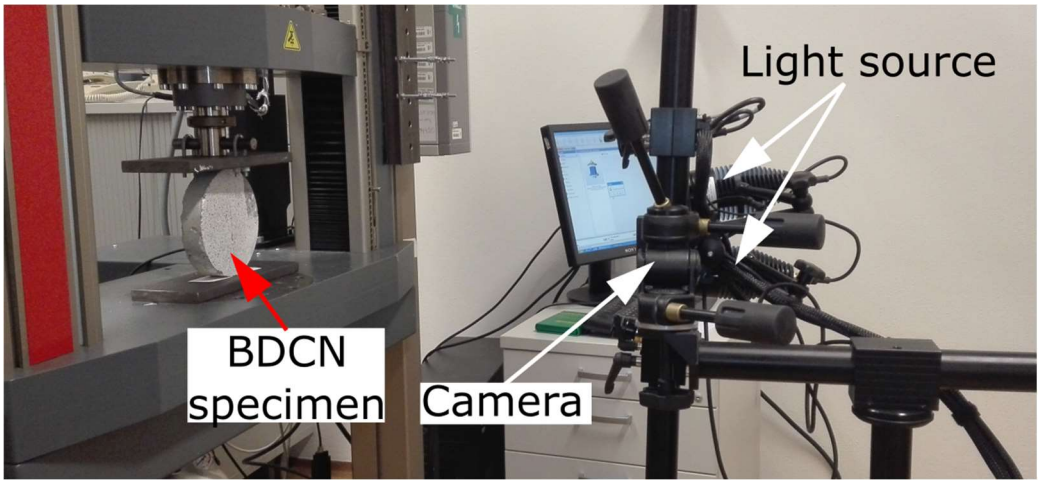

Figure 34: DIC experimental setup.

The camera was tilted so that the positive x coordinate matched the direction of crack growth and the y coordinate matched the crack opening direction. Accordingly, the angle of camera tilt was changed for the different angles α studied (Table 11). This improves the resolution of the analysis and makes post-processing easier and faster [220, 221]. DIC generated a pair of matrices, u and

v, with displacement values that were combined with an analytical model to infer fracture mechanical parameters.

3.2 DIC data extraction

It is recognized that plastic deformation will occur at the crack tip as a result of the high stresses that are generated by the sharp stress concentration. To estimate the extent of this plastic deformation, Irwin equated the yield strength to the *Y*-direction stress along the *X*-axis and solved it for the radius. Determinated radius value was the distance along the *X*-axis where the stress perpendicular to the crack direction would equal the yield strength; thus, Irwin[109] found that the extent of plastic deformation (critical distance r_C) was [117].

To evaluate the SIFs and the *T*-stress a displacement field measured by DIC in front of the crack tip was chosen at various distances from the crack tip. The displacements were chosen outside of the critical distance, whose radius/size r_C can be evaluated by Eqs. (2.50) or (2.51) on p. 19. The estimated critical distance was an r_C of 1.56 mm for the plane strain and 4.67 mm for the plane stress boundary conditions. The calculated critical distance r_C values justify the use of the LEFM concept, and especially the use of the WE.

Although the digital image correlation method uses a grid with a constant increment ΔX, ΔY in both directions *X* and *Y*, the numerical evaluation uses a grid in polar coordinates. The difference between the used grids is presented in Figure 35.

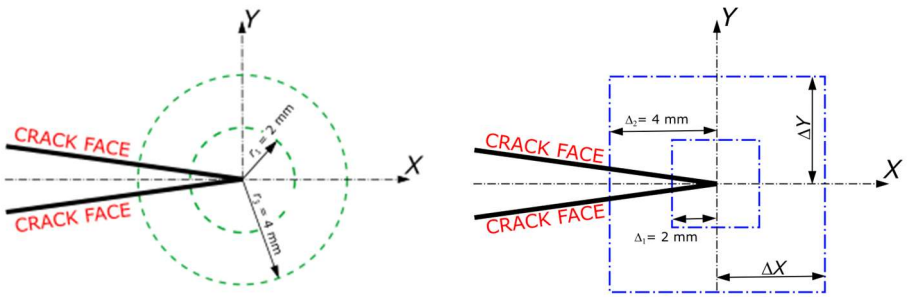

(a) (b)

Figure 35: Schema of the points whose displacements were used for the evaluation of the WE terms via the combination of the ODM and: (a) FEM model; (b) DIC.

In this study, two different ΔX, ΔY distances of 2 and 4 mm for the extraction of the DIC's displacement were selected due to size of fine aggregate. As in the case of the DIC measurement, a radius *r* of 2 and 4 mm were selected in order to verify the accuracy of experimentally measured displacements with data generated by the FEM model. Sobel's algorithm, implemented in the edge-finding routine in the MATLAB image processing toolbox [225], was used for the determination of the crack tip position. Sobel's routine is often used for image processing analysis. It works by comparing values within a 2D displacement map. It gives a value of 1 in the regions where there is a significant discontinuity, and a value of 0 elsewhere. The edge is then located along the positions where a value of 1 was obtained. The crack is identified along the points where an edge was detected, and the crack tip is located at the end of the identified crack. This approach was previously used in fatigue and fracture applications [226, 227]. An interesting comparison of different methods for locating the crack tip from DIC maps [228] is also available. To the authors' knowledge, this is the first time that such a procedure has been applied to concrete.

Typical horizontal displacement fields *u* and vertical displacements fields *v* with marked crack tip locations and locations for displacement extraction are shown in Figure 36.

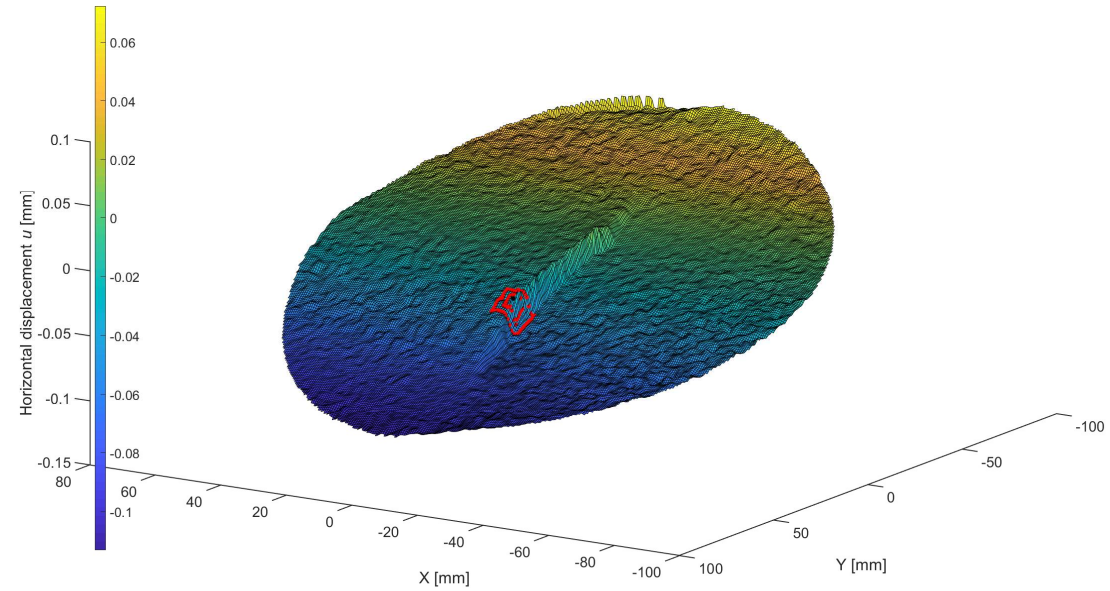

(a)

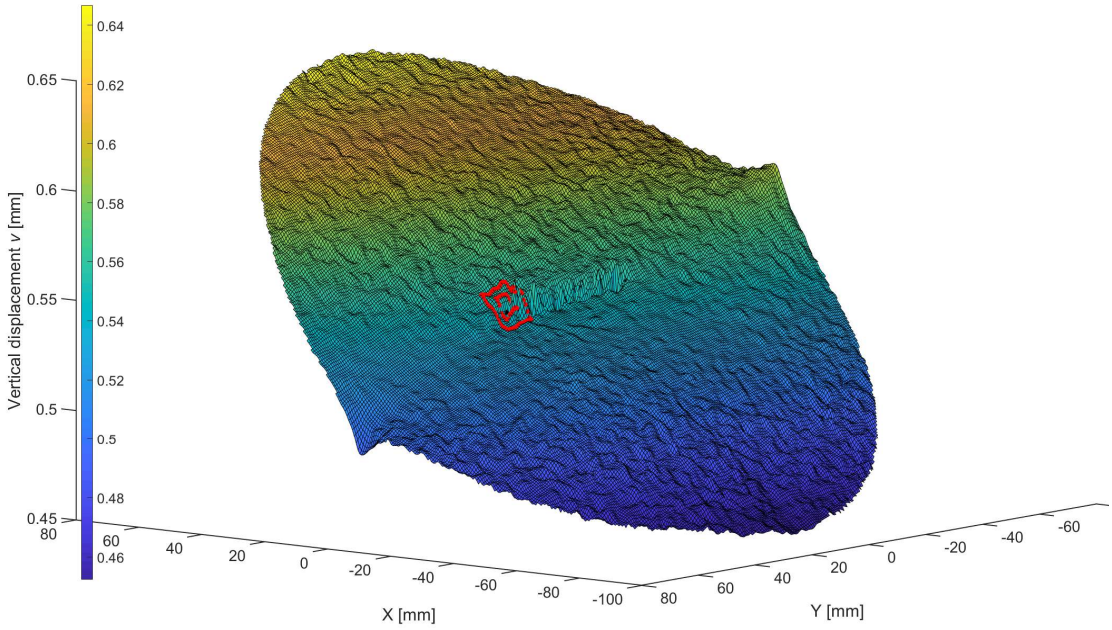

(b)

Figure 36: Displacement fields measured via the DIC technique with a marked notch tip and the chosen distance for the evaluation of the WE coefficients (a) – horizontal displacement *u* and (b) – vertical displacement *v*.

Figure 36 shows both the horizontal (Figure 36(a)) and vertical (Figure 36(b)) displacement maps collected around the crack. The slight non-symmetry observed in both maps is indicative of mode II deformation measured in the neighbourhood of the crack. Such mode II deformation plays a key role in the onset of fracture and has a major influence on the acquired results. The discontinuity generated by the crack can be observed in Figure 36(a) and in Figure 36(b) running parallel to the *Y* axis. Such a discontinuity was detected by Sobel's edge-finding routine and was used to estimate the crack tip position following the strategy previously described [221]. Similar experimental study was performed on the rock specimen by Ji et al [229] with focus set on the mode II deformations.

4. Influence of Aggressive Environment

Hereunder, an experimental procedure used on quantification of the influence of the chloride ingress to the concrete body is presented on the HPC batch B mixture. Moreover, colorimetric experimental technique of obtaining the chloride boundary in the saturated specimen is described. Lastly, the specimens' dimensions are showed together with the environmental conditions.

4.1 Chloride Penetration Depth

In this part of the thesis the value of chloride penetration depth will be assessed by the colorimetric method [56]. This method uses silver nitrate ($AgNO_3$) solution, which is sprayed on the concrete sample saturated with chloride ions directly after the destructive test. Silver nitrate reacts with the sodium chloride NaCl as follows:

$$AgNO_3 + NaCl^- \rightarrow AgCl + NaNO_3 \tag{3.7}$$

This chemical reaction creates the silver chloride (AgCl), which converts itself upon illumination or heating to silver Ag and chlorine Cl, which can be noticed by changing of the coloration of the area saturated with chloride ions.

The tested samples (BD and BDCN) were rinsed by tap water and were left to air dry. Then, the load was applied on the samples. After performing the splitting test, the $AgNO_3$ solution with concentration of 0.1 mol/l was carefully sprayed onto the fresh surface. After approximately 15 minutes from the application of the $AgNO_3$ solution, the area that contains free chloride ions changes its colour to light grey or silver. On the contrary to this, the area with low or zero concentration of chloride ions transforms to brownish colour, see Figure 37.

To highlight the colour boundary, the photo was slightly edited in graphic editor Zoner Photo Studio[230], see Figure 37(b). It can be observed, that the colour change boundary is not the actual boundary of contaminated and uncontaminated zones by chlorides, but it is very close to this curve [59].

(a) (b)

Figure 37: Sprayed specimen with AgNO3 solution after splitting test used for in the measurement of the chloride penetration dept – (a) original photo (b) adjusted photo with more clear boundaries of the chloride affected surface.

The concentration of chloride ions at the colour change boundary is approximately 0.07 mol/l [61]. Nonetheless, according to [231, 232] the concentration value can change in a wide range. Despite the simplicity of this method, the chemical reaction, which triggers the colour to change, is influenced by the concentration and volume of used $AgNO_3$ solution, the pH of studied concrete (or presence of carbonates), and by the chloride content of concrete [59, 233]. This colorimetric method provides fast and straight forward results of the depth affected by chloride ions, even though the exact value of chloride concentration at the boundary of colours was not determined.

This drawback in the proper identification of the chloride boundary was simplified in order to clearly understand the effects of the chlorides on the FMPs of studied HPC concrete. This simplification is based on the found experimental results from both, splitting tests and the colorimetric method, respectively. Generally, the assessment of the chloride penetration depth showed in Figure 37, shows an unpenetrated ligament, in which the chloride ions Cl^- are not

present. If the cross-sections at the middle of the saturated discs with chlorides are shown, one can notice the difference in the size and shape of the unpenetrated ligament area. Simplified chloride penetration depth together with unpenetrated ligament area for the BD specimens is shown in Figure 38(a), while for the BDCN specimen is shown in Figure 38(b).

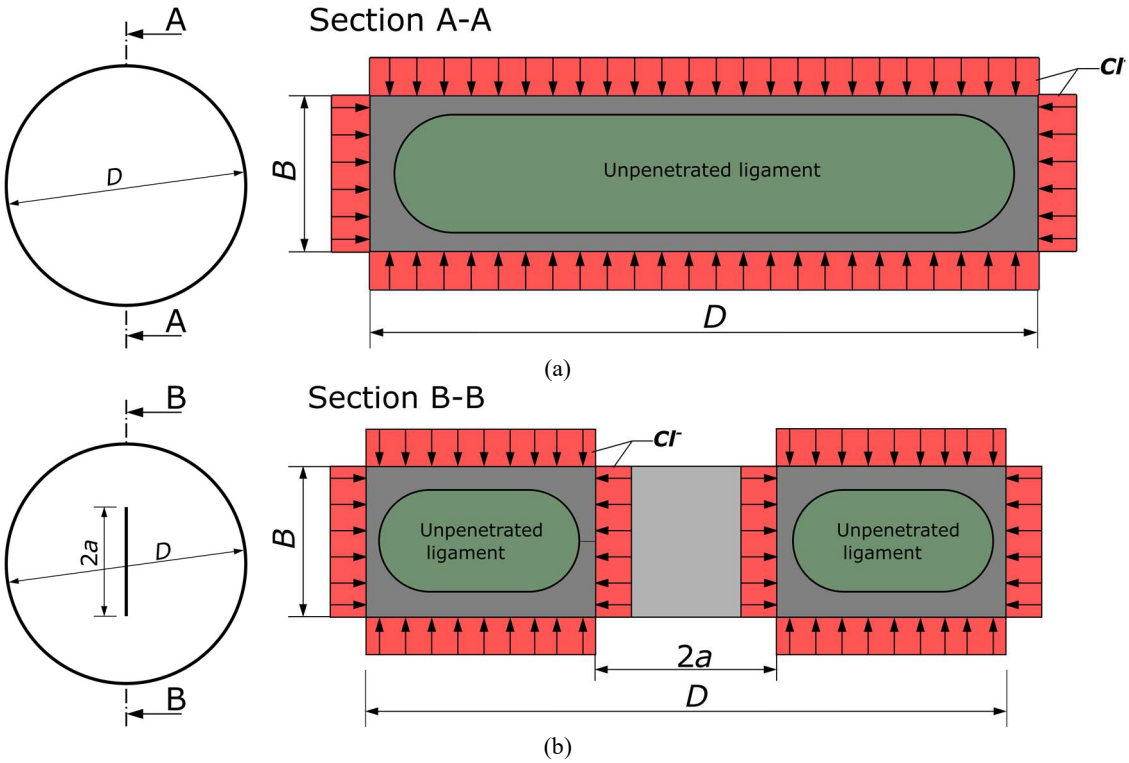

Figure 38: Simplified penetration depth of the HPC samples saturated with the chloride solution – (a) Brazilian disc used in indirect tensile testing and (b) Brazilian disc with central notch used in fracture tests.

From Figure 38(a), the case of the BD sample, the unpenetrated ligament area is extended over the disc's diameter D and width B. On the other hand, the BDCN sample (Figure 38(b)) show the unpenetrated ligament divided into two parts by notch with equivalent ligament area. Both of this chloride contaminated cross-sections show higher chloride content in the corners. This results to a specimen's thickness reduction, which lead to the reduction of the load disc's load-bearing capacity. However, in the case of BDCN, the chloride ions can penetrate into the specimen's ligament from another four surfaces. The major influence has the ions penetrating from the notch end to the specimen's body as they are reducing the ligament area ahead of the notch tip. This additional penetration of chlorides Cl^- ions into the specimen's body lowers the load bearing capacity, which leads to the lower value of fracture loads and equivalent value of the fracture toughness K_{IC} as the load bearing ligament area is highly reduced.

The measurement of the chloride penetration depth was conducted by $AgNO_3$ colorimetric method as described in [61]. After the tests the chloride contaminated specimens were sprayed with the $AgNO_3$ solution and then the depths were measured at intervals of approximately 10 mm to obtain seven values. To mitigate the 2D chloride ingress process near the edges, no measurement was done in the zone within about 10 mm from the edges of the sample.

4.2 Specimen's Dimensions

In this experimental investigation, the BD specimens were used in order to obtain material's indirect tensile strength f_t and the BDCN specimen were tested to get material's FMPs under the mixed mode I/II loading conditions. Such discs were manufactured from standardized cylinders with a diameter D = 150 mm and thickness B approximately of 28 mm. Afterwards discs were stored in two different environments with a different level of aggressivity conditions. First set of discs, was stored in a chloride free environment i.e. in a water tank placed in the laboratory-

controlled conditions. The others samples/discs were stored in chloride-contaminated environment i.e. in the fully saturated sodium chloride $NaCl^-$ solution. The measured dimensions of the BD specimens were diameter *D* and thickness *B*. Measured discs dimensions are presented in Table 12 for both studied cases of different environmental conditions.

Table 12: Dimension of BD specimens used in the indirect tensile strength f_t test for both studied environmental conditions.

		D [mm]	*B* [mm]
Cl^- free samples	**HPC_50_K16**	149.26	27.78
	HPC_51_K16	149.27	27.88
	HPC_52_K16	149.22	27.75
	HPC_53_K16	149.29	27.89
	HPC_54_K16	149.15	28.04
Cl^- saturated samples	**HPC_45_K16_CL**	149.28	28.03
	HPC_46_K16_CL	149.18	27.64
	HPC_48_K16_CL	149.15	28.16
	HPC_49_K16_CL	149.21	29.68

The initial notches of the BDCN specimens were made by water jet cutter in order to provide straight through notch. The notch length 2*a* was 60 mm which gives a relative notch length ratio *a*/*R* of 0.4. The specimens prepared in such process have been used in the measurement of the FMPs of studied material. To have complete information of mixed mode I/II loading conditions and related fracture process, the BDCN specimens were testes for pure mode I (α = 0°), for pure mode II (α = 25.2°) and for mixed mode I/II (α = < 5°; 10°; 15°; 20°>). Three specimens have been tested for each notch inclination angle α in order to cover material's variability on the results, which gives in total 18 samples for both studied cases of the various level of environment aggressivity. The measured dimensions of each tested specimen are presented in Table 13 for the Cl- free case and in Table 14 for the Cl^- saturated case.

Table 13: Dimensions of BDCN test specimens made from HPC batch B material for relative notch length *a*/*R* = 0.4, for the specimens stored in water.

		Inclination angle α [°]	Radius *R* [mm]	Notch length *a* [mm]	Thickness *B* [mm]
Cl^- free samples	**HPC_30_K16**	0.00	74.57	30.03	28.16
	HPC_31_K16	0.00	74.62	30.01	29.46
	HPC_32_K16	0.00	74.67	30.01	27.77
	HPC_40_K16	5.00	74.57	29.79	28.19
	HPC_41_K16	5.00	74.42	29.98	27.75
	HPC_42_K16	5.00	74.66	29.62	27.50
	HPC_14_K16	10.00	74.66	29.98	27.65
	HPC_15_K16	10.00	74.65	29.87	27.66
	HPC_36_K16	10.00	74.52	29.29	28.96
	HPC_13_K16	15.00	74.28	29.95	27.41
	HPC_19_K16	15.00	74.75	29.98	27.88
	HPC_20_K16	15.00	74.65	29.92	27.67
	HPC_10_K16	20.00	74.55	30.02	27.89
	HPC_11_K16	20.00	74.60	30.12	27.59
	HPC_12_K16	20.00	74.57	30.15	27.80
	HPC_04_K16	25.2	74.45	30.09	27.87
	HPC_05_K16	25.2	74.54	30.02	27.48
	HPC_06_K16	25.2	74.35	30.06	27.51

Table 14: Dimensions of BDCN test specimens made from HPC batch B material for relative notch length $a/R = 0.4$, for aggressive environment tests.

		Inclination angle α [°]	Radius R [mm]	Notch length a [mm]	Thickness B [mm]
Cl^- saturated samples	**HPC_27_K16_CL**	0.00	74.53	30.01	27.63
	HPC_28_K16_CL	0.00	74.63	30.02	27.49
	HPC_29_K16_CL	0.00	74.55	29.93	27.97
	HPC_37_K16_CL	5.00	74.47	29.95	28.13
	HPC_38_K16_CL	5.00	74.80	30.04	28.06
	HPC_39_K16_CL	5.00	74.67	30.00	27.84
	HPC_33_K16_CL	10.00	74.57	30.01	27.82
	HPC_34_K16_CL	10.00	74.62	29.99	27.78
	HPC_35_K16_CL	10.00	74.59	30.04	27.69
	HPC_16_K16_CL	15.00	74.60	30.14	28.07
	HPC_17_K16_CL	15.00	74.55	30.06	28.00
	HPC_18_K16_CL	15.00	74.60	29.84	28.68
	HPC_07_K16_CL	20.00	74.59	30.07	27.63
	HPC_08_K16_CL	20.00	74.59	30.02	27.68
	HPC_09_K16_CL	20.00	74.51	30.05	27.68
	HPC_01_K16_CL	25.2	74.54	29.98	27.56
	HPC_02_K16_CL	25.2	74.57	30.01	27.64
	HPC_03_K16_CL	25.2	74.59	30.12	27.60

The prepared BD and BDCN samples were stored in plastic containers filled to the maximum capacity and cover with plastic lid to eliminate excessive evaporation of the water and sodium chloride solution. These samples were stored with adequate distance between each other which allowed the solution (water and sodium chloride $NaCl^-$ solution) to penetrate to the body equally through all free surfaces. The samples were stored in such conditions for 30 days. The containers are shown in Figure 39.

Figure 39: Prepared BD and BDCN specimens stored in plastic containers filled with water and chloride solution in a laboratory room with constant room temperature.

Chapter IV
Numerical Modelling

This chapter firstly presents the numerical model used in the LEFM analysis together with used geometry and boundary conditions. Then, the geometry, boundary conditions, mesh and input material characteristics of the CDP material model as used in the non-linear analysis. The CDP material model input parameters were based on the experimentally measured characteristic of the C 50/60 material. Furthermore, the focus is set on the calibration of the CDP input parameters and the boundary conditions. Both numerical studies are done on the BDCN specimen geometry.

Afterwards, the numerical results, geometry functions and the ODM results for the HO terms of the WE, as generated by LEFM model are presented and discussed. Then the results of the comprehensive non-linear numerical study, which focuses on the influence of the softening behaviour, as represented by post-peak load-displacement curves, on the total load-displacement curves, the crack mouth opening displacement curves, the sliding-displacement curves in mode I, mode II, and mixed mode I/II configuration are presented.

1. LEFM Numerical Model

In order to assess the relevance of the displacement measured by the DIC technique and to measure the fracture mechanical parameters of selected concrete grades, a two-dimensional (2D) numerical model was created in a FEM software ANSYS [234]. The numerical model's material of the BDCN specimen is considered to be linear elastic.

1.1 Geometry, Boundary Conditions and Mesh

The full BDCN specimen was modelled due to the presence of mode II deformations (no symmetry available). The modelled BDCN had dimension corresponding to the dimensions of actual BDCN specimen used in the experiments. Input material parameters were a Young's modulus E of 41 GPa and a Poisson's ratio ν of 0.2. The meshed numerical model with together detail of a crack tip mesh is showed in Figure 40.

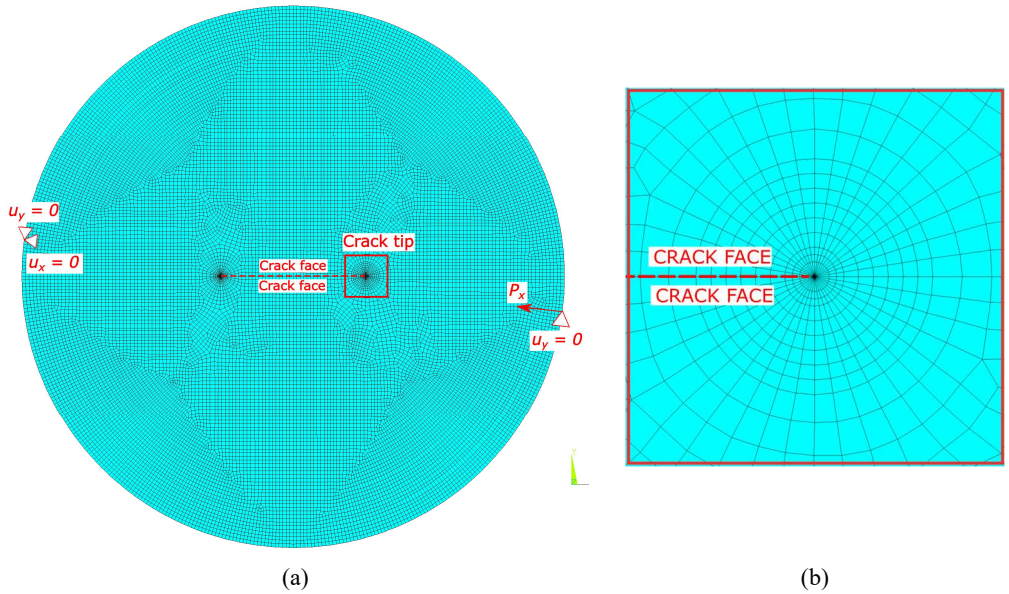

(a) (b)

Figure 40: Meshed numerical model with applied boundary conditions (a) and a detail of the crack tip refinement (b).

The model was meshed with quadrilateral 8-node elements (PLANE183) with plane strain conditions (see Figure 40(a)). The crack tip was meshed using the KSCON command in order to take into account the crack tip singularity and to provide angularly structured mesh. The KSCON command deforms the original quadratic elements around the crack tip into triangular ones and shifts the mid-side nodes to a distance of ¼ of the element's edge (towards the crack tip) [234]. The notch tip refinement is presented in Figure 40(b). Furthermore, the crack faces are modelled without any contact nor interaction due to the notch thickness, which allows crack faces not to interact with each other. In other words in the experiments, the crack faces will not interact with each other due to small gap.

The mesh with refinements around the crack tip mentioned above is then used to extract the numerically generated nodal displacements at the demanded radial distance (ring) from the crack tip. These nodal displacements serve as input data for the ODM calculation of SIFs and *T*-stress. This procedure was chosen in order to verify the relevance of the calculated SIF and *T*-stress values, for which the optically measured displacements served as the input data.

The model was loaded with the force *P* at the right edge of the disc, while the left edge was considered as a rigid support (u_x and $u_y = 0$). Adequate boundary conditions were added to prevent translation of the rigid body (see Figure 40(a)).

The nodal displacements served as an input to the ODM calculation. The horizontal *u* and vertical *v* displacements are taken from the nodes in the demanded radial distance *r*. The accuracy of the ODM method increases with the number of nodal displacements used for calculation. Therefore, the polar angle θ was selected to be 5° which generated in total 142 nodes for quadratic element PLANE183 (mid node is selected as well). This procedure of data extraction is showed in Figure 41.

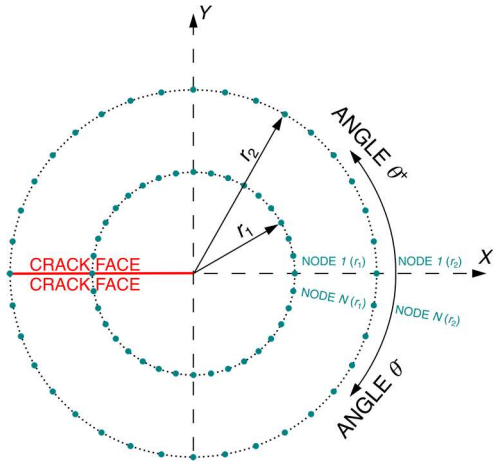

Figure 41: Extraction of nodal displacements from FE model.

The LEFM model was loaded by the force *P* of 100 N in order to obtain geometry functions for mode I Y_I and for mode II Y_{II} and to have values of *T*-stress for various *a*/*R* ratios. Moreover, the same force of 100 N was used in order to obtain values horizontal *u* and vertical *v* displacement ahead of the crack, which were used as input parameters for the ODM to calculate higher order terms of the WE for BDCN geometry. On the other hand, the LEFM model was loaded with experimentally measured forces *P* as presented in Table 15 for each crack length. The use of the actual forces allows to generate the displacement *u* and *v*, which served as an inputs to the ODM method for the WE coefficients calculations. Then the WE coefficients were compared to WE coefficients obtained based on the experimentally measured displacements by DIC.

Moreover, the actual material's Young's modulus of 41 GPa and Poisson's number of 0.2 served as inputs to obtain more accurate results (see HPC mixture batch A on p. 37).

The measured maximum load P_C for various relative notch lengths a/R and various notch inclination angles α are presented in Table 15.

Table 15: Maximum loading force values during the experiment for different BDCN specimens.

	a/R = 0.267		
Specimen No.	HPC_4_3_2	HPC_4_3_3	HPC_4_3_4
Notch inclination angle α [°]	5	10	27.7
Force P_{max} [kN]	22.5	24.3	27.4
	a/R = 0.4		
Specimen No.	HPC_6_3_1	HPC_6_3_2	HPC_6_3_3
Notch inclination angle α [°]	0	5	15
Force P_{max} [kN]	13.09	18.01	17.22

The *I*-integral, as presented in Eq. (2.20) and (2.21) is associated with ANSYS's command CINT. The software's manual recommends using at least four different radial distances for which an interaction integral is calculated, as the first one directly on the crack tip, contains great errors of calculated SIF and *T*-stress values. The results are then the average value of calculated SIFs and *T*-stress values over the selected distances with excluded first solution. Both the SIFs and the *T*-stress are calculated as an average of four contours around the crack tip.

2. Non-linear Analysis

Firstly, the model's geometry and boundary conditions, together with an adopted mesh are presented. Then, the adopted material model's input material properties used in the parametric study are introduced. Lastly, the input parameters for the post-peak behaviour of concrete are discussed.

2.1 Geometry and Boundary Conditions

In order to assess the relevance of the BDCN test, a parametric study of a BDCN was performed using the FEM software Abaqus [195]. For this, 2D plane stress model was created with a radius of R = 75 mm corresponding to the disc's size in [100], and an initial notch length $2a$ = 60 mm corresponding to a relative crack length a/R = 0.4, a notch thickness t of 2 mm and inclination notch angles α of 0°, 5° 10°, 15°, 20° and 25.2°. The initial notch angle α_n was selected to investigate the tensile mode I fracture i.e. α = 0°, the mixed mode I/II fracture for angle α, which varies from 5° to 20°. The pure shear mode II fracture should be present when α = 25.2° [100, 144].

The numerical study was performed with a displacement-controlled loading applied at the top edge of the BDCN, while the bottom edge was considered a rigid support. The total induced vertical displacement was u_y = -0.1 mm (u_x = 0 mm) over the pseudo time step (static analysis). Adequate boundary conditions were added to prevent rigid body translations and rotations (See Figure 42(a)).

The disc's radius was locally reduced by approximately ΔR = 0.17 mm over a 10 mm extended width Δw (See Figure 42(b) and Subsection 3.2 of this thesis) near the loaded edges [235] to limit local compressive stress concentrations to a value lower than the compressive strength f_{cm}.

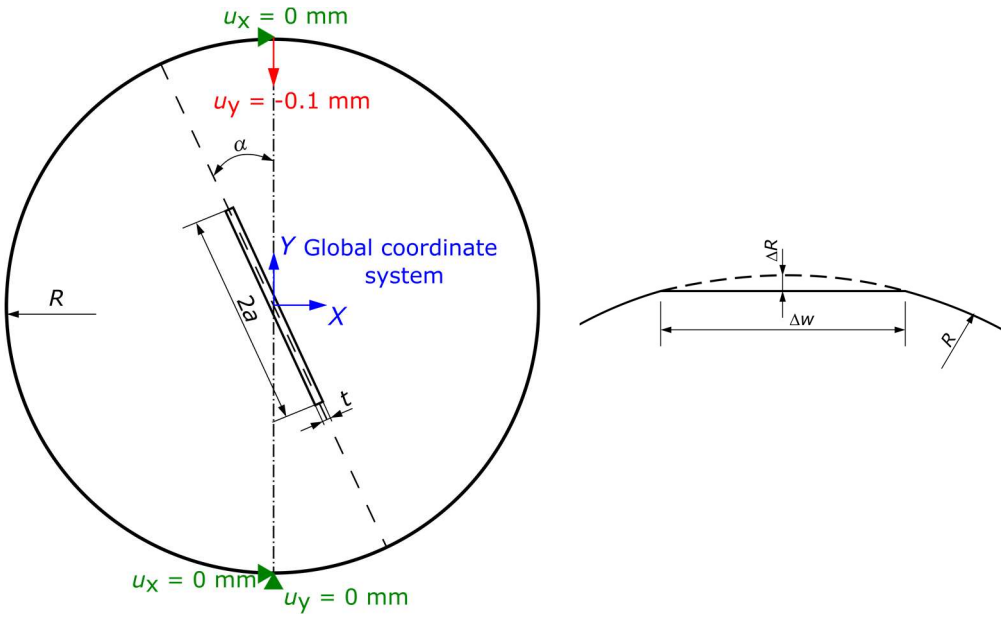

(a) (b)

Figure 42: Geometry and boundary conditions (a) and flattened edge of BDCN model (b).

2.2 Mesh

The non-linear numerical model was meshed with a 4-node linear quadrilateral plane stress element (type CPS4). A fine mesh (Figure 43(a)) with a basic element size of 3 mm was studied with refinements around the notch tip of 0.5 mm (Figure 43(b)). This model shows a mapped mesh pattern, which is crucial to get accurate numerical results. The mapped mesh was created by using sufficient partitioning and refinement of the geometry.

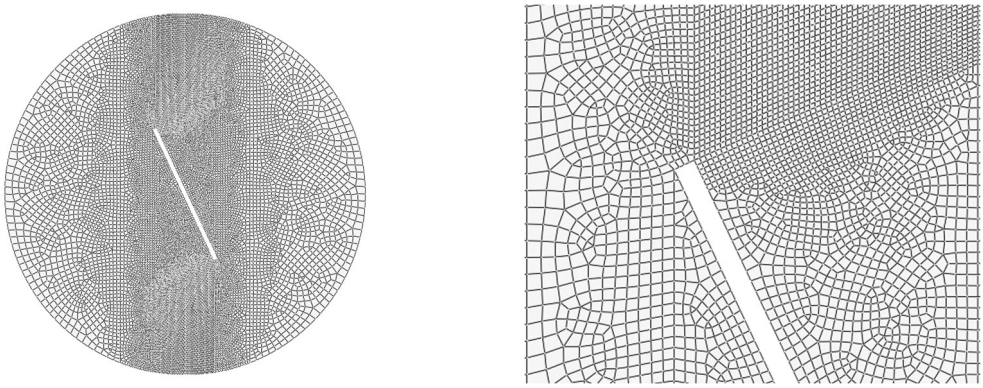

(a) (b)

Figure 43: Meshed numerical model (a) with a detail on the notch tip refinement (b): 17924 elements.

2.3 Input Parameters

In the non-linear numerical analysis, the input parameters are based on test data from [100], which describes the mixture details, the experimental measurement and the relevant material parameters. The compressive behaviour is based on the MC2010 recommendation [18], which provides the uniaxial stress–strain (σ_c–ε curve) response of concrete in compression and assumes a non-linear material behaviour, which can be evaluated from experimental data. MC2010 assumes a linear compressive behaviour up to 40% of the mean compressive strength f_{cm}, and after this point a quadratic function is used, which can be characterized by Eq. (4.1).

$$\frac{\sigma_c}{f_{cm}} = -\left(\frac{k \cdot \eta_c - \eta_c^2}{1 + (k-2) \cdot \eta_c}\right) \text{ for } |\varepsilon_c| < |\varepsilon_{c,lim}|, \tag{4.1}$$

where f_{cm} is the mean compressive strength, $\varepsilon_{c,1}$ is the compressive strain at maximum compressive stress, $\varepsilon_{c,lim}$ is the ultimate compressive strain, k is the plasticity number and $\eta_c = \varepsilon_c/\varepsilon_{c,1}$. Figure 44 shows the uniaxial material response in compression and tension represented by σ–ε relationship.

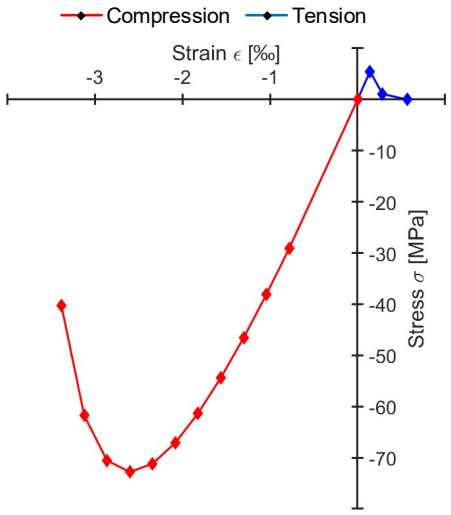

Figure 44: Uniaxial material response in compression and tension represented by the σ_c–ε relationship.

To obtain a post peak response, damage parameters d_c for compression were calculated according to Eq. (2.73) on p. 33. Figure 45(a) shows the material's non-linear compressive input parameters and Figure 45(b) shows the damage parameters for the CDP material model.

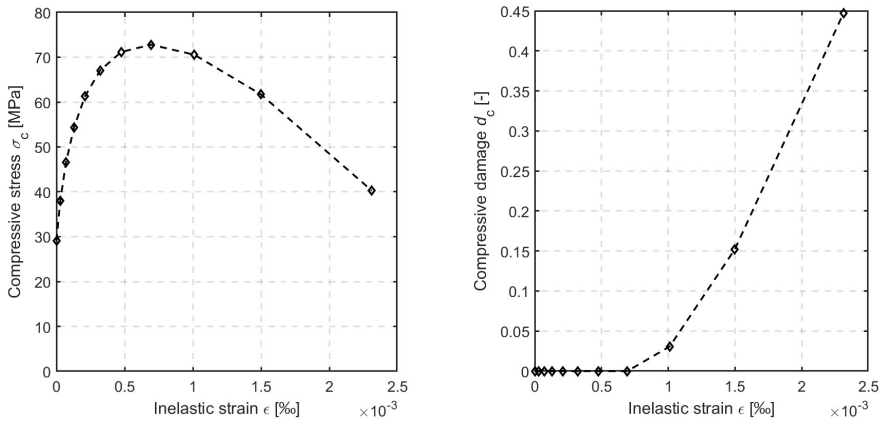

(a) (b)

Figure 45: Material input parameters in compression – stress-strain relationship (compressive stress/inelastic strain) (a) and evolution of compressive damage d_c (b).

The uniaxial stress–strain (σ_t–ε curve) response of concrete in tension assumes a linear elastic behaviour up to the tensile strength f_{ct}. After reaching this tensile strength, a smeared cracking behaviour is assumed, and the cracking process is modelled by the descending branch in a softening process which ends at a maximum tensile strain ε_u, where zero residual tensile strength exists i.e. σ_t = 0 MPa. The concrete's tensile behaviour can be characterized by a stress-crack displacement (σ_t–w curve) response or stress-strain (σ_t–ε) relationship.

The area under the tensile σ_t–w curve represents the fracture energy G_f. The fracture energy can be measured experimentally or calculated from MC2010 by Eq. (4.2).

$$G_F = 0.73 \cdot f_{cm}^{0.18}. \tag{4.2}$$

In study by Seitl et al. on the C 50/60 material [100], the fracture energy was measured on 3PB test specimens and evaluated by using Karihaloo's and Nallathambi's effective crack model [19]. The measured value of G_C was 61 N/m, which is 2.58 × lower than calculated from Eq. (4.2) from which G_F = 157 N/m. A similar material to this one was comprehensively studied by Zimmerman [236].

Table 16 gives an overview of material characteristics measured at 28 days of the C 50/60 material.

Table 16: Material characteristics of the C 50/60 mixture at 28 days adapted from [100].

Young's modulus E [GPa]	38.8
Mean compressive cube strength $f_{c,cube}$ [MPa]	85.8
Mean compressive cylindrical strength $f_{c,cyl}$ [MPa]	72.8
Mean indirect tensile strength f_{ct} [MPa]	5.52
Fracture energy G_C [N/m]	61.6

The maximum tensile strength f_{ct} was measured as an indirect tensile strength from unnotched Brazilian disc test specimens and used in the σ_t–w diagrams.

The σ_t–w descending branch for the softening response was studied in detail by Hillerborg [148], and by Peterson [192], can be defined with different options such as linear, bilinear or exponential behaviour. In this study, one linear and two bilinear softening responses were used.

The linear softening descending branch can be calculated as:

$$\sigma_t(\mathrm{w}) = f_{ct}\left(1 - \frac{w}{w_c}\right) \text{ for } 0 \le w \le w_c, \tag{4.3}$$

$$w_c = \frac{2G_f}{f_{ct}} \text{ when } \sigma_t = 0. \tag{4.4}$$

The linear softening tensile behaviour branch intersects the horizontal axis at a crack width of $2G_F/f_{ct}$.

The first bilinear softening response was determined according to MC2010 [18] and assumes a branch transition at $\sigma_t = 1/5 f_{ct}$, and $G_F/f_{ct} = 1$, and intersects the horizontal axis at a crack width of $5.0G_F/f_{ct}$. The bilinear softening response according MC2010 can be calculated from:

$$\begin{aligned} \sigma_t(\mathrm{w}) &= f_{ct}\left(1 - 0.8\frac{w}{w_1}\right) \text{ for } w \le w_1, \\ \sigma_t(\mathrm{w}) &= f_{ct}\left(0.25 - 0.05\frac{w}{w_1}\right) \text{ for } w_1 < w \le w_c, \end{aligned} \tag{4.5}$$

$$w_1 = \frac{G_f}{f_{ct}} \text{ when } \sigma_t = {}^1\!/_5 \cdot f_t \,;\; w_c = \frac{5G_F}{f_{ct}} \text{ when } \sigma_t = 0. \tag{4.6}$$

The second bilinear softening was calculated according to Hillerborg [148] with a branch transition $\sigma_t = 1/3 f_{ct}$ and $G_f/f_{ct} = 0.8$ and intersects the horizontal axis at a crack width of $3.6G_F/f_{ct}$. The bilinear response according to Hillerborg can be expressed as:

$$\begin{aligned} \sigma_t(\mathrm{w}) &= f_{ct}\left(1 - \frac{2w}{3w_1}\right) \text{ for } w \le w_1, \\ \sigma_t(\mathrm{w}) &= f_{ct}\left(\frac{3}{7} - \frac{2}{21}\frac{w}{w_1}\right) \text{ for } w_1 < w \le w_c, \end{aligned} \tag{4.7}$$

$$w_1 = \frac{0.8G_F}{f_{ct}} \text{ when } \sigma_t = {}^1\!/_3 \cdot f_{ct} \,;\; w_c = \frac{3.6G_F}{f_{ct}} \text{ when } \sigma_t = 0. \tag{4.8}$$

Damage parameters d_t in tension can be calculated by Eq. (2.74). Figure 46(a) shows a comparison of the used material σ_t–w curves, and Figure 46(b) shows corresponding damage parameter d_t.

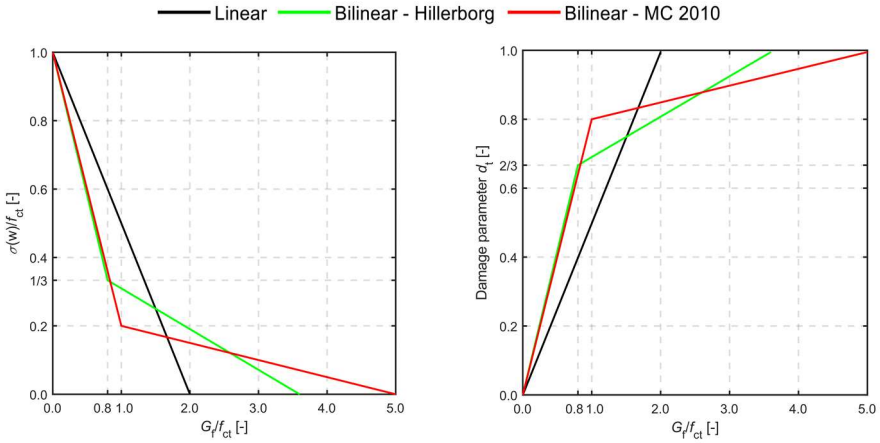

(a) (b)

Figure 46: Comparison of various material inputs for tensile descending stress-displacement curves: linear, bilinear according to MC2010 and bilinear according to Hillerborg, respectively.

As demonstrated further in this paper, the fracture energy G_F has a major influence on the material response in the BDCN test, thus a parametric study of the influence of various G_F/G_C ratios on the numerical results was carried out. This parametric study is based on the equivalent (characteristic) element length l_{eq} [237-239], which covers the strain localization in the numerical analysis. For 2D elements, the characteristic length can be calculated as a square root of element's area, which gives $\sqrt{l_e}$, where l_e is the element length (See following section). The strain localization is then minimized by assumption of G_F/l_{eq}. In order to cover various element size over the studied geometry, the investigated ratios G_F/G_C were chosen as 1.0; 1.5; 2.0 and 2.58 for all studied tensile softening σ_t–w curves.

Table 17: Overview of various ratio G_F/G_C ratios for the studied σ_t–w curves with nomenclature used in numerical results.

G_F/G_C [-]	1.0	1.5	2.0	2.58
Bilinear model- MC2010	Mat_1	Mat_2	Mat_3	Mat_4
Bilinear model- Hillerborg	Mat_5	Mat_6	Mat7	Mat_8
Linear model	Mat_10	Mat_11	Mat_12	Mat_9

The combinations mentioned in Table 17 lead to the softening σ_t–w curves and the damage parameters d_t displayed hereunder in Figure 47(a-c) and in Figure 48(a-c).

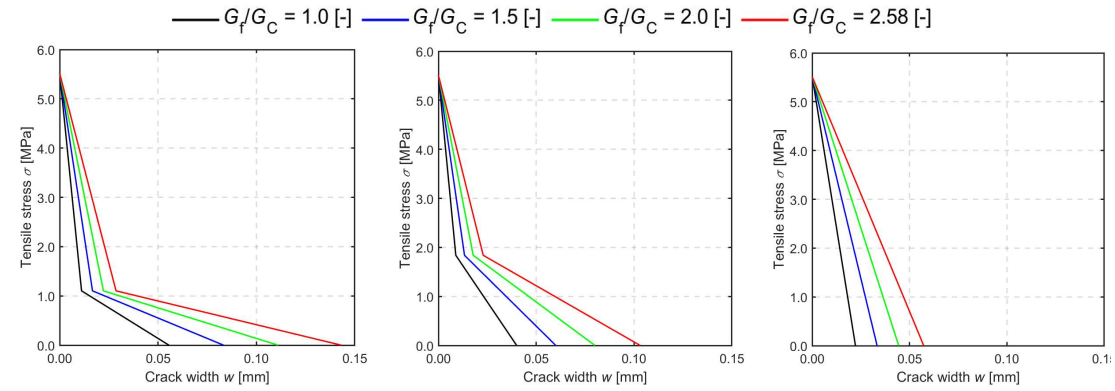

(a) – MC 2010 (b) – Hillerborg (c) – Linear

Figure 47: Material input in tension using bilinear softening branch based on MC2010 recommendation (a), Hillerborg model (b) and linear softening (c).

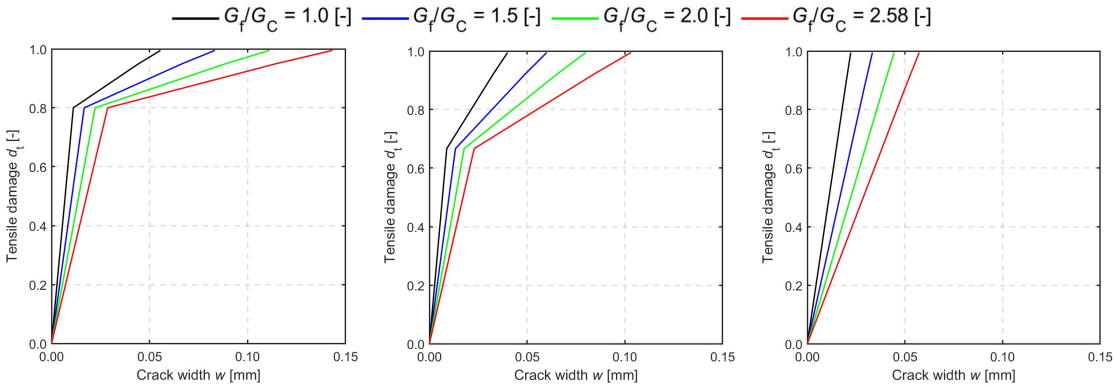

(a) – MC 2010 (b) – Hillerborg (c) – Linear

Figure 48: Damage parameters in tension using bilinear softening branch based on MC2010 recommendation (a), Hillerborg model (b) and linear softening (c).

3. Numerical Results and Discussion

Hereunder, numerical results are presented of both LEFM analysis and of the non-linear analysis employing the CDP material model. Firstly the LEFM results of SIFs for mode I and mode II together with the *T*-stress values are presented then the results obtained from the ODM method solution for HO terms of the WE. Afterwards, the calibration of the input parameters for the non-linear material model's is showed. Lastly, the results of the CDP model are showed in form of numerically generated stress, strains and *P*-δ diagrams of the BDCN specimen.

A discussion is added on the required geometrical transformation of the nodal displacement at the notch tip to distinguish mode I and mode II. In this, nodal transformations were done for various transformation angles based on geometry (i.e. the notch inclination angle), fracture mechanics (i.e. MTS and GMTS criteria) and plasticity (i.e. the actual numerically measured crack initiation angle) crack initiation conditions. Finally, the non-linear analysis's results, as generated by the CDP material model, are showed and compared to the experimentally obtained results.

3.1 LEFM Numerical Results

Most of this thesis deals, in the experimental part, with the application of the GMTS criterion. Thus, it was necessary to perform comprehensive numerical study to calculate geometry functions for mode I and mode II, which were then used for the evaluation of the SIFs and fracture toughness K_{IC}. Since the GMTS uses *T*-stress in its fracture evaluation, this value was calculated as well. Then the ODM was used in order to determinate the HO terms of the WE.

3.1.1 Geometry Function for BDCN specimen

To evaluate the values of geometry function Y_I and Y_{II} a numerical model, presented in section 1.1, was used. The CINT command was used to calculate SIFs for mode I and mode II for various notch lengths a/R and initial notch inclination angle α. The relative notch lengths were selected as {0.2; 0.267; 0.3; 0.5; 0.6} and values of notch inclination angle α were <0° - 45°>.

The geometry function for mode I and mode II can be obtained from (3.2) and (3.3) on p. 42 by manipulating them into following form:

$$Y_I(a/R,\alpha) = \frac{K_I RB\sqrt{\pi}}{P\sqrt{a}}\sqrt{1-\frac{a}{R}}, \tag{4.9}$$

$$Y_{II}(a/R,\alpha) = \frac{K_{II} RB\sqrt{\pi}}{P\sqrt{a}}\sqrt{1-\frac{a}{R}}. \tag{4.10}$$

Using the numerically generated values of K_I and K_{II} into Eqs. (4.9) and (4.10) one can obtain the values of geometry function Y_I and Y_{II}. The values of the shape functions for mode I and mode II can be found in the literature, e.g. Ayatollahi and Aliha [144] and in [217], Seitl et al. [208] et al. and Fett [129]. In this study, various notch lengths a/R were chosen, which results in different values being obtained for SIF and the level of constraint.

The evaluated geometry functions Y_I and Y_{II} for various a/R ratios are presented in Figure 49.

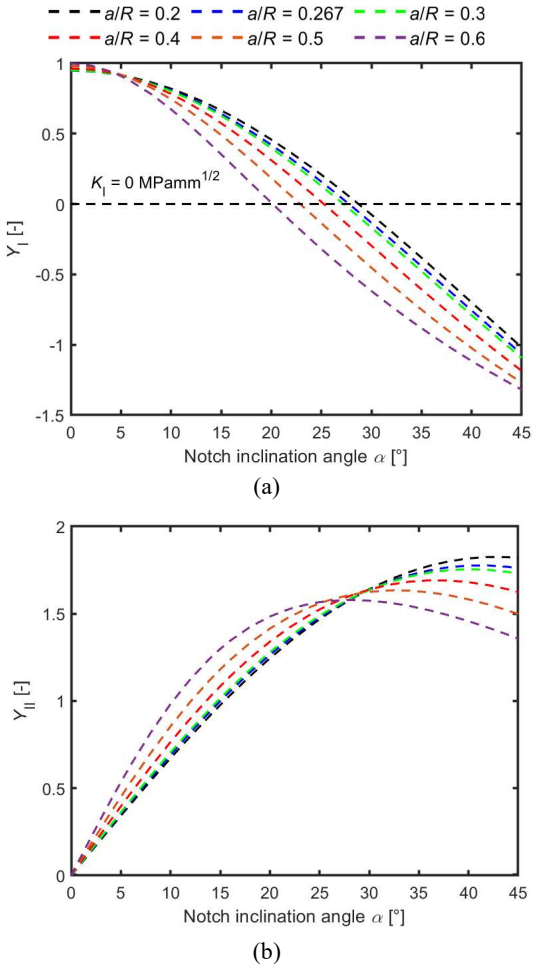

Figure 49: Comparison of geometry function values for various a/R ratios - (a) for mode I Y_I and (b) for mode II Y_{II}.

The negative values of geometry functions Y_I, as observed in Figure 49, is related to the interface free crack faces, which results into overlapping the crack faces in the numerical solution. In practice, the negative value of Y_I and K_I would arrest the crack initiation.

Similarly to SIFs, *T*-stress values can be generated by FEM model. The numerically calculated *T*-stress values for various *a*/*R* ratios are shown in Figure 50.

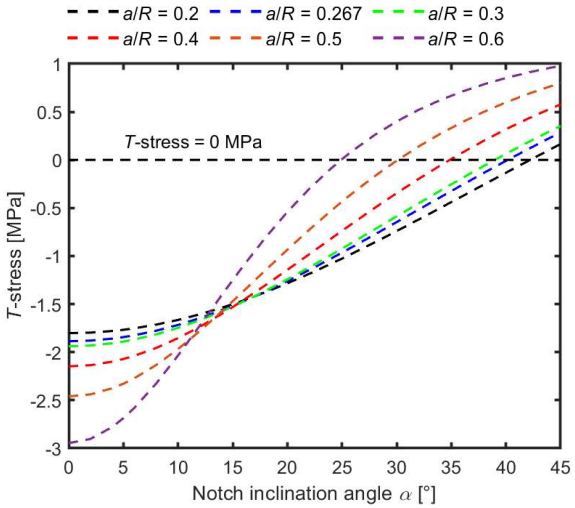

Figure 50: Comparison the numerical generated *T*-stress values for various relative notch length *a*/*R* corresponding to load *P* = 100 N.

From Figure 50 an increase of *T*-stress values can be noticed for *a*/*R* ratio greater than 0.3. This is due to the longer notch lengths, which are affected by the loading force *P*, i.e. the loading point starts to influence the stress ahead of the crack tip, which are decreasing when the notch inclination angle *α* is changing. Another observation can be made, that for the BDCN *T*-stress in valid *α* range (for which Y_I is equal to 0) has negative value.

Wide range of notch inclination angle *α* was chosen to demonstrate the fact that the pure mode II is present for different angle *α* for each studied *a*/*R* ratio. Moreover, the angle α for which a pure mode II is present is decreasing with an increasing *a*/*R* ratio. Similarly to this, the values of the *T*-stress are presented in order to show for which angle *α* is *T*-stress equal to 0. The detailed values of notch inclination angles *α* for which $Y_I = 0$ ($\alpha_{Y_I=0}$) and *T*-stress = 0 ($\alpha_{T=0}$) are showed in Table 18. Please note that the values for the *α* of 27.7°and 25.2° were estimated more precisely due to experimental measurements, while the rest of the presented values of notch inclination angles *α* has only illustrative character.

Table 18: Comparison of angle *α* for which $Y_I = 0$ and *T*-stress = 0 for various notch lengths *a*/*R*.

a/*R* [-]	$\alpha_{Y_I=0}$ [°]	Y_I [-]	$\alpha_{T=0}$ [°]	*T*-stress [MPa]
0.2	29	0.05	42	-0.013
0.267	27.7	0.003	40	-0.001
0.3	28	0.201	38	-0.061
0.4	25.2	0.002	34	-0.058
0.5	22	0.374	26	-0.008
0.6	20	0.078	25	0.008

From the results presented in Table 18, it can be observed that the $\alpha_{Y_I=0}$ and $\alpha_{T=0}$ significantly vary from each other. Moreover, *T*-stress value of 0 is not when $Y_I = 0$, which again plays key role in the crack initiation and propagation.

3.1.2 ODM Results of HO Terms

Similarly to geometry functions Y_I and Y_{II} and to *T*-stress values the HO terms of the WE can be evaluated by using the ODM procedure. Akbardoorst showed calculation of HO of the WE in [240] by using same method as its presented here.

For the calculation of HO terms, 15 numbers of *N* and *M* were used for a radius *r* of 1 mm. These parameters were selected as they were producing results with sufficient accuracy. The values of A_1 and B_1 are showed in Figure 51.

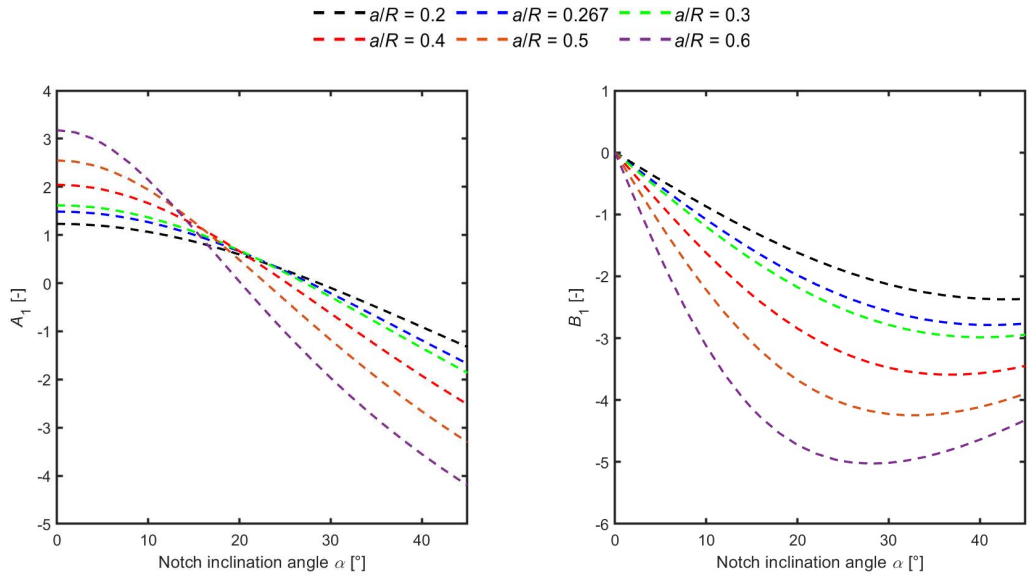

(a) (b)

Figure 51: Comparison of first singular terms of WE for various notch lengths (a) A_1 and (b) B_1.

From Figure 51 a similar trend of A_1 and B_1 to the values of Y_I and Y_{II} in Figure 49 can be seen. Please note that the K_{II} is expressed as $-\sqrt{2\pi}B_1$ therefore the Figure 51(b) shows the negative values, while the Figure 49(b) shows positive values of Y_{II}. Furthermore, the A_2 values are presented, which again showed great agreement to the values of T-stress as generated by the FEM model and Eq. (2.21) on p. 14. The A_2 values are presented in Figure 52.

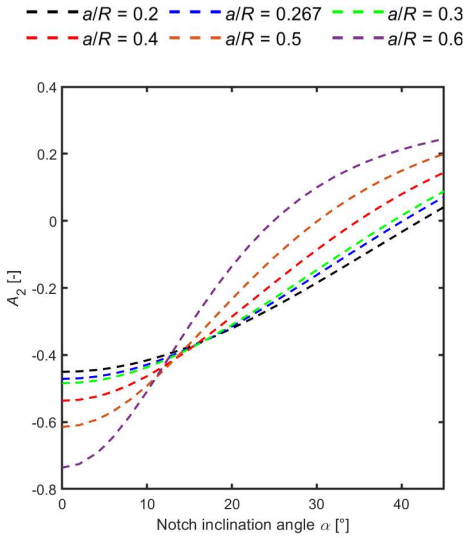

Figure 52: Comparison of the A_2 values for various a/R ratio calculated by using the ODM.

Subsequently, coefficients A_3 and B_3 were calculated. Both A_3 and B_3 were calculated using 15 N and M terms and for the distance r = 1 mm and r = 4 mm to show dependency on the radial distance r. The calculated values of A_3 and B_3 coefficients are presented in Figure 53.

From Figure 53 clearly A_3 and B_3 depends on the distance r. This is in agreement stated in section 1.3.3 in Chapter II as the HO terms are more dominant in further distance from the crack tip. However, the A_3 value is influenced less than the B_3. This difference is again more observable for the higher values of a/R. Thus it is recommended to choose distance r greater than 1 mm for the calculation of A_3 and B_3 as they can be greatly affected.

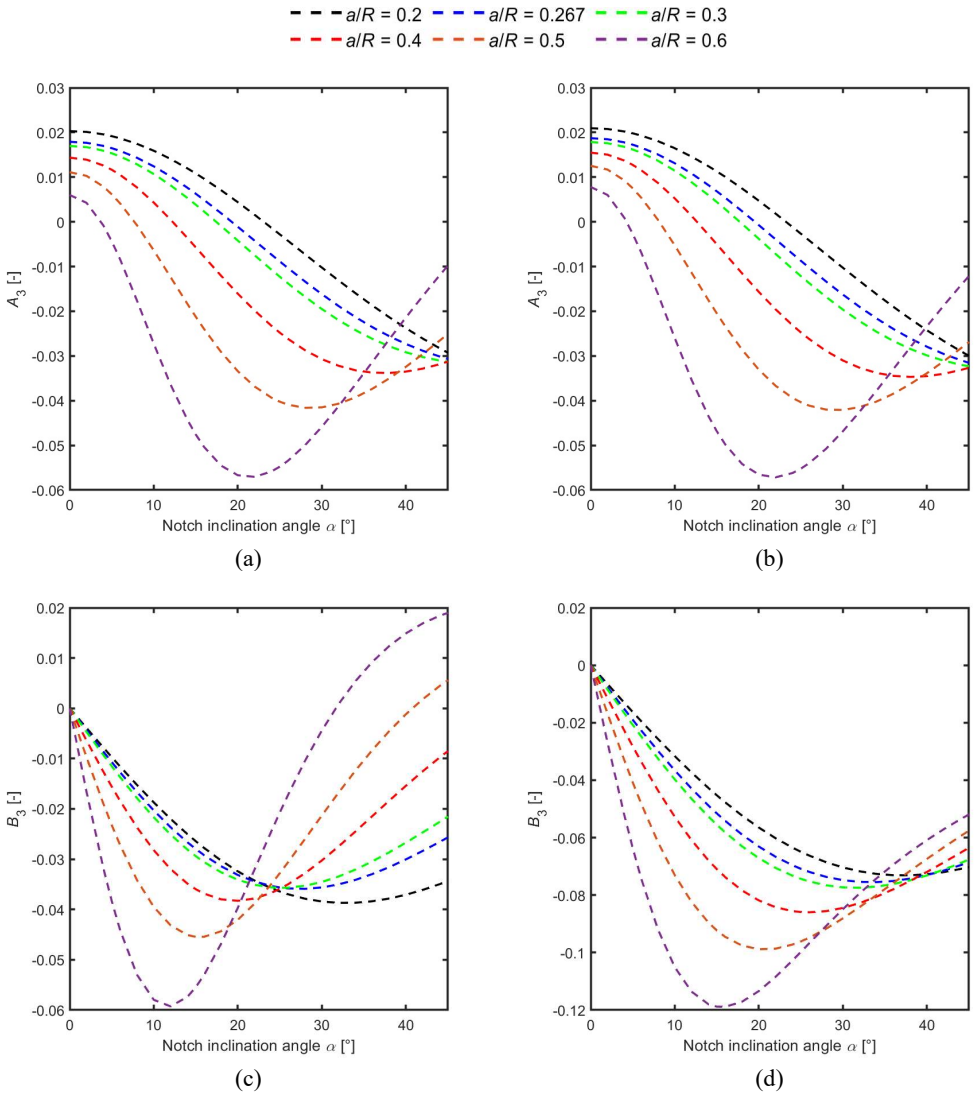

Figure 53: Comparison of influence of the distance r on the values of HO terms of WE for various a/R ratios – (a) A_3 for r = 1 mm – (b) A_3 for r = 4 mm – (c) B_3 for r = 1 mm and (d) B_3 for r = 4 mm.

3.2 Material Model Calibration

In this subsection, a calibration of the input parameters of used CDP material model in non-linear analysis is presented with focus set on obtaining the typical brittle/splitting response of the BDCN specimen under compressive loading. In this model calibration, input parameters were used for material 2(mat_2 from Table 17 and Figure 47(a) i.e. the ratio of G_F/G_C was 1.5 with bi-linear softening branch according to MC2010, if it is not stated differently. The initial notch inclination angle α was set to 25.2° to represent the pure shear loading. The calibrated input parameters of the CDP material model were the constitutive parameters mentioned in the Table 1 i.e. viscosity parameter η and dilatation angle ψ, together with tensile softening branch and its maximum tensile strength f_t, and equivalent tensile damage parameter d_t. Subsequently, various boundary conditions at the bottom and top of the disc together with various mesh size and element type were investigated.

3.2.1 CDP input parameters

The first calibrated parameter was the tensile strength f_t, which has varied by 20% from the measured experimental value i.e. $0.8f_t$ = 4.412 MPa, $1.0f_t$ = 5.515 MPa and $1.2f_t$ = 6.618 MPa using a tensile bilinear softening branch according to the MC 2010 recommendations. The fracture energy in the model's calibration was set to $1.5G_C$ to take into account the characteristic

length l_{ch}. The material post-peak tensile behaviour together with the tensile damage are presented in Figure 54(a) and Figure 54(b), respectively.

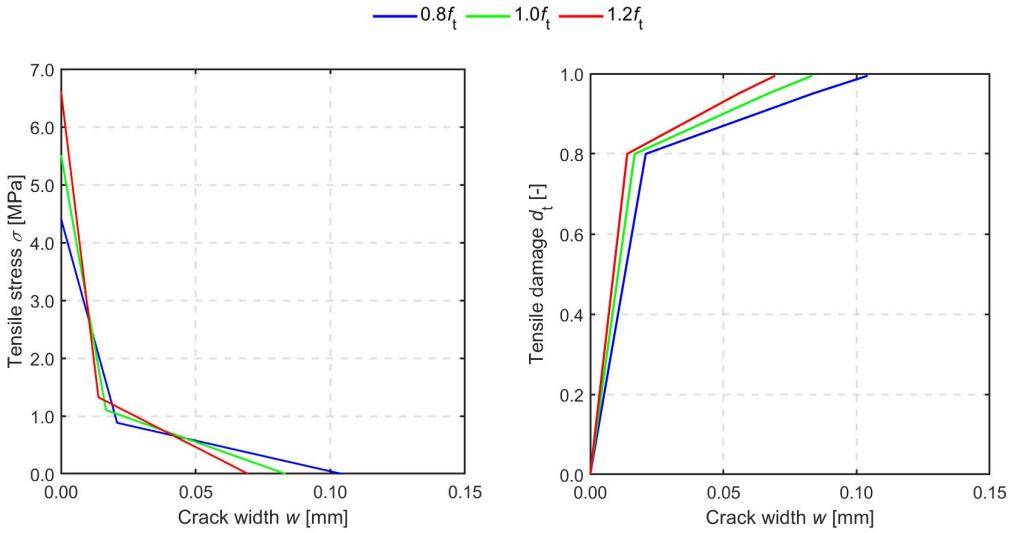

(a) (b)

Figure 54: Material input in tension using bilinear softening branch based on MC2010 recommendation (a), damage parameters in tension (b).

The influence of the viscosity parameter η was verified in range of $\eta = 0$, $\eta = 0.00001$, $\eta = 0.0001$ and $\eta = 0.001$ based on the numerical results presented in [36, 241] for all three material inputs shown in Figure 54. The influence of the viscosity parameter η on the P-δ diagram is presented in Figure 55.

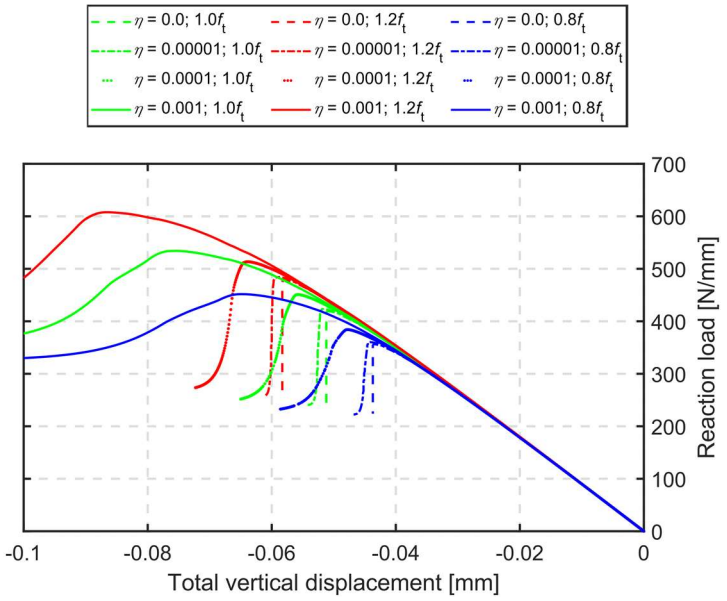

Figure 55: Influence of the viscosity parameter η and tensile strength f_t on the total P-δ diagram of the BDCN specimen for $\alpha = 25.2°$.

The numerical results presented in Figure 55 show overall responses from brittle for $\eta = 0$ to what can be considered as plastic for $\eta = 0.001$. Therefore, the viscosity parameter was set to $\eta = 0$ to generate the brittle/splitting behaviour of the BDCN specimen. The influence of the tensile strength on the maximum reaction load P_{max} is in agreement with the general expectation, increasing with increasing values of tensile strength f_t. The difference in P_{max} is limited to 15% for both $0.8f_t$ and $1.2f_t$. All maximum loads P_{max} are presented in Table 19.

Table 19: Overview of maximum reaction loads P_{max} [N/mm] for various tensile strength values f_t and viscosity parameters η.

	$\eta = 0$	$\eta = 0.00001$	$\eta = 0.0001$	$\eta = 0.001$
$0.8f_t$	356.26	360.26	384.17	451.70
$1.0f_t$	418.93	423.28	450.85	534.19
$1.2f_t$	478.45	484.19	513.40	607.80

The other studied material parameter was dilation angle ψ, which varied from 26° to 44°. This range of angle ψ was based on data found in literature [198, 199] to see its influence on the P-δ diagram. The generated P-δ curves for various dilation angles are presented in Figure 56.

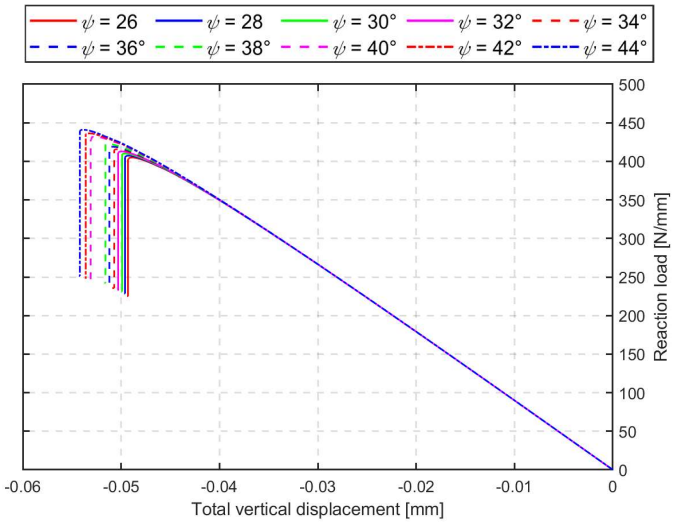

Figure 56: Influence of the dilatation angle ψ on the generated P-δ diagrams for $\alpha = 25.2°$.

The influence of the dilatation angle ψ on the P-δ diagrams is again in agreement with general expectation, maximum reaction loads P_{max} are increasing with increasing values of dilatation angle ψ. The difference in calculated maximum reaction loads P_{max} is limited up to 1%. Therefore, in further numerical analysis an artificial value of $\psi = 36°$ was considered as it is recommended in the literature [36, 198, 199]. All generated maximum reaction loads P_{max} for various ψ angles are presented in Table 20.

Table 20: Overview of influence of the dilation angle ψ on the maximum reaction loads P_{max} [N/mm].

ψ [°]	26	28	30	32	34	36	38	40	42	44
P_{max} [kN/mm]	405.05	407.43	410.43	412.83	415.85	418.93	422.56	432.15	436.26	440.89

3.2.2 Element Type and Mesh Size

Since the mesh size and element type have direct influence on the specimen's response to compressive loading a three different mesh sizes and two different element types were used in model's calibration.

4-node (CPS4) and 8-node (CPS8) quadrilateral plane stress elements have been compared since the CPS4 element can show shear and volumetric locking. However, in such case the Abaqus manual recommends to use more than 3 elements per height of the bended beam. In this case of BDCN, the disc is not primarily bended but only locally bended, and the main failure or crack initiation is due to indirect tensile forces/stresses present in the geometry. Also, more than 50 elements over the disc's radius were used.

To verify the element type dependence models meshed with CPS4 and with CPS8 element type were considered. The generated stresses were taken from the path with origin at the notch tip going parallelly with y-axis to the disc's edge. The normal stress σ_{22} generated by using the CPS8

element differs by 75% from the CPS4 element (CPS8 has +75% higher stress). The other stresses have reasonable error limited up to 10% and for the first principal stress σ it is only 5%. The stress distributions over the disc's radius are presented in Figure 57.

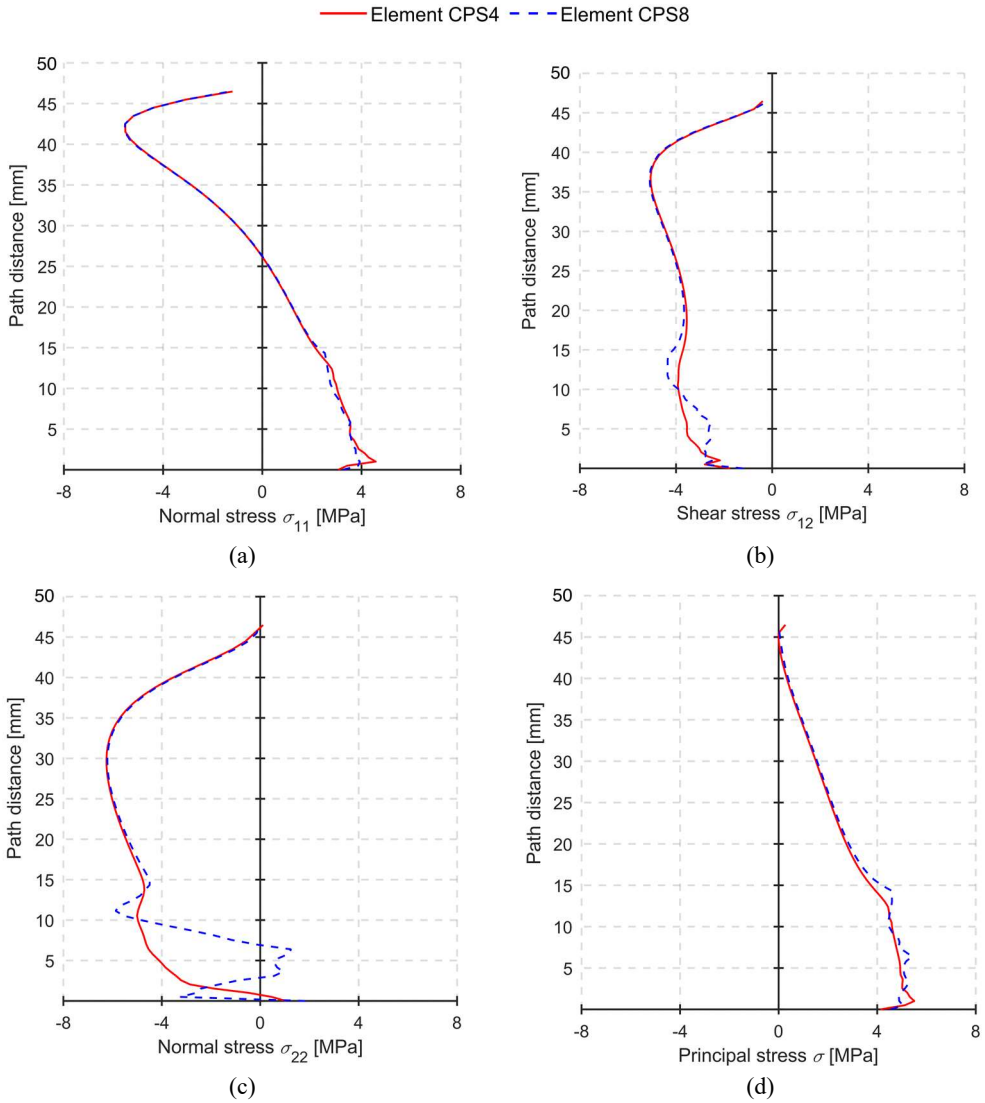

Figure 57: A comparison of various stress distributions over the disc's radius generated by CPS4 and CPS8 element type for $\alpha = 25.2°$ (a) – normal stress σ_{11}, (b) – normal stress σ_{22}, (c) – shear stress σ_{12} and (d) first principal stress σ.

Since the element type directly influences stress distributions, a similar observation can be noticed on the P-δ diagram. The maximum reaction load for element type CPS4 P_{max} is 418 N/mm while for CPS8 element P_{max} is 408 N/mm. This difference can be spotted in Figure 58.

For clarity reason, please note that stress σ_{11} corresponds to stress σ_{xx}, that stress σ_{22} corresponds to stress σ_{yy}. This notation is used in FEM software Abaqus.

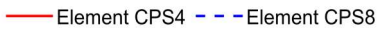

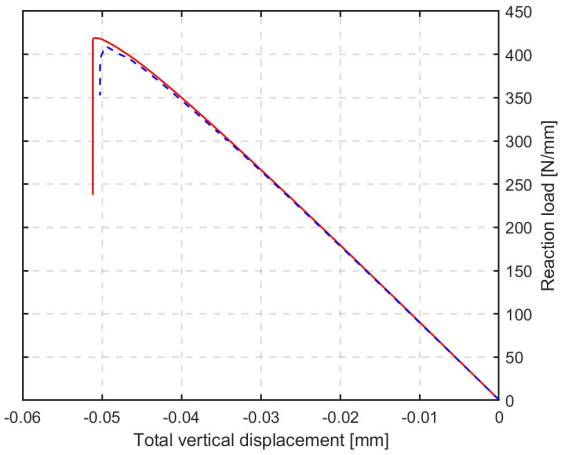

Figure 58: P-δ diagram generated by 4-node CPS4 and 8-node CPS8 element type for $\alpha = 25.2°$.

Due to the combination of negligible difference in the stress distributions, the maximum reaction load P_{max} and to generate a reasonable convergence time the element type CPS4 is used further in the numerical analysis.

Subsequently, the influence of the mesh size on the numerical results was validated. In total, three different mesh sizes were adopted i.e. fine mesh (Figure 59(a)), medium-sized mesh (Figure 59(b)) and coarse mesh (Figure 59(c)). The basic element size for fine mesh was of 3 mm, for medium-sized mesh of 4 mm and for coarse mesh of 6 mm. In all these cases, a refinement around the notch tip was applied. The applied refinement has a length of 0.5 mm (Figure 59(e)) for the fine mesh, of 1 mm for medium-sized mesh (Figure 59(f)) and of 2 mm for coarse mesh (Figure 59(g)). These mesh configurations reduce the total number of adopted elements from nearly 17 500 to only 2950 elements. A comparison of these meshes with detail on the notch tip is presented in Figure 59.

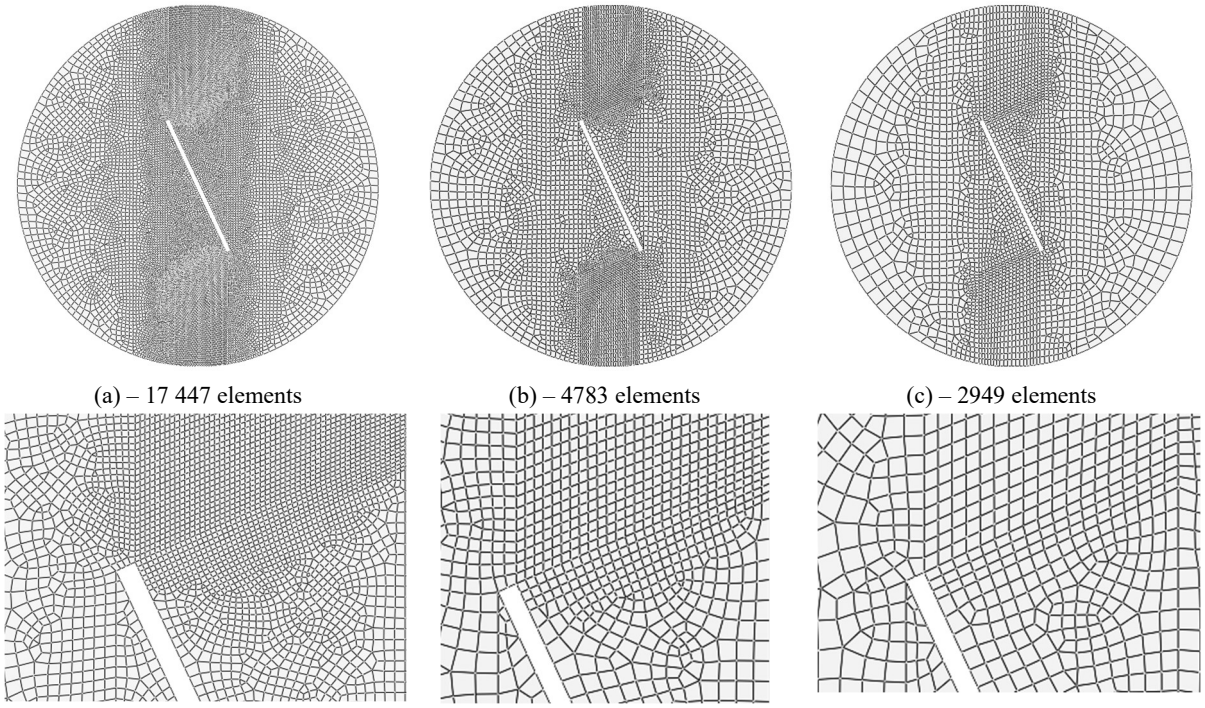

(a) – 17 447 elements (b) – 4783 elements (c) – 2949 elements

(e) (f) (g)

Figure 59: Comparison of various mesh sizes with detail on refinement around the notch tip – (a), (e) fine mesh, (b), (f) medium sized mesh and (c), (d) coarse mesh.

Subsequently, with the various element sizes a tensile post-peak behaviour was adopted to take into account the characteristic length l_{ch}. This was done by changing ratio of fracture energy G_F/G_C. The G_F/G_C ratio used in mesh size verification was 1.5 for the fine mesh (material 2 See Table 17), 0.707 for the medium-sized mesh and 0.8 for the coarse mesh. Consequently, the tensile damage parameter was changed for the same reasons. The influence of these material input parameters on the overall response of the BDCN specimen was verified for all abovementioned mesh sizes. The material tensile softening branches used in mesh size study are shown in Figure 60.

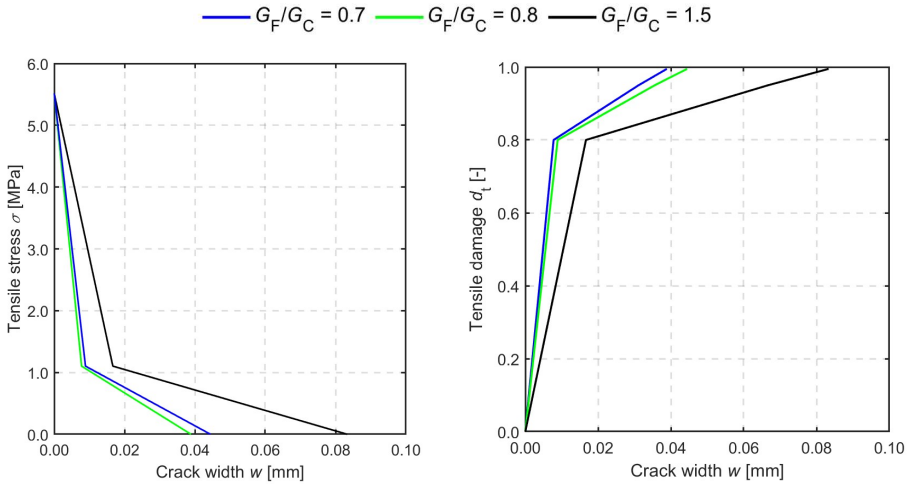

Figure 60: Material input in tension using bilinear softening branch based on MC2010 recommendation (a), damage parameters in tension (b) adapted for various elements sizes.

The numerical results confirm that the element size directly influences the *P*-*δ* diagrams generated for each mesh size. The *P*-*δ* curve for the fine mesh size shows brittle/splitting behaviour i.e. the force/reaction load drops, while the total vertical displacement *δ* does not increase when P_{max} is reached. In this case, there is no softening behaviour observed. Simultaneously, this brittle/splitting behaviour can be observed for the case of fine mesh for all fracture energy variations. The comparison of the generated *P*-*δ* curves is shown in Figure 61.

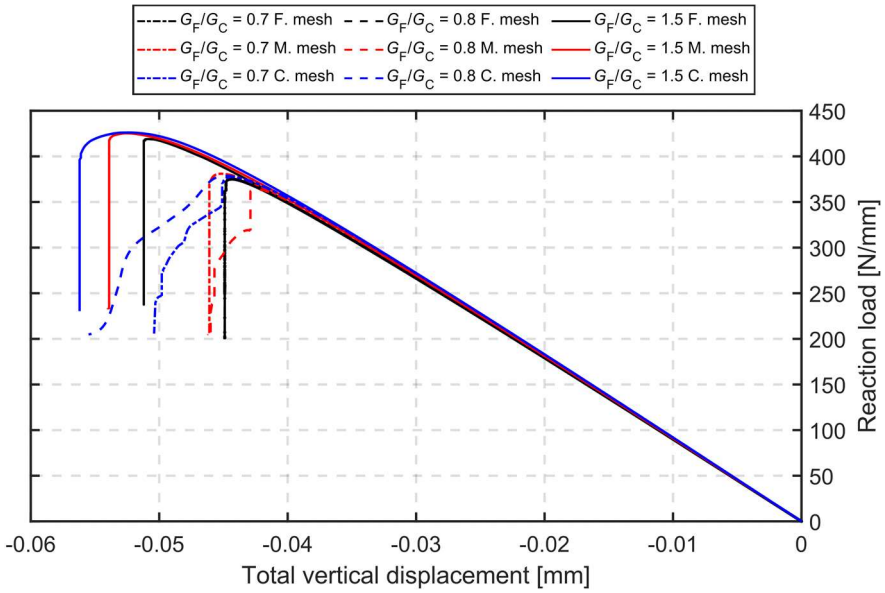

Figure 61: Comparison various *P*-*δ* diagrams generated for different mesh size and for the G_F/G_C ratio fracture energy input.

However for the other studied cases, the *P*-*δ* curve shows major softening behaviour i.e. the difference in the total vertical displacement is higher for the G_F/G_C ratio as for mesh size.

Nevertheless, the difference in maximum load P_{max} is less significant, as it is limited up to 2%. This comparison of maximum reaction loads P_{max}, and maximum vertical displacements δ_{max}, as generated for various meshes and G_F/G_C ratios, is presented in Table 21.

Table 21: Comparison of maximum reaction load P_{max} and maximum vertical displacements δ_{max} generated for various mesh size and various G_F/G_C ratio.

Mesh size	$G_F/G_C = 0.7$		$G_F/G_C = 0.8$		$G_F/G_C = 1.5$	
	P_{max} [kN/mm]	δ_{max} [mm]	P_{max} [kN/mm]	δ_{max} [mm]	P_{max} [kN/mm]	δ_{max} [mm]
Fine	375.03	-0.0449	375.03	-0.0449	418.12	-0.0512
Medium-sized	380.932	-0.0462	364.017	-0.0461	425.36	-0.0540
Coarse	377.521	-0.0504	378.663	-0.0556	426.11	-0.0562

A similar observation of the softening behaviour can be found in the inelastic strains and equivalent principal stresses at $P = P_{max}$. The inelastic strains generated for the fine mesh show one major crack smeared similarly through the disc's radius for all considered G_F/G_C ratios, while for the other mesh sizes the crack pattern is spread over a wider area, where the inelastic strains have higher magnitude. This is due to the larger maximum vertical displacement and is in agreement with phenomenon observed in Figure 61 (P-δ curves). The inelastic strains are presented in Figure 62 and the equivalent principal stresses in Figure 63.

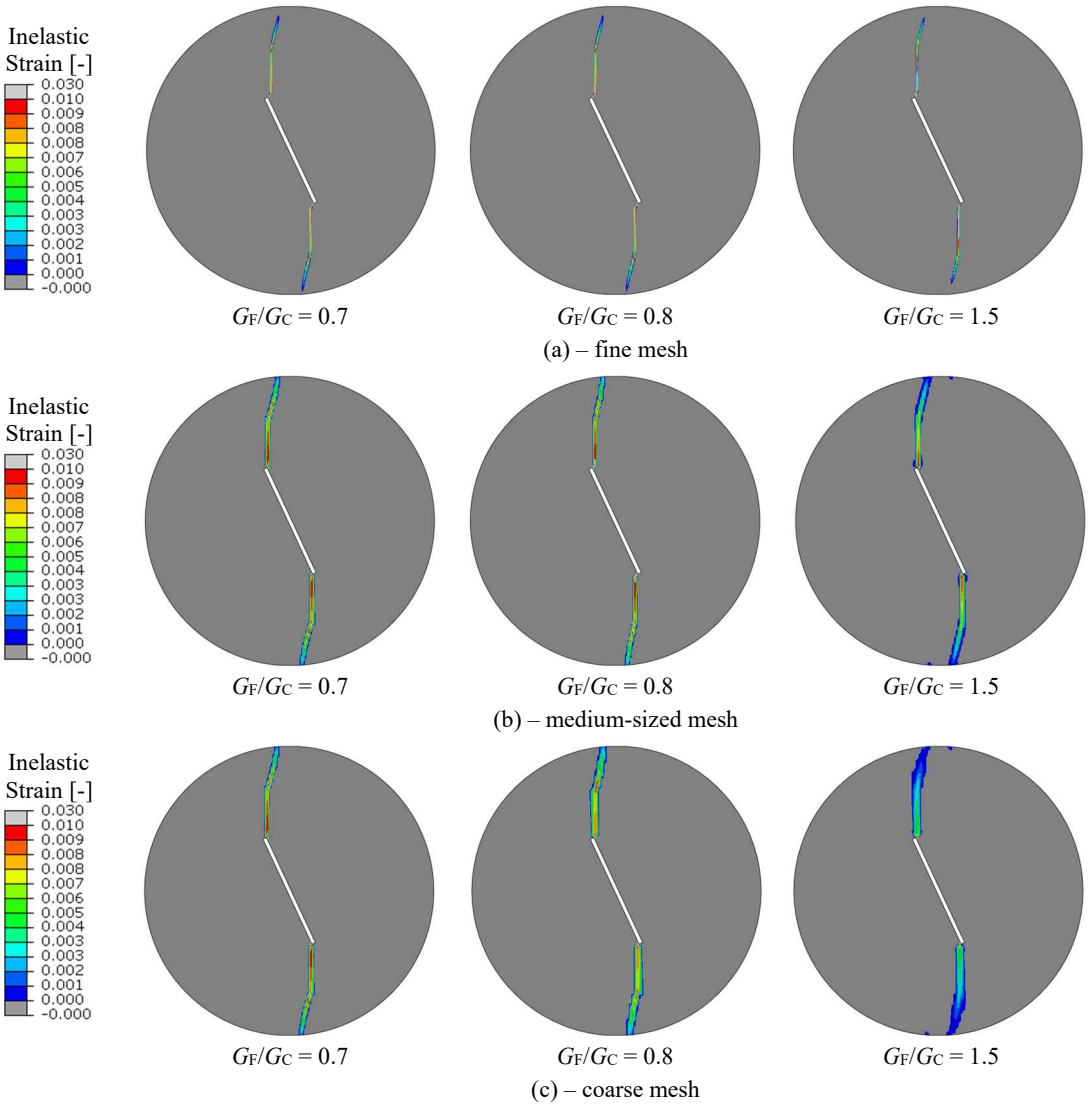

Figure 62: Comparison of maximum principal inelastic strains at $P = P_{max}$ for notch inclination angle $\alpha = 25.2°$ generated by various mesh size – (a) fine mesh, (b) medium-sized mesh and (c) coarse mesh.

In Figure 62 yielding of the specimen can be observed at the bottom and at the top support for the case of $G_F/G_C = 1.5$ for the medium-sized and coarse meshes, respectively. This yielding of the specimen is caused by indirect tensile failure, which is reached at the compressed zones surrounding the supports. This again confirms the observation found in Figure 61.

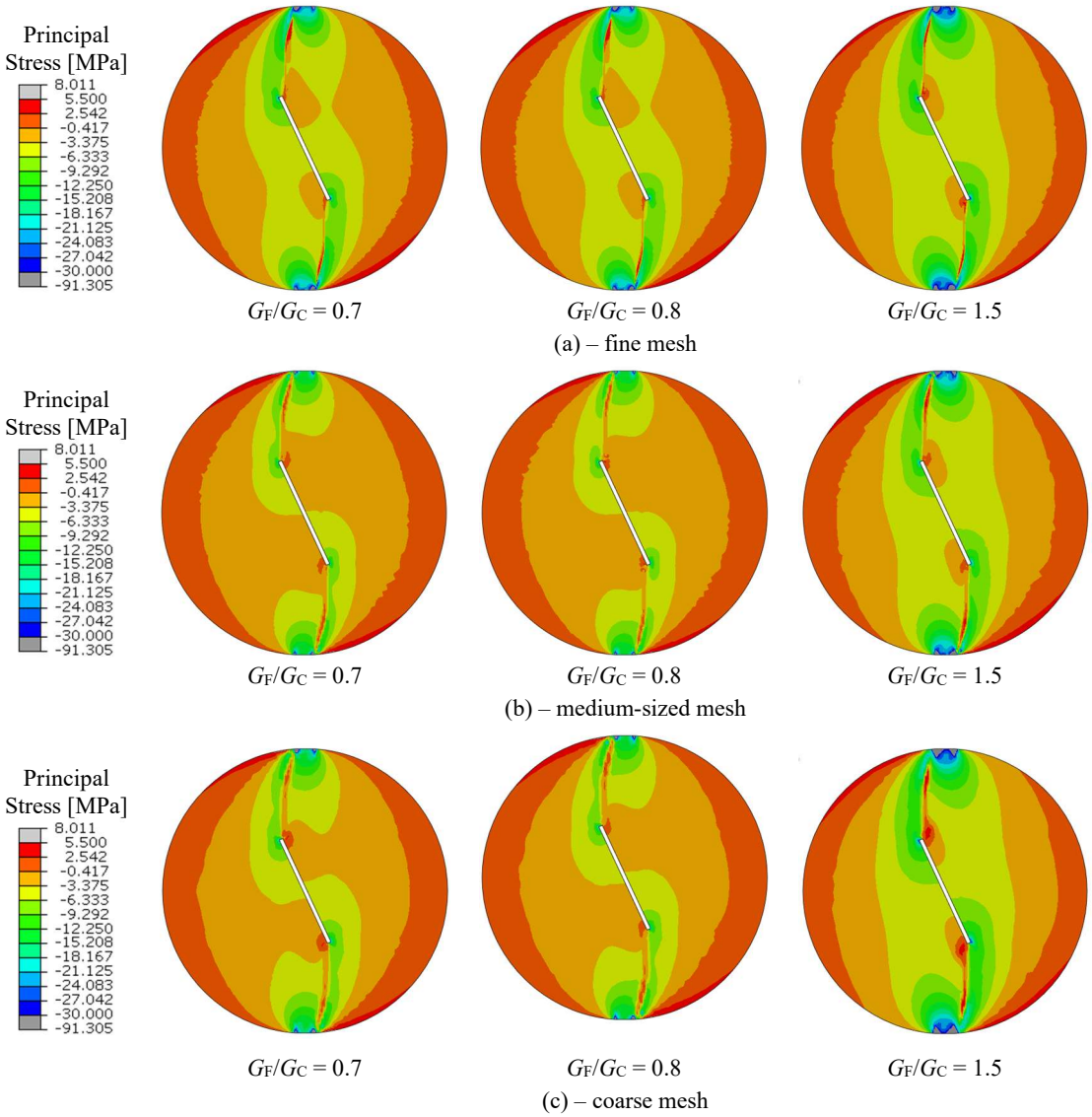

Figure 63: Comparison of maximum principal stress at $P = P_{max}$ for notch inclination angle $\alpha = 25.2°$ generated by various mesh size – (a) fine mesh, (b) medium-sized mesh and (c) coarse mesh.

In further numerical analysis the fine mesh was used, due to reasonable representation of the experimental *P-δ* curve and due to the reasonable crack illustration in BDCN geometry.

3.2.3 Boundary Conditions

This numerical study was performed with a displacement-controlled loading applied at the top edge of the BDCN, while the bottom edge is considered as a rigid support. Such a loading generates compressive forces/stress in the area around the supports, while a tensile stress is present at the notch tip. Due to the indirect tension in front of the notch tip the BDCN starts to crack. This is the major failure mechanism of the BDCN specimen. Theoretically this occurs when the disc is loaded at a single point. However, this single point loading of the BDCN specimen is causing convergence problems and the numerical results does not fully represent the typical brittle/splitting behaviour of the BDCN specimen. Therefore various boundary conditions were considered to see its influence on the stress and strain fields in the disc's geometry.

To quantify the influence of the boundary conditions on numerical results the radius of the disc was locally reduced by ΔR over an extended width Δw near the loaded edges. This reduction of the disc's radius has a major influence on the stress and strain fields in the BDCN specimen. Therefore, the influence of the boundary conditions on the overall response of the BDCN specimen was verified with focus on the P-δ diagram and on the strain and equivalent stress distributions. The geometrical parameter that was varied was Δw as it represents the boundary conditions from a single point loading of $\Delta w = 0$ mm to a line loading of $\Delta w = 2.5$; 5; 10; 20 mm (See Figure 64(a)).

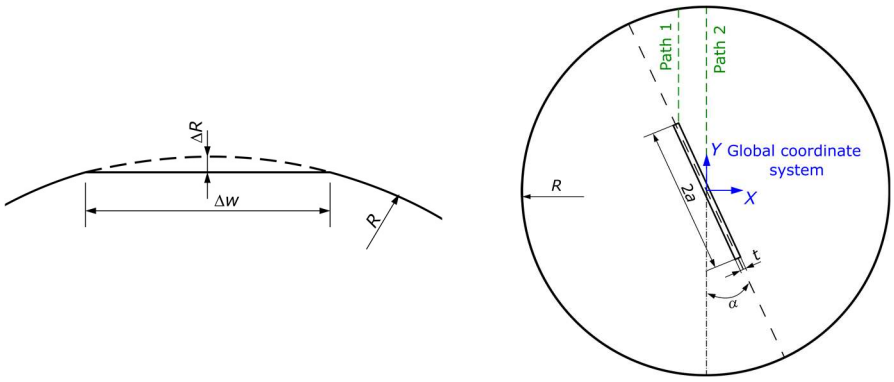

(a) (b)

Figure 64: Detail of flattened edge (a) and the location of paths used on extraction of stress distribution (b).

To see the influence of the radius reduction ΔR on the stress distributions two different paths were considered. These paths were chosen to cover the compressive stresses at the loaded edge and the tensile stresses at the notch tip for various boundary conditions. For this, the first path has its origin at the notch tip (See Figure 64(b) Path1) and the other path has its origin at the centre of the disc (See Figure 64(b) Path2). Both paths continue than parallel to the global Y-axis to the disc's edge. The P-δ curves representing various extended width are shown in Figure 65.

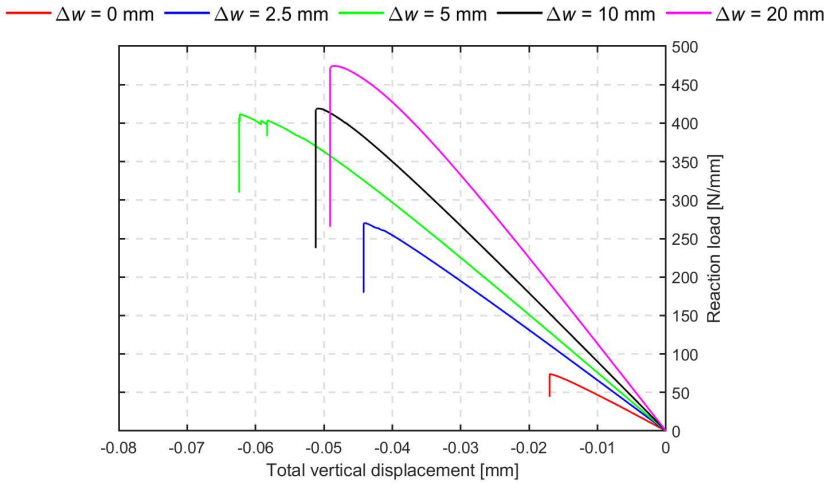

Figure 65: Generated P-δ diagrams for various width extension Δw for notch inclination angle $\alpha = 25.2°$.

A comparison of the various width extensions Δw to the equivalent radius reduction ΔR are presented in Table 22.

Table 22: Comparison of calculated maximum reaction loads P_{max} for various width extensions Δw and equivalent radius reduction ΔR

Δw [mm]	0	2.5	5	10	20
ΔR [mm]	0	0.01	0.04	0.17	0.6
P_{max} [kN/mm]	73.52	270.13	411.83	418.925	474.331

From Table 22 in can be noticed that the maximum reaction load P_{max} is increasing with the increasing width extension Δw. This is in agreement with the general expectation, since the load is distributed over a wider area. This observation confirms the generated *P-d* curves for each case of the extended width Δw. These *P-δ* curves show different stiffnesses of the BDCN specimen i.e. the slope of each curve increases with increasing Δw. The *P-δ* curves for Δw = 5 and 10 mm show similar value of P_{max}. However, the total displacement for Δw = 5 mm is higher than for Δw = 10 mm. This difference is caused by arsing inelastic strains in the area around the loaded edge, where the high compressive stress is present. This inelastic strain is produced by indirect tensile stress present in the BDCN geometry.

From the stress distribution obtained from the Path1 it can be observed that with the increasing Δw value the overall stress peak in its distribution is increasing. This confirms the observation found in Figure 65. However, for the case of Δw = 20 mm the overall trend in the stress distribution differs significantly from other cases. This can be noticed at the peaks of the stress at the top edge of the BDCN. The acquired stress distributions over the Path1 are presented in Figure 66 and over Path2 in Figure 67.

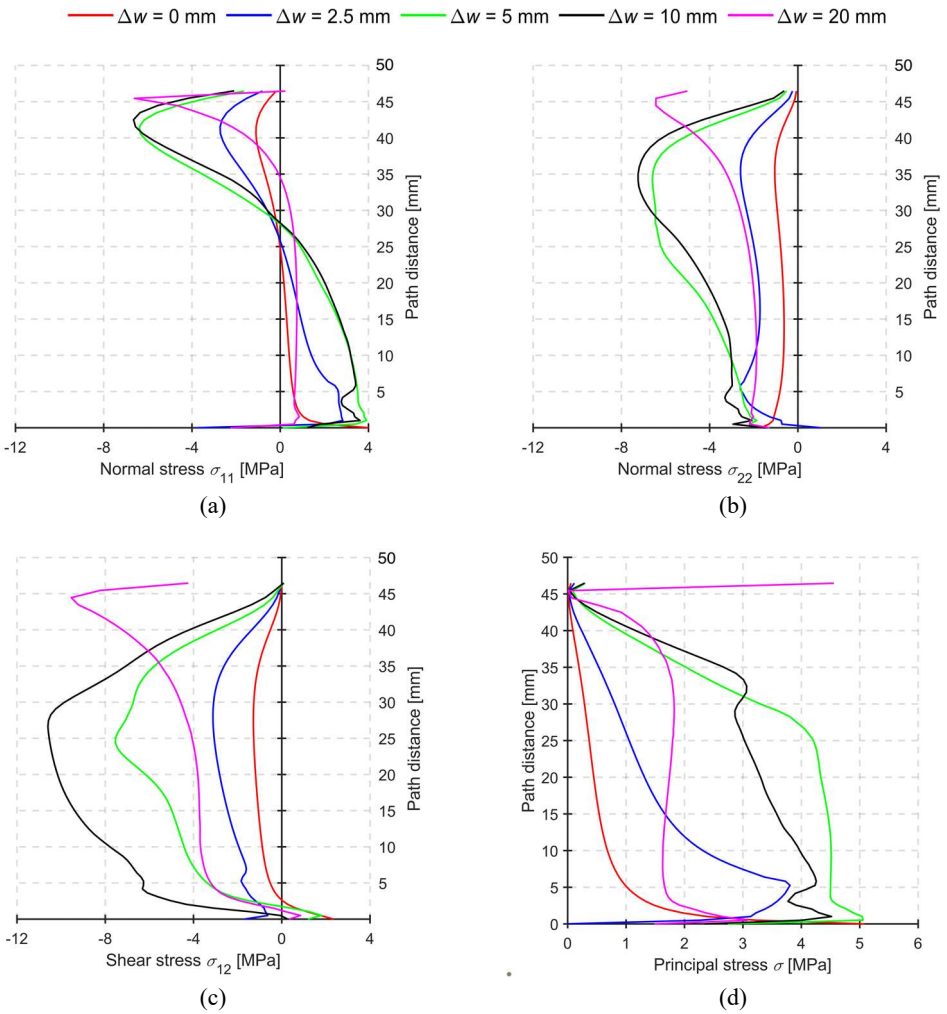

Figure 66: A comparison of stress distributions over the disc's radius for various radius reductions ΔR for $\alpha = 25.2°$ with origin at the notch end (Path1) (a) – normal stress σ_{11}, (b) – normal stress σ_{22}, (c) – shear stress σ_{12} and (d) first principal stress σ.

A similar trend of an increasing overall peak in the stress distributions can be observed again in the centre of the BDCN (Path2). These high compressive stress concentrations cause inelastic strains of the specimen near the extended width Δw, where the stress is reaching values higher than $0.4f_{cm}$ elastic branch in compression (See Figure 67(b)). However, failure is again caused by

the indirect tensile stresses present in the BDCN geometry. This was observable for cases of Δw = 0; 2.5 and 5 mm, while for the Δw of 10 and 20 mm the specimen failure was due to the crack propagating from the notch tip. The stress distributions over the Path2 are demonstrated in Figure 67.

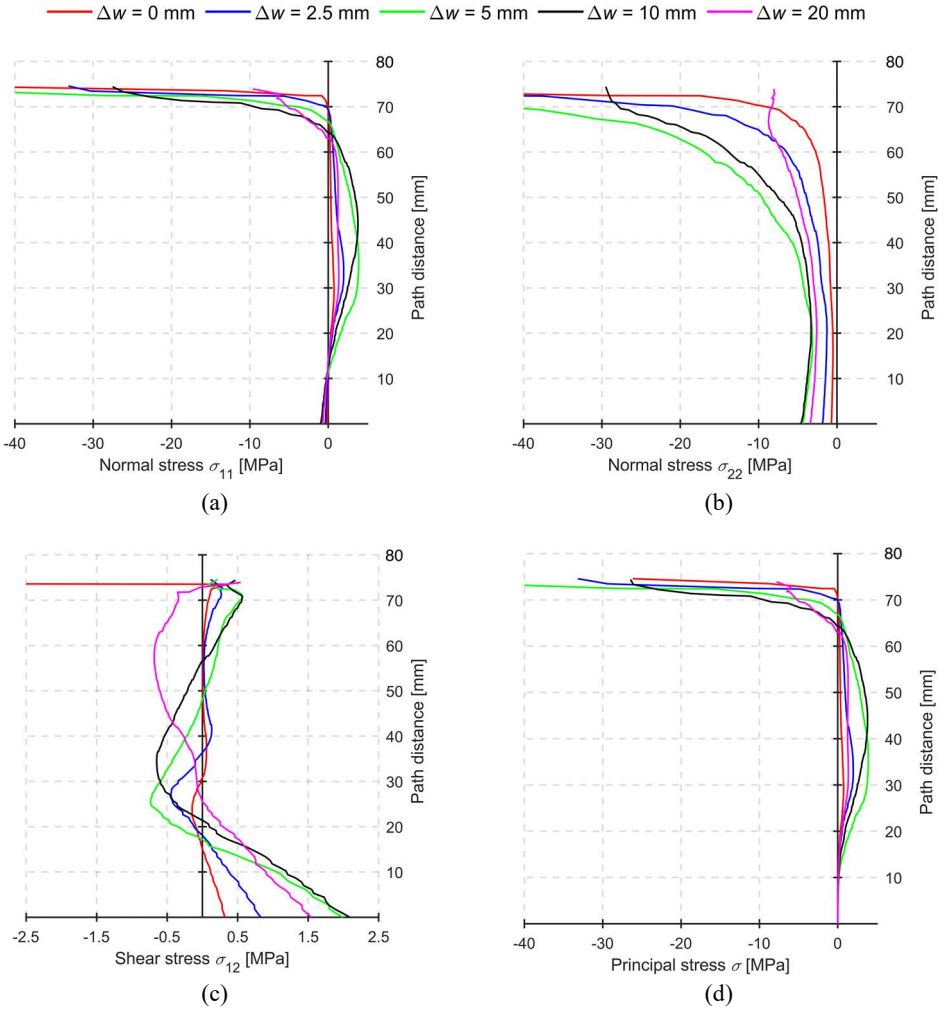

Figure 67: A comparison of stress distributions over the disc's radius for various radius reductions ΔR for $\alpha = 25.2°$ with origin at the centre of disc (Path2) (a) – normal stress σ_{11}, (b) – normal stress σ_{22}, (c) – shear stress σ_{12} and (d) first principal stress σ.

A similar observation can be found from the inelastic strain distributions presented in Figure 68. Here, it can be concluded that the extended width Δw of 0 mm does not provide accurate crack representation. In this case a specimen starts to crack at the support i.e. the tensile strength was not reached at the notch tip (See Figure 68(a)). For cases of extended width Δw of 2.5 and 5 mm the specimen starts to crack simultaneously at the support and in from of notch tip, which cannot be considered as a typical failure behaviour for BDCN specimen (See Figure 68 (b) and (c)). Lastly, for the cases Δw of 10 and 20 mm the crack propagates from the notch to the loaded edge (See Figure 68 (c) and (d)). However, for the case of Δw = 20 mm the strain and stress fields are non-representative of the BDCN behaviour, due to the wide area used as a loading edge. This can be spotted in abovementioned stresses over the disc's radius.

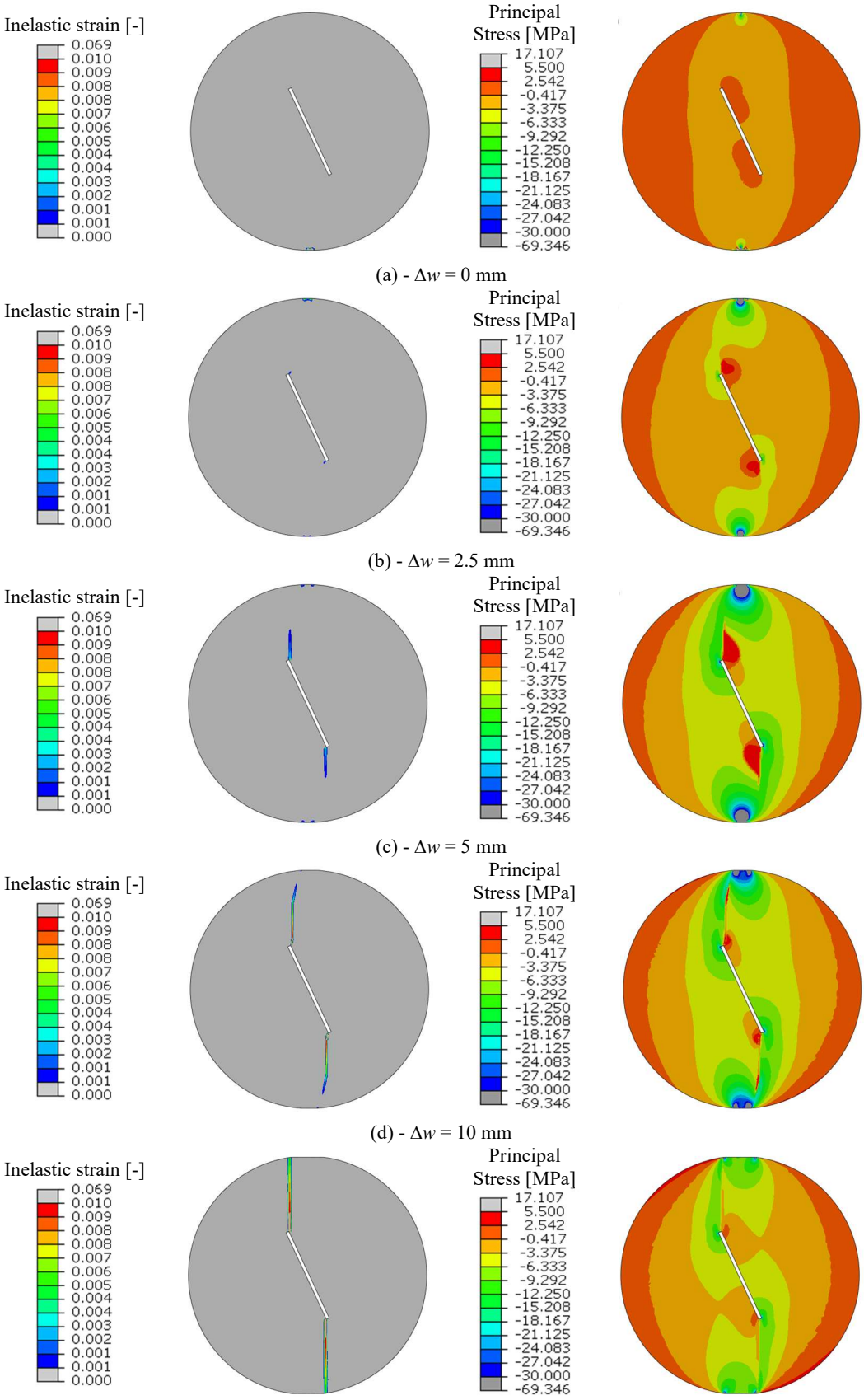

(a) - $\Delta w = 0$ mm

(b) - $\Delta w = 2.5$ mm

(c) - $\Delta w = 5$ mm

(d) - $\Delta w = 10$ mm

(e) - $\Delta w = 20$ mm

Figure 68: Comparison of inelastic strain and equivalent principal stress for various width extension Δw for $\alpha = 25.2°$ (a) - $\Delta w = 0$ mm, (b) - $\Delta w = 2.5$ mm, (c) - $\Delta w = 5$ mm, (d) - $\Delta w = 10$ mm and (e) - $\Delta w = 20$ mm.

Based on the presented numerical results a width extension of 10 mm was used since it provides reasonable P-δ curves together with relatively good crack trajectories through the disc' radius. The other key aspect was that the use of Δw of 10 mm also provides a reasonable convergency time.

3.3 Non-linear Analysis results

In what follows, a comprehensive numerical study of a BDCN specimen is presented, with focus on the influence of the softening behaviour, as represented by post-peak load-displacement curves, on the total load-displacement curves, the crack mouth opening displacement curves (*P-CMOD*), the sliding-displacement (*P-CMOS*) curves in mode I, mode II, and mixed mode I/II configuration. The material characteristics, used as input parameters for the numerical model, were selected to correspond to C50/60 material on p. 35 obtained from a series of presented by Seitl et al. in [100]. A discussion is added on the required geometrical transformation of the nodal displacement at the notch tip to distinguish mode I and mode II. In this, nodal transformations were done for various transformation angles based on geometry (i.e. the notch inclination angle), fracture mechanics (i.e. MTS and GMTS criteria) and plasticity (i.e. the actual numerically measured crack initiation angle) crack initiation conditions.

Since the test is displacement controlled, the force drop observable in Figure 69 is caused by the splitting force i.e. the specimen splits into two halves and there is no body to carry load. This is a typical brittle/splitting behaviour of the BDCN specimen, and the following numerical study is intended to model such a behaviour by common numerical approaches The typical experimental P-δ diagrams are showed in Figure 98 on p. 103 of this thesis.

Results from the numerical analysis are usually represented by a stress or strain distribution. The focus is on both general (whole geometry) and local (notch tip) response. The numerical analysis allows the generation of such a diagram and investigation of the material failure.

Figure 69 shows an illustrative P-δ diagram generated by the numerical model for material Mat_2 (G_f/G_C = 1.5) and a notch inclination angle α = 25.2° with points of interest. The points A-F were selected based on the material response. Point A represents the end of linear elastic material response, point B is a point with equal reaction force as point E, point C is the point at the 90% of the maximum load, point D corresponds the maximum load, point E to the curve transition, and point F is the last point calculated before brittle fracture.

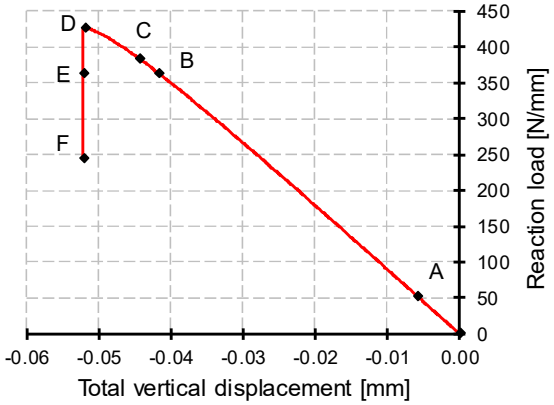

Figure 69: Typical Load-displacement diagram generated by FEA, with marked points for α = 25.2° and material Mat_2.

In this case however, the presented P-δ diagram primarily provides an overall response of the specimen. Also, the measurement of the fracture energy can be questioned because the diagram

presents the relation of the reaction force to the total vertical displacement and does not provide any information about the crack initiation process for mode I or mode II.

Information about the fracture process and the material response can be provided by examining various stress and strain distributions. The CDP material model generates typical principal stress and inelastic strain distributions shown in Figure 70. As this is a smeared cracking model these inelastic strains are representation for the location and width of the localized concrete cracks. Typical pre- and post-cracking principal inelastic strain distribution and equivalent principal stresses are shown in Figure 70.

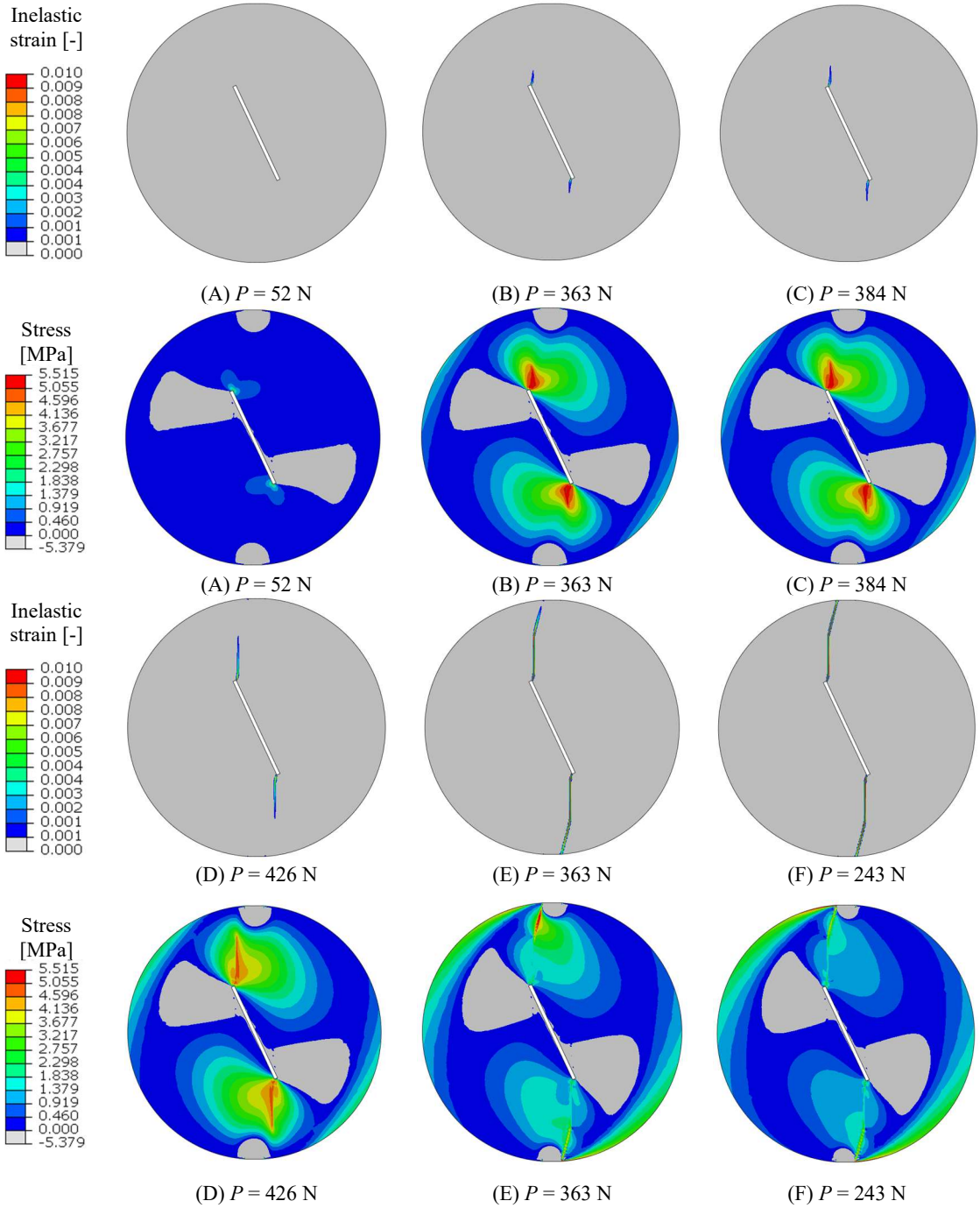

Figure 70: Maximum principal inelastic strains and equivalent maximum principal stresses related to the points marked in Figure 69, and total loads for $\alpha = 25.2°$ and material Mat_2 ($G_F/G_C = 1.5$).

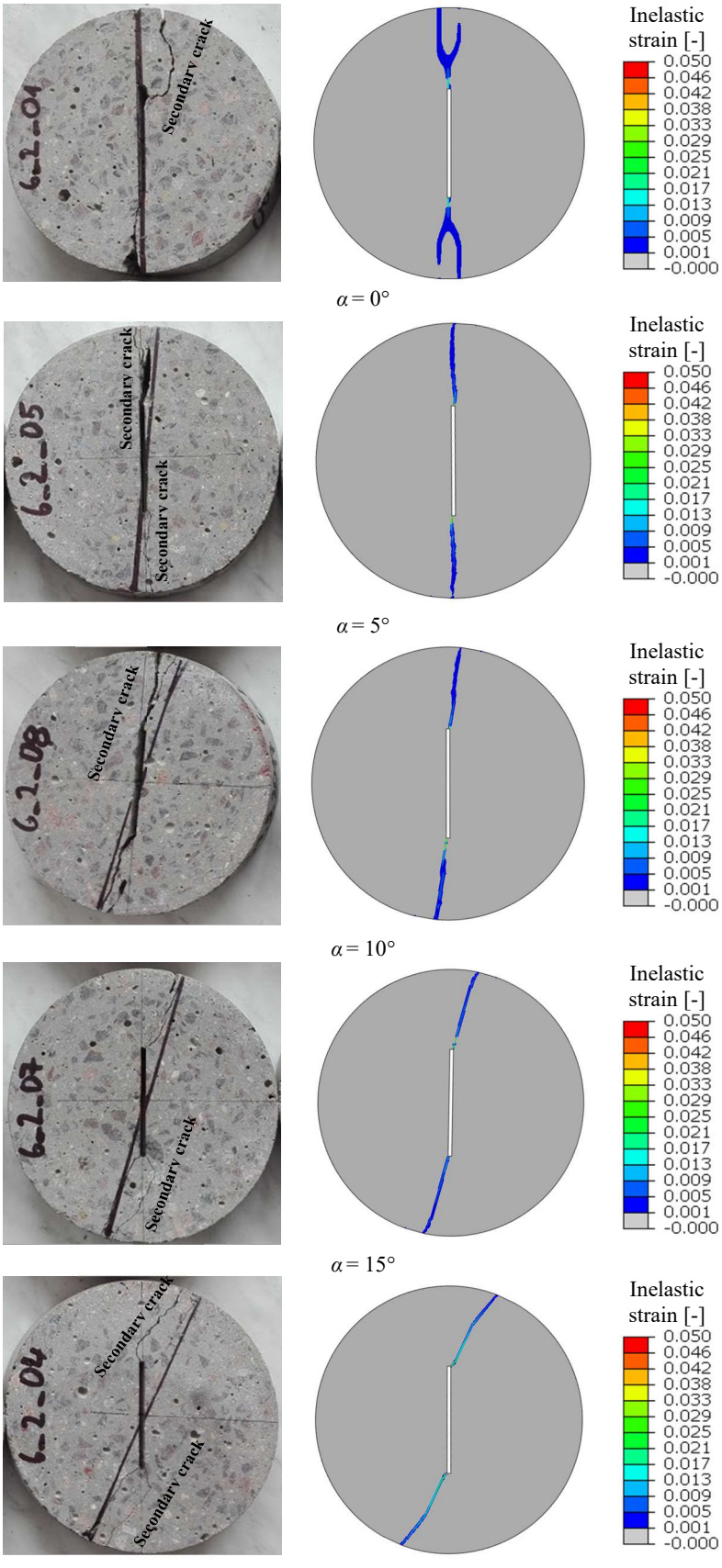

Figure 71: Comparison of crack patterns and equivalent maximum principal inelastic strains for α = <0°; 5°; 10°; 15°; 25.2° > and material Mat_2 (G_F/G_C = 1.5).

In order to verify the presented numerical results, the inelastic strains were compared to crack patterns on the C 50/60 material as presented by Seitl et al. [100]. It should be pointed out that all crack patterns taken from [100] show secondary cracks, which appeared after splitting of the BDCN specimen because one half of the specimen remained locked in the testing apparatus. The comparison of inelastic strains (smeared crack pattern) shows good agreement with the crack patterns on the tested specimens.

This comparison is presented in Figure 71 for all studied notch inclination angles α (the position of the secondary cracks are marked). The inelastic strain generated for $\alpha = 0°$ shows crack branching (secondary cracks) as in the experiment. However, this crack branching is due to high confinement stresses in the specimen, which generate high indirect tensile stresses producing such a phenomenon. In some cases, these so-called crack branching can appear under a pure mode II condition [242-244]. In this case crack branching was only present for the $\alpha = 0°$, due to an appropriate mesh pattern and low stress concentrations in front of the notch tip.

3.3.1 Transformation of Notch Tip Displacements

Inelastic maximum principal strains, which are different from zero, arise when the maximum tensile strength is reached. This strain distribution then propagates through the specimen towards the loading points. This way, near the notch tip, two nodes can be distinguished in between where the inelastic strain distribution is situated, and these nodes can be considered as the "crack tip". The process of crack initiation and propagation in between two nodes is shown in Figure 72.

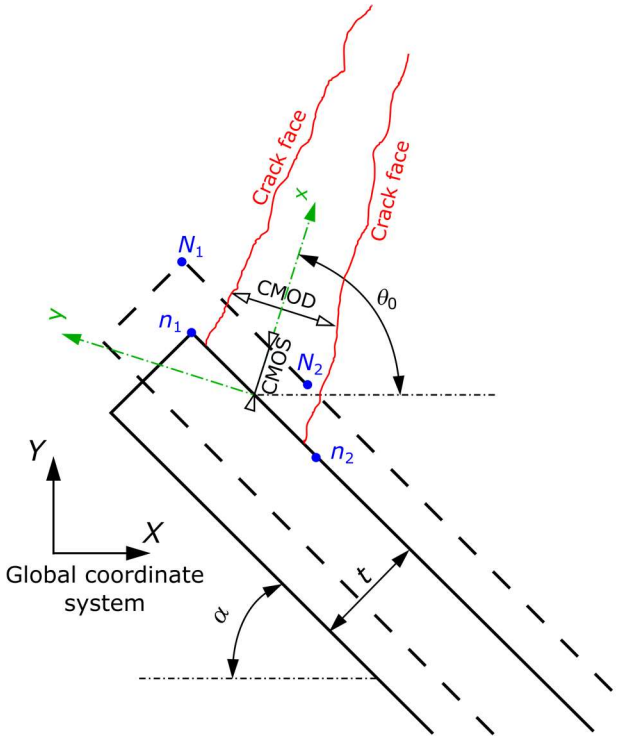

Figure 72: Transformation of nodal displacements into local a coordinate system.

The transformation to the new coordinate system can be done by the following equation:

$$\begin{bmatrix} u_x \\ u_y \end{bmatrix} = \begin{bmatrix} \cos\theta_0 & \sin\theta_0 \\ -\sin\theta_0 & \cos\theta_0 \end{bmatrix} \begin{bmatrix} u_X \\ u_Y \end{bmatrix}, \tag{4.11}$$

where θ_0 is the counter-clockwise angle of transformation, u_X and u_Y are the original nodal displacements of nodes N1 and N2 in global coordinate system X Y, u_1 and u_2 are the nodal displacements of nodes N1 and N2 transformed in the local coordinate system, which depends on the transformation angle θ_0. The choice of this angle will be discussed in the following section.

Figure 72 shows the undeformed and the deformed position of the nodes, where a principal strain different from zero is found. In this representation, we can calculate Δu_x and Δu_y values as the difference between the displacements of node N2 and node N1 in an arbitrary *x*- and *y*-direction.

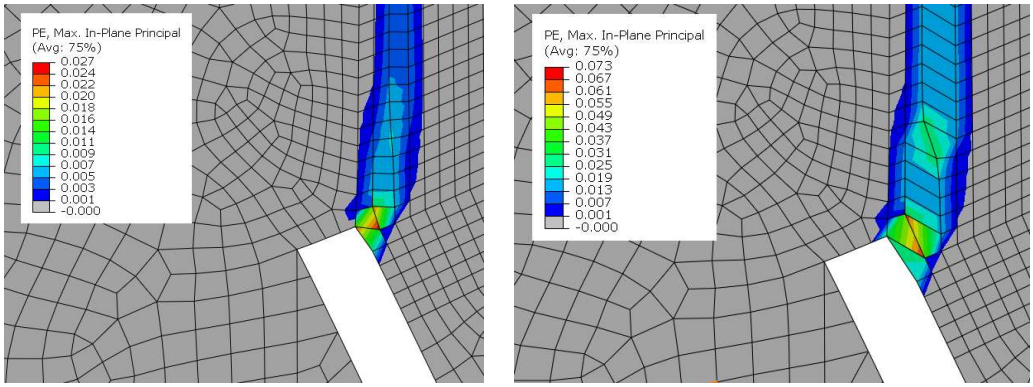

(a) (b)

Figure 73: Deformation of notch tip generated by numerical model in FE software Abaqus with exaggerated scale by 50 times for $\alpha = 25.2°$ and material Mat_2 ($G_F/G_C = 1.5$). Point A (a) and point E (b).

If we choose the *x*-axis parallel to the initial crack face, the displacement Δu_x describes the crack opening in the direction parallel to that face and represents the crack mouth opening sliding (*CMOS*). In the same way Δu_y then describes the displacement perpendicular to the crack face and represents a crack mouth opening displacement (*CMOD*). These *CMOS*s and *CMOD*s provide much more information about fracture process in the specimen and distinguish the effects of tensile mode I and shear mode II. However, if the nodal displacements remain in a global coordinate system *X-Y,* the values of *CMOD* and *CMOS* can be misleading and do not provide accurate information about the fracture process. Therefore, the nodal displacements are to be transformed into a local coordinate system, which has an *x*-axis parallel to the crack face. After this transformation a *CMOD* (Δu_y) is then perpendicular and a *CMOS* is parallel (Δu_x) to the initial crack surface in the model.

3.3.2 Transformation Angle

There are several approaches to determinate the crack initiation angle θ_0. It can consider the geometry, e.g. $\theta_0 = \alpha$, or can be calculated from plasticity or LEFM conditions.

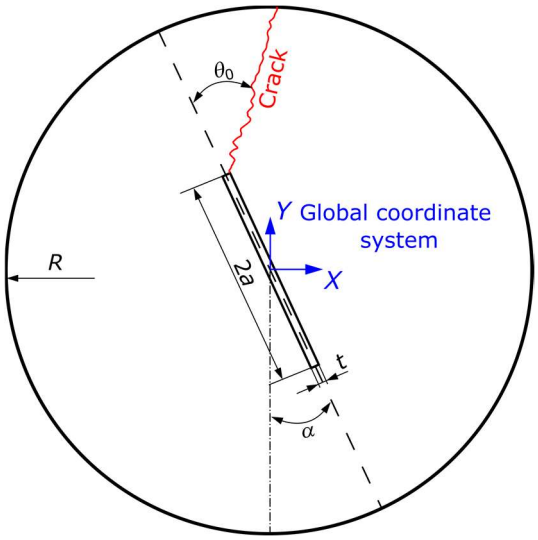

Figure 74: Measurement of the crack initiation angle calculated from MTS, GMTS and plasticity criteria.

In the plasticity approach, the crack initiation angle for a 2D problem can be expressed as the angle of principal stress/strain. The angle of principal stress is calculated using Mohr's circle, which has the following form:

$$\tan 2\theta_{0,p} = \frac{\tau_{xy}}{\sigma_{xx} - \sigma_{yy}}, \tag{4.12}$$

where $\theta_{0,p}$ is the angle of the principal stress direction, σ_{xx} and σ_{yy} are the normal stresses in X and Y-axis respectively and τ_{XY} is the shear stress in the global coordinate system X-Y (Figure 74).

By applying the LEFM approach, the crack initiation under the mixed mode I/II can be expressed via MTS criterion Eq. (2.31) or a GMTS criterion Eq. (2.32) as presented in section 1.3 on p. 15.

The critical distance r_C can be defined using plane strain or plane stress boundary conditions [117] or can be based on the physical base i.e. size of grains or aggregate. The critical distance r_C has a direct influence on the crack initiation angle θ_0 [245], therefore three different values were considered i.e. r_C = 1.6 mm – plane strain, r_C = 4.7 mm – plane stress (See Table 32 on p. 91 of this thesis) and r_C = 4 mm. Further in this study the r_C = 4 mm is chosen based on the aggregate size. Table 23 gives overview of calculated crack initiation angles from various criteria for the specimen under consideration.

Table 23: Overview of used transformation angles θ_0 for various criteria.

α [°]	MTS $\theta_{0,MTS}$ [°]	GMTS for r_C = 1.6 mm $\theta_{0,GMTS}$ [°]	GMTS for r_C = 4 mm $\theta_{0,GMTS}$ [°]	GMTS for r_C = 4.7 mm $\theta_{0,GMTS}$ [°]	ABAQUS $\theta_{0,Plasticity}$ [°]
0	0	0	0	0	0
5	-36.89	-9.44	-6.38	-5.97	-7.43
10	-52.67	-19.91	-13.65	-12.77	-13.63
15	-60.75	-32.37	-22.93	-21.52	-20.05
20	-66.12	-46.84	-35.83	-33.92	-24.40
25.2	-70.52	-60.99	-53.30	-51.57	-27.57

The angle of transformation θ_0 can be chosen as a $\theta_0 = \alpha$ (rotation by the initial notch inclination angle i.e. the y-axis is parallel to notch edge), $\theta_0 = \alpha - \theta_{0,MTS}$ (crack initiation angle calculated by means of the MTS criterion using linear elastic fracture mechanics), $\theta_0 = \alpha - \theta_{0,GMTS}$ (crack initiation angle calculated by means of the GMTS criterion using the two parameter linear elastic fracture mechanics) and $\theta_0 = \alpha - \theta_{0,p}$ (actual numerically measured angle of principal stress from the FE calculation in ABAQUS). An overview of the derived transformation angles can be found in Figure 75.

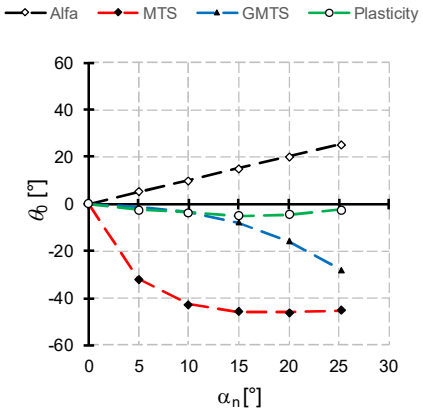

Figure 75: Comparison of transformation angle θ_0 for various cases.

Since all of the calculated crack initiation angles have negative value and are larger than α, all transformation angles θ_0 are negative except for the geometrical rotation, where the $\theta_0 = \alpha$. The largest difference is shown in angles calculated by MTS criterion in whole range of α. This is caused by only using SIFs. The angles for the GMTS vary for α higher than 15°, while the angles calculated from the plasticity conditions remain almost constant in the whole range of α.

Illustrative P-Δu_x (*P-CMOS*) and P-Δu_y (*P-CMOD*) diagrams, which were created from nodal displacements in the global coordinate system X-Y with base at the notch tip are shown in Figure 76(a), and an example of such values transformed into the local coordinate system by an angle obtained from the GMTS criterion is shown in Figure 76(b).

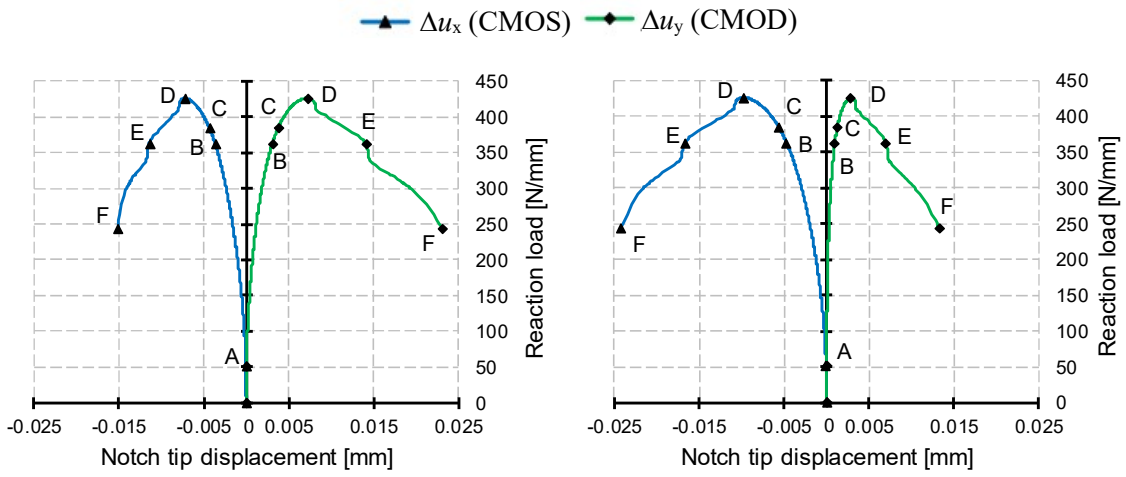

(a) – Original (b) – GMTS

Figure 76: *P-CMOS* and *P-CMOD* diagram (a) for nodal displacements in the global coordinate system and *P-CMOS* and *P-CMOD* diagram (b) after transformation into a local coordinate system governed by the GMTS criterion for α = 25.2° and material Mat_2 (G_F/G_C = 1.5).

Figure 76(b) shows the diagram transformed by angle an $\theta_0 = \alpha - \theta_{0,GMTS}$. From this figure it can be noted that the deformation Δu_x (*CMOS*) is more dominant than the Δu_y (*CMOD*). In general, a mode II dominance in the fracture process can be seen except for α = 0°. However, a mode I opening appears after the load reaches 90% of its maximum (point C) for every inclination angle α_n, even for the case where the pure shear mode II should be present, i.e. for α = 25.2°. The mode II dominance can be expressed as a ratio of Δu_x to Δu_y at point C, which for the example of Figure 76(b) is equal to 1.2.

A comparison of original and transformed Load-*CMOS* and Load-*CMOD* curves for various transformation angles can be found in Figure 77 for α = 25.2° and material Mat_2 (G_F/G_C = 1.5). Numerical results for all investigated cases can be found in the appendix of this study.

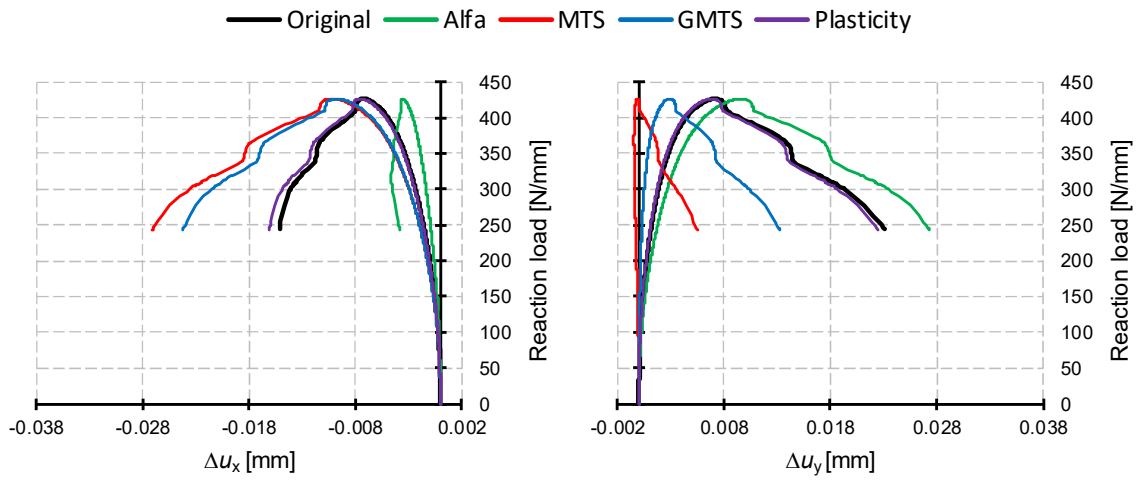

(a) - Δu_x (*CMOS*) (b) - Δu_y (*CMOD*)

Figure 77: Comparison of original and transformed *P-CMOS* and *P-CMOD* curves for various transformation angles θ_0 for $\alpha = 25.2°$ and material Mat_2 ($G_F/G_C = 1.5$).

From Figure 77, it can be seen that the transformation angle from the MTS criterion misrepresents the crack opening behaviour since Δu_y values become negative, which would represent a crack tip closure instead of an opening. This is in agreement with the earlier observation in Figure 75 regarding the angles found through the MTS criterion. On the other hand, the transformed curves for the angle calculated by the plasticity conditions and the original untransformed values are almost identical. This is, again, in agreement with the earlier observation in Figure 75 that the crack initiation angle is always almost 90°, irrespective of the notch angle.

A comparison of ratios $\Delta u_x/\Delta u_y$ at points A and C for all presented material input parameters and all inclination angles α can be found in Figure 78. The values at $\alpha = 0°$ are omitted from the comparison as they are not representative for the mode I/II comparison.

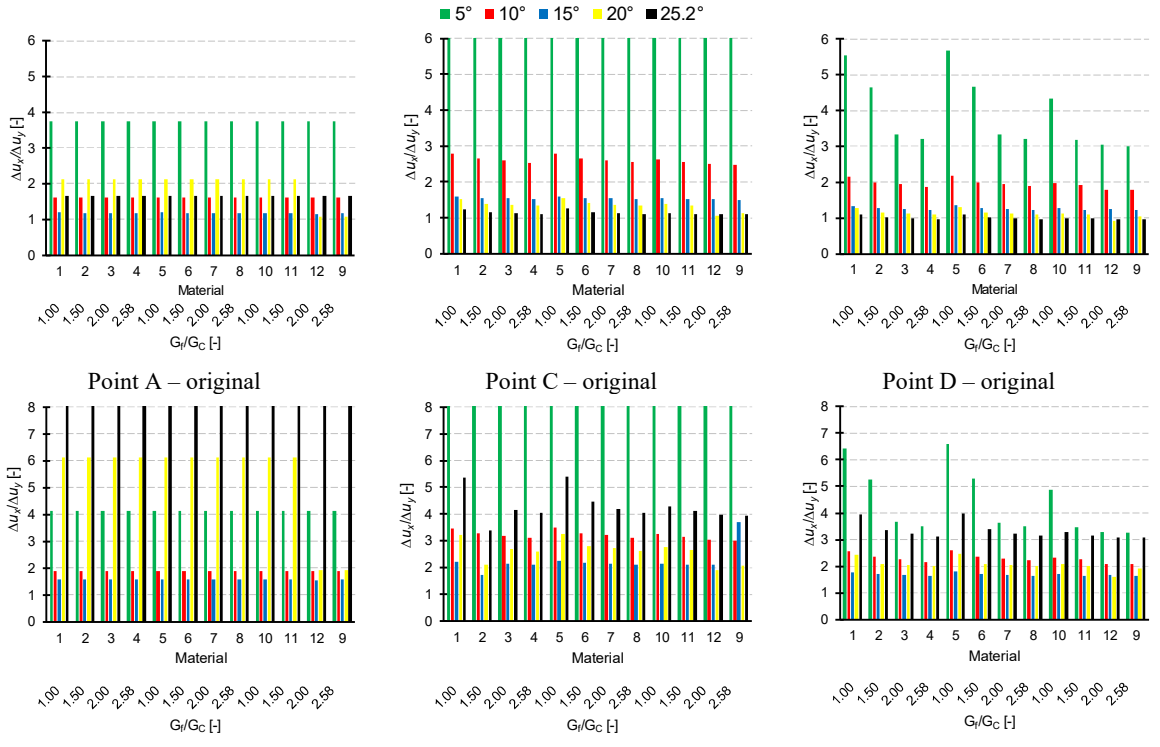

Point A – original Point C – original Point D – original

Point A – GMTS Point C - GMTS Point D – GMTS

Figure 78: Comparison of the $\Delta x/\Delta y$ ratio for selected points of interest from *P-δ* diagrams for all presented material input parameters and all inclination angles α.

From Figure 78, we can conclude that the differences in the ratio of $\Delta u_x/\Delta u_y$ remain equal at point A irrespective of the material parameters due to the use of only one value of the Young's modulus, responsible for the elastic deformation. The differences in the ratio of $\Delta u_x/\Delta u_y$ at point A are only governed by the transformation angle θ_0.

However, the ratios of $\Delta u_x/\Delta u_y$ at point C and D depend on the G_F/G_C ratio as well as on the shape of the softening curve. From Figure 78 we can see that the differences in the $\Delta u_x/\Delta u_y$ ratio decrease with an increasing ratio of G_F/G_C. This trend is observable for all crack inclination angles α_n, and the ratio itself decreases with the inclination angle. This is again in agreement with the variation of the post peak tensile softening curves, which have an influence on the uniaxial crack opening. Therefore, the ratios of $\Delta u_x/\Delta u_y$ have to be decreasing with increasing values of the fracture energy G_F and simultaneously decreasing with the increasing notch inclination angle α. With increasing value of the angle α, the mode II displacements start to appear, which reduce the ratio $\Delta u_x/\Delta u_y$. This fact is demonstrated in Figure 76(a) and (b), where the observation of the mode I and mode II displacements can be seen.

An equal observation can be found in the comparison of the calculated maximum reaction loads P_{max}. These P_{max} values increase as expected with the increasing ratio G_F/G_C. Maximum calculated loads P_{max} for all crack inclination angles and G_F/G_C ratio are summed up in Table 24 to Table 26.

Table 24: Overview of calculated maximum force per unit width P_{max} (N/mm) for various initial notch inclination angles and material input parameters.

G_f/G_C [-]		MC 2010			
		1.0	1.5	2.0	2.58
Angle α [°]	0	482	517	535	542
	5	491	523	539	550
	10	451	485	501	513
	15	425	454	469	478
	20	415	436	447	455
	25	401	426	446	401

Table 25: Overview of calculated maximum force per unit width P_{max} (N/mm) for various initial notch inclination angles and material input parameters.

G_f/G_C [-]		Hillerborg			
		1.0	1.0	1.0	1.0
Angle α [°]	0	479	479	479	542
	5	488	488	488	550
	10	449	449	449	513
	15	422	422	422	478
	20	412	412	412	455
	25	425	425	425	401

Table 26: Overview of calculated maximum force per unit width P_{max} (N/mm) for various initial notch inclination angles and material input parameters.

G_f/G_C [-]		Linear			
		1.0	1.0	1.0	1.0
Angle α [°]	0	484	484	484	542
	5	529	529	529	550
	10	492	492	492	513
	15	461	461	461	478
	20	441	441	441	455
	25	432	432	432	401

These reaction loads agree with the experimentally measured forces published by Seitl et al. [100]. For comparison, the numerical plane strain loads (N per unit width) were converted into a total

loads trough multiplication using the thickness of the specimen. Evaluated numerical data is shown in Table 27.

Table 27: Comparison converted P_{max} (kN) for various initial notch inclination angles and material input parameters.

B [mm]	Exp. [kN]	G_f/G_C [-]		MC 2010			
				1.0	1.5	2.0	2.58
30.9	18.5	Angle α [°]	0	14.9	16.0	16.5	16.8
31.4	16.3		5	15.4	16.5	17.0	17.3
30.8	16.9		10	13.9	14.9	15.4	15.8
31.0	16.0		15	13.2	14.1	14.5	14.8
31.0			20	12.5	13.1	13.4	13.7
31.2	16.1		25	12.5	13.3	13.7	13.9

Table 28: Comparison converted P_{max} (kN) for various initial notch inclination angles and material input parameters.

B [mm]	Exp. [kN]	G_f/G_C [-]		Hillerborg			
				1.0	1.5	2.0	2.58
30.9	18.5	Angle α [°]	0	14.8	15.9	16.5	16.7
31.4	16.3		5	15.3	16.4	16.9	17.3
30.8	16.9		10	13.8	14.9	15.4	15.8
31.0	16.0		15	13.1	14.0	14.5	14.8
31.0			20	12.4	13.0	13.4	13.6
31.2	16.1		25	12.5	13.2	13.6	13.9

Table 29: Comparison converted P_{max} (kN) for various initial notch inclination angles and material input parameters.

B [mm]	Exp. [kN]	G_f/G_C [-]		Linear			
				1.0	1.5	2.0	2.58
30.9	18.5	Angle α [°]	0	14.7	16.2	16.9	16.9
31.4	16.3		5	16.6	17.2	17.6	17.6
30.8	16.9		10	15.2	15.6	16.1	16.3
31.0	16.0		15	14.3	14.7	15.1	15.2
31.0			20	13.3	13.6	13.8	13.9
31.2	16.1		25	13.5	13.8	14.1	14.2

An overview of the experimental and numerical data can be found in Figure 80, from which the same observation can be found as in Figure 78. The reaction loads decrease with the increasing notch inclination angle α and G_F to G_C ratio. However, the reaction loads for the $\alpha = 0°$ contradict this statement. This is because no mode II deformation is present, which redistributes the mode I (crack mouth opening) force to the other direction and slows down the fracture process.

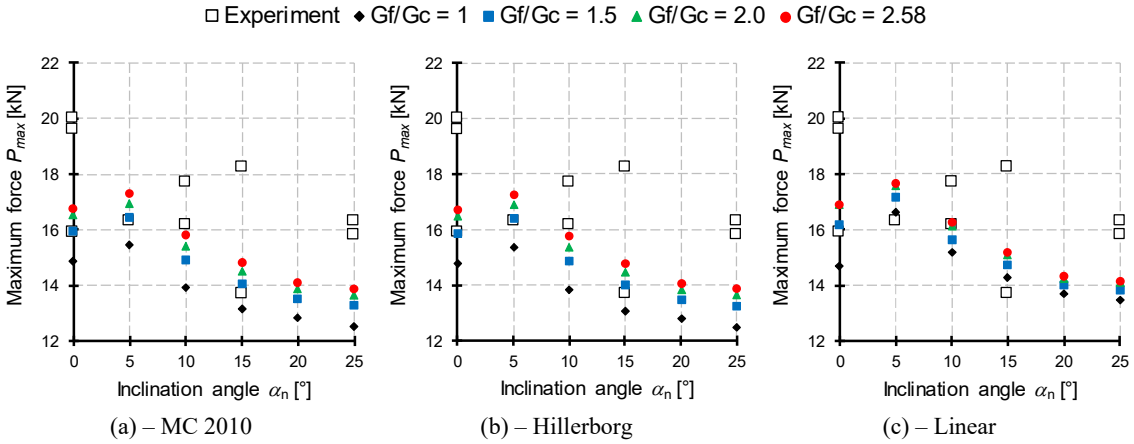

Figure 79: Comparison of maximum calculated forces P_{max} based on MC2010 recommendation (a), Hillerborg model (b) and linear softening (c) with experimentally measured fracture force P_c from [100].

An overall comparison of the maximum reaction loads is presented in Figure 80 (a), where the difference between average values of numerical and experimental data is limited to 16% for

angles α higher than 25°. Nevertheless, the numerical and experimental values of P_{max} show similar trend. This can be seen in the Figure 80(b), where the linear function based on the least square method was used on the average values.

The scatter of the numerical results can be eliminated by increasing the number of experimental tests, using average values of disc's thickness or by slightly adjusting the input parameters of the CDP which have a direct influence on the numerical results i.e. increasing the tensile strength f_t, the dilatation angle ψ and the fracture energy G_F.

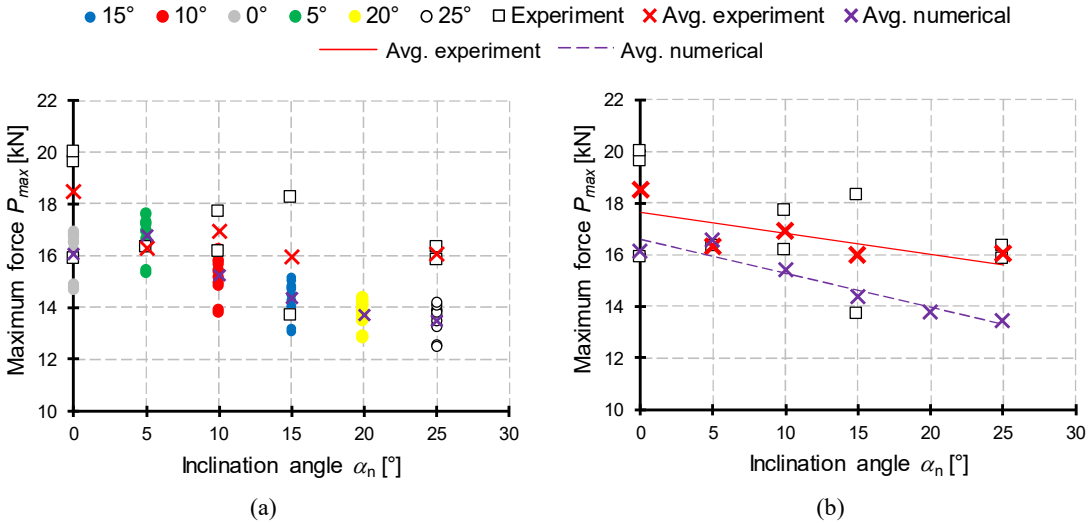

Figure 80: Comparison of maximum calculated forces P_{max} with experimentally measured fracture forces P_C from Seit et al. [100] i.e. on the C 50/60 material.

The scatter of the numerical results can be eliminated by increasing the number of experimental tests, using average values of disc's thickness or by slightly adjusting the input parameters of the CDP which have a direct influence on the numerical results i.e. increasing the tensile strength f_t, the dilatation angle ψ and the fracture energy G_F.

Chapter V
Experimental Results

In this chapter, the experimentally obtained results of fracture mechanical properties of each tested concrete mixture are provided together with evaluated fracture resistance under the mixed mode I/II load, critical distance r_C and the calculated crack initiation direction θ_0. Afterwards, the influence of aggressive environment on the fracture resistance is showed on the HPC mixture batch B. Then the evaluated values of Williams's expansion coefficients based on the DIC measurement are provided. The aim of this chapter is to bring insight into the fracture resistance under the mixed mode I/II of concrete by employing the advanced methods based on LEFM and verify its accuracy.

1. Fracture Mechanical Parameters

Firstly, the fracture loads P_C together with equivalent values of SIFs for mode I and mode II are presented as determined on the BDCN specimen with two different relative notch ratios a/R. Then, the fracture toughness K_{IC} was determined on the BDCN specimen of all studied mixture. From the values of K_{IC} the values of critical distance r_C were calculated, which then served as an input to the GMTS fracture criterion.

1.1 Fracture Loads

To provide complete information of the measured FMPs from the experimental campaign, it is necessary to present measured fracture load P_C. These measured forces are presented for each material and test configuration, i.e. a/R ratio. This provides simple yet conclusive comparison of the experimental results. Please note, that the measured forces P_C vary due to differences in the specimen's thickness, therefore it would be more explanatory to show forces over the length as kN/mm. However, for the SIFs calculation the force P_C enters into the Eqs. (3.2) and (3.3) as a force P together with the measured specimen's thickness B as presented in Appendix A of this thesis. Thus, the comparison is showed in form of P-α diagrams for each material and exact data presented hereunder in graphs are sum up in tables in Appendix A.

Firstly the measured fracture forces P_C and SIFs for mode I and mode II for the C 50/60 material are presented in Figure 81. Generally the fracture forces P_C are higher for the ratio a/R of 0.267 (see Figure 81(a)), this is in agreement with the general expectation as the a/R ratio of 0.4 (see Figure 81(b)) has larger ligament area ahead of the notch. This observation applies to all tested materials.

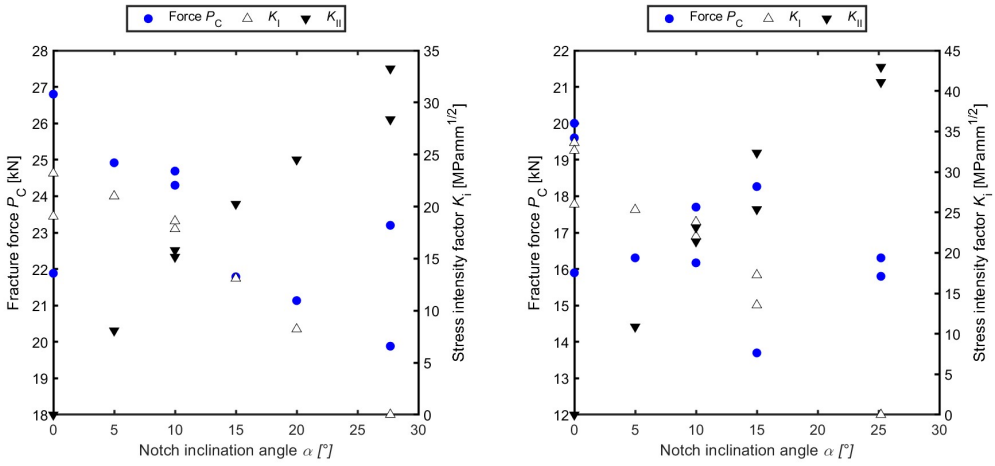

Figure 81: Measured fracture forces P_C and equivalent values of K_I and K_{II} for C 50/60 material (a) – a/R 0.267 and (b) – a/R = 0.4.

The measured fracture forces P_C and SIFs for mode I and mode II for the HSC material for the ratio a/R of 0.267 are presented in Figure 82(a) and for the ratio a/R of 0.4 are presented in Figure 82(b).

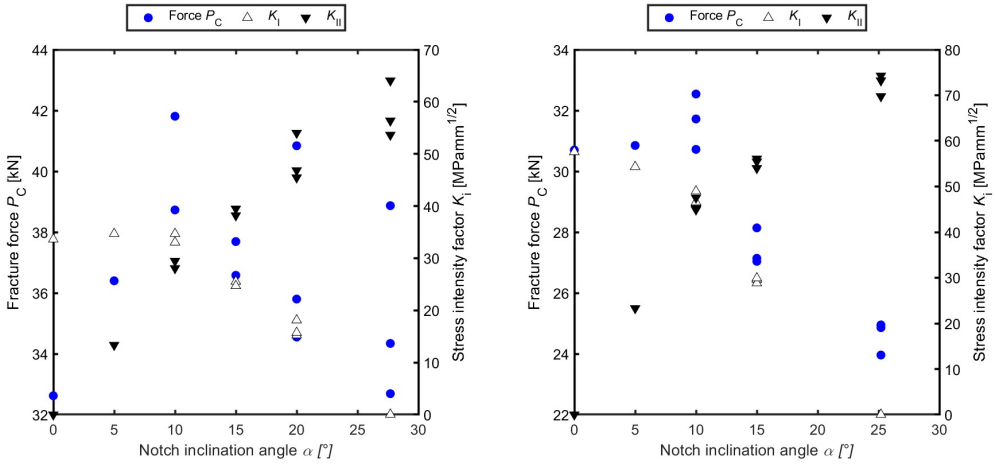

Figure 82: Measured fracture forces P_C and equivalent values of K_I and K_{II} for HSC material (a) – a/R 0.267 and (b) – a/R = 0.4.

The measured fracture forces P_C for the HSC material show overall greater values than for the C 50/60 material. Consequently, this results into the higher values of SIFs and as well as into higher values of fracture toughness K_{IC} and K_{IIC}. This agrees with the general expectation as the HSC showed overall better mechanical performance and highest tensile splitting strength f_t.

The measured fracture forces P_C and SIFs for mode I and mode II for the HPC material for the ratio a/R of 0.267 are presented in Figure 83Figure 82(a) and for the ratio a/R of 0.4 are presented in Figure 83Figure 82(b).

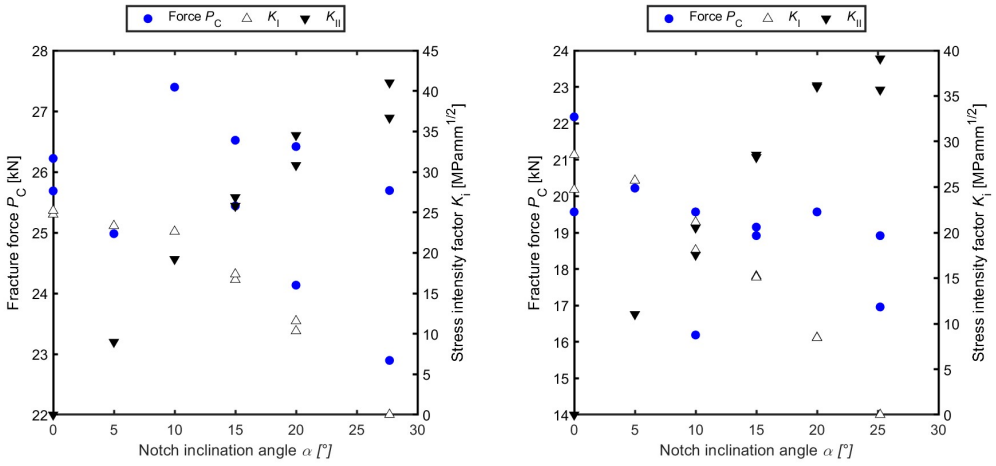

(a) (b)

Figure 83: Measured fracture forces P_C and equivalent values of K_I and K_{II} for HPC batch A material (a) – a/R 0.267 and (b) – a/R = 0.4.

The measured fracture forces P_C for the HPC material show similar values as for the C 50/60 material. Consequently, this results into similar values of SIFs and as well as into similar values of fracture toughness K_{IC} and K_{IIC}.

The measured fracture forces P_C and SIFs for mode I and mode II for the AAC material for the ratio a/R of 0.267 are presented in Figure 84(a) and for the ratio a/R of 0.4 are presented in Figure 84(b).

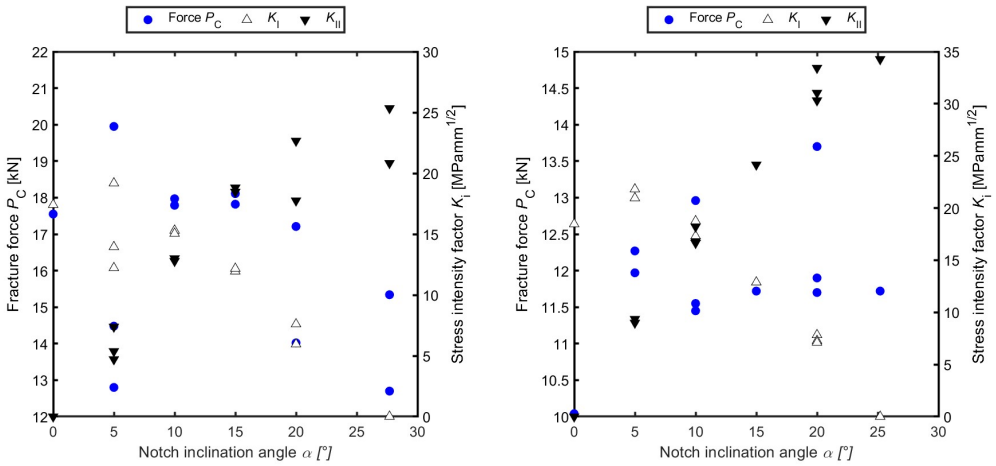

(a) (b)

Figure 84: Measured fracture forces P_C and equivalent values of K_I and K_{II} for AAC material (a) - a/R 0.267 and (b) – a/R = 0.4.

The measured fracture forces P_C for the AAC material show the lowest values compared to C 50/60 and other materials. Consequently, this results into the lowest values of SIFs and as well as into the lowest measured values of fracture toughness K_{IC} and K_{IIC}. This agrees with the general expectation as the AAC showed overall lower mechanical performance and the lowest tensile splitting strength f_t.

1.2 Fracture Toughness

The fracture toughness K_{IC} for mode I was determined by using Eq. (3.2) on p. 42 with input geometry data presented in Tables from Appendix A on p. 134. Similarly, to mode I fracture toughness, fracture toughness for mode II K_{IIC} was determined by using Eq. (3.3) on p. 42 with the same geometry data as presented in Tables A in Appendix A. The pure mode I is present for both relative ratios a/R of 0.267 and 0.4 for notch inclination angle $\alpha = 0°$. On the other hand, the pure mode II is present at different inclination angle for each ratio a/R. Thus, the mode II fracture toughness was determined for angle $\alpha = 27.7°$ for the ratio $a/R = 0.267$ and for angle $\alpha = 25.2°$ for the ratio $a/R = 0.4$. The measured maximum fracture forces P_C are showed for each studied a/R ratio and for each material are presented in Appendix A on p. 134 in Tables A1 – 1 to A4 – 3. Determined values of fracture toughness for mode I K_{IC} for each studied material are presented in Table 30, while values of fracture toughness for mode II K_{IIC} are showed in Table 31.

Table 30: Comparison of evaluated fracture toughness K_{IC} for mode I on the BDCN geometry for various relative notch lengths.

Material	$a/R = 0.267$ K_{IC} [MPam$^{1/2}$]	$a/R = 0.4$ K_{IC} [MPam$^{1/2}$]
C 50/60	0.668	0.972
High-strength concrete	1.064	1.821
High-performance concrete – Batch A	0.790	0.8423
Alkali activated concrete	0.551	0.584
HPC - Batch B- Cl^- free	-	0.919
HPC - Batch B - Cl^- saturated	-	0.782

Table 31: Comparison of evaluated fracture toughness K_{IIC} for mode II on the BDCN geometry for various relative notch lengths.

Material	$a/R = 0.267$ K_{IIC} [MPam$^{1/2}$]	$a/R = 0.4$ K_{IIC} [MPam$^{1/2}$]
C 50/60	0.974	1.329
High-strength concrete	1.835	2.290
High-performance concrete – Batch A	1.229	1.182
Alkali activated concrete	0.730	1.084
HPC – Batch B - Cl^- free	-	1.105
HPC – Batch B - Cl^- saturated	-	1.073

From values presented in Table 30 and Table 31 it can be observed, that the values of both fracture toughness vary heavily. This difference is caused by geometry and by material itself, which vary in the mixture composition. Clear increase by at least 15% of both values K_{IC} and K_{IIC} for the mixtures categorized as HPC or HSC can be observed, if compared to C 50/60 material. The highest difference shows HSC mixture with almost 55 % increase of the K_{IC} value and by 60% increase of the K_{IIC} value. On the other hand, if C 50/60 is compared to AAC material a decrease by 40% of K_{IC} and by 25% of K_{IIC} can be observed.

Both changes are mainly related to the value of indirect tensile strength f_t, which depends on the bond between the aggregate and matrix. Decrease of K_{IC} value in case of AAC material is due to overall lower mechanical performance (compressive strength, tensile strength) of the material, which results to an earlier crack initiation and specimen failure. On the other hand, decrease in in case of chloride environment is related to the possible formation of the Friedel's salt as the Portland cement blend contains Metakaolin, which increase the chance of the Friedel's salt formation.

1.3 Critical Distance

In further evaluation of the mixed mode I/II fracture resistance, the critical distance r_C plays key role and varies for each material. Critical distance r_C depends on the fracture toughness K_{IC} for mode I and on the tensile strength f_t, simultaneously it is parameter which governs the fracture resistance under the mixed mode I/II evaluated by GMTS criterion. In case of the BDCN specimen, the indirect tensile strength f_t measured on the BD specimen is used to determinate values of critical distances r_C as it is measured on the similar geometry.

In this study, the critical distance was calculated by traditional approach as showed in [117]. Such approach offers two variants of the r_C calculation. Fist one is for the plane stress conditions as showed in Eq. (2.50), while the second considers plane strain conditions as showed in Eq. (2.51) on p. 19. The calculated r_C for all investigated concrete mixtures and relative notch ratios a/R are presented in Table 32.

Table 32: Comparison of calculated critical distance r_C for various studied concrete materials.

Material	Plane stress r_C [mm]		Plane strain r_C [mm]	
	$a/R = 0.267$	$a/R = 0.4$	$a/R = 0.267$	$a/R = 0.4$
C 50/60	2.336	4.945	0.779	1.648
HSC 7.6.	1.607	4.711	0.536	1.570
HPC 31.5.	2.402	2.730	0.801	0.91
ACC	4.856	5.459	1.619	1.820
HPC – Cl^--free	-	3.975	-	1.325
HPC – Cl^--saturated	-	2.873	-	0.958

From Table 31 a similar observation as in the case of the fracture toughness K_{IC} can be made i.e. the critical distance The discussion is about the selection of the critical distance r_C from the crack tip and its influence on the shape and size of the fracture resistance curve.

2. Mixed Mode I/II Fracture Resistance

To evaluate the fracture resistance under the mixed mode I/II the GMTS criterion was used. The GMTS criterion was selected as the tangential stress $\sigma_{\theta\theta}$ opens crack in mode I (in tension) even when mode II deformations are present. The mixed mode fracture resistance of each studied concrete mixture is present in form of the fracture resistance curve, which was calculated from Eq. (2.15) on p.12 for various critical distances. Such curves are presented in relative and absolute values. Together with fracture resistance curve a crack initiation direction θ_0 is presented in order to provide full insight of problem.

Generally, the mixed mode I/II fracture resistance is presented in relative coordinates, i.e. K_I/K_{IC} as for the x-axis and K_{II}/K_{IC} as for the y-axis. This provides great illustration of how accurate the theoretical prediction by the fracture criterion is. However, in case of comparing various materials, it is more definite to provide fracture resistance curve in absolute coordinates, i.e. K_I as for the x-axis and K_{II} as for the y-axis. This presentation in absolute values provides clear and conclusive comparison of fracture behaviour between compared mixtures. Subsequently, the goodness of fracture resistance predicted by fracture criteria was estimated by the root mean squared error (RSME) to give explicit conclusions.

Furthermore, for the C 50/60 material all of the important results are showed and discussed, later for other mixtures the text will limit itself to major results and the rest will be presented in the Appendix B so the text flow will not be affected. Moreover, the mixed mode I/II fracture resistance for other materials will be presented in comparison with C 50/60 material.

2.1 C 50/60

The BDCN specimen made of C 50/60 material were used in preliminary experiments for first try out of such experimental setup. Experiments were performed with the BDCN possessing the notch of relative crack ratio a/R of 0.267 and a/R of 0.4.

Mixed mode I/II fracture resistance for C 50/60 evaluated by using the MTS (Eq. (2.31) on p. 16) and GMTS criterion (Eq. (2.32) and (2.31) on p. 16) with the values of fracture toughness from Table 30 for a/R of 267 and from Table 31 for a/R of 0.4. Subsequently, values of critical distance as presented in Table 32 were used as input parameters for the fracture criteria. The estimated fracture resistance curves in relative coordinates, i.e. K_I/K_{IC} and K_{II}/K_{IC} are shown in Figure 85.

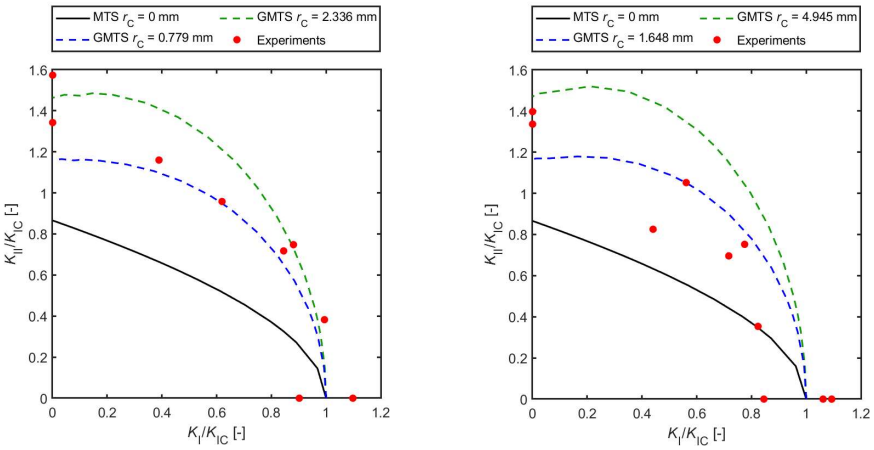

Figure 85: Mixed mode I/II fracture resistance of C 50/60 material relative notch ratio (a) – a/R = 0.267 and (b) – a/R = 0.4.

The estimated fracture resistance curves in relative coordinates, i.e. K_I against K_{II} are shown in Figure 86.

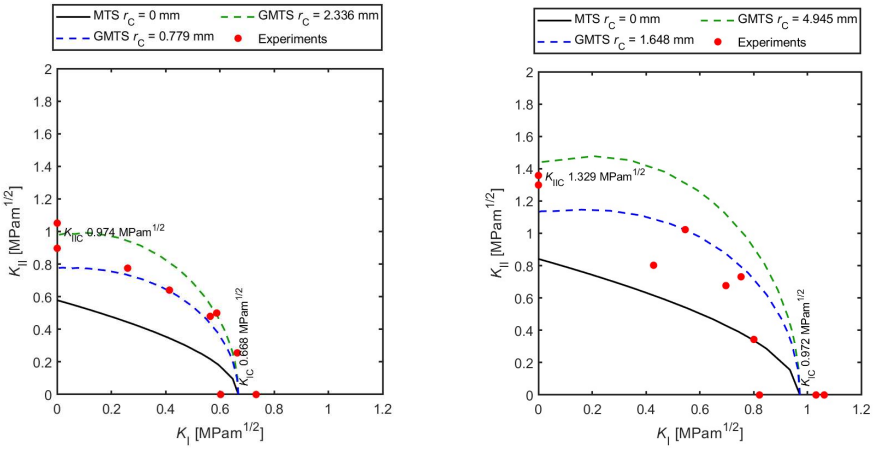

Figure 86: Mixed mode I/II fracture resistance of C 50/60 material resented in absolute coordinates for relative notch ratio (a) – a/R = 0.267 and (b) – a/R = 0.4.

The crack initiation direction θ_0 used for fracture resistance curves as presented in Figure 85 and in Figure 86 are showed in Figure 87. A clear influence of the T-stress on the crack initiation angle θ_0 angle observable for both a/R ratio.

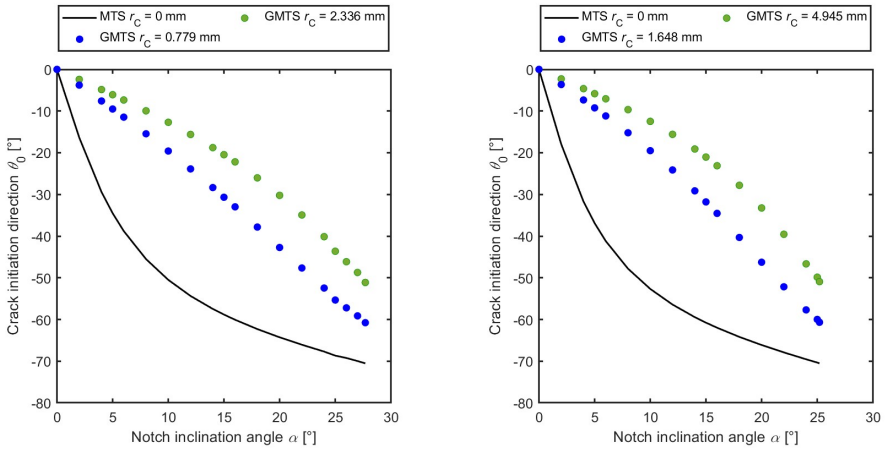

(a) (b)

Figure 87: Crack initiation direction θ_0 of C 50/60 material (a) – $a/R = 0.267$ and (b) – $a/R = 0.4$.

Moreover, the MTS criterion cannot predict onset of fracture accurately, while the GMTS curves can. This again confirms the observation made in Figure 85 and in Figure 86, i.e. the GMTS criterion can predict the mixed-mode I/II accurately. However, the difference between experimentally measured θ_0 and the calculated by GMTS criterion increases with increasing mode II load.

2.2 High-strength Concrete

The HSC concrete mixture shows generally better mechanical performance than the C 50/60 (see Table 4 on p. 36), especially for the values of compressive strength f_c and for the indirect tensile strength f_t (this value is almost double to the value of C 50/60). Such good mechanical properties resulted into almost double value of fracture K_{IC} if compared to the C50/60, however only one specimen was used to measure fracture toughness K_{IC} of the HSC

If the fracture resistance curves calculated by GMTS criterion are compared in the relative coordinates, the difference between each mixture is virtually low. The evaluated fracture resistance curves via GMTS criterion for the HSC mixtures in relative coordinates are showed in Figure 88.

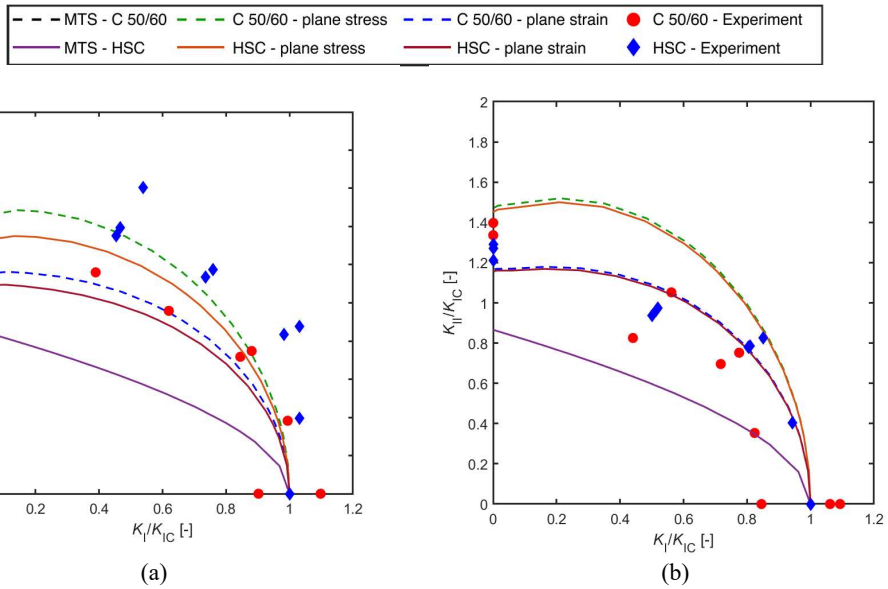

(a) (b)

Figure 88: Comparison of the fracture resistance curves between C 50/60 and HPC material in relative coordinates (a) – $a/R = 0.267$ and (b) – $a/R = 0.4$.

Furthermore, if the more specimens would be used for the K_{IC} measurement, the curve for ratio of a/R 0.267(see Figure 88(a)) would widen and predict the failure under the mixed mode I/II more accurately.

On the other hand, if the GMTS curves are compared in absolute values, evident improvement in the mixed-mode I/II fracture resistance can be observed. The GMTS curves for the ratio of a/R of 0.267 are showed in Figure 89(a) and for the ratio a/R of 0.4 in Figure 89(b).

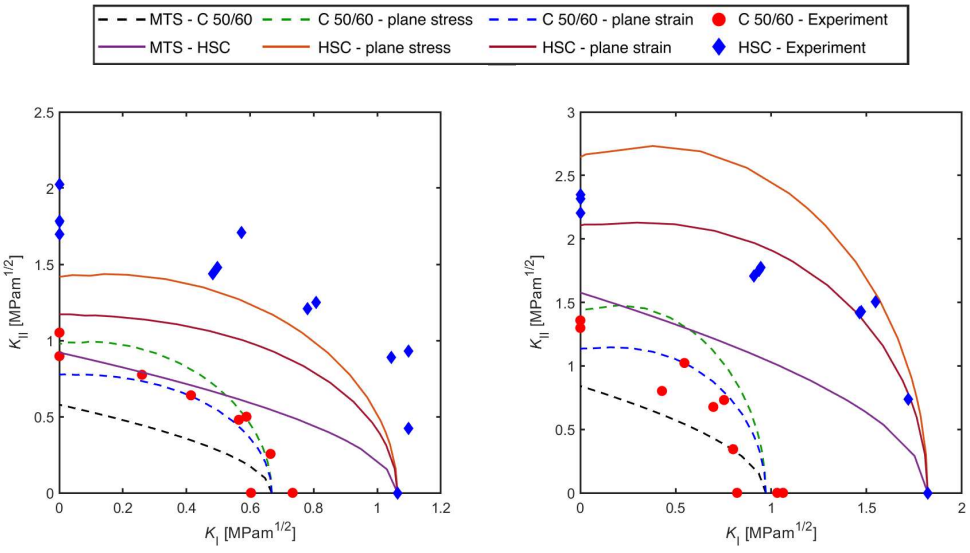

(c) (d)

Figure 89: Comparison of the fracture resistance curves between C 50/60 and HSC material in absolute coordinates (a) – a/R = 0.267 and (b) – a/R = 0.4.

2.3 High-performance Concrete Batch A

The HPC mixture batch A, shows improved properties from the C 50/60 material. Improved mechanical performance can be observed for the compressive strength f_c and for the tensile strength f_t (see Table 6 on p. 37). However, this material is more brittle, if the fracture toughness K_{IC} is compared for the ratio a/R of 0.4. This resulted, for the ratio a/R of 0.4, into a lower fracture resistance under the mixed mode I/II load that for the C 50/60 material. The evaluated GMTS curves for the HPC mixture are showed in the Figure 90.

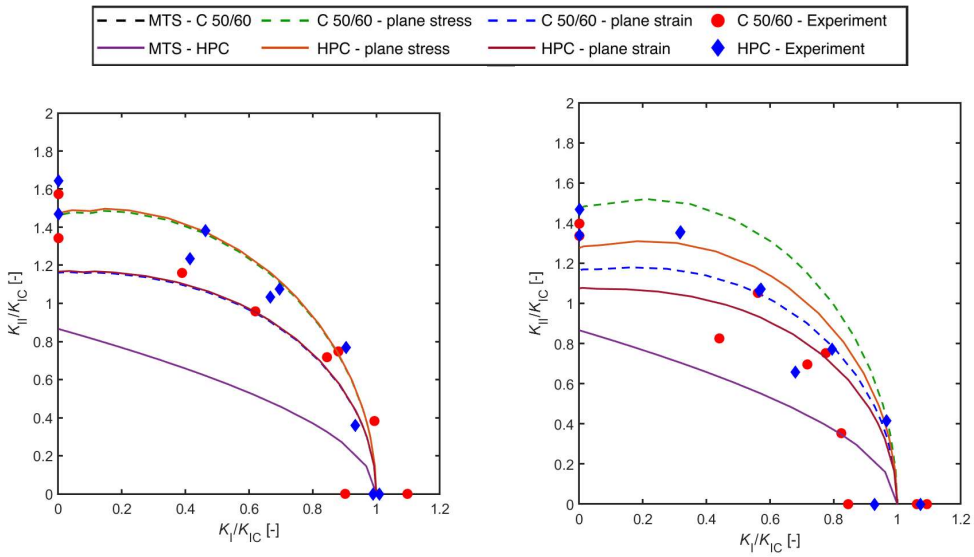

(a) (b)

Figure 90: Comparison of the fracture resistance curves between C 50/60 and HPC batch A material in relative coordinates
(a) – a/R = 0.267 and (b) – a/R = 0.4.

On the other hand, the GMTS curves for the ratio a/R of 0.267 align with the curves for the C 50/60, this is related to the similar value of the K_{IC} for the a/R of 0.267.

Subsequently, if the GMTS curves for the HPC batch A material are presented in absolute values, the HPS shows better mixed-mode I/II resistance for the ratio a/R of 0.267, while for the a/R of 0.4 the C 50/60 material. This is again related to the different values of K_{IC} for each ratio of a/R. The calculated GMTS curves for the a/R ratio of 0.267 are showed in Figure 91(a) and for the ratio a/R of 0.4 are showed in Figure 91(b).

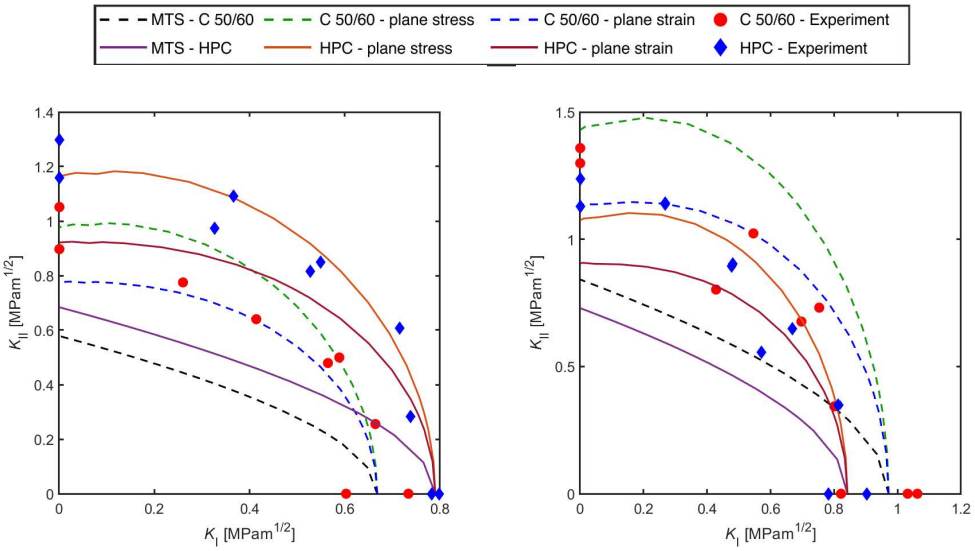

(a) (a)

Figure 91: Comparison of the fracture resistance curves between C 50/60 and HPC batch A material in absolute coordinates
(a) – $a/R = 0.267$ and (b) – $a/R = 0.4$.

2.4 Alkali-activated Concrete

Generally, the used AAC material shows worse mechanical performance compared to the C50/60 material. Nonetheless, if the fracture resistance curves are compared, the GMTS for the a/R of 0.267 predict the mixed mode I/II failure with relatively good agreement, while for the ratio a/R of 0.4 the GMTS curve shows higher discrepancy for the AAC material. Both the fracture resistance curve in relative and absolute coordinates for the AAC material are presented in Figure 92.

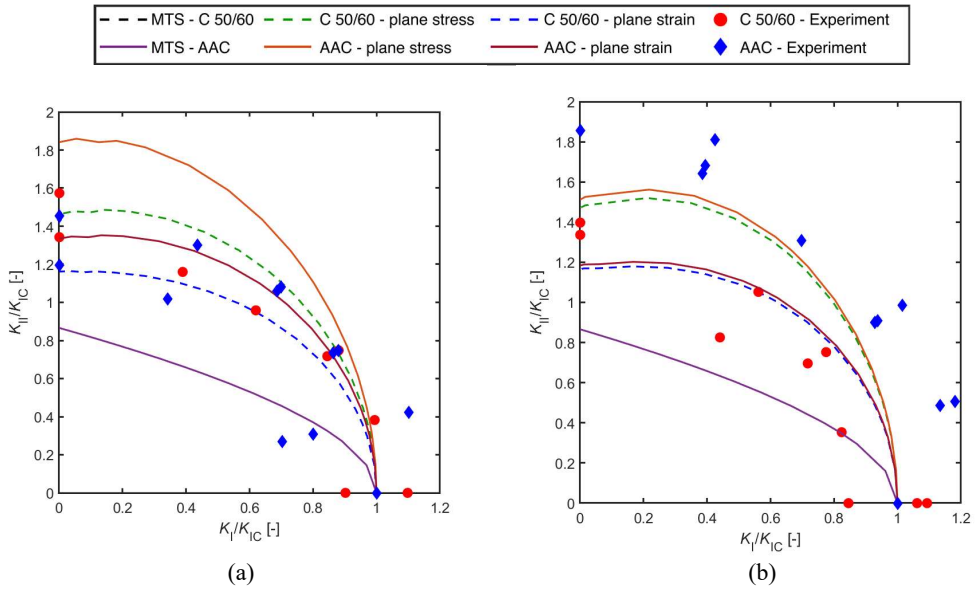

(a) (b)

Figure 92: Comparison of the fracture resistance curves between C 50/60 and AAC material in relative coordinates (a) – $a/R = 0.267$ and (b) – $a/R = 0.4$.

This error observed in Figure 92(b), see also values of RSME in Table 33 and in Table 34, is related to the insufficient number of specimens tested for mode I fracture, i.e. $\alpha = 0°$ with only one specimen tested. In comparison to the C 50/60 for which the GMTS shows relatively good agreement due to sufficient number of specimens tested for mode I failure.

If the fracture resistance curves are showed in the absolute coordinates, the difference between C 50/60 and AAC material and the error from the GMTS prediction is more observable. The fracture resistance curves in absolute coordinates for the AAC material are showed in Figure 93.

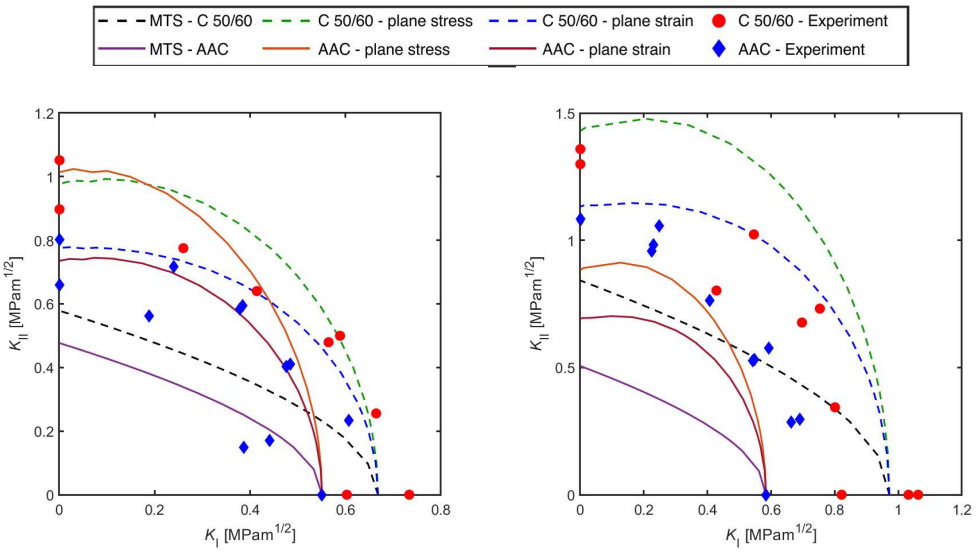

(a) (b)

Figure 93: Comparison of the fracture resistance curves between C 50/60 and AAC material in absolute coordinates (a) – $a/R = 0.267$ and (b) – $a/R = 0.4$.

From both Figure 93(a) and Figure 93(b), it can be observed, that the AAC is less resistance to the mix-mode I/II fracture toughness compared to the C 50/60. This again confirms the general expectation based on the mechanical properties, particularly to the lower value of the indirect tensile strength f_t.

2.5 Mixture Comparison

In this subsection all studied mixtures are compared by means of the value of RSME as it provides clear conclusion of the goodness of fracture resistance made by fracture criteria of above presented graphical results. The calculate RSME values for relative notch ratio a/R of 0.267 are presented in Table 33 and for relative notch ratio a/R of 0.4 are presented in Table 34.

Table 33: Comparison of RSME values for the fracture criteria for various materials for ratio a/R of 0.267.

Material	C 50/60	HSC	HPC	AAC
RSME – MTS [-]	0.7349	0.5865	0.6760	0.7451
RSME – GMTS – plane stress [-]	0.9384	0.8608	0.9615	0.8112
RSME – GMTS – plane strain [-]	0.9322	0.7522	0.8732	0.9679

Table 34: Comparison of RSME values for the fracture criteria for various materials for ratio a/R of 0.4.

Material	C 50/60	HSC	HPC	AAC
RSME – MTS [-]	0.8132	0.8064	0.7120	0.8132
RSME – GMTS – plane stress [-]	0.8845	0.8973	0.9428	0.8845
RSME – GMTS – plane strain [-]	0.9155	0.9577	0.8725	0.9155

From both Table 33 and Table 34 can be seen that the traditional fracture criterion MTS predicts mixed mode I/II failure inaccurately with almost 40 % of difference. Subsequently, the values of RSME for the GMTS criterion confirms the observation made in Figure 89 - Figure 93, i.e. that the GMTS shows more accurate results and predicts the mixed-mode I/II more accurately.

On the other hand, it has to be mentioned, that for some mixture only one of the test was done for demanded angle α. The author believes that the more (at least set of three experiments) for each investigated angle α will bring even better predictions of the mixed-mode I/II failure assessed by the GMTS criterion.

3. DIC Analysis

In what follows, the values of the WE terms calculated based on the experimentally obtained displacement fields for the selected crack lengths are presented.

3.1 Williams's Expansion Coefficients

As mentioned above, the focus of this study was the evaluation of the SIFs values for mode I and mode II, *T*-stress values for selected notch inclination angles α and relative notch lengths a/R. For this ODM was used with the inputs of experimentally captured displacements by the DIC technique.

Firstly, the SIFs for mode I and mode II were calculated using the analytical expression stated in Eqs. (3.2) and (3.3) on p. 42, with geometry inputs from Table 11 and the maximum loading force P_{max} from Table 15 under various mixed mode I/II loading conditions.

Afterwards, this maximum force P_C served as an input for FEM model validated FEM model's results. The SIF results were calculated by means of Eq. (2.19). The compared results of the evaluated SIF values are presented in Table 35 for the relative notch length $a/R = 0.267$.

Table 35: Comparison of SIFs values calculated by the analytical formula and generated by the FE model for the relative crack length ratio $a/R = 0.267$.

	$a/R = 0.267$		
Specimen No.	HPC_4_3_2	HPC_4_3_3	HPC_4_3_4
Notch inclination angle α [°]	5	10	27.7
Force P_{max} [kN]	22.5	24.3	27.4
K_I – FEM [MPam$^{1/2}$]	0.834	0.803	0.048
K_I – Eq. (3.2) [MPam$^{1/2}$] - [144]	0.625	0.597	0
K_{II} – FEM [MPam$^{1/2}$]	0.3223	0.687	1.675
K_{II} – Eq.(3.3) [MPam$^{1/2}$] - [144]	0.240	0.507	1.642

A similar set of results, but for the specimens with a relative notch length a/R of 0.4, is presented in Table 36.

Table 36: Comparison of SIFs values calculated by the analytical formula and generated by the FE model for the relative crack length ratio $a/R = 0.4$.

	$a/R = 0.4$		
Specimen No.	HPC_6_3_1	HPC_6_3_2	HPC_6_3_3
Notch inclination angle α [°]	0	5	15
Force P_{max} [kN]	13.09	18.01	17.22
K_I – FEM [MPam$^{1/2}$]	0.3503	0.9109	0.544
K_I – Eq. (3.2) [MPam$^{1/2}$] - [144]	0.3459	0.9212	0.5515
K_{II} – FEM [MPam$^{1/2}$]	0	0.3994	1.028
K_{II} –Eq. (3.3) [MPam$^{1/2}$] - [144]	0.05	0.3958	1.033

In both tables, a relatively good agreement between the SIF results from the analytical solution and finite element analysis can be observed. This agreement is for both loading modes; however, the biggest difference is for $a/R = 0.4$ and $\alpha = 5°$, which was the first specimen to be tested and

the loading speed was higher than in previous studies. The results for longer cracks, i.e. $a/R = 0.4$, exhibit better accuracy due to lower loads, which caused lower compressive stresses in the area close to the supports.

The experimentally obtained SIFs values were compared with experimental data obtained by Miarka et al. [250], where exactly the same concrete mixture was studied. The SIFs values, currently obtained by employing Eqs. (3.2) and (3.3) on p. 42 have a similar trend to the data found in the literature. This verified the validity of the experimentally captured displacements by the DIC measurement. The difference between the data found in the literature and that which is currently being evaluated is related to the deterioration of the concrete mixture over time and the different loading rate. A comparison is shown in Figure 94.

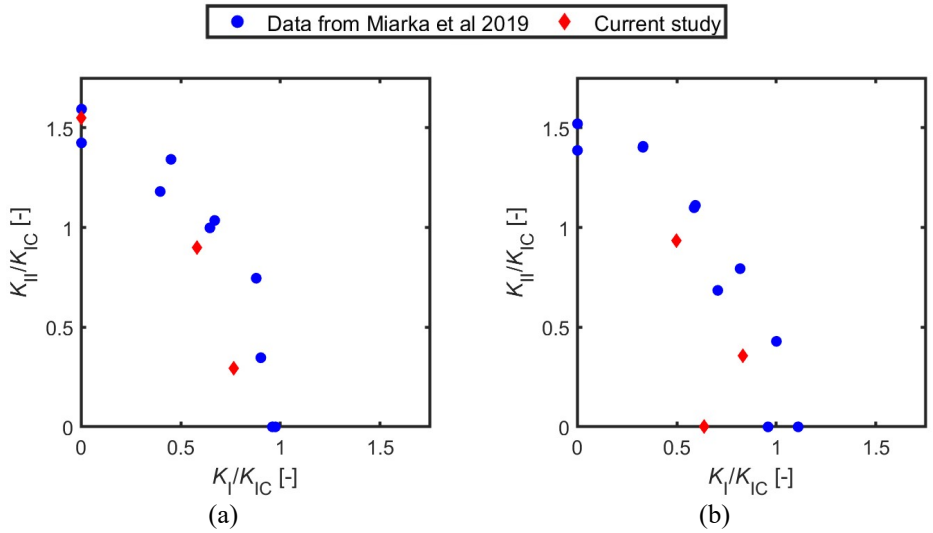

Figure 94: Comparison of the currently measured SIF values (normalized via the fracture toughness) with data found in the literature – $a/R = 0.267$ (a) and $a/R = 0.4$ (b).

After verification of the material's behaviour, the ODM calculation convergence was verified for various numbers of N and M terms. The stress intensity factors were calculated from the ODM based on the numerically obtained displacement field taking into account various numbers of the initial WE terms. A comparison of the numerical SIF values calculated by means of Eq. (2.19) on p. 13 is shown in Figure 95. It was found that this method shows good agreement with the value generated by FEA with the use of more than 5 N and M terms.

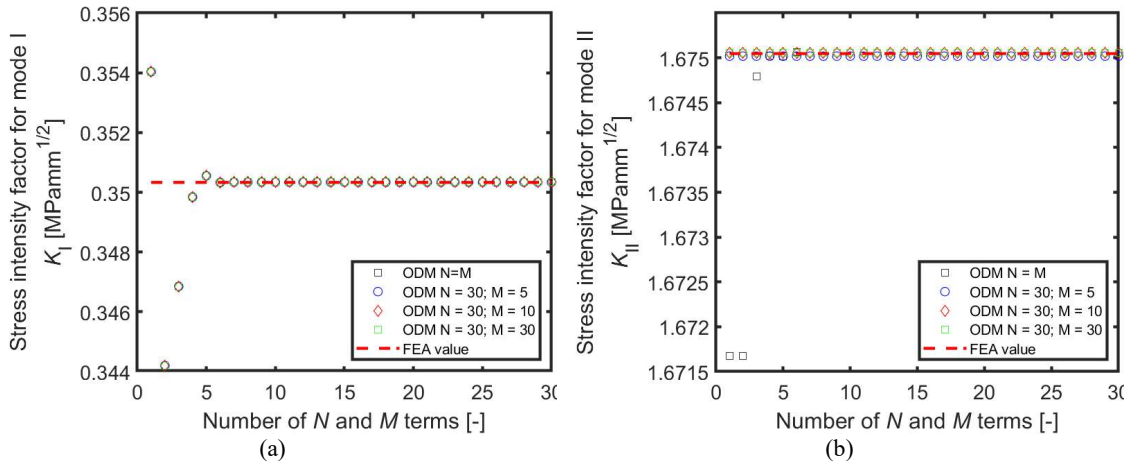

Figure 95: Convergence of the evaluation of the ODM using FEM generated displacements – K_I for the pure mode I case HPC_6_3_1 specimen (a) and K_{II} for the pure mode II case HPC_4_3_4 (b).

In the next step, the displacements captured by the DIC method were used as an input for the ODM calculation. Then, a comparison with the results obtained from the ODM was performed,

considering the numerically generated displacements as inputs. The results, for which the DIC displacements were used, are K_I^{ODM} - DIC, while the results calculated using the FE displacements are marked as K_I^{ODM} – FEA. A comparison of such results for the relative crack length $a/R = 0.267$ is given in Table 37 for K_I and in Table 38 for K_{II}, respectively. Note that the results are presented again for two different radial distances from the crack tip, 2 and 4 mm.

Table 37: Comparison of K_I values generated by FEM model and DIC displacement for various numbers of WE coefficients N and M for the relative notch length $a/R = 0.267$.

		$a/R = 0.267$					
Specimen No.		HPC_4_3_2		HPC_4_3_3		HPC_4_3_4	
Notch inclination angle α [°]		5		10		27.7	
r [mm]		2	4	2	4	2	4
K_I^{ODM} FEM [MPam$^{1/2}$]	$N, M = 2$	0.821	0.808	0.792	0.7811	0.0576	0.0647
	$N, M = 4$	0.837	0.832	0.802	0.8067	0.0476	0.0453
	$N, M = 10$	0.833	0.833	0.803	0.8026	0.0485	0.0485
K_I^{ODM} DIC [MPam$^{1/2}$]	$N, M = 10$	0.6291	0.7298	0.9123	0.8053	0.1148	0.0968

Table 38: Comparison of K_{II} values generated by FEM model and DIC displacement for various numbers of WE coefficients N and M for the relative notch length $a/R = 0.267$.

		$a/R = 0.267$					
Specimen No.		HPC_4_3_2		HPC_4_3_3		HPC_4_3_4	
Notch inclination angle α [°]		5		10		27.7	
r [mm]		2	4	2	4	2	4
K_{II}^{ODM} FEM [MPam$^{1/2}$]	$N, M = 2$	0.3221	0.3216	0.6851	0.6838	1.6717	1.6679
	$N, M = 4$	0.3234	0.3237	0.6875	0.6862	1.6750	1.6748
	$N, M = 10$	0.3236	0.3233	0.6874	0.6866	1.6751	1.6751
K_{II}^{ODM} DIC [MPam$^{1/2}$]	$N, M = 10$	0.4822	0.5489	0.5930	0.5286	1.6408	1.6366

The results presented in Table 37 and Table 38 for DIC displacements show relatively good agreement with the SIFs obtained from FE displacement. Of course, configurations exist for which the results correspond better (for example the deviations between the K_{II} values for the case of $\alpha = 27.7°$ are around 2%) than for others (for the same case of $\alpha = 27.7°$ the deviations between the K_I values are up to approx. 50%). This is surely connected to the high heterogeneity of the concrete specimens and the existence of a high amount of micro-cracks, voids or pores. As with the results performed on $a/R = 0.267$, a comparison for $a/R = 0.4$ is given in Table 39 and in Table 40.

Table 39: Comparison of K_I values generated by FEM model and DIC displacement for various numbers of WE coefficients N and M for the relative notch length $a/R = 0.4$.

		$a/R = 0.4$					
Specimen No.		HPC_6_3_1		HPC_6_3_2		HPC_6_3_3	
Notch inclination angle α [°]		0		5		15	
r [mm]		2	4	2	4	2	4
K_I^{ODM} - FEM [MPam$^{1/2}$]	$N, M = 2$	0.34723	0.3503	0.9040	0.8968	0.5467	0.5481
	$N, M = 4$	0.3502	0.3498	0.9105	0.9093	0.5438	0.5418
	$N, M = 10$	0.3503	0.3503	0.9109	0.9109	0.5445	0.5445
K_I^{ODM} DIC [MPam$^{1/2}$]	$N, M = 10$	0.4593	0.5174	1.0142	1.0502	0.7342	0.6812

Table 40: Comparison of K_{II} values generated by FEM model and DIC displacement for various numbers of WE coefficients N and M for the relative notch length $a/R = 0.4$.

		$a/R = 0.4$					
Specimen No.		HPC_6_3_1		HPC_6_3_2		HPC_6_3_3	
Notch inclination angle α [°]		0		5		15	
r [mm]		2	4	2	4	2	4
K_{II}^{ODM} - FEM [MPam$^{1/2}$]	$N, M = 2$	1.034×10^{-8}	1.052×10^{-8}	0.3927	0.3916	1.0256	1.0223
	$N, M = 4$	2.223×10^{-8}	4.275×10^{-8}	0.3934	0.3931	1.0275	1.0269
	$N, M = 10$	2.746×10^{-8}	4.0712×10^{-8}	0.3935	0.3935	1.0277	1.0277
K_{II}^{ODM} DIC [MPam$^{1/2}$]	$N, M = 10$	0.0102	0.0203	0.6473	0.5713	1.1638	1.0955

The results presented in Table 39 and in Table 40 show relatively good agreement, in a similar manner to the results for the relative notch length ratio $a/R = 0.267$. The maximum deviation is limited to a maximum of 40%. Because of the different stress distribution around the longer notch tip, which provides stable crack growth, no unambiguous trends and conclusions can be stated.

As in the case of the SIFs, the T-stress was estimated using the same abovementioned procedure. The convergence study conducted on the T-stress values showed similar results to K_I, i.e. that the T-stress converges well with the use of 5 or more mode I WE terms in the calculations. The convergence study results for the FEA study (and not the DIC data) are shown in Figure 96, while the comparison of T-stress values is shown in Table 41 and in Table 42 for both studied a/R ratios.

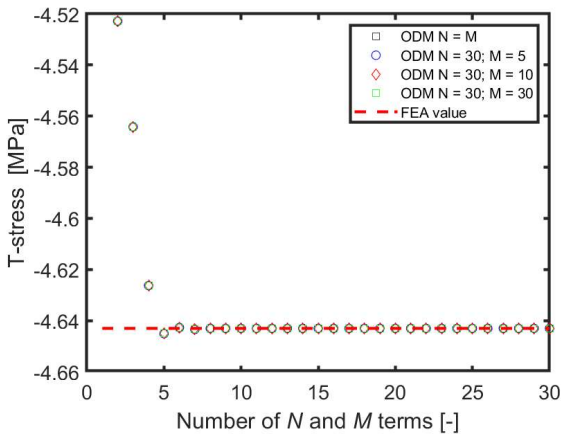

Figure 96: Convergence of the evaluation of the T-stress values using the ODM with FE-generated displacements.

The experimentally obtained results displayed in Table 41 and in Table 42 show high disagreement with the values generated by FEM model. This can be caused by the fact that the horizontal displacement captured by DIC showed a crack propagating from the notch tip, while the vertical displacement showed no crack propagation. This was found at the load value of P_{max} and in case of the specimens with an inclined notch, for which mode II deformations are presented. For the specimen with the pure tensile mode I ($\alpha = 0°$), this phenomenon was not observed. Therefore, the shear deformation governs the crack initiation.

Table 41: Comparison of *T*-stress values generated by FEM model and calculated by using DIC displacement for various numbers of WE coefficients *N* and *M* for the relative notch length *a*/*R* = 0.267.

		a/*R* = 0.267					
Specimen No.		HPC_4_3_2		HPC_4_3_3		HPC_4_3_4	
Notch inclination angle α [°]		5		10		27.7	
T-stress – FEM – Eq. (2.20) [MPa]		-13.53		-13.69		-6.90	
r [mm]		2	4	2	4	2	4
$T\text{-stress}^{ODM}$ - FEM [MPa]	*N*, *M* = 2	-13.2335	-13.086	-13.4586	-13.3257	-7.5069	-7.5593
	N, *M* = 4	-13.5132	-13.4832	-13.6865	-13.6507	-7.2683	-7.2219
	N, *M* = 10	-13.5269	-13.5265	-13.7046	-13.7053	-7.2975	-7.2974
$T\text{-stress}^{ODM}$ - DIC [MPa]	*N*, *M* = 10	-25.4572	-20.4834	-21.6518	-22.2918	-12.5999	-6.0078

Table 42: Comparison of *T*-stress values generated by FEM model and calculated by using DIC displacement for various numbers of WE coefficients *N* and *M* for the relative notch length *a*/*R* = 0.4.

		a/*R* = 0.4					
Specimen No.		HPC_6_3_1		HPC_6_3_2		HPC_6_3_3	
Notch inclination angle α [°]		0		5		15	
T-stress – FEM – Eq. (2.20) [MPa]		-4.64		-12.23		-8.62	
r [mm]		2	4	2	4	2	4
$T\text{-stress}^{ODM}$ FEM [MPa]	*N*, *M* = 2	-4.5655	-4.5228	-12.0540	-11.9507	-8.6675	-8.6543
	N, *M* = 4	-4.6382	-4.6263	-12.2154	-12.1809	-8.5943	-8.5517
	N, *M* = 10	-4.6430	-4.6430	-12.2307	-12.2308	-8.6189	-8.6189
$T\text{-stress}^{ODM}$ DIC [MPa]	*N*, *M* = 10	-5.5649	-5.3046	-18.3196	-19.4057	-12.4568	-14.7247

From both Table 41 and Table 42 a clear difference between numerical and experimental values can be observed. On the other hand, the results using Eq. (2.20) validates the use of the ODM method to evaluate the *T*-stress based on the numerically generated displacements. The difference between numerical and experimental values is due to development the FPZ ahead of the crack tip which affects wider area than the 2 or 4 mm from found crack tip.

4. Chloride Penetration and the Resistance under the Mixed mode I/II

In what follows, the experimentally measured chloride penetration depth is presented. Subsequently, the influence of chloride penetration on the indirect tensile strength, on the evaluated fracture mechanical parameters under the mixed I/I, and on the fracture toughness were quantified and discussed.

4.1 Chloride Penetration Depth

As it was mentioned above, the focus of this study was set on the evaluation of the influence of the chloride penetration of the concrete specimen. Therefore, it was investigated whether the weakened cross-section had an effect on the fracture properties. For this purpose, a chloride penetration depth was measured by the aforementioned colorimetric method. The chloride depth was measured in consecutive distances over the specimen's radius. The average values of the measured penetration depth are shown in Table 43.

Table 43: Measured chloride penetration depth.

Specimen	Penetration depth from the bottom [mm]	Penetration depth from the top [mm]	Mean value of penetration depth [mm]
HPC_37	4.79	3.11	3.95
HPC_38	6.45	5.72	6.09
HPC_39	3	5.29	4.15
Mean value	4.74	4.71	4.73

The specimens were not covered by epoxide layer on any of the outer surfaces, hence the chloride ions diffusion from every side. Therefore, 7 penetration depths in total were measured from the top and the bottom of the specimens' surfaces. Based on the results, one can notice that the specimens were affected by chloride ions approximately 4.73 mm from both the top and the bottom. For comparison, the mean value of chloride penetration depths of ordinary Portland Cement concrete (OPC) from the same test is 7.22 mm. Specimens made of HPC show higher resistance to chloride ions than those made of OPC, which was proved also in research, e.g. [8].

The measurement of the chloride penetration depth was conducted by the $AgNO_3$ colorimetric method as described in [61]. After the splitting tests, the chloride-contaminated specimens were sprayed with the $AgNO_3$ solution then the depths were measured at intervals of approximately 10 mm to obtain seven values. To mitigate the 2D chloride ingress process near the edges, no measurement should be done in the zone within about 10 mm from the edges of the sample. The measurement of chloride penetration depths is presented in Figure 97, where the un-penetrated ligament is highlighted with a green line, and the specimen is divided into regular sections.

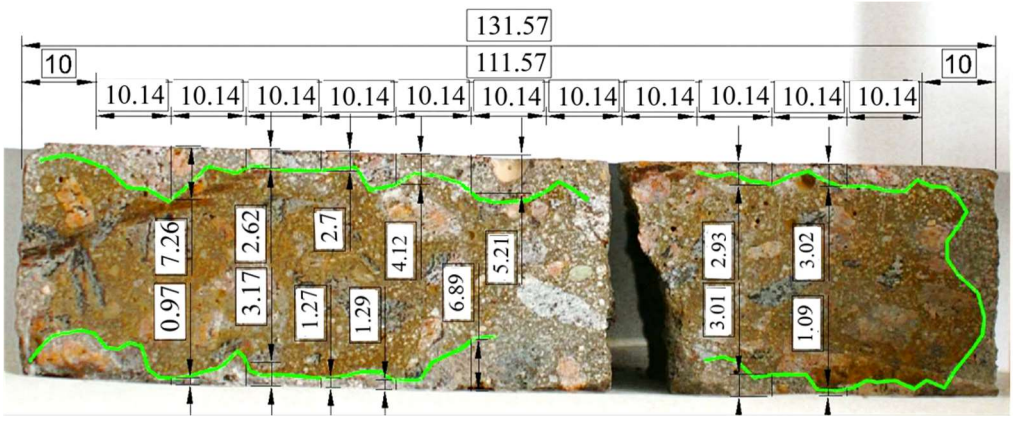

Figure 97: Measured chloride penetration depth by colorimetric method on one of the specimens.

Please note that in this pilot experimental study, the 30-day interval for chloride exposure was selected as a reference value, to which a future long-term study will be referred.

4.2 Indirect Tensile Test

The dimensions for Eq. (3.1) on p. 40 were used from Table 12. The evaluated values of the indirect tensile strength f_t together with the measured loads P_{max} for both studied cases are presented in Table 44.

Table 44: Measured maximum loads P_{max} and the evaluated indirect tensile strengths f_t for both studied cases (with and without exposure to chloride environment).

	P_{max} [kN]	f_t [MPa]
HPC_50_K16	34.220	5.254
HPC_51_K16	38.140	5.835
HPC_52_K16	39.360	6.051
HPC_53_K16	37.430	5.723
HPC_54_K16	40.900	6.226
HPC_45_K16_CL	32.770	4.986
HPC_46_K16_CL	38.630	5.964
HPC_48_K16_CL	40.460	6.132
HPC_49_K16_CL	43.100	6.196

To distinguish the studied cases of the Cl^- environment, the indirect tensile strength evaluated on the Cl^--free specimens was set as f_t, while for the Cl^--saturated case it was set as $f_t^{Cl^-}$. Thus, from the results presented in Table 44, an average value of the indirect tensile strength f_t is 5.818 MPa,

and $f_t^{Cl^-}$ is 5.820 MPa. These measured average values show virtually no influence of Cl^- on the material's indirect tensile strength f_t. This is related to the assumption presented in Figure 38(a), where the Cl^- ions penetrate the specimen's body mainly from the bottom and the top surfaces. This results in a shallow chloride penetration depth, which does not reduce the specimen's thickness load-bearing role.

4.3 Fracture Mechanical Parameters

The measurement of FMP on the BDCN geometry was done for various notch inclination angles α, which represent the various levels of mode-mixity present in the geometry. The FMPs were measured using Eqs. (3.2) and (3.3) on p. 42 to obtain values of K_I and K_{II}, respectively. The geometry inputs were used from Table 13 for the Cl^--free samples as well as for the Cl^--saturated samples.

In Figure 98(a) the recorded fracture forces P over the normalized time t_i/t_{max} (time over the total duration of the test), and in Figure 98(b) the recorded forces P over the vertical deformation δ are presented to illustrate the experimental measurement in more detail. Except for the difference in the measured fracture force P_c, another observation can be made, which is related to the specimen's stiffness and total deformation. This confirms the observation made in Figure 99, as, with the increasing mode II load, the fracture force increases in size, while the maximum deformation δ has a similar value of 0.2 mm. Similarly, a difference in the specimen's stiffness increases with an increasing mode II load.

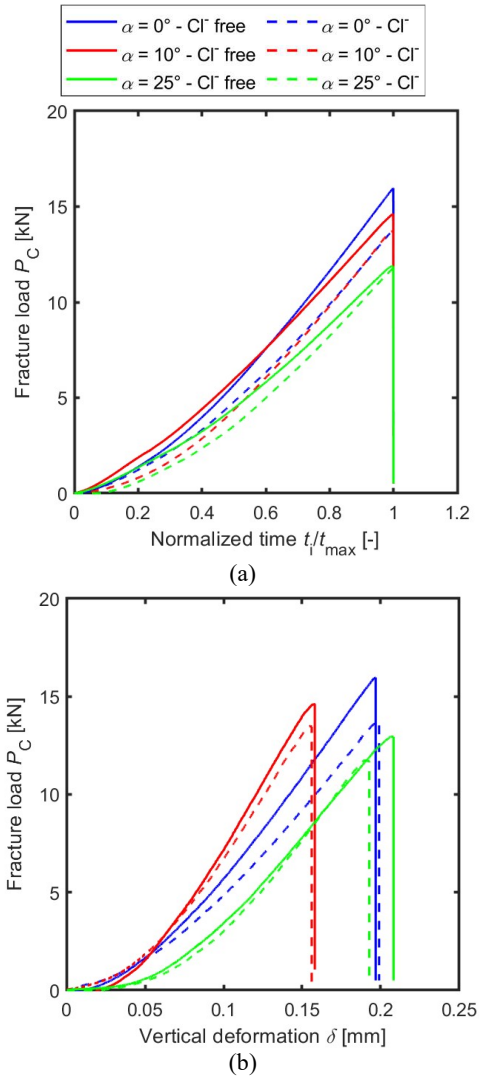

Figure 98: Comparison of the measured *P-t* diagram and *P-δ* diagrams for the various notch inclination angles *α*.

The experimentally measured fracture forces P_C for each notch inclination angle α together with the evaluated equivalent values of K_I and K_{II} for the case of Cl^- environment are presented in Table 45.

Table 45: Measured fracture forces P_C for various notch inclination angles α and equivalent K_I and K_{II} values for the Cl^--free environment.

	Notch inclination angle α [°]	Fracture load Pc [kN]	K_I [MPam$^{1/2}$]	K_{II} [MPam$^{1/2}$]
HPC_30_K16	0.0	15.970	0.928	0.000
HPC_31_K16	0.0	16.610	0.921	0.000
HPC_32_K16	0.0	15.810	0.929	0.000
HPC_40_K16	5.0	17.810	0.977	0.419
HPC_41_K16	5.0	16.660	0.936	0.402
HPC_42_K16	5.0	15.840	0.886	0.380
HPC_14_K16	10.0	15.670	0.751	0.729
HPC_15_K16	10.0	14.610	0.698	0.678
HPC_36_K16	10.0	16.660	0.750	0.728
HPC_13_K16	15.0	11.920	0.426	0.798
HPC_19_K16	15.0	14.020	0.489	0.916
HPC_20_K16	15.0	12.890	0.453	0.849
HPC_10_K16	20.0	15.210	0.289	1.233
HPC_11_K16	20.0	12.570	0.242	1.032
HPC_12_K16	20.0	14.990	0.287	1.223
HPC_04_K16	25.2	10.860	0.000	1.011
HPC_05_K16	25.2	12.960	0.000	1.220
HPC_06_K16	25.2	11.880	0.000	1.122

Similarly to the specimens saturated with clean water, the SIFs were evaluated for the specimens exposed to the Cl^- environment. The measured values of fracture forces P_C together with the equivalent SIFs values evaluated from Cl^--saturated samples are presented in Table 46.

Table 46: Measured fracture forces P_C for various notch inclination angles α and equivalent K_I and K_{II} values for the Cl^- environment.

	Notch inclination angle α [°]	Fracture load Pc [kN]	K_I [MPam$^{1/2}$]	K_{II} [MPam$^{1/2}$]
HPC_27_K16_CL	0.0	13.730	0.813	0.000
HPC_28_K16_CL	0.0	12.670	0.753	0.000
HPC_29_K16_CL	0.0	13.650	0.797	0.000
HPC_37_K16_CL	5.0	11.690	0.647	0.278
HPC_38_K16_CL	5.0	13.090	0.724	0.310
HPC_39_K16_CL	5.0	12.830	0.716	0.307
HPC_33_K16_CL	10.0	13.730	0.656	0.637
HPC_34_K16_CL	10.0	13.490	0.644	0.625
HPC_35_K16_CL	10.0	13.350	0.641	0.622
HPC_16_K16_CL	15.0	11.420	0.398	0.746
HPC_17_K16_CL	15.0	13.790	0.481	0.902
HPC_18_K16_CL	15.0	14.900	0.504	0.945
HPC_07_K16_CL	20.0	9.780	0.188	0.801
HPC_08_K16_CL	20.0	11.890	0.228	0.971
HPC_09_K16_CL	20.0	10.300	0.198	0.843
HPC_01_K16_CL	25.2	10.110	0.000	0.948
HPC_02_K16_CL	25.2	12.820	0.000	1.198
HPC_03_K16_CL	25.2	11.740	0.000	1.102

The fracture loads P_C for the BDCN samples saturated with Cl^- (Table 46) are approximately lower by 15% than the fracture loads P_C measured on the Cl^--free BDCN samples as presented in Table 45 for the same thickness B. This influence of the aggressive chloride environment on the fracture loads is more observable in Figure 99, where a comparison of the measured fracture loads P_C for both studied cases is shown.

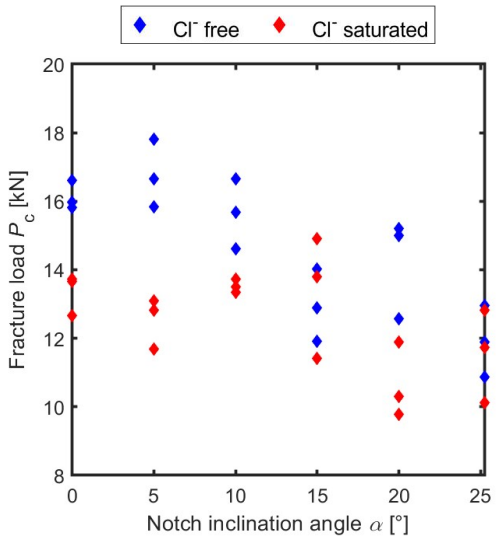

Figure 99: Comparison of measured fracture loads P_C under various mixed mode I/II load conditions for chloride-free and chloride-saturated discs.

This difference in the measured fracture forces P_C is more noticeable for the cases where mode I load prevails. For the case of pure mode II, i.e. for the case of $\alpha = 25°$, where the measured fracture forces P_C show a similar value for both investigated cases of Cl^- environment.

Similarly to the values of indirect tensile strength f_t, it is necessary to distinguish between the values of fracture toughness K_{IC} measured for the different Cl^- environments. Thus, K_{IC} is used for the values of fracture toughness experimentally measured on the Cl^--free samples, and $K_{IC}^{Cl^-}$ is used for the values of fracture toughness experimentally measured on the specimens saturated with Cl^-. Both values K_{IC} and $K_{IC}^{Cl^-}$ can be calculated as an average value for the cases with the angle $\alpha = 0°$ as shown in Table 45 and Table 46. The measured values of the fracture toughness of the HPC concrete mixture exposed to different environments are K_{IC} of 0.926 MPam$^{1/2}$ and $K_{IC}^{Cl^-}$ of 0.788 MPam$^{1/2}$, respectively.

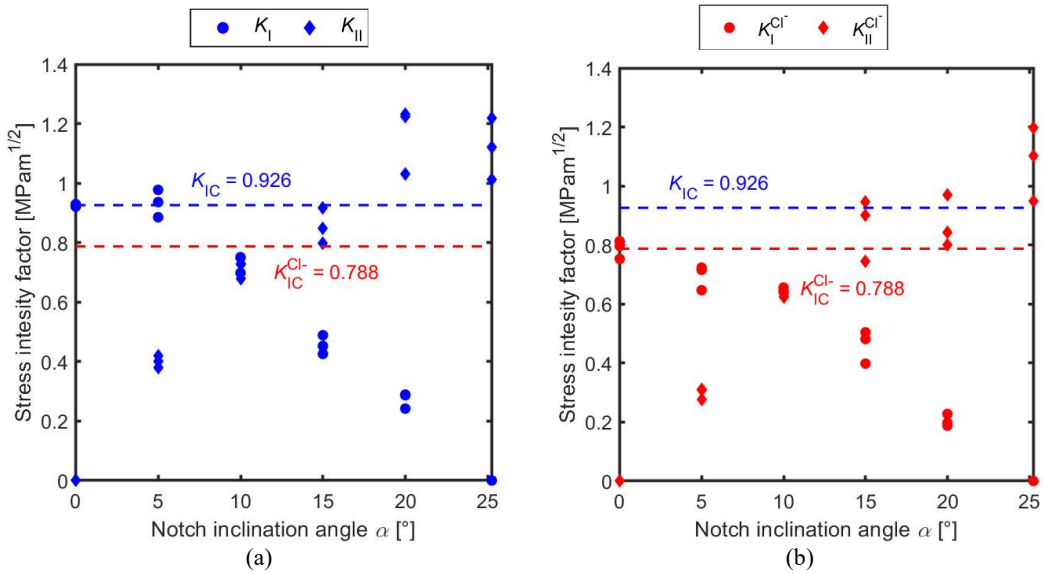

Figure 100: Comparison of the evaluated SIF values for various environmental conditions with highlighted values of fracture toughness K_{IC} and $\boldsymbol{K_{IC}^{Cl^-}}$, respectively - (a) Cl^--free samples and (b) Cl^--saturated samples.

The experimental results presented in Figure 100(b) for the case of the Cl^--saturated samples show overall lower values of K_I and K_{II}, as they are directly related to the measured fracture forces P_C shown in Figure 99.

This difference seems to be linked to the assumption made in Figure 38(b), as the Cl^- ions penetrate the disc's body not only from both the top and the bottom surface, as in the case of the samples used for the indirect tensile strength measurement, but also Cl^- ions can penetrate from the notch, which creates another surface exposed to the Cl^- environment. This leads to a lower value of fracture toughness $K_{IC}^{Cl^-}$, as the crack initiates from the notch end. A comparison of the calculated SIF values for various notch inclination angles α with marked values of evaluated K_{IC} for both cases are presented in Figure 100.

Putting both values of fracture toughness K_{IC} and $K_{IC}^{Cl^-}$ and both values of indirect tensile strength f_t and $f_t^{Cl^-}$ into Eqs. (2.50) and (2.51) on p. 19, a critical distance r_C can be calculated. The calculated values of critical distance r_C for both studied cases of environment aggressivity are presented in Table 47.

Table 47: Calculated values of critical distance r_C for both studied cases of Cl^--free and Cl^--saturated environment aggressivity, respectively.

Fracture toughness [MPam$^{1/2}$]	r_C [mm] - plane strain	r_C [mm] - plane stress
K_{IC} = 0.926	1.344	4.033
$K_{IC}^{Cl^-}$ = 0.788	0.972	2.917

Similar values of critical distance r_C of 1.5 mm for fine grain cement mortar with a similar value of fracture toughness K_{IC} [90] and of 1.45 mm for sandstone with a similar value of tensile strength f_t [95] can be found in the literature. The calculated critical distances for the case of the Cl^--saturated specimens show again a lower value by approx. 30%, which results in an earlier crack initiation and a lower value of fracture toughness K_{IC}. According to the GMTS criterion, the onset of a fracture begins when the critical value of tangential stress $\sigma_{\theta\theta,C}$ is reached. In the case of the Cl^--saturated samples, the value of $\sigma_{\theta\theta,C}$ is reached in the closer distance from the crack tip, which results in an earlier failure. This assumption is again supported by the measured values of the fracture loads P_C and fracture toughness K_{IC}, for which the Cl^--saturated discs show an overall lower value of fracture load P_C, while keeping a similar specimen's thickness B of approx. 28 mm.

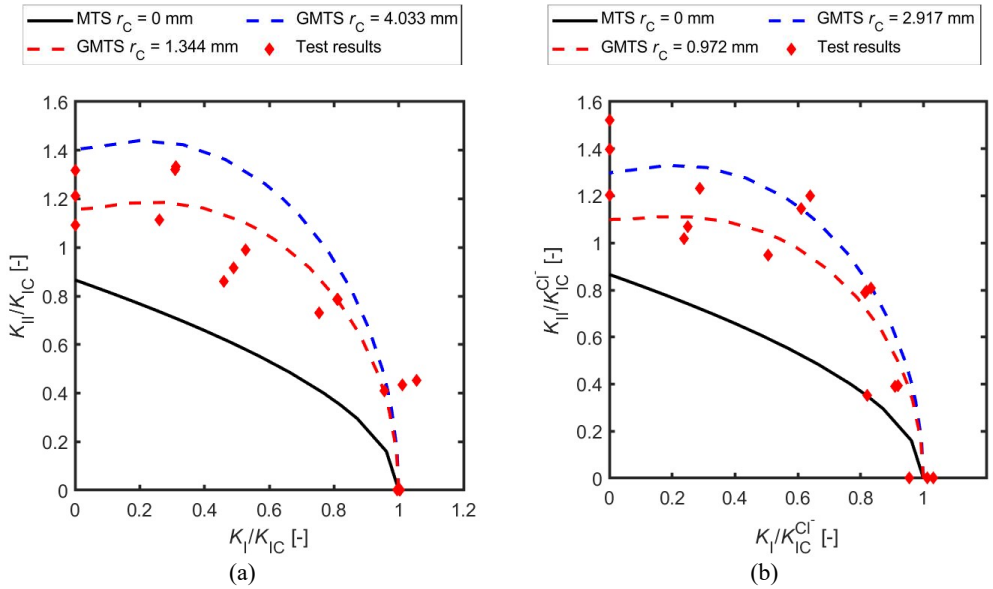

Figure 101: Comparison of evaluated fracture resistance curve under the mixed mode I/II loading conditions - (a) chloride Cl^--free samples and (b) chloride Cl^--saturated samples.

Using the calculated critical distances r_C from Table 47 in the Eq. (2.32) on p. 1643, one can derive the fracture resistance curves for the mixed mode I/II loading conditions. Please note that if the critical distance r_C is equal to 0, the Eq. (2.32) simplifies itself to the traditional MTS criterion. The evaluated fracture resistance curves of the BDCN geometry for both studied cases of various environment aggressivity levels are showed in Figure 101.

From the fracture resistance curves presented in Figure 101, a similar observation to the previous statements can be made, i.e. the chloride saturated BDCN specimens show a better fracture resistance to the mixed mode I/II conditions. The GMTS fracture criterion predicts the fracture resistance with a relatively good agreement for both cases of the Cl^- environment. However, for the cases of pure mode II, the fracture resistance shows a relatively high dispersion for the cases of Cl^--saturated BDCN specimens. A visible discrepancy between the experimental results and the prediction of fracture criteria (MTS and GMTS) was evaluated by using the root mean squared error (RMSE). The calculated values of RMSE for both studied cases and various critical distances r_C are presented in Table 48.

Table 48: Evaluated root mean square error for given fracture resistance curves for both studied cases of environment aggressivity and various boundary conditions.

	MTS	GMTS – plane stress	GMTS – plane strain
RSME for Cl^- free	0.7735	0.8814	0.9477
RSME for Cl^- saturated	0.7451	0.9353	0.9299

From the values of RSME presented in Table 48, a notable difference in the accuracy of the MTS and the GMTS criterion can be seen. Although, the MTS criterion predicts the failure with a good agreement only for the cases of mode I, the GMTS criterion can predict the fracture in the whole range of various mode mixite conditions with a relatively good agreement with a difference limited to 22%. Another observation from Table 48 can be made, that the GMTS criterion for the Cl^--free samples predicts the failure more accurately for the plane stress conditions, the samples saturated with Cl^- shows a better agreement for the plane stress boundary conditions. This phenomenon is due to the fact that the Cl^- ions can penetrate the specimen's body through the surface, where the plane stress conditions are assumed.

The reduction of the critical distance r_C and reducing the load-bearing capacity can be caused by various reasons, e.g. chloride binding to the concrete matrix and crystallization in pores. However, in this case, the notch preparation by the water jet could also disrupt the concrete structure (bound between the aggregate and cement paste) with micro-cracks. These micro-cracks act as a stress concentrator and more importantly, they created another free surface, where the chloride ions could penetrate the concrete body. In addition to this, chlorides can transform themselves into Friedel's salt, which extends in its volume and damages the pores. Recently, it has been showed that metakaolin in Portland cement blends increases the formation of Friedel's salt [246], which is used in the studied HPC mixture.

The differences caused by chloride penetration in the calculated values of critical distances r_C influence the calculated crack initiation directions θ_0 from Eq. (2.32) on p. 16 used in the evaluation of the GMTS fracture resistance curves. The-chloride saturated case showed higher values of the angle θ_0 compared to the chloride-free cases, while the values of θ_0 are the same for both cases. This difference in the values of θ_0 increases with an increasing mixed mode I/II load. This leads to a lower fracture resistance to the applied load. The calculated crack initiation directions θ_0 are showed in Figure 102.

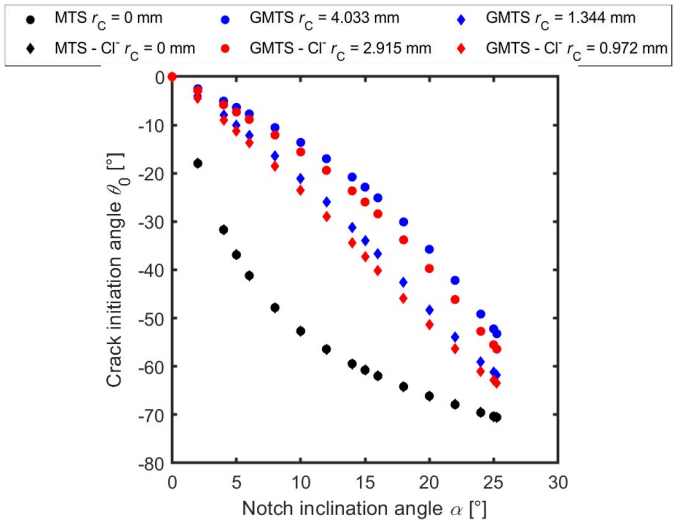

Figure 102: Crack initiation angle θ_0 calculated by MTS and GMTS for various boundary conditions and for various environmental conditions.

This influence of various levels of the environment aggressivity is more observable, if the fracture resistance curves are plotted in absolute values, i.e. plotted as K_{II} against K_I instead of the ratio of K_I/K_{IC} and K_{II}/K_{IC}, respectively. The mixed mode I/II fracture resistance curves with various levels of environment aggressivity are shown for plane stress in Figure 103(a) and for plane strain in Figure 103(b).

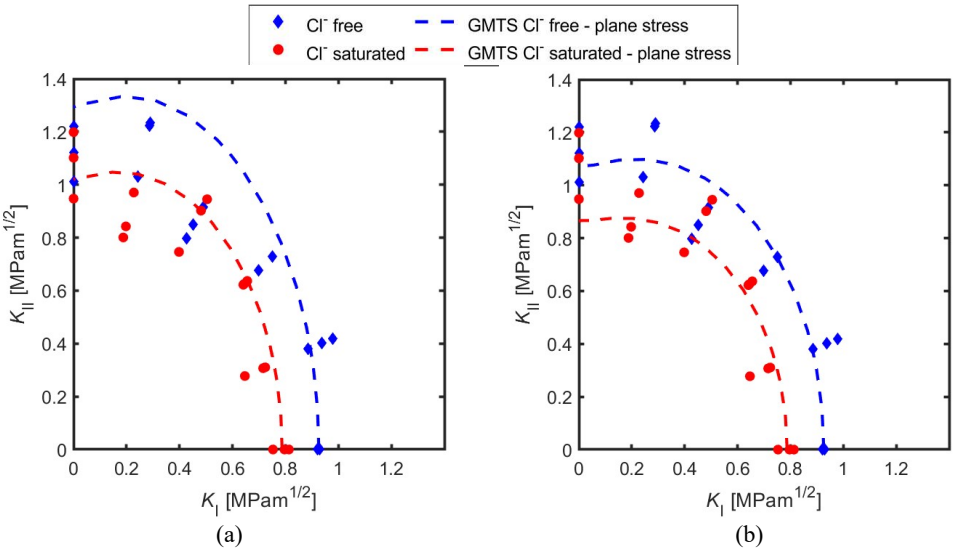

Figure 103: Fracture resistance under mixed mode I/II expressed in absolute values of stress intensity factors for mode I and mode II – (a) plane stress and (b) plane strain.

The fracture resistance curves presented in Figure 103 again show a clear influence of the chloride aggressivity on the fracture resistance under the mixed mode I/II load. This difference for both studied cases of the aggressive environment is again about 15%. Consequently, this influence of the chloride penetration on the fracture resistance under mixed mode I/II should be taken into account, as it can lower the fracture load, for which a crack can initiate in a real structure. Moreover, this result has a major influence as it was experimentally proven before, that if HPC mixture has some content of metakaolin, it improves the mixture's resistance to chloride penetration [247-249].

4.3.1 Influence of the Thickness

The above-presented results of the fracture toughness, SIFs, and related fracture resistance, were evaluated on the specimens with a similar thickness B of 28 mm. This was done to provide a direct

and clear comparison for both studied environmental conditions. However, if there is introduced an effective thickness B_{eff}, which is reduced by a fracture toughness ratio K_{IC}^{Cl} /K_{IC} as follows:

$$B_{eff,KIC} = B\frac{K_{IC}^{Cl-}}{K_{IC}}, \tag{5.1}$$

or by reducing the specimen's thickness by a measured penetration depth $h^{\text{Cl-}}$ as:

$$B_{eff,Cl-} = B - h^{Cl-}, \tag{5.2}$$

then the clear influence of the chloride's damage on the measured SIFs values can be seen.

Both Eqs. (5.1) and (5.2) assume statement presented in Figure 38(b). This effective thickness is used in Eqs. (3.2) and (3.3) on p.42 for each measured fracture force P_{C} of the chloride-saturated case. A clear increase of K_{I} values can be seen. The evaluated K_{I} values using only load-bearing thickness, i.e. by using effective thickness B_{eff} are presented in Figure 104(a).

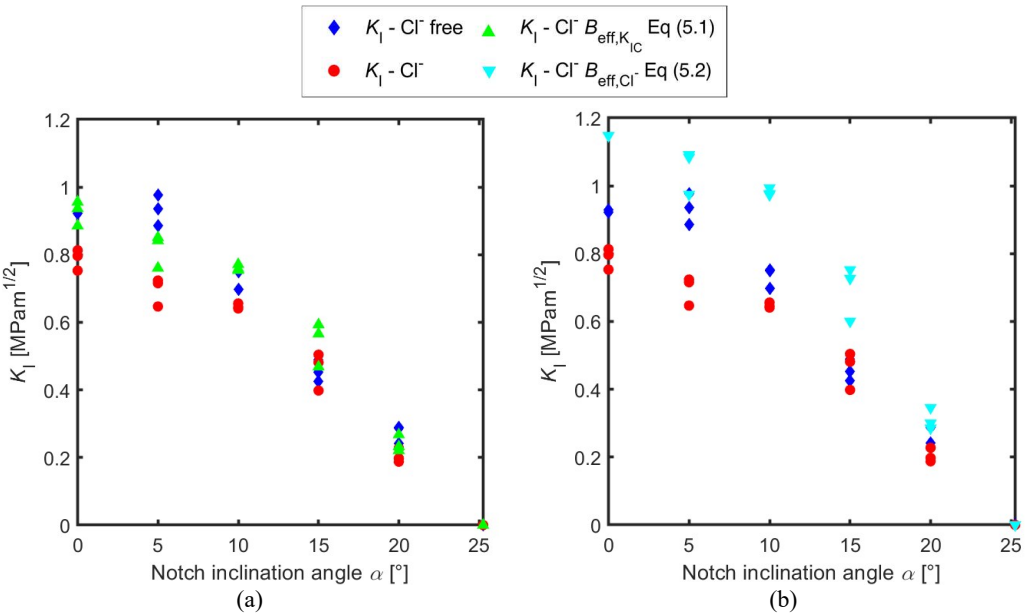

Figure 104: Influence of effective thickness of the specimens on the values of K_{I} (a) – fracture toughness ratio $\boldsymbol{K_{IC}^{Cl-}}$/$K_{\text{IC}}$ and (b) chloride penetration depth $h^{\text{Cl-}}$.

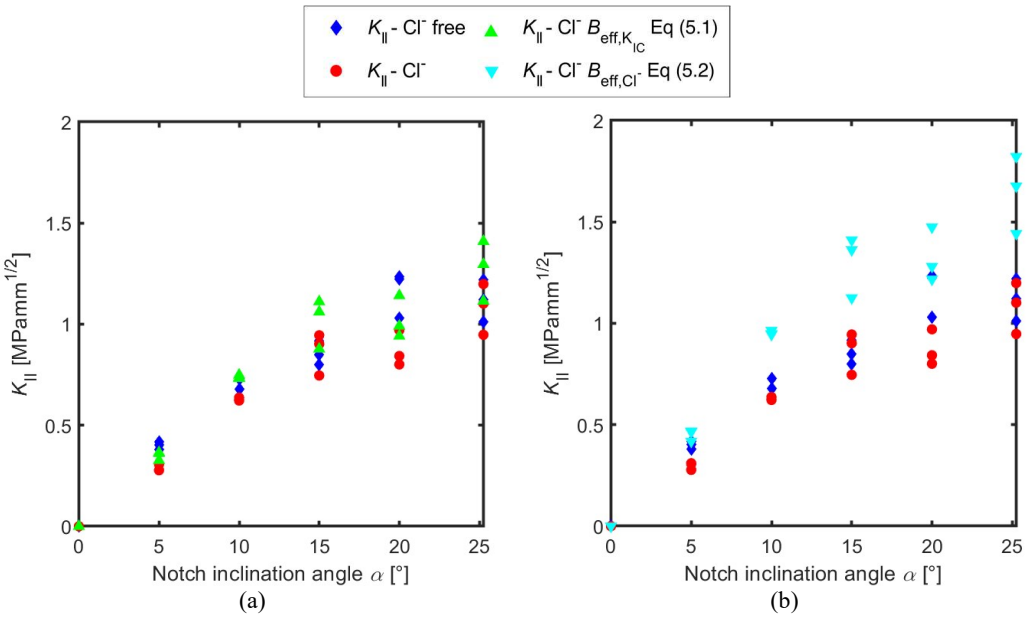

Figure 105: Influence of effective thickness of the specimen on the values of K_{II} (a) – based on fracture toughness ratio $\boldsymbol{K_{IC}^{Cl^-}}/K_{IC}$ and (b) based on chloride penetration depth h^{Cl-}.

From the both results presented in Figure 104 and in Figure 105, a clear influence of the chloride penetration of the concrete body can be seen. The transformation of the effective thickness B_{eff} by the fracture toughness ratio K_{IC}^{Cl-}/K_{IC} by using Eq. (5.1), shows more accurate results than by the transformation done by the actual chloride penetration depth h^{Cl-} using Eq. (5.2). This difference is caused, due to overestimation of the chloride penetration depth, as it is not very clear where the boundary of the chloride ingress is. The equivalent specimen's thickness B_{eff} evaluated by the fracture toughness ratio, to provide the same SIF values as the chloride free samples, is approximately 23.7 mm. This, again, agrees with the assumption made in Figure 38(b), i.e. the thickness is reduced due to the higher surface area exposed to the chloride ions.

Chapter VI
General Conclusions and Perspectives

The aim of this research was to study the crack initiation under the mixed-mode I/II conditions of various concrete materials used in building practice. The measured fracture mechanical properties and fracture resistance under the mixed-mode I/II of commonly used C 50/60 concrete material were compared to newly developed high-strength, high performance and alkali-activated concrete materials. The mixed mode I/II crack initiation problem was analysed numerically and experimentally on the concrete Brazilian disc with central notch (BDCN) specimen.

The numerical part, focused on the evaluation of the geometry functions of the BDCN geometry and higher order terms of the Williams' expansion by using the over-deterministic method. Furthermore, the crack initiation and propagation in the BDCN specimen was analysed by the means of the non-linear analysis by employing the concrete damage plasticity material model.

In experimental part, the focus was placed to evaluate the value of material's fracture toughness K_{IC} and the critical distance r_C as they serve as an input parameters to the generalised maximum tangential stress (GMTS) fracture criterion. Furthermore, the influence of the aggressive environment on the values of K_{IC}, r_C and the shape of the fracture resistance curve was study on chloride saturated specimens. The application of the Williams' expansion on the concrete BDCN geometry was validated by experimental measurements of the displacement fields captured by digital image correlation technique.

Found numerical and experimental results should contribute to the understanding of crack initiation and propagation process of concrete material.

1. Experimental Outcome

Experimental results proved that the each mixture shows different behaviour under the mixed-mode I/II load. Subsequently, the experimental results validated the applicability of the DIC technique to the concrete material, which provided the displacements field for the calculation of the WE terms. Furthermore, the experimental part showed that the mixed-mode I/II resistance can be influenced by the aggressive environment.

1.1 Fracture Properties and Resistance under Mixed-mode I/II.

The fracture properties were evaluated on the BDCN geometry for various concrete materials and compared between each other. Analysed FMPs were fracture toughness K_{IC} and the critical distance r_C have governing role in the mixed mode I/II fracture resistance. Furthermore, the evaluated fracture resistance curves by the GMTS criterion were presented for each material and compared to the commonly used C 50/60 material.

Generally, it was found that the mixed-mode I/II fracture resistance curve, evaluated by the MTS criterion, shows poor prediction of the specimen failure, while the GMTS curve shows overall better prediction. In addition to this, the GMTS curves are highly affected by the number of the tests used for the K_{IC} evaluation. Therefore, it is recommended to use more specimens for the K_{IC} testing in the mixed mode I/II fracture analysis. Besides this, the general conclusion can be made, i.e. that with the increasing mechanical and material's fracture mechanical properties the fracture resistance under the mixed mode I/II improves as well.

1.2 DIC Analysis

The performed DIC analysis on the BDCN specimen showed reliable results of the application of the LEFM to the HPC batch A. It showed good agreement between numerically generated and experimentally obtained WE terms. This was done for the BDCN specimen with two a/R ratio of 0.267 and 0.4. Furthermore, the DIC analysis showed dominance of the mode II deformation and its role on the crack initiation and following crack propagation. This fact has affected the values of second WE term, i.e. T-stress.

Other interesting results were showed in regards of selecting the proper distance from the crack for calculation of the WE terms. It was observed, that further from the crack tip, the WE terms will have better accuracy. This confirms the assumption of the existence of the very large non-linear fracture process zone ahead of the crack tip.

1.3 Influence of Aggressive Environment

The experimental results evaluated on the specimens saturated in chloride solution, showed generally lower value of fracture toughness K_{IC} and lower resistance to the mixed mode I/II loading if compared to the water saturated specimens. The chloride penetration depth was measured by the colorimetric method. The chloride ingress to the specimen body was studied and the effective thickness was calculated. Traditionally, the chloride influence is analysed on the resistance of the reinforcement's corrosion, while in this case of unique study, the results showed, that the chlorides can have major influence on the durability of the concrete itself.

2. Numerical Study

The numerical study was dedicated to the calculation of the geometry function used for the SIFs calculation, calculation of the HO terms of the WE and to the non-linear analysis of the BDCN specimen employing the CDP material model.

2.1 LEFM Numerical Results

The LEFM analysis of the BDCN specimen showed importance of the calculation of the geometry function for various ratio a/R. The geometry functions and consequent values of SIFs and T-stress are affected by the notch length which resulted into negative values. The HO terms of WE were calculated by using the over-deterministic method. The ODM results showed dependency of the WE terms on the number of N, M terms selected in the calculation and the radial distance from the crack tip. Moreover, it was showed, that the HO order terms starts to be dominant further from the crack tip.

2.2 Non-linear Analysis results

The non-linear analysis showed importance of the calibration of the input parameters on the generated results which resulted into the reasonable differences between the numerical prediction and the experimental results. Therefore, the author believe, that his presented results can be used in the future nonlinear analysis.

Furthermore, the influence of mode I and mode II deformation on the onset and further crack propagation process was analysed. It was showed, that the mode II deformations are dominant in the crack initiation process, while in the crack propagation the mode I deformations prevail. This was analysed by the *P-CMOS* and *P-CMOD* curves generated by the CDP material model.

The numerical model showed relatively good accuracy of the predicted inelastic strain, which represents the cracks. The numerically generated inelastic strains were compared to the experimental crack paths and similar initiation direction.

3. Perspectives for further Research

This thesis dealed with the mixed mode I/II fracture from various viewpoints and it can be stated, after finishing it, that it opened even more interesting topics to be investigated.

An interesting topic to be studied could be the comparison the DIC displacements fields and the CDP numerically generated ones. This would validate the applicability of the CDP model and bring more insight into the mixed-mode I/II fracture analysis. Furthermore, it would be interesting to compare the *P-CMOS* and *P-CMOD* curves for the DIC and CDP case.

The influence of the aggressive environment on the fracture toughness and fracture resistance under the mixed mode I/II can be extended as well. This analysis could consider progress of the chloride ingress to the concrete body over the time, i.e. from 1 month to 1 year. Furthermore, an advanced screening methods could be employed, i.e. tomography, to analyse micro-structure, defects and size of the pores. Also some microscope technique could be employed to locate the Friedel's salt crystallization and consequent damaging microstructure.

From the LEFM experimental viewpoint, it would be beneficial to find the circular geometry for which the *T*-stress is less than zero. This would lead to improvement of the fracture toughness accuracy and leading into improvement of the GMTS fracture predictions.

References

[1] M.A. Caldarone, High-Strength Concrete: A Practical Guide, CRC Press (2019).
[2] P.-C. Aïtcin, R.J. Flatt, Science and technology of concrete admixtures, Woodhead publishing 2015.
[3] E.G. Nawy, Fundamentals of High-Performance Concrete, Wiley (2001).
[4] M. Schneider, The cement industry on the way to a low-carbon future, Cement and Concrete Research 124 (2019) 105792.
[5] S.A. Miller, V.M. John, S.A. Pacca, A. Horvath, Carbon dioxide reduction potential in the global cement industry by 2050, Cement and Concrete Research 114 (2018) 115-124.
[6] K.E. Hassan, J.G. Cabrera, R.S. Maliehe, The effect of mineral admixtures on the properties of high-performance concrete, Cement and Concrete Composites 22(4) (2000) 267-271.
[7] R. Yu, P. Spiesz, H.J.H. Brouwers, Development of an eco-friendly Ultra-High Performance Concrete (UHPC) with efficient cement and mineral admixtures uses, Cement and Concrete Composites 55 (2015) 383-394.
[8] Q. Tran, P. Ghosh, Influence of pumice on mechanical properties and durability of high performance concrete, Construction and Building Materials 249 (2020) 118741.
[9] E. Vejmelková, D. Koňáková, T. Kulovaná, M. Keppert, J. Žumár, P. Rovnaníková, Z. Keršner, M. Sedlmajer, R. Černý, Engineering properties of concrete containing natural zeolite as supplementary cementitious material: Strength, toughness, durability, and hygrothermal performance, Cement and Concrete Composites 55 (2015) 259-267.
[10] J.L. Provis, J.S.J. van Deventer, Alkali Activated Materials: State-of-the-Art Report, RILEM TC 224-AAM, Springer Netherlands (2013).
[11] J.L. Provis, Alkali-activated materials, Cement and Concrete Research 114 (2018) 40-48.
[12] J.L. Provis, 4 - Activating solution chemistry for geopolymers, in: J.L. Provis, J.S.J. van Deventer (Eds.), Geopolymers, Woodhead Publishing (2009), pp. 50-71.
[13] A. McIntosh, S.E.M. Lawther, J. Kwasny, M.N. Soutsos, D. Cleland, S. Nanukuttan, Selection and characterisation of geological materials for use as geopolymer precursors, Advances in Applied Ceramics 114(7) (2015) 378-385.
[14] S. Donatello, O. Maltseva, A. Fernandez-Jimenez, A. Palomo, The Early Age Hydration Reactions of a Hybrid Cement Containing a Very High Content of Coal Bottom Ash, Journal of the American Ceramic Society 97(3) (2014) 929-937.
[15] M.A. Longhi, E.D. Rodríguez, S.A. Bernal, J.L. Provis, A.P. Kirchheim, Valorisation of a kaolin mining waste for the production of geopolymers, Journal of Cleaner Production 115 (2016) 265-272.
[16] Eurocode 2: Design of concrete structures—Part 1-1: General rules and rules for buildings, Brussels, Belgium (2004).
[17] AASHTO LRFD bridge design specifications, Transportation. American Association of State Highway and Transportation Officials, Inc.: Washington, DC (2007).
[18] CEB-FIP Model Code, First complete draft, Bulletin 55 (2010).
[19] B.L. Karihaloo, P. Nallathambi, Effective crack model for the determination of fracture toughness (KIce) of concrete, Engineering Fracture Mechanics 35(4) (1990) 637-645.
[20] B.L. Karihaloo, Fracture Mechanics and Structural Concrete (Concrete Design and Construction Series), Ed. Longman Scientific & Technical. United States (1995).
[21] H. Cifuentes, B.L. Karihaloo, Determination of size-independent specific fracture energy of normal- and high-strength self-compacting concrete from wedge splitting tests, Construction and Building Materials 48 (2013) 548-553.
[22] B.L. Karihaloo, H.M. Abdalla, T. Imjai, A simple method for determining the true specific fracture energy of concrete, Magazine of concrete research 55(5) (2003) 471-481.
[23] D. Novák, D. Lehký, ANN inverse analysis based on stochastic small-sample training set simulation, Engineering Applications of Artificial Intelligence 19(7) (2006) 731-740.
[24] O. Sucharda, V. Bilek, P. Mateckova, L. Pazdera, AAM for Structure Beams and Analysis of Beam without Shear Reinforcement, Solid State Phenomena 292 (2019) 3-8.
[25] E.O.L. Lantsoght, C. van der Veen, A. de Boer, Proposal for the fatigue strength of concrete under cycles of compression, Construction and Building Materials 107 (2016) 138-156.

[26] M.K. Lee, B.I.G. Barr, An overview of the fatigue behaviour of plain and fibre reinforced concrete, Cement and Concrete Composites 26(4) (2004) 299-305.
[27] S. Korte, V. Boel, W. De Corte, G. De Schutter, Behaviour of fatigue loaded self-compacting concrete compared to vibrated concrete, Structural Concrete 15(4) (2014) 575-589.
[28] C. Gaedicke, J. Roesler, S. Shah, Fatigue crack growth prediction in concrete slabs, International Journal of Fatigue 31(8) (2009) 1309-1317.
[29] R. François, S. Laurens, F. Deby, Corrosion and its Consequences for Reinforced Concrete Structures, ISTE Press - Elsevier2018.
[30] S. Bhalla, N. Kaur, Prognosis of low-strain fatigue induced damage in reinforced concrete structures using embedded piezo-transducers, International Journal of Fatigue 113 (2018) 98-112.
[31] A. Baktheer, J. Hegger, R. Chudoba, Enhanced assessment rule for concrete fatigue under compression considering the nonlinear effect of loading sequence, International Journal of Fatigue 126 (2019) 130-142.
[32] M. Fernández Ruiz, A. Muttoni, J. Sagaseta, Shear strength of concrete members without transverse reinforcement: A mechanical approach to consistently account for size and strain effects, Engineering Structures 99 (2015) 360-372.
[33] F. Cavagnis, M. Fernández Ruiz, A. Muttoni, Shear failures in reinforced concrete members without transverse reinforcement: An analysis of the critical shear crack development on the basis of test results, Engineering Structures 103 (2015) 157-173.
[34] F. Cavagnis, M. Fernández Ruiz, A. Muttoni, A mechanical model for failures in shear of members without transverse reinforcement based on development of a critical shear crack, Engineering Structures 157 (2018) 300-315.
[35] P. Huber, T. Huber, J. Kollegger, Investigation of the shear behavior of RC beams on the basis of measured crack kinematics, Engineering Structures 113 (2016) 41-58.
[36] A.S. Genikomsou, M.A. Polak, Finite element analysis of punching shear of concrete slabs using damaged plasticity model in ABAQUS, Engineering Structures 98 (2015) 38-48.
[37] A.S. Genikomsou, M.A. Polak, 3D finite element investigation of the compressive membrane action effect in reinforced concrete flat slabs, Engineering Structures 136 (2017) 233-244.
[38] Z.-H. Lu, Y.-G. Zhao, Z.-W. Yu, F.-X. Ding, Probabilistic evaluation of initiation time in RC bridge beams with load-induced cracks exposed to de-icing salts, Cement and Concrete Research 41(3) (2011) 365-372.
[39] M.G. Stewart, D.V. Rosowsky, Time-dependent reliability of deteriorating reinforced concrete bridge decks, Structural Safety 20(1) (1998) 91-109.
[40] B. Teplý, M. Chromá, P. Rovnaník, Durability assessment of concrete structures: reinforcement depassivation due to carbonation, Structure and Infrastructure Engineering 6(3) (2010) 317-327.
[41] B. Teplý, D. Vorechovská, Reinforcement Corrosion: Limit States, Reliability and Modelling, Journal of Advanced Concrete Technology 10(11) (2012) 353-362.
[42] F. Fanous, H. Wu, Performance of Coated Reinforcing Bars in Cracked Bridge Decks, Journal of Bridge Engineering 10(3) (2005) 255-261.
[43] M. Kušter Marić, J. Ožbolt, G. Balabanić, Reinforced concrete bridge exposed to extreme maritime environmental conditions and mechanical damage: Measurements and numerical simulation, Engineering Structures 205 (2020) 110078.
[44] L. Yu, R. François, V.H. Dang, V. L'Hostis, R. Gagné, Structural performance of RC beams damaged by natural corrosion under sustained loading in a chloride environment, Engineering Structures 96 (2015) 30-40.
[45] A. Neville, Chloride attack of reinforced concrete: an overview, Materials and Structures 28(2) (1995) 63-70.
[46] Y. Cao, C. Gehlen, U. Angst, L. Wang, Z. Wang, Y. Yao, Critical chloride content in reinforced concrete — An updated review considering Chinese experience, Cement and Concrete Research 117 (2019) 58-68.
[47] P. Grassl, T. Davies, Lattice modelling of corrosion induced cracking and bond in reinforced concrete, Cement and Concrete Composites 33(9) (2011) 918-924.

[48] Z. Pan, A. Chen, X. Ruan, Spatial variability of chloride and its influence on thickness of concrete cover: A two-dimensional mesoscopic numerical research, Engineering Structures 95 (2015) 154-169.
[49] Z. Amalia, D. Qiao, H. Nakamura, T. Miura, Y. Yamamoto, Development of simulation method of concrete cracking behavior and corrosion products movement due to rebar corrosion, Construction and Building Materials 190 (2018) 560-572.
[50] G. Pijaudier-Cabot, F. Dufour, M. Choinska, Damage and Permeability in Quasi-brittle Materials: from Diffuse to Localized Properties, Wiley Online Library (2010) 277-292.
[51] X. Cheng, Q. Su, F. Ma, X. Liu, X. Liang, Investigation on crack propagation of concrete cover induced by non-uniform corrosion of multiple rebars, Engineering Fracture Mechanics 201 (2018) 366-384.
[52] A. Boddy, R.D. Hooton, K.A. Gruber, Long-term testing of the chloride-penetration resistance of concrete containing high-reactivity metakaolin, Cement and Concrete Research 31(5) (2001) 759-765.
[53] A. Noushini, A. Castel, J. Aldred, A. Rawal, Chloride diffusion resistance and chloride binding capacity of fly ash-based geopolymer concrete, Cement and Concrete Composites 105 (2020) 103290.
[54] X. Hu, C. Shi, Q. Yuan, J. Zhang, G. De Schutter, Changes of pore structure and chloride content in cement pastes after pore solution expression, Cement and Concrete Composites 106 (2020) 103465.
[55] Y. Sakai, Relationship between pore structure and chloride diffusion in cementitious materials, Construction and Building Materials 229 (2019) 116868.
[56] N. Otsuki, S. Nagataki, K. Nakashita, Evaluation of the AgNO3 solution spray method for measurement of chloride penetration into hardened cementitious matrix materials, Construction and Building Materials 7(4) (1993) 195-201.
[57] M.-Y. Kim, E.-I. Yang, S.-T. Yi, Application of the colorimetric method to chloride diffusion evaluation in concrete structures, Construction and Building Materials 41 (2013) 239-245.
[58] E. Cavaco, R. Pimenta, J. Valença, A new method for corrosion assessment of reinforcing bars based on close-range photogrammetry: Experimental validation, Structural Concrete 20(3) (2019) 996-1009.
[59] F. He, C. Shi, Q. Yuan, X. An, B. Tong, Calculation of chloride concentration at color change boundary of AgNO3 colorimetric measurement, Cement and Concrete Research 41(11) (2011) 1095-1103.
[60] NT BUILD 443 Concrete, hardened: Accelerated chloride penetration., NORDTEST, Espoo, Finland, 1995.
[61] NT BUILD 492 Concrete, mortar and cement-based repair materials:, Chloride migration coefficient from non-steady-state migration experiments, NORDTEST, Espoo, Finland, 1999.
[62] AASHTO T277-93. Electrical Indication of Concrete's Ability to Resist Chloride, Washington, DC, USA, (1993).
[63] AASHTO T259-02. Standard Method of Test for Resistance of Concrete to Chloride Ion Penetration, Washington, DC, USA, (2002).
[64] ASTM C-1421-01b 2001 . Standard Test Methods for Determination of Fracture Toughness of Advanced Ceramics at Ambient Temperature.
[65] D.P. Bentz, J.R. Clifton, K. A. Snyder, Predicting Service Life Of Chloride-Exposed Steel-Reinforced Concrete, Concrete International 18(12) (1996) 42-47.
[66] F.H. Wittmann, K. Rokugo, E. Brühwiler, H. Mihashi, P. Simonin, Fracture energy and strain softening of concrete as determined by means of compact tension specimens, Materials and Structures 21(1) (1988) 21-32.
[67] Rilem Recommendation, Determination of the fracture energy of mortar and concrete by means of three-point bend tests on notched beams, Materials and structures 18(106) (1985) 285-290.
[68] EN 12390-5 Testing hardened concrete Part 5: Flexural strength of test specimenes, European Committee for Standardization, (2009).
[69] H. Linsbauer, E. Tschegg, Fracture energy determination of concrete with cube-shaped specimens, Zement und Beton 31(1) (1986) 38-40.

[70] E. Brühwiler, F.H. Wittmann, The wedge splitting test, a new method of performing stable fracture mechanics tests, Engineering Fracture Mechanics 35(1) (1990) 117 - 125.
[71] S. Seitl, V. Veselý, L. Řoutil, Two-parameter fracture mechanical analysis of a near-crack-tip stress field in wedge splitting test specimens, Computers and Structures 89(21-22) (2011) 1852-1858.
[72] S. Seitl, B. Nieto García, I. Merta, Wedge splitting test method: Quantification of influence of glued marble plates by two-parameter fracture mechanics, Frattura ed Integrita Strutturale 30 (2014) 174-181.
[73] L. Malíková, V. Veselý, S. Seitl, Estimation of the crack propagation direction in a mixed-mode geometry via multi-parameter fracture criteria, Frattura ed Integrità Strutturale (33) (2015) 25.
[74] L. Malíková, V. Veselý, S. Seitl, Crack propagation direction in a mixed mode geometry estimated via multi-parameter fracture criteria, International Journal of Fatigue 89(Supplement C) (2016) 99-107.
[75] M.R.M. Aliha, M.R. Ayatollahi, B. Kharazi, Mode II Brittle Fracture Assessment Using ASFPB Specimen, International Journal of Fracture 159(2) (2009) 241.
[76] J.C. Gálvez, M. Elices, G.V. Guinea, J. Planas, Mixed Mode Fracture of Concrete under Proportional and Nonproportional Loading, International Journal of Fracture 94(3) (1998) 267-284.
[77] D.A. Cendón Franco, J.C. Gálvez Ruiz, M. Elices Calafat, The double-edge notched specimen (DENS) applied to study the fracture of concrete under shear loading: experimental approach, ACHE 54(227).
[78] Y.S. Jenq, S.P. Shah, Mixed-mode fracture of concrete, International Journal of Fracture 38(2) (1988) 123-142.
[79] P. Bocca, A. Carpinteri, S. Valente, Mixed mode fracture of concrete, International Journal of Solids and Structures 27(9) (1991) 1139-1153.
[80] A. Carpinteri, S. Valente, G. Ferrara, G. Melchiorrl, Is mode II fracture energy a real material property?, Computers & Structures 48(3) (1993) 397-413.
[81] Q. Lin, H. Yuan, L. Biolzi, J.F. Labuz, Opening and mixed mode fracture processes in a quasi-brittle material via digital imaging, Engineering Fracture Mechanics 131 (2014) 176-193.
[82] Q. Lin, D. Mao, S. Wang, S. Li, The influences of mode II loading on fracture process in rock using acoustic emission energy, Engineering Fracture Mechanics 194 (2018) 136-144.
[83] W. Dong, Z. Wu, X. Tang, X. Zhou, A comparative study on stress intensity factor-based criteria for the prediction of mixed mode I-II crack propagation in concrete, Engineering Fracture Mechanics 197 (2018) 217-235.
[84] W. Dong, Z. Wu, X. Zhou, L. Dong, G. Kastiukas, FPZ evolution of mixed mode fracture in concrete: Experimental and numerical, Engineering Failure Analysis 75 (2017) 54-70.
[85] D. Li, L.N.Y. Wong, The Brazilian Disc Test for Rock Mechanics Applications: Review and New Insights, Rock Mechanics and Rock Engineering 46(2) (2013) 269-287.
[86] C. Atkinson, R.E. Smelser, J. Sanchez, Combined mode fracture via the cracked Brazilian disk test, International Journal of Fracture 18(4) (1982) 279-291.
[87] M. Abshirini, N. Soltani, P. Marashizadeh, On the mode I fracture analysis of cracked Brazilian disc using a digital image correlation method, Optics and Lasers in Engineering 78 (2016) 99-105.
[88] M.R. Ayatollahi, M.R.M. Aliha, Cracked Brazilian disc specimen subjected to mode II deformation, Engineering Fracture Mechanics 72(4) (2005) 493-503.
[89] M.R.M. Aliha, M.R. Ayatollahi, Rock fracture toughness study using cracked chevron notched Brazilian disc specimen under pure modes I and II loading – A statistical approach, Theoretical and Applied Fracture Mechanics 69 (2014) 17-25.
[90] M. Aliha M. R, R. Ayatollahi M, Brittle fracture evaluation of a fine grain cement mortar in combined tensile-shear deformation, Fatigue & Fracture of Engineering Materials & Structures 32(12) (2009) 987-994.
[91] M.R.M. Aliha, M.R. Ayatollahi, J. Akbardoost, Typical Upper Bound–Lower Bound Mixed Mode Fracture Resistance Envelopes for Rock Material, Rock Mechanics and Rock Engineering 45(1) (2012) 65-74.

[92] M. Fakhri, E. Amoosoltani, M.R.M. Aliha, Crack behavior analysis of roller compacted concrete mixtures containing reclaimed asphalt pavement and crumb rubber, Engineering Fracture Mechanics 180 (2017) 43-59.
[93] M. Mirsayar, X. Shi, D. Zollinger, Evaluation of interfacial bond strength between Portland cement concrete and asphalt concrete layers using bi-material SCB test specimen, Engineering Solid Mechanics 5(4) (2017) 293-306.
[94] A.O. Olubanwo, J.N. Karadelis, M. Saidani, M. Khorami, S.J. Abbey, Investigation of intrinsic de-bonding in bonded concrete overlays: Material characterisation and numerical Study, Engineering Solid Mechanics 6(2) (2018) 155-174.
[95] M.R.M. Aliha, M.R. Ayatollahi, Two-parameter fracture analysis of SCB rock specimen under mixed mode loading, Engineering Fracture Mechanics 103 (2013) 115-123.
[96] J. Akbardoost, M.R. Ayatollahi, M.R.M. Aliha, M.J. Pavier, D.J. Smith, Size-dependent fracture behavior of Guiting limestone under mixed mode loading, International Journal of Rock Mechanics and Mining Sciences 71 (2014) 369-380.
[97] M.R.M. Aliha, M.R. Ayatollahi, Mixed mode I/II brittle fracture evaluation of marble using SCB specimen, Procedia Engineering 10 (2011) 311-318.
[98] Z. Huang, Y. Tu, S. Meng, C. Sabau, C. Popescu, G. Sas, Experimental study on shear deformation of reinforced concrete beams using digital image correlation, Engineering Structures 181 (2019) 670-698.
[99] C. Hou, Z. Wang, W. Liang, J. Li, Determination of fracture parameters in center cracked circular discs of concrete under diametral loading: A numerical analysis and experimental results, Theoretical and Applied Fracture Mechanics 85 (2016) 355-366.
[100] S. Seitl, P. Miarka, V. Bílek, The Mixed-Mode Fracture Resistance of C 50/60 and its Suitability for Use in Precast Elements as Determined by the Brazilian Disc Test and Three-Point Bending Specimens, Theoretical and Applied Fracture Mechanics (2018).
[101] V. Veselý, P. Konečný, P. Lehner, Influence of crack propagation on electrical resistivity and ultrasonic characteristics of normal concrete assessed by sequential TPB fracture test, Theoretical and Applied Fracture Mechanics 80 (2015) 2-13.
[102] D. Chen, S. Mahadevan, Chloride-induced reinforcement corrosion and concrete cracking simulation, Cement and Concrete Composites 30(3) (2008) 227-238.
[103] M. Moazzami, M.R. Ayatollahi, H.R. Chamani, M. Guagliano, L. Vergani, Determination of higher order stress terms in cracked Brazilian disc specimen under mode I loading using digital image correlation technique, Optics & Laser Technology 107 (2018) 344-352.
[104] A.A. Griffith, G.I. Taylor, VI. The phenomena of rupture and flow in solids, Philosophical Transactions of the Royal Society of London. Series A, Containing Papers of a Mathematical or Physical Character 221(582-593) (1921) 163-198.
[105] C.E. Inglis, Stresses in a plate due to the presence of cracks and sharp corners, Trans Inst Naval Archit 55 (1913) 219-241.
[106] G.R. Irwin, Analysis of stresses and strains near the end of a crack traversing a plate, Journal of Applied Mechanics 24 (1957) 361-364.
[107] M.L. Williams, On the Stress Distribution at the Base of a Stationary Crack, Journal of Applied Mechanics 24(1) (1956) 6.
[108] M. Williams, The bending stress distribution at the base of a stationary crack, J Appl Mech 24 (1957) 109-14.
[109] G.R. Irwin, Plastic Zone Near a Crack and Fracture Toughness., Sagamore Research Conference, 1961, pp. 63-78.
[110] D.S. Dugdale, Yielding of steel sheets containing slits, Journal of the Mechanics and Physics of Solids 8(2) (1960) 100-104.
[111] G.I. Barenblatt, The Mathematical Theory of Equilibrium Cracks in Brittle Fracture, Advances in Applied Mechanics, Elsevier1962, pp. 55-129.
[112] M.F. Kaplan, Crack propagation and the fracture of concrete, pp. 591-610.
[113] J.R. Rice, A Path Independent Integral and the Approximate Analysis of Strain Concentration by Notches and Cracks, Journal of Applied Mechanics 35(2) (1968) 379-386.
[114] J.W. Hutchinson, Singular behaviour at the end of a tensile crack in a hardening material, Journal of the Mechanics and Physics of Solids 16(1) (1968) 13-31.

[115] J.R. Rice, G.F. Rosengren, Plane strain deformation near a crack tip in a power-law hardening material, Journal of the Mechanics and Physics of Solids 16(1) (1968) 1-12.
[116] L.P. Pook, Linear Elastic Fracture Mechanics for Engineers: Theory and Applications, WIT Press2000.
[117] T.L. Anderson, Fracture mechanics: fundamentals and applications, CRC press2017.
[118] C.-T. Sun, Fracture Mechanics, Academic Press2011.
[119] P. Paris, F. Erdogan, A Critical Analysis of Crack Propagation Laws, Journal of Basic Engineering 85(4) (1963) 528-533.
[120] Z.Z. Du, J.W. Hancock, The effect of non-singular stresses on crack-tip constraint, Journal of the Mechanics and Physics of Solids 39(4) (1991) 555-567.
[121] P. Hutař, S. Seitl, Z. Knésl, Quantification of the effect of specimen geometry on the fatigue crack growth response by two-parameter fracture mechanics, Materials Science and Engineering: A 387-389 (2004) 491-494.
[122] P. Hutař, S. Seitl, Z. Knésl, Effect of constraint on fatigue crack propagation near threshold in medium carbon steel, Computational Materials Science 37(1) (2006) 51-57.
[123] P. Miarka, A.S. Cruces, S. Seitl, L. Malíková, P. Lopez-Crespo, Influence of the constraint effect on the fatigue crack growth rate in S355 J2 steel using digital image correlation, Fatigue & Fracture of Engineering Materials & Structures n/a(n/a) (2020).
[124] M. Gupta, R.C. Alderliesten, R. Benedictus, A review of T-stress and its effects in fracture mechanics, Engineering Fracture Mechanics 134 (2015) 218-241.
[125] A.P. Kfouri, Some evaluations of the elastic T-term using Eshelby's method, International Journal of Fracture 30(4) (1986) 301-315.
[126] B. Yang, K. Ravi-Chandar, Evaluation of elastic T-stress by the stress difference method, Engineering Fracture Mechanics 64(5) (1999) 589-605.
[127] P.S. Leevers, J.C. Radon, Inherent stress biaxiality in various fracture specimen geometries, International Journal of Fracture 19(4) (1982) 311-325.
[128] Z. Knésl, K. Bednář, Two parameter fracture mechanics: calculation of parameters and their values, IPM of AS of Czech Republic, (1997).

[129] T. Fett, Stress intensity factors and T-stress for internally cracked circular disks under various boundary conditions, Engineering Fracture Mechanics 68(9) (2001) 1119-1136.
[130] M.R. Ayatollahi, M. Nejati, An over-deterministic method for calculation of coefficients of crack tip asymptotic field from finite element analysis, Fatigue & Fracture of Engineering Materials & Structures 34(3) (2011) 159-176.
[131] L.P. Pook, Crack Paths, WIT Press (2002).
[132] F. Erdogan, G.C. Sih, On the Crack Extension in Plates Under Plane Loading and Transverse Shear, Journal of Basic Engineering 85(4) (1963) 519-525.
[133] G.C. Sih, Strain-energy-density factor applied to mixed mode crack problems, International Journal of Fracture 10(3) (1974) 305-321.
[134] J. Qian, A. Fatemi, Mixed mode fatigue crack growth: A literature survey, Engineering Fracture Mechanics 55(6) (1996) 969-990.
[135] M.R. Ayatollahi, M. Rashidi Moghaddam, F. Berto, A generalized strain energy density criterion for mixed mode fracture analysis in brittle and quasi-brittle materials, Theoretical and Applied Fracture Mechanics 79 (2015) 70-76.
[136] M.R. Ayatollahi, M. Rashidi Moghaddam, F. Berto, T-stress effects on fatigue crack growth – Theory and experiment, Engineering Fracture Mechanics 187 (2018) 103-114.
[137] P. Lazzarin, R. Zambardi, A finite-volume-energy based approach to predict the static and fatigue behavior of components with sharp V-shaped notches, International Journal of Fracture 112(3) (2001) 275-298.
[138] M.R.M. Aliha, F. Berto, A. Mousavi, S.M.J. Razavi, On the applicability of ASED criterion for predicting mixed mode I+II fracture toughness results of a rock material, Theoretical and Applied Fracture Mechanics 92 (2017) 198-204.
[139] M.R.M. Aliha, F. Berto, A. Bahmani, P. Gallo, Mixed mode I/II fracture investigation of Perspex based on the averaged strain energy density criterion, Physical Mesomechanics 20(2) (2017) 149-156.

[140] M.M. Mirsayar, Mixed mode fracture analysis using extended maximum tangential strain criterion, Materials & Design 86 (2015) 941-947.
[141] M.M. Mirsayar, F. Berto, M.R.M. Aliha, P. Park, Strain-based criteria for mixed-mode fracture of polycrystalline graphite, Engineering Fracture Mechanics 156 (2016) 114-123.
[142] M.M. Mirsayar, A. Razmi, M.R.M. Aliha, F. Berto, EMTSN criterion for evaluating mixed mode I/II crack propagation in rock materials, Engineering Fracture Mechanics 190 (2018) 186-197.
[143] D.J. Smith, M.R. Ayatollahi, M.J. Pavier, The role of T-stress in brittle fracture for linear elastic materials under mixed-mode loading, Fatigue & Fracture of Engineering Materials & Structures 24(2) (2001) 137--150.
[144] M.R. Ayatollahi, M.R.M. Aliha, On the use of Brazilian disc specimen for calculating mixed mode I-II fracture toughness of rock materials, Engineering Fracture Mechanics 75(16) (2008) 4631-4641.
[145] Y.G. Matvienko, Maximum Average Tangential Stress Criterion for Prediction of the Crack Path, International Journal of Fracture 176(1) (2012) 113-118.
[146] J. Klusák, O. Krepl, T. Profant, An easy and engineering stability criterion of general singular stress concentrators, Theoretical and Applied Fracture Mechanics 104 (2019) 102341.
[147] J. Klusák, Z. Knésl, Reliability assessment of a bi-material notch: Strain energy density factor approach, Theoretical and Applied Fracture Mechanics 53(2) (2010) 89-93.
[148] A. Hillerborg, The theoretical basis of a method to determine the fracture energyG F of concrete, Materials and Structures 18(4) (1985) 291-296.
[149] J.P. Zdenek P. Bazant, Fracture and Size Effect in Concrete and Other Quasibrittle Materials, Taylor & Francis2019.
[150] M.R. Ayatollahi, M. Nejati, Experimental evaluation of stress field around the sharp notches using photoelasticity, Materials & Design 32(2) (2011) 561-569.
[151] B.L. Karihaloo, Size effect in shallow and deep notched quasi-brittle structures, Fracture Scaling, Springer, Dordrecht, The Netherlands, (1999), pp. 379-390.
[152] M.R. Ayatollahi, J. Akbardoost, Size effects on fracture toughness of quasi-brittle materials – A new approach, Engineering Fracture Mechanics 92 (2012) 89-100.
[153] R.J. Sanford, J.W. Dally, A general method for determining mixed-mode stress intensity factors from isochromatic fringe patterns, Engineering Fracture Mechanics 11(4) (1979) 621-633.
[154] H. Tada, P.C. Paris, G.R. Irwin, American Society of Mechanical Engineers., ASM International., The stress analysis of cracks handbook, 3rd ed., ASME Press : Professional Engineering Pub. : ASM International, New York, 2000.
[155] Z.P. Bažant, Mechanics of fracture and progressive cracking in concrete structures, Fracture mechanics of concrete: Structural application and numerical calculation, Springer, Dordrecht, The Netherlands, 1985, pp. 1-94.
[156] H.T. Nguyen, M. Pathirage, G. Cusatis, Z.P. Bažant, Gap Test of Crack-Parallel Stress Effect on Quasibrittle Fracture and Its Consequences, Journal of Applied Mechanics 87(7) (2020).
[157] Z.P. Bažant, Concrete fracture models: testing and practice, Engineering Fracture Mechanics 69(2) (2002) 165-205.
[158] L. Cedolin, G. Cusatis, Identification of concrete fracture parameters through size effect experiments, Cement and Concrete Composites 30(9) (2008) 788-797.
[159] H. Mihashi, N. Nomura, S. Niiseki, Influence of aggregate size on fracture process zone of concrete detected with three dimensional acoustic emission technique, Cement and Concrete Research 21(5) (1991) 737-744.
[160] S. Mindess, S. Diamond, A preliminary SEM study of crack propagation in mortar, Cement and Concrete Research 10(4) (1980) 509-519.
[161] L. Cedolin, S. Dei Poli, I. Iori, Experimental determination of the fracture process zone in concrete, Cement and Concrete Research 13(4) (1983) 557-567.
[162] Y.-S. Jenq, S.P. Shah, Features of mechanics of quasi-brittle crack propagation in concrete, International Journal of Fracture 51(2) (1991) 103-120.
[163] Z.P. Bažant, Size Effect in Blunt Fracture: Concrete, Rock, Metal, Journal of Engineering Mechanics 110(4) (1984) 518-535.

[164] S. Burtscher, B. Chiaia, J.P. Dempsey, G. Ferro, V.S. Gopalaratnam, P. Prat, K. Rokugo, V.E. Saouma, V. Slowik, L. Vitek, K. Willam, RILEM TC QFS 'quasibrittle fracture scaling and size effect'-final report, Materials and Structures 37(8) (2004) 547-568.
[165] Z.P. Bažant, Size effect, International Journal of Solids and Structures 37(1) (2000) 69-80.
[166] M. Elices, J. Planas, Fracture mechanics parameters of concrete: An overview, Advanced Cement Based Materials 4(3) (1996) 116-127.
[167] C. Carloni, M. Santandrea, R. Wendner, An investigation on the "width and size effect" in the evaluation of the fracture energy of concrete, Procedia Structural Integrity 3 (2017) 450-458.
[168] C. Carloni, M. Santandrea, G. Baietti, Influence of the width of the specimen on the fracture response of concrete notched beams, Engineering Fracture Mechanics 216 (2019) 106465.
[169] G.V. Guinea, M. Elices, J. Planas, Stress intensity factors for wedge-splitting geometry, International Journal of Fracture 81(2) (1996) 113-124.
[170] H. Cifuentes, M. Lozano, T. Holušová, F. Medina, S. Seitl, A. Fernández-Canteli, Modified Disk-Shaped Compact Tension Test for Measuring Concrete Fracture Properties, International Journal of Concrete Structures and Materials 11(2) (2017) 215-228.
[171] S. Khalilpour, E. BaniAsad, M. Dehestani, A review on concrete fracture energy and effective parameters, Cement and Concrete Research 120 (2019) 294-321.
[172] G.V. Guinea, J. Planas, M. Elices, Measurement of the fracture energy using three-point bend tests: Part 1—Influence of experimental procedures, Materials and Structures 25(4) (1992) 212-218.
[173] J. Planas, M. Elices, G.V. Guinea, Measurement of the fracture energy using three-point bend tests: Part 2—Influence of bulk energy dissipation, Materials and Structures 25(5) (1992) 305-312.
[174] A. Ramachandra Murthy, B.L. Karihaloo, N.R. Iyer, B.K. Raghu Prasad, Bilinear tension softening diagrams of concrete mixes corresponding to their size-independent specific fracture energy, Construction and Building Materials 47 (2013) 1160-1166.
[175] P. Miarka, L. Pan, V. Bílek, S. Seitl, H. Cifuentés, Influence of the chevron notch type on the values of fracture energy evaluated on alkali-activated concrete, Engineering Fracture Mechanics 236 (2020) 107209.
[176] M.R.M. Aliha, E. Mahdavi, M.R. Ayatollahi, Statistical Analysis of Rock Fracture Toughness Data Obtained from Different Chevron Notched and Straight Cracked Mode I Specimens, Rock Mechanics and Rock Engineering 51(7) (2018) 2095-2114.
[177] M.-D. Wei, F. Dai, N.-W. Xu, Y. Liu, T. Zhao, A novel chevron notched short rod bend method for measuring the mode I fracture toughness of rocks, Engineering Fracture Mechanics 190 (2018) 1-15.
[178] H. Zielke, M. Abendroth, M. Kuna, B. Kiefer, Determining the fracture toughness of ceramic filter materials using the miniaturized chevron-notched beam method at high temperature, Ceramics International 44(12) (2018) 13986-13993.
[179] DIN EN 14425-3 2010. Advanced technical ceramics - Test methods for determination of fracture toughness of monolithic ceramics - Part 3: chevron notched beam (CNB) method.
[180] H.G. Tattersall, G. Tappin, The work of fracture and its measurement in metals, ceramics and other materials, Journal of Materials Science 1(3) (1966) 296-301.
[181] S.-X. Wu, Fracture toughness determination of bearing steel using chevron-notch three point bend specimen, Engineering Fracture Mechanics 19(2) (1984) 221-232.
[182] A.M. Calomino, L.J. Ghosn, Optimum notch configurations for the chevron-notched four-point bend specimens, International Journal of Fracture 72(4) (1995) 311-326.
[183] D.G. Munz, J.L. Shannon, R.T. Bubsey, Fracture toughness calculation from maximum load in four point bend tests of chevron notch specimens, International Journal of Fracture 16(3) (1980) R137-R141.
[184] D. Munz, R.T. Bubsey, J.E. Srawley, Compliance and stress intensity coefficients for short bar specimens with chevron notches, International Journal of Fracture 16(4) (1980) 359-374.
[185] D. Munz, R.T. Bubsey, J.L. Shannon, Fracture Toughness Determination of A12O3 Using Four-Point-Bend Specimens with Straight-Through and Chevron Notches, Journal of the American Ceramic Society 63(5-6) (1980) 300-305.

[186] X.Z. Hu, F.H. Wittmann, Fracture energy and fracture process zone, Materials and Structures 25(6) (1992) 319-326.
[187] X. Hu, K. Duan, Influence of fracture process zone height on fracture energy of concrete, Cement and Concrete Research 34(8) (2004) 1321-1330.
[188] H.M. Abdalla, B.L. Karihaloo, A method for constructing the bilinear tension softening diagram of concrete corresponding to its true fracture energy, Magazine of Concrete Research (2004).
[189] S. Muralidhara, B.K.R. Prasad, H. Eskandari, B.L. Karihaloo, Fracture process zone size and true fracture energy of concrete using acoustic emission, Construction and Building Materials 24(4) (2010) 479-486.
[190] Y. Jenq, S.P. Shah, Two parameter fracture model for concrete, Journal of engineering mechanics 111(10) (1985) 1227-1241.
[191] A. Hillerborg, M. Modéer, P.E. Petersson, Analysis of crack formation and crack growth in concrete by means of fracture mechanics and finite elements, Cement and Concrete Research 6(6) (1976) 773-781.
[192] P.E. Petersson, Fracture energy of concrete: Practical performance and experimental results, Cement and Concrete Research 10(1) (1980) 91-101.
[193] D.A. Hordijk, Local approach to fatigue of concrete, Civil Engineering and Geosciences, Technical university Delft, Delft, Netherlands, 1991, p. 208.
[194] Z.P. Bažant, B.H. Oh, Crack band theory for fracture of concrete, Matériaux et Construction 16(3) (1983) 155-177.
[195] Abaqus, Analysis User's Manual 6.14, Dassault Systemes Simulia Corp., (2011).
[196] J. Lubliner, J. Oliver, S. Oller, E. Oñate, A plastic-damage model for concrete, International Journal of Solids and Structures 25(3) (1989) 299-326.
[197] J. Lee, L. Fenves Gregory, Plastic-Damage Model for Cyclic Loading of Concrete Structures, Journal of Engineering Mechanics 124(8) (1998) 892-900.
[198] P. Kmiecik, M. KamiŃSki, Modelling of reinforced concrete structures and composite structures with concrete strength degradation taken into consideration, Archives of Civil and Mechanical Engineering 11(3) (2011) 623-636.
[199] T. Jankowiak, T. Lodygowski, Identification of parameters of concrete damage plasticity constitutive model, Foundations of civil and environmental engineering 6(1) (2005) 53-69.
[200] G. Duvaut, J.L. Lions, Inequalities in mechanics and physics, Springer-Verlag, Berlin Heidelberg New York, 1976.
[201] J. Mazars, G. Pijaudier-Cabot, Continuum Damage Theory—Application to Concrete, Journal of Engineering Mechanics 115(2) (1989) 345-365.
[202] P. Grassl, M. Jirásek, Plastic model with non-local damage applied to concrete, International Journal for Numerical and Analytical Methods in Geomechanics 30(1) (2006) 71-90.
[203] P. Grassl, D. Xenos, U. Nyström, R. Rempling, K. Gylltoft, CDPM2: A damage-plasticity approach to modelling the failure of concrete, International Journal of Solids and Structures 50(24) (2013) 3805-3816.
[204] F. Dufour, G. Pijaudier-Cabot, M. Choinska, A. Huerta, Extraction of a crack opening from a continuous approach using regularized damage models, Computers & Concrete 5(4) (2008) 375-388.
[205] G. Pijaudier-Cabot, P. Bažant Zdeněk, Nonlocal Damage Theory, Journal of Engineering Mechanics 113(10) (1987) 1512-1533.
[206] R.H.J. Peerlings, M.G.D. Geers, R. de Borst, W.A.M. Brekelmans, A critical comparison of nonlocal and gradient-enhanced softening continua, International Journal of Solids and Structures 38(44) (2001) 7723-7746.
[207] E.C.f. Standardization, Testing fresh concrete, Part 5: Flow table test, European Committee for Standardization, 2009.
[208] S. Seitl, P. Miarka, V. Bílek, The mixed-mode fracture resistance of C 50/60 and its suitability for use in precast elements as determined by the Brazilian disc test and three-point bending specimens, Theoretical and Applied Fracture Mechanics 97 (2018) 108-119.

[209] F. Pacheco-Torgal, J.A. Labrincha, C. Leonelli, A. Palomo, P. Chindaprasirt, Handbook of Alkali-Activated Cements, Mortars and Concretes, Woodhead Publishing2015.
[210] V. Bilek, T. Opravil, F. Soukal, Searching for practically applicable alkali-activated concretes, in: C.S.a.X. Shen (Ed.) First International Conference on Advances in Chemically-Activated Materials CAM'2010, 2010, pp. 28-35.
[211] V. Bilek, J. Hurta, P. Done, L. Zidek, Development of alkali-activated concrete for structures – Mechanical properties and durability, Perspectives in Science 7(Supplement C) (2016) 190-194.
[212] H. Szklorzova, V. Bilek, Influence of alkali ions in the activator on the performance of alkali-activated mortars, in: B.a. Kersner (Ed.) 3rd International symposium Nontraditional cement and concrete composites, Brno, 2003, pp. 777-784.
[213] G. Fang, W.K. Ho, W. Tu, M. Zhang, Workability and mechanical properties of alkali-activated fly ash-slag concrete cured at ambient temperature, Construction and Building Materials 172 (2018) 476-487.
[214] B.-w. Jo, S.-k. Park, J.-b. Park, Properties of concrete made with alkali-activated fly ash lightweight aggregate (AFLA), Cement and Concrete Composites 29(2) (2007) 128-135.
[215] F. Dai, M.D. Wei, N.W. Xu, Y. Ma, D.S. Yang, Numerical Assessment of the Progressive Rock Fracture Mechanism of Cracked Chevron Notched Brazilian Disc Specimens, Rock Mechanics and Rock Engineering 48(2) (2015) 463-479.
[216] M. Aliha, R., M.,, E. Mahdavi, M. Ayatollahi, R.,, The Influence of Specimen Type on Tensile Fracture Toughness of Rock Materials, Pure and Applied Geophysics 174(3) (2017) 1237-1253.
[217] M.R. Ayatollahi, M.R.M. Aliha, Wide range data for crack tip parameters in two disc-type specimens under mixed mode loading, Computational Materials Science 38(4) (2007) 660-670.
[218] B. Pan, K. Qian, H. Xie, A. Asundi, Two-dimensional digital image correlation for in-plane displacement and strain measurement: a review, Measurement Science and Technology 20(6) (2009) 062001.
[219] M.A. Sutton, J.J. Orteu, H. Schreier, Image Correlation for Shape, Motion and Deformation Measurements - Basic Concepts,Theory and Applications | Michael A. Sutton | Springer, Springer US2009.
[220] M. Mokhtarishirazabad, P. Lopez-Crespo, B. Moreno, A. Lopez-Moreno, M. Zanganeh, Optical and analytical investigation of overloads in biaxial fatigue cracks, International Journal of Fatigue 100 (2017) 583-590.
[221] P. López-Crespo, R.L. Burguete, E.A. Patterson, A. Shterenlikht, P.J. Withers, J.R. Yates, Study of a Crack at a Fastener Hole by Digital Image Correlation, Experimental Mechanics 49(4) (2009) 551-559.
[222] M. Mokhtarishirazabad, P. Lopez-Crespo, M. Zanganeh, Stress intensity factor monitoring under cyclic loading by digital image correlation, Fatigue & Fracture of Engineering Materials & Structures 41(10) (2018) 2162-2171.
[223] S. Seitl, L. Malíková, V. Růžička, B. Moreno, P. Lopez-Crespo, Williams' expansion-based approximation of the displacement field in an Al 2024 compact tension specimen reconstructed from optical measurements, Fatigue & Fracture of Engineering Materials & Structures 41(10) (2018) 2187-2196.
[224] *Vic-2D V6 Reference Manual,Correlated Solutions Incorporated (C.S.Inc)*.
[225] Matlab, version 9.10.0 (R2018a), The MathWorks Inc. (2018).
[226] P. Lopez-Crespo, A. Shterenlikht, E.A. Patterson, J.R. Yates, P.J. Withers, The stress intensity of mixed mode cracks determined by digital image correlation, Journal of Strain Analysis for Engineering Design 43(8) (2008) 769-780.
[227] P. Lopez-Crespo, A. Shterenlikht, J.R. Yates, E.A. Patterson, P.J. Withers, Some experimental observations on crack closure and crack-tip plasticity, Fatigue & Fracture of Engineering Materials & Structures 32(5) (2009) 418-429.
[228] M. Zanganeh, P. Lopez-Crespo, Y.H. Tai, J.R. Yates, Locating the Crack Tip Using Displacement Field Data: A Comparative Study, Strain 49(2) (2013) 102-115.

[229] W.-W. Ji, P.-Z. Pan, Q. Lin, X.-T. Feng, M.-P. Du, Do disk-type specimens generate a mode II fracture without confinement?, International Journal of Rock Mechanics and Mining Sciences 87 (2016) 48-54.
[230] Zoner Photo Studio 18 - Zoner Photo Studio X, 2017.
[231] V. Baroghel-Bouny, P. Belin, M. Maultzsch, D. Henry, AgNO3 spray tests: advantages, weaknesses, and various applications to quantify chloride ingress into concrete. Part 1: Non-steady-state diffusion tests and exposure to natural conditions, Materials and Structures 40(8) (2007) 759-781.
[232] V. Baroghel-Bouny, P. Belin, M. Maultzsch, D. Henry, AgNO3 spray tests: advantages, weaknesses, and various applications to quantify chloride ingress into concrete. Part 2: Non-steady-state migration tests and chloride diffusion coefficients, Materials and Structures 40(8) (2007) 783-799.
[233] F. He, C. Shi, Q. Yuan, C. Chen, K. Zheng, AgNO3-based colorimetric methods for measurement of chloride penetration in concrete, Construction and Building Materials 26(1) (2012) 1-8.
[234] *ANSYS® Academic Research Mechanical, Release 19.1*, (2018).
[235] M.R. Khosravani, M. Silani, K. Weinberg, Fracture studies of Ultra-High Performance Concrete using dynamic Brazilian tests, Theoretical and Applied Fracture Mechanics 93 (2018) 302-310.
[236] T. Zimmermann, D. Lehký, Fracture parameters of concrete C40/50 and C50/60 determined by experimental testing and numerical simulation via inverse analysis, International Journal of Fracture 192(2) (2015) 179-189.
[237] J. Oliver, A consistent characteristic length for smeared cracking models, International Journal for Numerical Methods in Engineering 28(2) (1989) 461-474.
[238] W.B. Krätzig, R. Pölling, An elasto-plastic damage model for reinforced concrete with minimum number of material parameters, Computers & Structures 82(15) (2004) 1201-1215.
[239] P. Bažant Zdeněk, G. Pijaudier-Cabot, Measurement of Characteristic Length of Nonlocal Continuum, Journal of Engineering Mechanics 115(4) (1989) 755-767.
[240] J. Akbardoost, A. Rastin, Comprehensive data for calculating the higher order terms of crack tip stress field in disk-type specimens under mixed mode loading, Theoretical and Applied Fracture Mechanics 76 (2015) 75-90.
[241] A. Wosatko, J. Pamin, M.A. Polak, Application of damage–plasticity models in finite element analysis of punching shear, Computers & Structures 151 (2015) 73-85.
[242] A. Carpinteri, Interaction between tensile strength failure and mixed mode crack propagation in concrete, Materials and Structures 21(6) (1988) 403.
[243] A. Razmi, M.M. Mirsayar, On the mixed mode I/II fracture properties of jute fiber-reinforced concrete, Construction and Building Materials 148 (2017) 512-520.
[244] L.F. Pereira, J. Weerheijm, L.J. Sluys, A numerical study on crack branching in quasi-brittle materials with a new effective rate-dependent nonlocal damage model, Engineering Fracture Mechanics 182 (2017) 689-707.
[245] M.R.M. Aliha, M.R. Ayatollahi, D.J. Smith, M.J. Pavier, Geometry and size effects on fracture trajectory in a limestone rock under mixed mode loading, Engineering Fracture Mechanics 77(11) (2010) 2200-2212.
[246] Z. Shi, M.R. Geiker, K. De Weerdt, T.A. Østnor, B. Lothenbach, F. Winnefeld, J. Skibsted, Role of calcium on chloride binding in hydrated Portland cement–metakaolin–limestone blends, Cement and Concrete Research 95 (2017) 205-216.
[247] E. Vejmelková, M. Pavlíková, M. Keppert, Z. Keršner, P. Rovnaníková, M. Ondráček, M. Sedlmajer, R. Černý, High performance concrete with Czech metakaolin: Experimental analysis of strength, toughness and durability characteristics, Construction and Building Materials 24(8) (2010) 1404-1411.
[248] X. Qian, Z. Li, The relationships between stress and strain for high-performance concrete with metakaolin, Cement and Concrete Research 31(11) (2001) 1607-1611.
[249] C.S. Poon, S.C. Kou, L. Lam, Compressive strength, chloride diffusivity and pore structure of high performance metakaolin and silica fume concrete, Construction and Building Materials 20(10) (2006) 858-865.

[250] P. Miarka, S. Seitl, V. Bílek, Mixed-mode fracture analysis in high-performance concrete using a Brazilian disc test, Materiali in Tehnologije 53(2) (2019) 233-238.

List of Abbreviations and Nomenclature

Greek Letters

α^{CDP}	constitutive parameter of the CDP material model
α	notch inclination angle (°)
α_1,α_0	relative notch ratio (-)
β^{SE}	parameter for GSED
β^{CDP}	constitutive parameter of the CDP material model
γ^{CDP}	constitutive parameter of the CDP material model
δ	displacement (mm)
ε	eccentricity (-)
ε_f	elongation (%)
ε_C	critical crack tip opening displacement expressed as strain (-)
κ	Kolosov's constant for plane strain 3 - 4ν, for plane stress (3 - ν)/(1 + ν)
ν	Poisson's ratio
μ	shear modules E/2(1 + ν) (MPa)
$\sigma_{\theta\theta}$	tangential stress (MPa)
$\sigma_{\theta\theta,C}$	critical tangential stress (MPa)
$\sigma_c\left(\varepsilon_c^{pl}\right)$	effective cohesion stresses for compression
$\sigma_c\left(\varepsilon_t^{pl}\right)$	effective cohesion stresses for tension
$\sigma_{i,j}$	stress tensor in Cartesian coordinates $i,j = x,y$ (MPa)
$\sigma_{i,j}$	stress tensor in polar coordinates $i,j = r,\theta$ (MPa)
σ_t	tensile strength (MPa)
σ_{b0}	biaxial compressive strength (MPa)
σ_y	yield tensile strength (MPa)
θ_0	crack initiation direction (°)
$\theta_{0,GMTS}$	crack initiation angle for generalised maximum tangential stress criterion (°)
$\theta_{0,MTS}$	crack initiation angle for maximum tangential stress criterion (°)
$\theta_{0,P}$	principal stress orientation angle (°)
λ_n	eigenvalues
ψ	dilation angle (°)
η	viscosity parameter (-)
r,θ	polar coordinates
$\phi(r,\theta)$	Airy function

Roman Letters

a_0	fatigue crack length (mm)
a	notch length (mm)
a_e	effective crack length (mm)
B	specimen's thickness (mm)
A_n, B_n	WE terms for mode I and mode II (-)
$C_1 - C_6$	Coefficients of the GSED criterion (-)
d_{avg}	averaging distance (mm)
d_{tot}	damage parameter (-)
d_c	damage parameter for compression (-)
d_t	damage parameter for tension (-)
d_v	damage parameter for visco-plasticity (-)
E	Young's modulus of elasticity (GPa)
E_{sec}	secant stiffness (GPa)
f_n^I, g_n^I	known shape functions for mode I (-)
f_m^{II}, g_m^{II}	known shape functions for mode II (-)
f	line load applied along the crack (kN/mm)
$f_{c,m}$	compressive strength (MPa)
f_t	tensile strength (MPa)
$F_n(\theta)$	eigenfunction
F	flow function (-)
g	aggregate size (mm)
g_f	local fracture energy (N/m)
G	energy release rate (N/m)
G_F	size independent fracture energy (N/m)
G_{IC}	fracture toughness using energetic approach (N/m)
h	band width (mm)
I_A, I_B	intensity distribution of the two digital images
l_e	element length (mm)
l_{ch}	characteristic length of the FPZ (mm)
l_t	transition length (mm)
k	plasticity number (-)
K_c	shape of yield surface (-)
K_I	stress intensity factor for mode I (MPam$^{1/2}$)
K_{II}	stress intensity factor for mode II (MPam$^{1/2}$)
K_{eff}	effective stress intensity factor (MPam$^{1/2}$)
K_{IC}^e	effective fracture toughness (MPam$^{1/2}$)
K_i^{aux}	auxiliary stress intensity factor for mode I, II
K_c	the yield surface parameter (-)
K_{IC}	fracture toughness using stress intensity approach (MPam$^{1/2}$)
n, m	number of WE terms for mode I and mode II (-)
N, M	number of WE terms for mode I and mode II used in the ODM (-)

$O_{i,j}$	higher order terms of the WE
$\bar{p}$	hydrostatic pressure (MPa)
P,P_{max}	load/force, limit load/force (kN)
P_C	critical load/force (kN)
$\bar{q}$	equivalent von Misses stress (MPa)
r_C	critical distance (mm)
R	disc's radius (mm)
ΔR	radius reduction (mm)
s_c, s_t	tensile and compressive stiffness recovery (-)
S,Σ	strain energy density factor
S_{cr},Σ_{cr}	critical strain energy density factor
t	notch thickness (mm)
T-stress	in crack plane T-stress (MPa)
t_i	time step (s)
t_{max}	total time (s)
u_X, u_Y	nodal displacement in the global coordinate system X-Y
u_x, u_y	nodal displacement in the local coordinate system x-y
Δu_x, Δu_y	the difference of nodal displacement in the local coordinate system x-y
u	horizontal displacements along the x-axis (mm)
v	vertical displacements along the y-axis (mm)
w_C	maximum/critical crack width (mm)
W	specimen's width (mm)
Y_I,Y_{II}	geometry function for mode I and mode II (-)

Abbreviations

2D	two-dimensional
3D	three-dimensional
3PB	three-point bending
4PB	four-point bending
AE	acoustic emission
AAC	Alkali-activated concrete
ASED	averaged strain energy density
BD	Brazilian disc
BDCN	Brazilian disc with central notch
BEM	boundary effect method
DIC	digital image correlation
CBM	crack band model
CC	cross-correlation
CDP	concrete damage plasticity
CINT	contour integral
CMOD	crack mouth opening displacement
CMOS	crack mouth opening sliding
CN3PB	chevron-notched three-point bending
CT	compact tension
CTOD	crack tip opening displacement
$CTOD_C$	critical tip opening displacement
DIC	digital image correlation
EA4PBT	eccentric asymmetric four-point bending test
EMTSN	extended maximum tangential strain
GBFS	granulated blast furnace slag
GMTS	generalised maximum tangential stress
GSED	generalizes strain energy density
FCM	fictious crack model
FE	finite element
FEA	finite element analysis
FMP	fracture mechanical property
FOV	field of view
FPZ	fracture process zone
HHR	Hutchinson, Rice and Rosengren solution
HO	higher order terms of the Williams' expansion
HPC	high-performance concrete
HSC	high-strength concrete
LEFM	linear elastic fracture mechanics
MATS	maximum average tangential stress
MTS	maximum tangential stress
ODM	over-deterministic method

OPC	ordinary Portland cement
ROI	region of interest
RSME	root mean square error
SBEM	simplified boundary effect
SED	strain energy density
SEL	size-effect law
SIF	stress intensity factor
SSD	sum-squared difference
WE	Williams' expansion
WST	wedge splitting test

About Author

Personal data

Petr Miarka

Institute of Structural Mechanics

Faculty of Civil Engineering

Brno University of Technology

Veveří 331/95, 602 00 Brno

Czech Republic

Email: Petr.Miarka@vut.cz

Education

Since 02/2017	Ph.D. student (4th year), Brno University of Technology, Faculty of Civil Engineering, Institute of Structural Mechanics,
01/2017	**Ing.**, Brno University of Technology, Faculty of Civil Engineering. Master thesis topic: "Numerical study of thin HPC overlays for orthotropic deck plates."
06/2014	**Bc.**, Brno University of Technology, Faculty of Civil Engineering. Bachelor's thesis topic: "Reinforced concrete staircase of apartment house - alternatives of structural design with reduction of footfall sound propagation."

Practical Experience

Since 01/2017	**Institute of Physics of Materials,** Czech Academy of Sciences, (IPM CAS), Žižkova 22, Brno – Ph.D. student
	Brno University of Technology, Faculty of Civil Engineering, **Institute of Structural Mechanics** (ISM FCE BUT) – Assistant lecturer
07-09/2015	Internship in company: **KPstatika stavby s.r.o**., Structural design and analysis

International Internships

11/2019	Research visit via mobility project of Czech Academy of Sciences at **Tohoku Institute of Technology**, Sendai Japan (prof. Hideo Koide).
02-08/2018	Traineeship via Erasmus+ mobility programme, nonlinear analysis of the fracture mechanical test of the cementitious composite, **Ghent University**, Ghent, Belgium (Assoc. prof. Wouter De Corte)
11/2017	Study internship via Freemovers+ mobility programme, fracture mechanical tests of cementitious material, **University of Seville**, Seville, Spain (Assoc. prof. Héctor Cifuentes Bulté)
09/2015 - 06/2016	Study exchange via Erasmus+ mobility programme, master thesis, **Ghent University**, Ghent, Belgium (Assoc. prof. Wouter De Corte)

Teaching Experience

Teaching basic topics from structural mechanics at FCE BUT.

BD001 – Fundamentals of Structural Mechanics

BD004 – Statics II

Since 2017 - supervision of Bachelor's and Master's thesis (currently > 8 students)

Other relevant information

Grants

Brno PhD Talent	Brno PhD Talent scholarship. **Brno city municipally and South Moravian Centre for International Mobility.**
FAST-J-20-6341	Influence of aggressive environment on the concrete's fracture mechanical parameters. **BUT Internal Grant Agency.**
FAST-J-19-5783	Analysis of the mixed-mode I/II fracture resistance of the alkali-activated concrete. **BUT Internal Grant Agency.**
FAST-J-18-5164	Evaluation of selected fracture mechanical parameters of cement-based composites under the mixed mode I/II load. **BUT Internal Grant Agency.**

Participation in Research Projects

FAST-S-20-6278	Analysis of the crack loaded with mixed-mode I/II load on semi-circular disc test made from environmental friendly concrete. **BUT internal grant agency**.
FAST-S-19-5896	Analysis of displacement fields under the mixed mode I/II by ODM: Evaluation of the experimental data obtained by DIC as measured on the building materials. **BUT Internal Grant Agency.**
FAST-S-18-5614	Establishing a procedure for evaluation of geometry shape functions for test specimens with a V-notch as a stress concentrator. **BUT Internal Grant Agency**
20-00761S	Influence of material properties of stainless steels on reliability of bridge structures. **Czech Science Foundation.**
CZ.01.1.02/0.0/0.0/15_019/0004505	Complex design of girders from advanced concrete. **Czech Ministry of Industry and Trade**
18-12289Y	Advanced characterization of cracks propagation in composites based on alkali activated matrix. **Czech Science Foundation.**
17-01589S	Advanced computational and probabilistic modelling of steel structures taking account fatigue damage. **Czech Science Foundation.**
16-18702S	AMIRI − Aggregate-Matrix-Interface Related Issues in silicate-based composites. **Czech Science Foundation.**

Awards

CONFERENCE ATTENDANCE AWARD 2018 on 18th International Conference on Experimental Mechanics in Brussel Belgium, 1st-5th July 2018
organized by **The European Society for Experimental Mechanics.**

Software Skills

Office software:	**Microsoft Office** (Word, Excel, PowerPoint), Adobe **Photoshop**, Autodesk **AutoCAD**, **Inscape.**
Software for structural analysis	**Dlubal – RFEM 5.0** and **Nemetschek – Scia Engineer**: FEM software for design of civil engineering structures according to Eurocodes
	Simulia ABAQUS: advanced FEM software or design of civil engineering structures (static linear/non-linear analysis),
	ANSYS Mechanical APDL: Certified user after workshop by SVS FEM (November 2017): ANSYS Mechanical APDL-1,2 ANSYS Mechanical APDL – Dynamics.
	Matlab Certified user after workshop by HUMUSOFT (September 2018 and November 2019)

List of Selected Papers

Complete list of author's publications:

https://www.vutbr.cz/en/people/petr-miarka-135903

MIARKA, P., SEITL, S., LEHNER, P., HORNAKOVA, M., KONEČNÝ, P., SUCHARDA, O., BÍLEK, V., Influence of Chlorides on the Fracture Toughness and Fracture Resistance Under the Mixed Mode I/II of High-Performance Concrete. *Theoretical and Applied Fracture Mechanics*, 2020, vol.110, 102812, pp. 1-15. ISSN: 0167-8442. DOI: 10.1016/j.tafmec.2020.102812 **IF**: 3.021 Q1/Q2

MIARKA, P., PAN, L., BÍLEK, V., SEITL, S., CIFUENTÉS, H., Influence of the Chevron Notch Type on the Values of Fracture Energy Evaluated on Alkali-Activated Concrete. *Engineering Fracture Mechanics*, 2020, vol. 236, 107209, pp. 1-18. DOI: 10.1016/j.engfracmech.2020.107209 **IF**: 3.426 Q1

MIARKA, P., CRUCES, A., SEITL, S., MALÍKOVÁ, L., LOPÉZ-CRESPO, P., Evaluation of the SIF and T-stress values of the Brazilian disc with a central notch by hybrid method. *International Journal of Fatigue*, 2020, vol. 135, no. 1, pp. 1-12. ISSN: 0142-1123. DOI: 10.1016/j.ijfatigue.2020.105562 **IF**: 4.369, Q1/Q2

MIARKA, P., CRUCES, A., SEITL, S., MALÍKOVÁ, L., LOPÉZ-CRESPO, P., Influence of the constraint effect on the fatigue crack growth rate in S355 J2 steel using digital image correlation. *Fatigue and Fracture of Engineering Materials and Structures*, 2020, vol. 43, no. 8, pp. 1703-1718. ISSN: 1460-2695. DOI: 10.1111/ffe.13198 **IF**: 3.031 Q1/Q2

MIARKA, P., SEITL, S., DE CORTE, W. Notch Tip Displacements of the Concrete Brazilian Disc Test with Central Notch Analysed by the Concrete Damaged Plasticity Model. *Theoretical and Applied Fracture Mechanics*, 2019, vol. 102, no. 1, pp. 122-150. ISSN: 0167-8442. DOI: 10.1016/j.tafmec.2019.04.006 **IF**: 3.021 Q1/Q2

SEITL, S., **MIARKA, P.,** BÍLEK, V., The Mixed-Mode Fracture Resistance of C 50/60 and its Suitability for Use in Precast Elements as Determined by the Brazilian Disc Test and Three-Point Bending Specimens. *Theoretical and Applied Fracture Mechanics*, 2018, vol. 2018, no. 97, pp. 108-119. ISSN: 0167-8442. DOI: 10.1016/j.tafmec.2018.08.003 **IF**: 3.021 Q1/Q2

MIARKA, P. SEITL, S. BÍLEK, V. Mixed-mode fracture analysis in High-performance concrete using brazilian disc test. *Materiali in tehnologije*, 2019, vol. 53, no. 2, pp. 233-238. ISSN: 1580-2949. DOI: 10.17222/mit.2018.161 **IF**: 0.697 Q4

MALÍKOVÁ, L., **MIARKA, P.**, KUCHARCZYKOVÁ, B., ŠIMONOVÁ, H. Williams expansion utilized for assessment of crack behaviour under mixed-mode loading in alkali-activated fine-grained composite. *Fatigue and Fracture of Engineering Materials and Structures*. 2021;1–11. DOI: 10.1111/ffe.13418 **IF**: 3.031 Q1/Q2

SEITL S., **MIARKA P.,** POKORNÝ P., KLUSÁK J. Influence of corrosion on fatigue behaviour of old crane runway steel. *The Journal of Strain Analysis for Engineering Design*, 2019, vol. 54, no. 7-8, pp. 416-423. ISSN: 0309-3247. DOI: 10.1177/0309324719891079 **IF**: 1.63 Q2/Q3

SEITL, S., **MIARKA, P.,** ŠIMONOVÁ, H., FRANTÍK, P., KERŠNER, Z., DOMSKI, J., KATZER, J. Change of Fatigue and Mechanical Fracture Properties of a Cement Composite due to Partial Replacement of Aggregate by Red Ceramic Waste. *Periodica Polytechnica - Civil Engineering*, 2019, vol. 1, no. 63, p. 152-159. ISSN: 0553-6626. DOI: 10.3311/PPci.12450 **IF**: 1.14 Q3

ŠIMONOVÁ, H., KUCHARCZYKOVÁ, B., BÍLEK, V., MALÍKOVÁ, L., **MIARKA, P.**, LIPOWCZAN, M. Mechanical Fracture and Fatigue Characteristics of Fine-Grained Composite Based on Sodium Hydroxide-Activated Slag Cured under High Relative Humidity. *Applied Sciences*, 2021, vol. 1, 259, pp. 1-20. DOI: 10.3390/app11010259 **IF**: 2.474 Q2/Q3

Appendix A. Specimen' Dimensions and Fracture Forces

A 1. C 50/60

Table A1 - 1: Dimensions of BD test specimens made from C 50/60 material used in indirect tensile test.

Specimen nmr.	Diameter D [mm]	Thickness B [mm]	Fracture force P_C [kN
01	149.234	29.37	39.789
02	149.746	30.37	40.441
03	149.548	29.06	35.223

Table A1 - 2: Dimensions of BDCN test specimens made from C 50/60 material for relative notch length a/R = 0.267.

Specimen nmr.	Inclination angle α [°]	Diameter D [mm]	Thickness B [mm]	Notch length $2a$ [mm]	Fracture force P_C [kN
4_01	0	149.095	31.630	39.680	21.884
4_05	0	149.280	31.827	40.060	26.800
4_07	5	149.214	31.460	39.660	24.917
4_06	10	149.120	32.490	40.090	24.689
4_09	10	149.200	30.680	40.000	24.300
4_03	15	149.207	31.020	39.750	21.786
4_08	20	149.180	31.460	39.660	21.134
4_02	27.2	149.320	31.790	40.120	19.881
4_04	27.2	149.273	31.650	40.085	23.200

Table A1 - 3: Dimensions of BDCN test specimens made from C 50/60 material for relative notch length a/R = 0.4.

Specimen nmr.	Inclination angle α [°]	Diameter D [mm]	Thickness B [mm]	Notch length $2a$ [mm]	Fracture force P_C [kN
6_03	0	149.200	31.380	60.210	15.896
6_09	0	149.182	29.927	60.170	19.600
6_01	0	149.155	31.440	60.920	20.000
6_01	5	149.162	31.440	60.920	16.307
6_05	10	149.143	30.580	60.140	16.170
6_04	10	149.162	30.973	60.040	17.700
6_04	15	149.208	30.970	60.040	13.698
6_06	15	149.214	32.390	60.150	18.264
6_02	25.2	149.180	30.770	60.110	16.307
6_07	25.2	149.205	31.173	59.940	15.800

A 2. High-strength Concrete

Table A2 - 4: Dimensions of BD test specimens made from HSC material used in indirect tensile test.

Specimen nmr.	Diameter D [mm]	Thickness B [mm]	Fracture force P_C [kN]
HSC_01	150	27.8	74.670
HSC_02	150	27.2	77.840
HSC_03	150	26.07	55.400
HSC_04	150	28.82	66.350
HSC_01	150	27.8	74.670

Table A2 - 2: Dimensions of BDCN test specimens made from HSC material for relative notch length $a/R = 0.4$.

Specimen nmr.	Inclination angle α [°]	Diameter D [mm]	Thickness B [mm]	Notch length $2a$ [mm]	Fracture force P_C [kN]
12	0	75.47	29.95	40.51	37.700
15	10	75.49	30.46	40.64	34.880
5	15	75.51	30.82	40.21	35.040
6	15	74.91	30.93	40.03	41.200
7	20	75.3	30.55	40.32	33.050
10	20	75.63	27.76	40.01	29.250
14	27.7	74.71	30.64	40.36	30.910
13	27.7	74.76	30.01	40.38	29.600

Table A2 - 5: Dimensions of BDCN test specimens made from HSC material for relative notch length $a/R = 0.4$.

Specimen nmr.	Inclination angle α [°]	Diameter D [mm]	Thickness B [mm]	Notch length $2a$ [mm]	Fracture force P_C [kN]
16	0	75.24	30.27	60.12	25.940
3	15	75.36	32.31	59.38	31.580
4	15	75.3	30.82	59.38	25.850
8	20	75.29	30.63	60.2	21.580
9	20	75.45	30.84	60.01	27.150
1	25.2	75.3	30.69	58.66	21.590
2	25.2	75.19	30.47	59.98	21.700

A 3. High-performance Concrete Batch A

Table A3 - 1: Dimensions of BD test specimens made from HPC batch A material used in indirect tensile test.

Specimen nmr.	Diameter D [mm]	Thickness B [mm]	Fracture force P_C [kN]
2_01	149.36	28.25	
2_02	149.36	29.59	
2_03	149.57	28.55	
2_04	149.43	27.83	
2_05	149.19	28.12	

Table A3 - 2: Dimensions of BDCN test specimens made from HPC batch A material for relative notch length $a/R = 0.267$.

Specimen nmr.	Inclination angle α [°]	Radius R [mm]	Thickness B [mm]	Notch length $2a$ [mm]	Fracture force P_C [kN]
4_2_01	0	74.61	25.69	40	25.687
4_2_02	0	74.65	26.22	40	26.222
4_2_04	5	74.60	24.98	40	24.982
4_2_11	10	74.62	27.40	40	27.396
4_2_09	15	74.61	25.44	40	25.439
4_2_10	15	74.60	26.52	40	26.522
4_2_07	20	74.63	24.13	40	24.134
4_2_08	20	74.63	26.41	40	26.417
4_2_03	27.2	74.50	22.89	40	22.895
4_2_06	27.2	74.58	25.69	40	25.693

Table A3 - 3: Dimensions of BDCN test specimens made from HPC batch A material for relative notch length $a/R = 0.4$.

Specimen nmr.	Inclination angle α [°]	Radius R [mm]	Thickness B [mm]	Notch length $2a$ [mm]	Fracture force P_C [kN]
6_2_02	0	74.55	22.18	60.210	22.177
6_2_01	0	74.58	19.57	60.170	19.568
6_2_05	5	74.62	20.22	60.920	20.221
6_2_10	10	74.66	19.57	60.920	19.568
6_2_11	10	74.51	16.19	60.140	16.190
6_2_08	15	74.59	18.92	60.040	18.916
6_2_09	15	74.64	19.15	60.040	19.151
6_2_06	20	74.61	19.57	60.150	19.568
6_2_07	20	74.56	19.57	60.110	19.568
6_2_03	25.2	74.59	16.96	59.940	16.959
6_2_04	25.2	74.62	18.92	60.047	18.916

A 4. Alkali-Activated Concrete

Table A4 - 1: Dimensions of BD test specimens made from C AA3 material used in indirect tensile test.

Specimen nmr.	Diameter D [mm]	Thickness B [mm]	Fracture force P_C [kN]
01	150.11	27.39	22.110
02	150.39	27.54	20.580
03	150.44	27.43	18.620

Table A4 - 2: Dimensions of BDCN test specimens made from ACC material for relative notch length $a/R = 0.267$.

Specimen nmr.	Inclination angle α [°]	Radius R [mm]	Thickness B [mm]	Notch length $2a$ [mm]	Fracture force P_C [kN]
1	0	74.81	27.76	40.234	17.550
2	5	74.70	27.57	40.741	19.950
3	5	74.86	27.76	40.458	12.800
4	5	74.88	27.52	40.234	14.480
5	10	74.90	27.58	40.249	17.970
6	10	74.24	27.77	40.176	17.790
7	15	74.95	27.81	40.182	17.820
8	15	75.27	27.71	40.793	18.110
9	20	75.08	27.74	40.741	17.210
10	20	74.94	28.82	40.243	14.020
11	27	74.92	27.66	40.476	12.700
12	27	75.12	27.46	40.167	15.340

Table A4 - 3: Dimensions of BDCN test specimens made from AAC material for relative notch length $a/R = 0.4$.

Specimen nmr.	Inclination angle α [°]	Radius R [mm]	Thickness B [mm]	Notch length $2a$ [mm]	Fracture force P_C [kN]
1	0	75.02	27.89	60.210	10.040
2	5	75.46	27.47	60.170	12.270
3	5	75.40	27.89	60.920	11.970
4	10	75.17	28.80	60.920	12.960
5	10	75.47	27.84	60.140	11.450
6	10	75.07	27.81	60.040	11.550
7	15	75.32	27.84	60.040	11.720
8	20	75.32	29.05	60.150	13.700
9	20	74.59	27.18	60.110	11.900
10	20	74.82	27.36	59.940	11.700
11	25	74.91	27.72	60.520	11.720

Appendix B. Measured Fracture Mechanical Parameters

B 1. High-strength Concrete

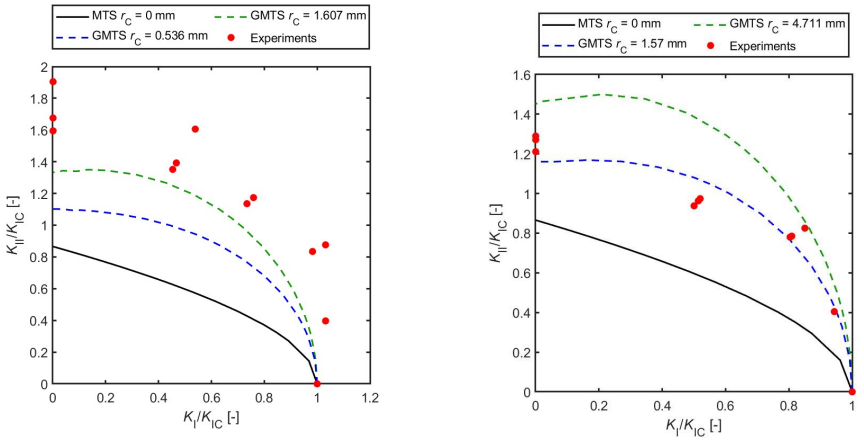

(a) (b)

Figure B1 - 1: Mixed mode I/II fracture resistance of High-strength concrete material relative notch ratio (a) - $a/R = 0.267$ and (b) $a/R = 0.4$.

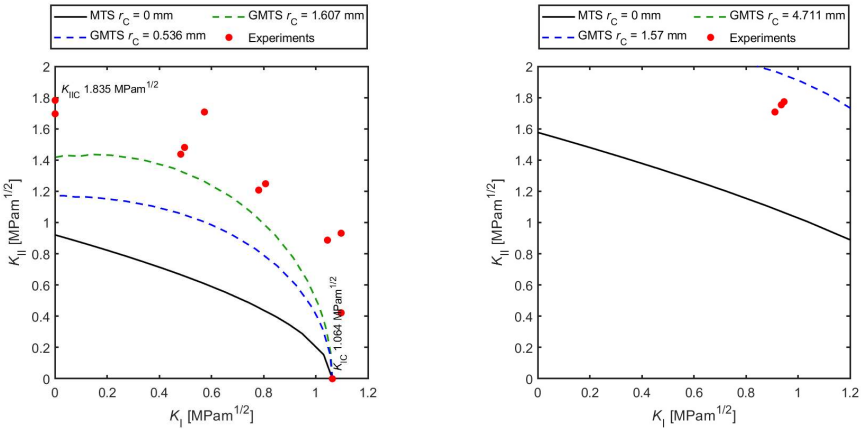

(a) (b)

Figure B1 - 2: Mixed mode I/II fracture resistance of High-strength concrete material resented in absolute coordinates for relative notch ratio (a) - $a/R = 0.267$ and (b) $a/R = 0.4$.

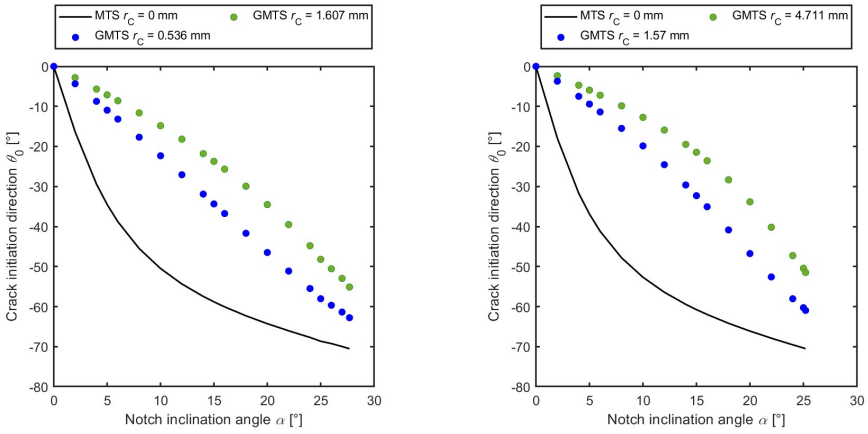

Figure B1 - 3: Crack initiation direction θ_0 of High-strength concrete (a) - a/R = 0.267 and (b) - a/R = 0.4.

D 1. High-performance Concrete Batch A

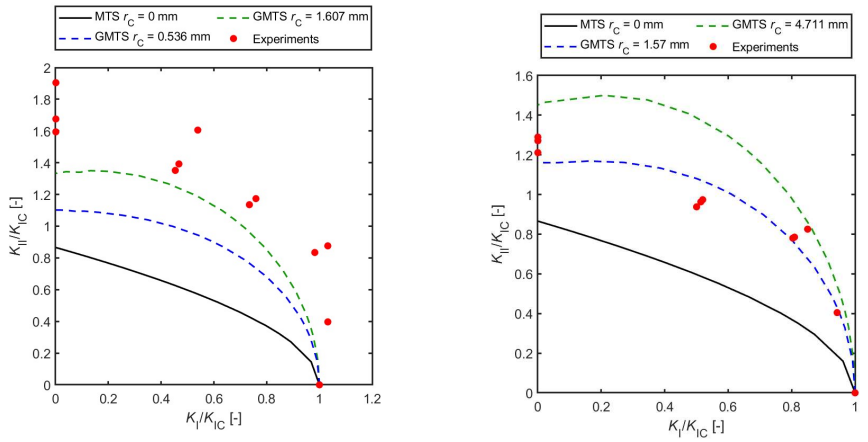

Figure B2 - 4: Mixed mode I/II fracture resistance of HPC batch A material relative notch ratio (a) - a/R = 0.267 and (b) a/R = 0.4.

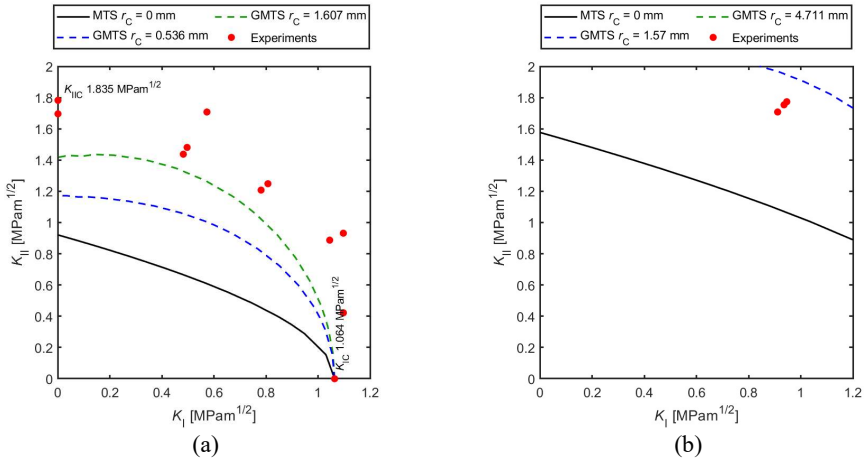

Figure B2 - 5: Mixed mode I/II fracture resistance of HPC batch A material resented in absolute coordinates for relative notch ratio (a) - a/R = 0.267 and (b) a/R = 0.4.

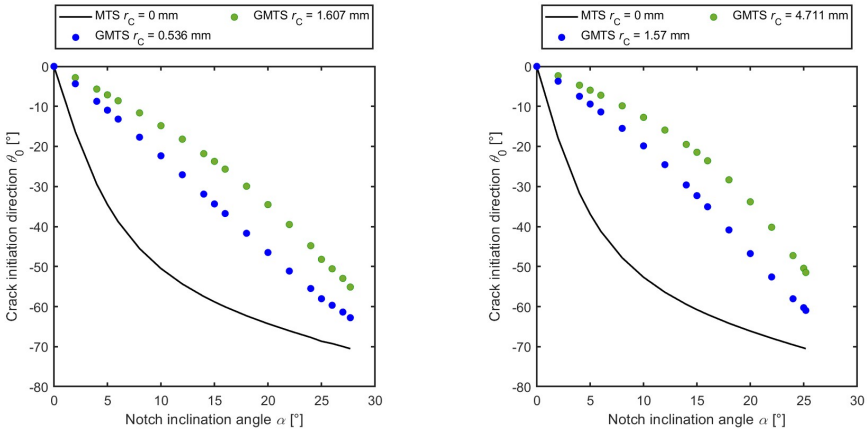

(a) (b)

Figure B2 - 3: Crack initiation direction θ_0 of HPC batch A (a) - a/R = 0.267 and (b) - a/R = 0.4.

D 2. Alkali-activated concrete

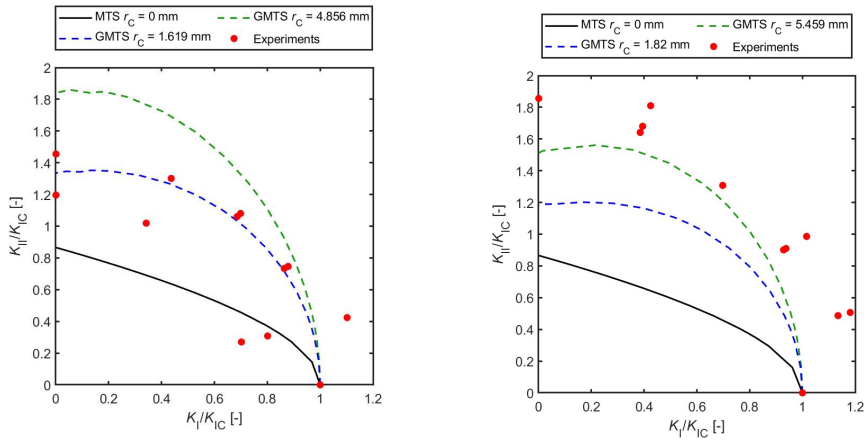

(a) (b)

Figure B3 - 1: Mixed mode I/II fracture resistance of Alkali-activated concrete material relative notch ratio (a) - a/R = 0.267 and (b) a/R = 0.4.

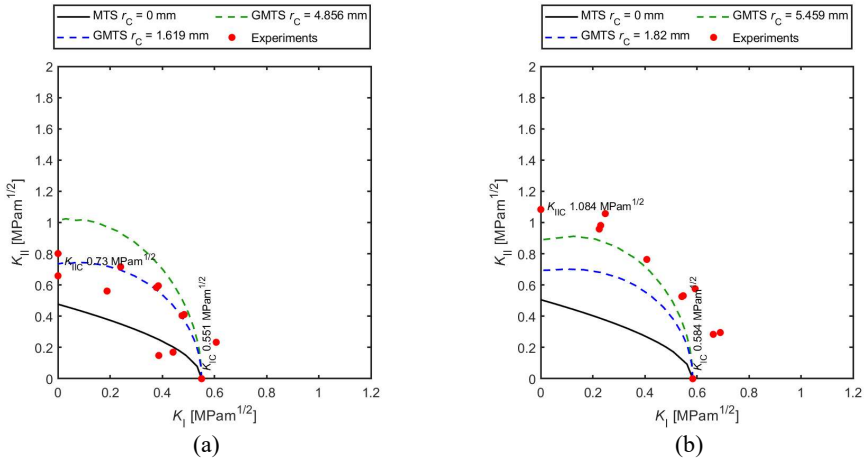

(a) (b)

Figure B3 - 2: Mixed mode I/II fracture resistance of Alkali Activated concrete material resented in absolute coordinates for relative notch ratio (a) - a/R = 0.267 and (b) a/R = 0.4.

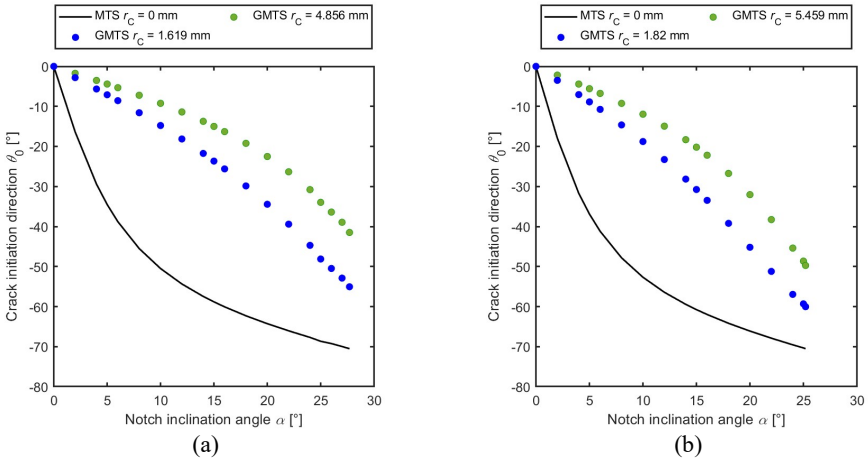

Figure B3 - 3: Crack initiation direction θ_0 of Alkali-activated concrete (a) - a/R = 0.267 and (b) - a/R = 0.4.

Appendix C. Numerically Generated *P-δ* diagrams

Table C149: Overview of reaction force against Δu_x diagrams for various transformation angles θ_0 and material input parameters.

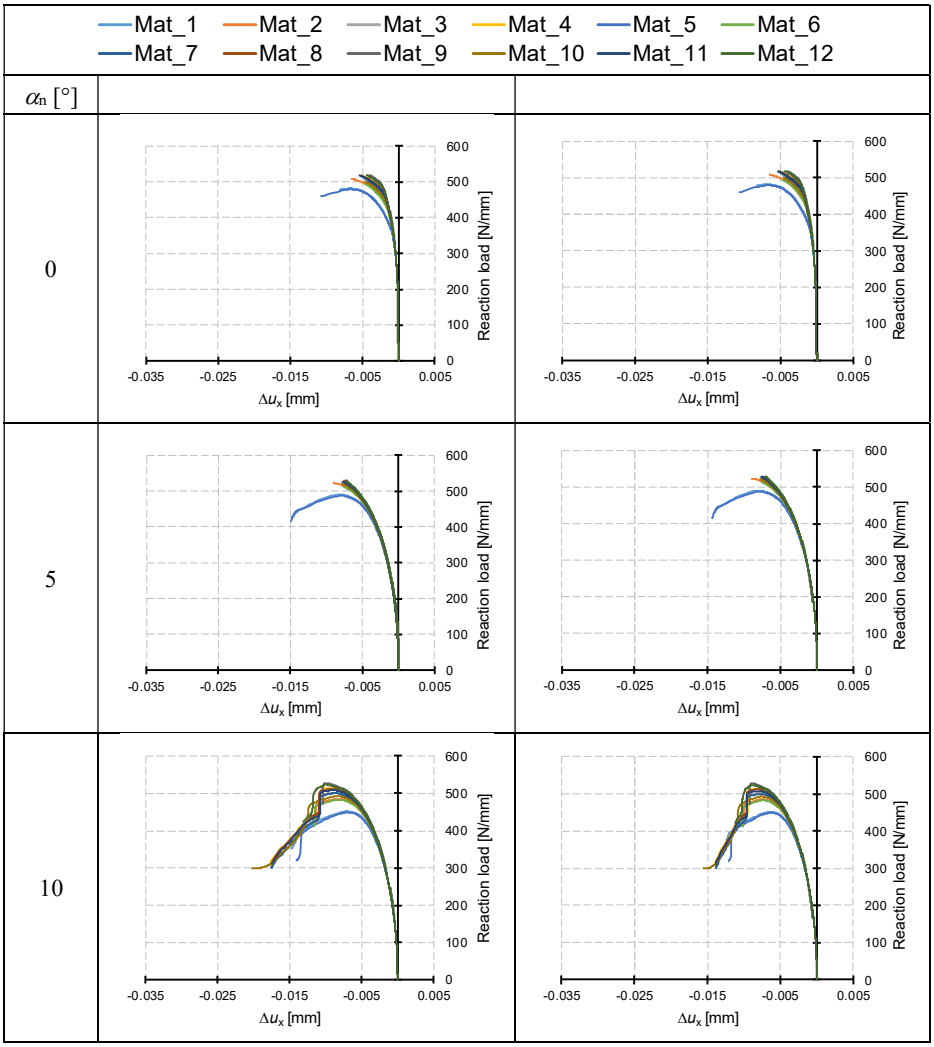

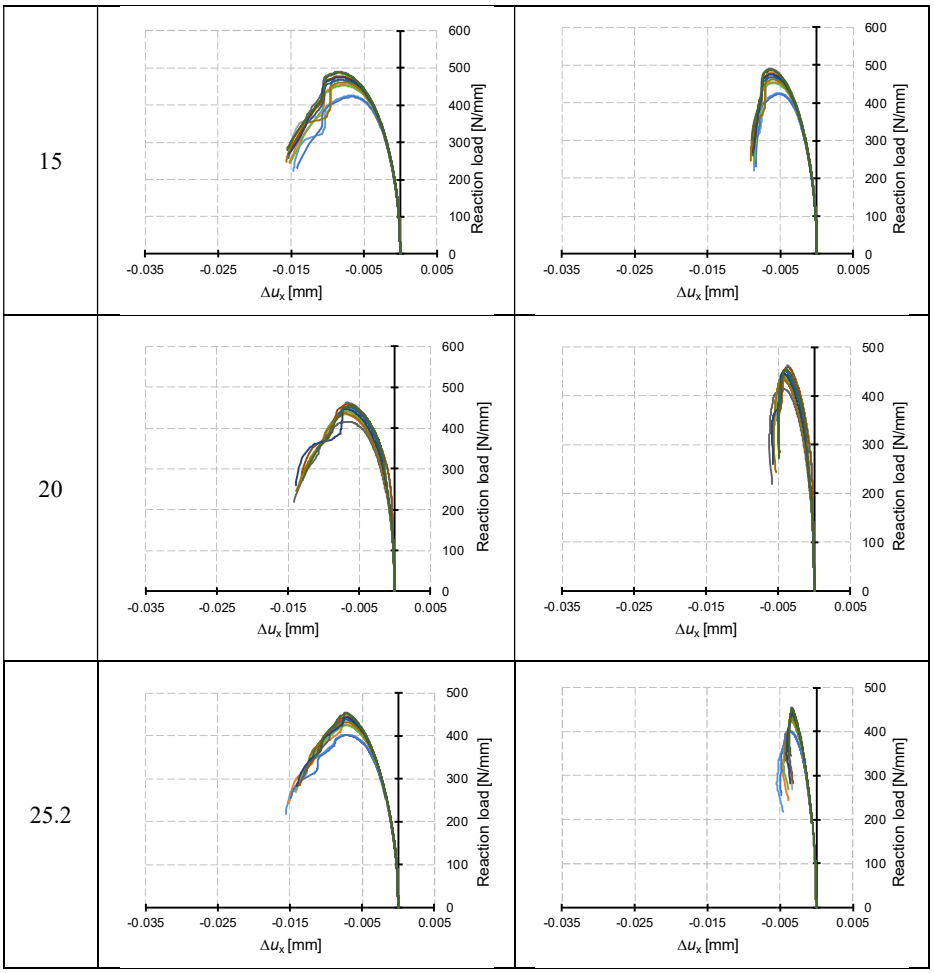

Table C250: Overview of reaction force against Δu_x diagrams for various transformation angles θ_0 and material input parameters.

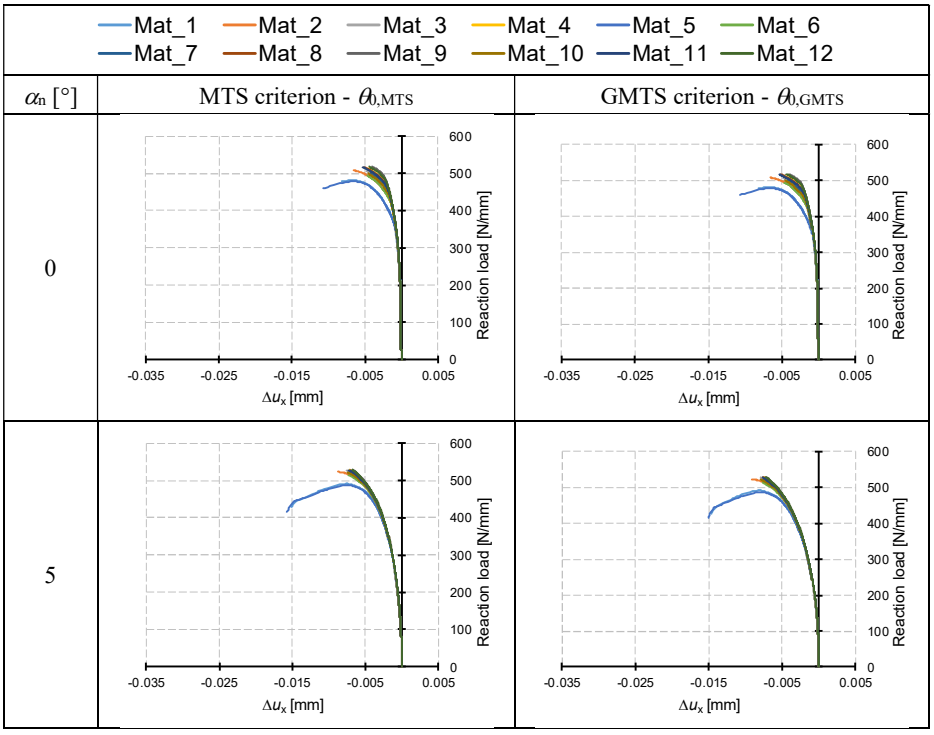

10	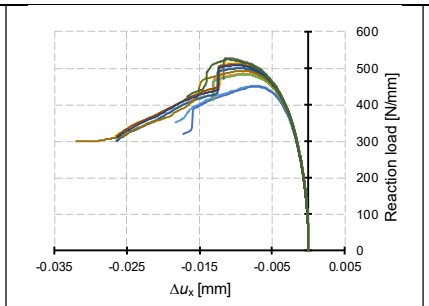	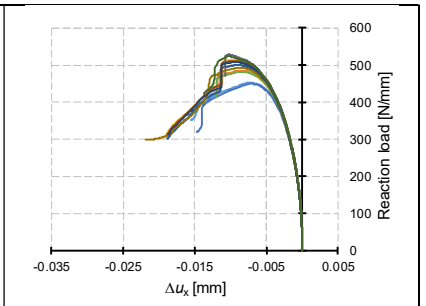
15	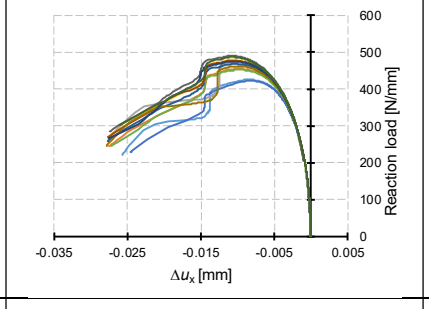	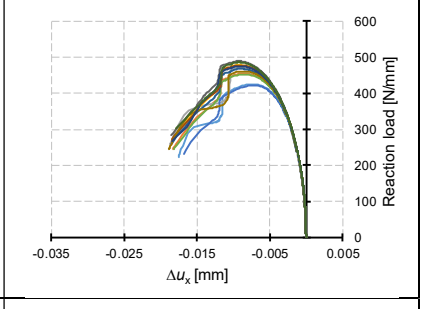
20	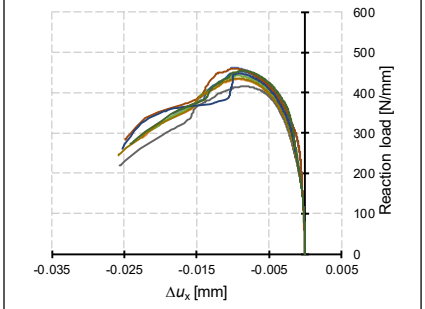	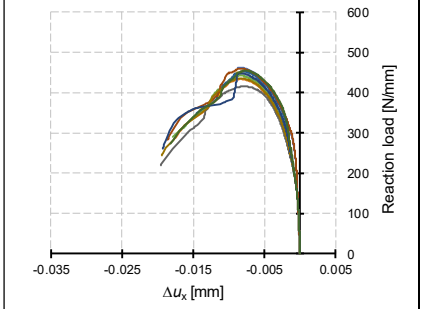
25.2	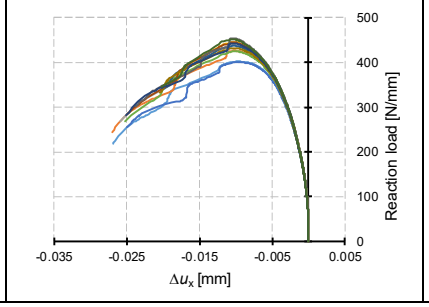	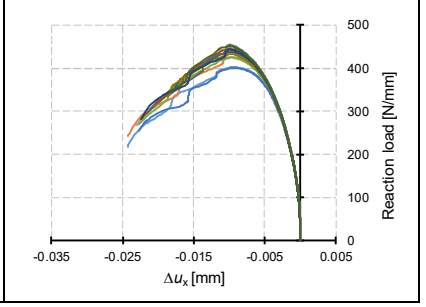

Table C351: Overview of reaction force against Δu_x diagrams for various transformation angles θ_0 and material input parameters.

	α_n [°]	Principal stress - $\theta_{0,p}$
	0	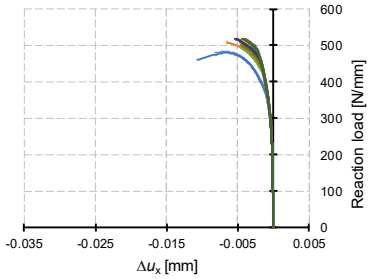

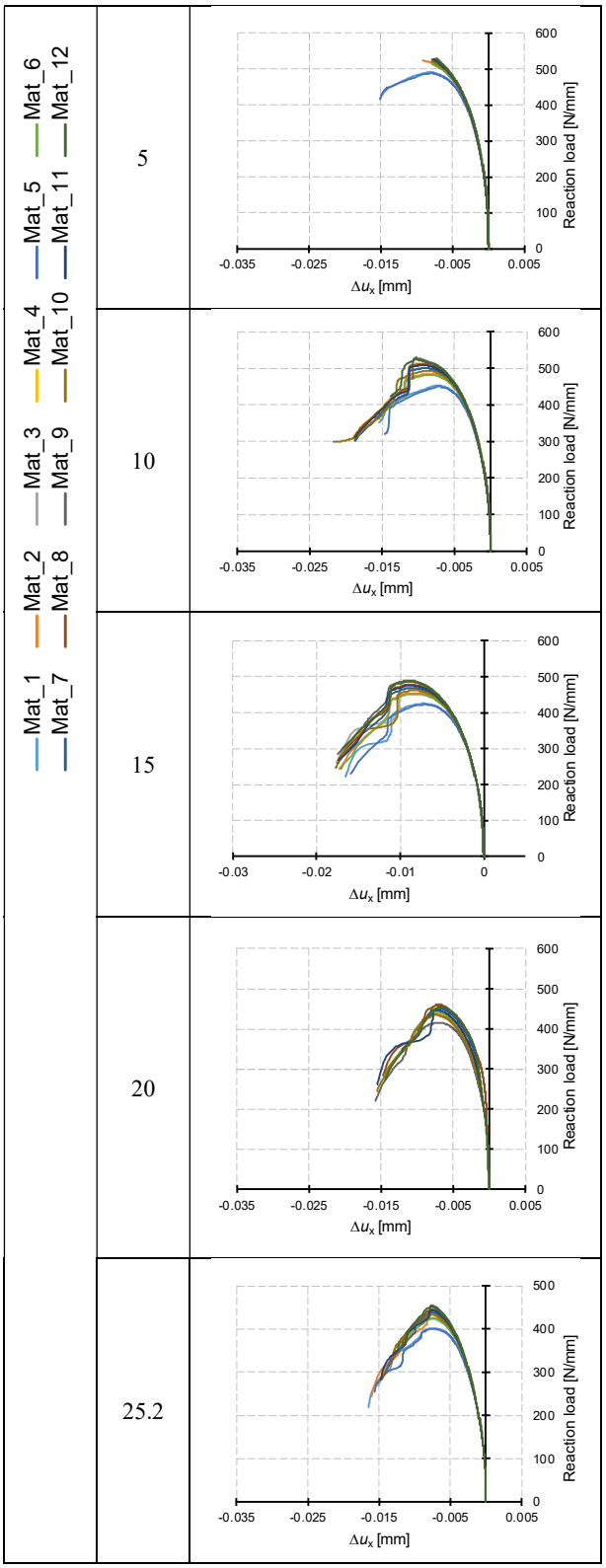
Mat_1
Mat_2
Mat_3
Mat_4
Mat_5
Mat_6
Mat_7
Mat_8
Mat_9
Mat_10
Mat_11
Mat_12
5
10
15
20
25.2
Reaction load [N/mm]
Δu_x [mm]

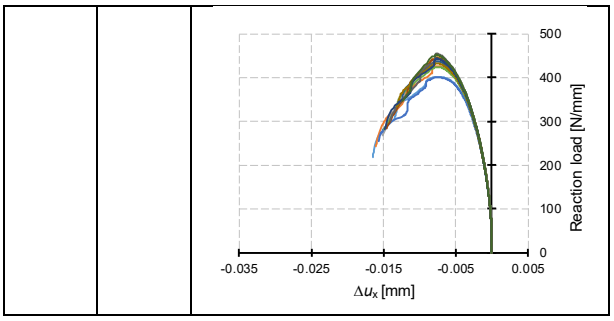

Table C452: Overview of reaction force against Δu_y diagrams for various transformation angles θ_0 and material input parameters.

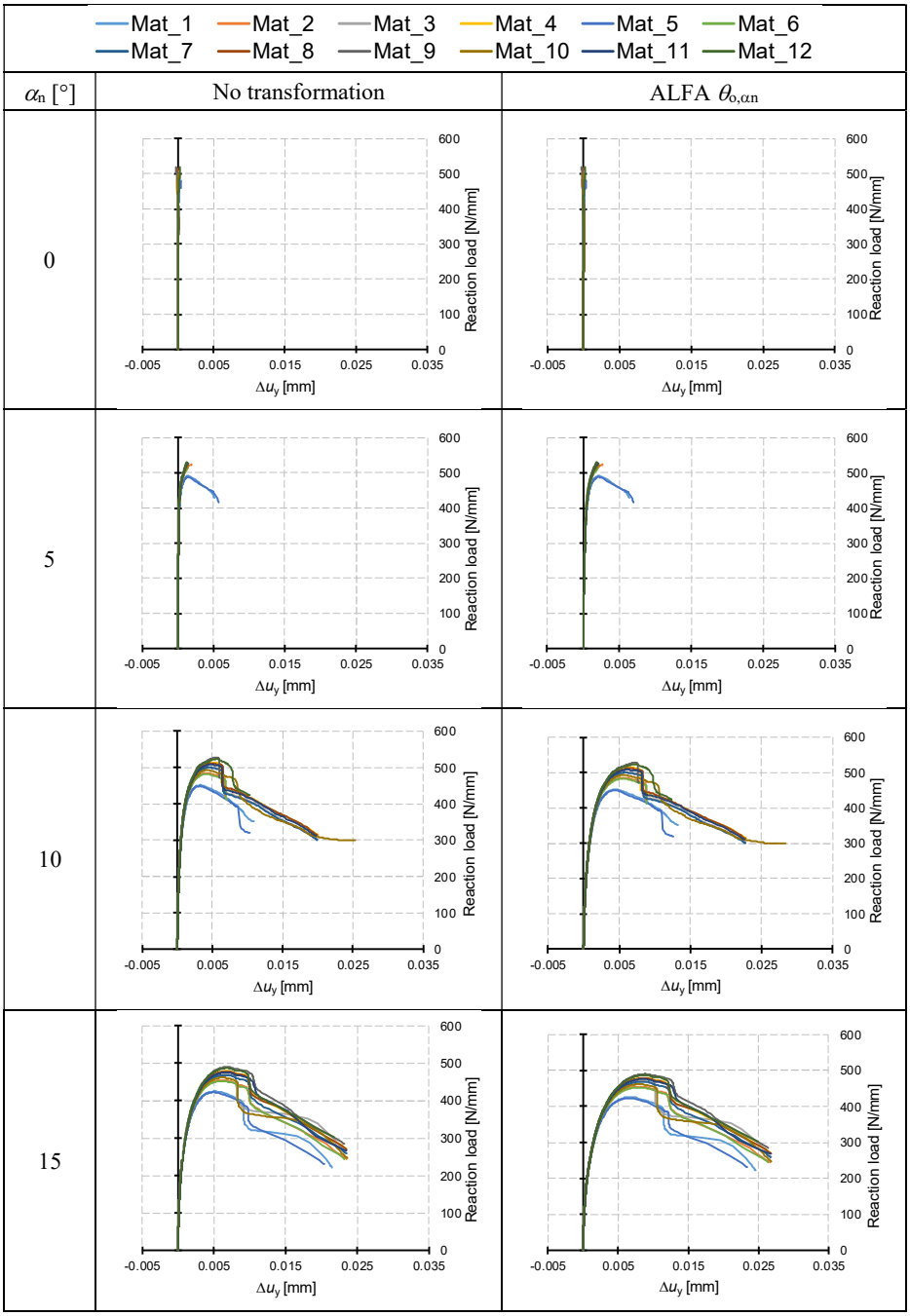

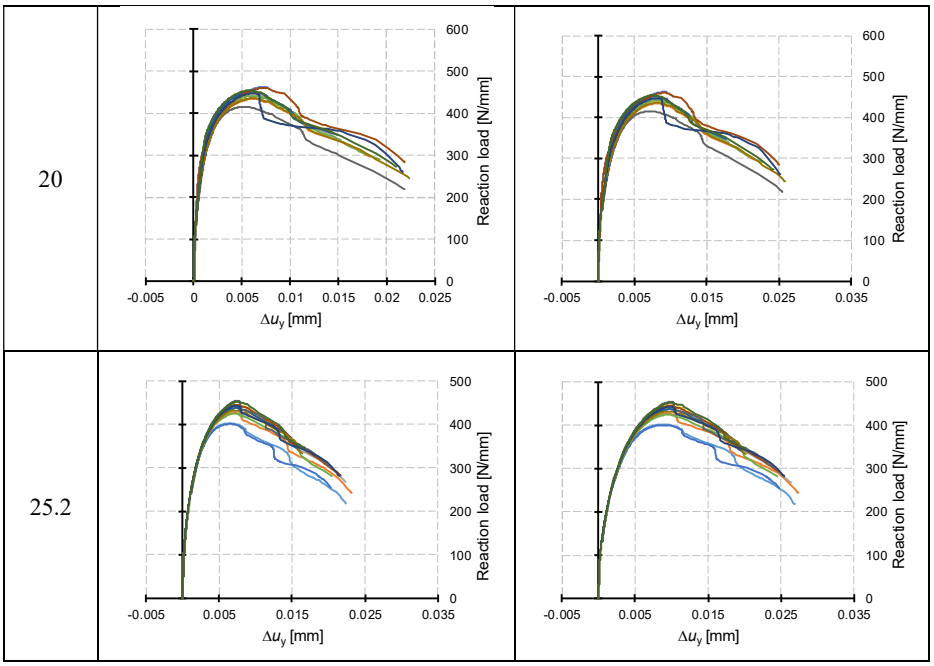

Table C553: Overview of reaction force against Δu_y diagrams for various transformation angles θ_0 and material input parameters.

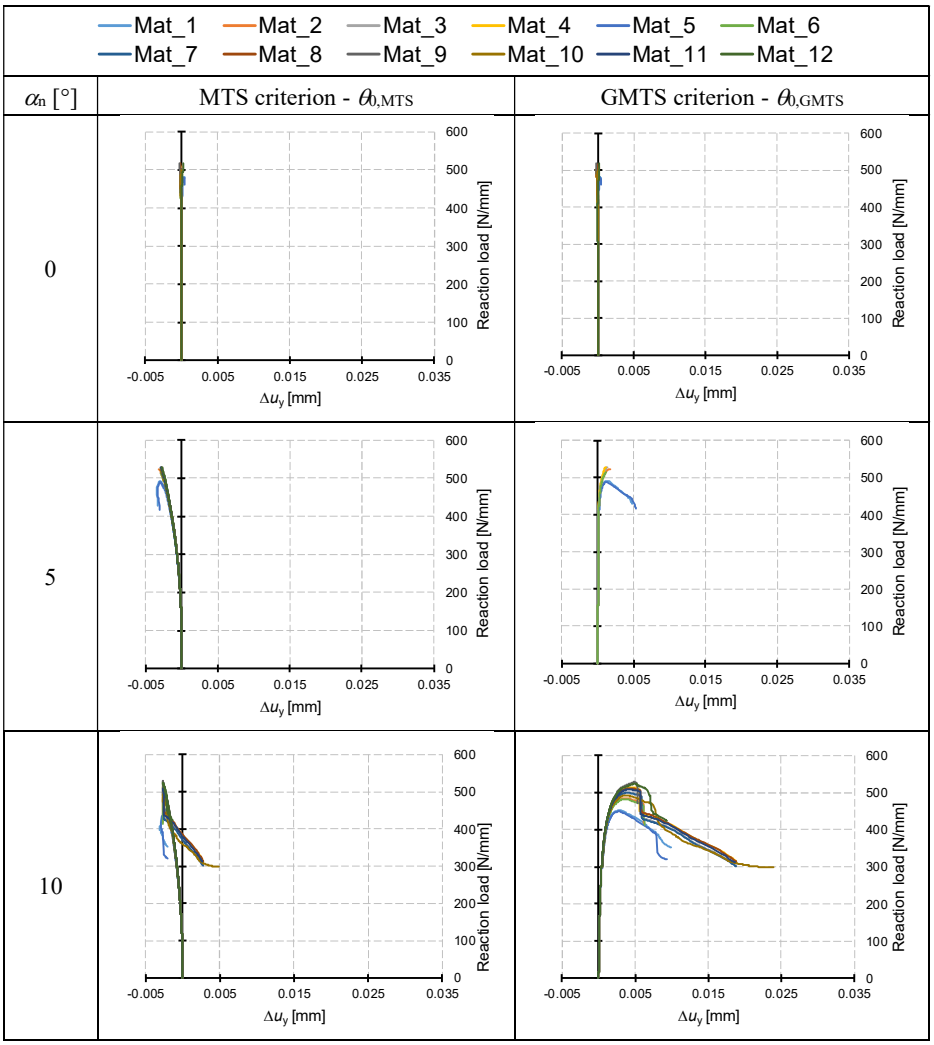

15	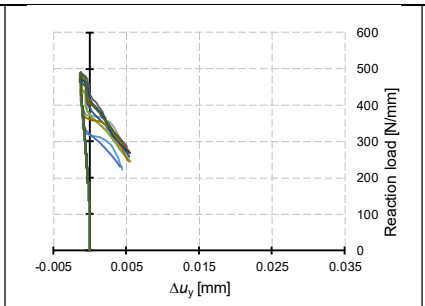	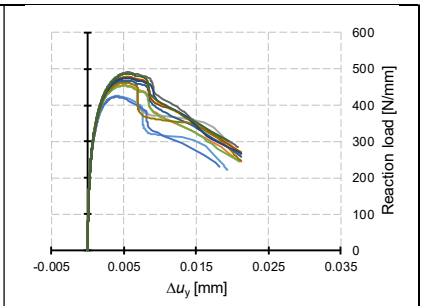
20	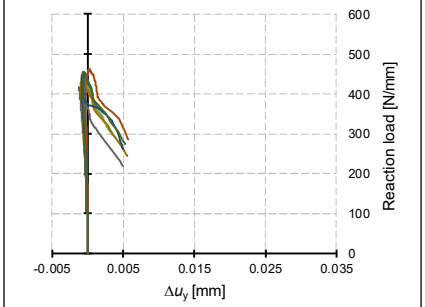	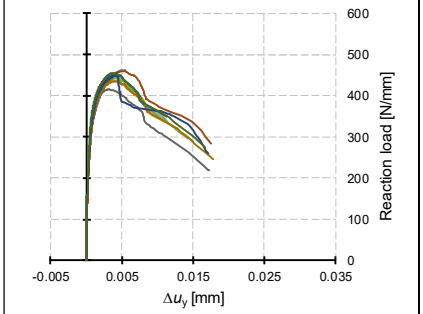
25.2	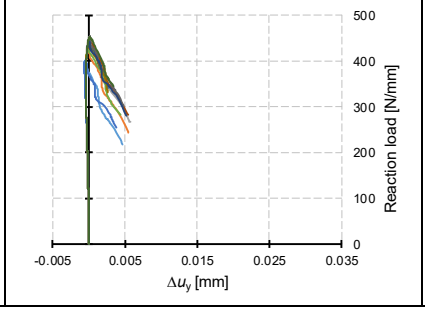	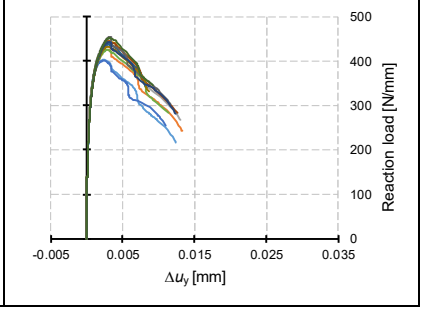

Table C654: Overview of reaction force against Δu_y diagrams for various transformation angles θ_0 and material input parameters.

	α_n [°]	Principal stress - $\theta_{0,p}$
	0	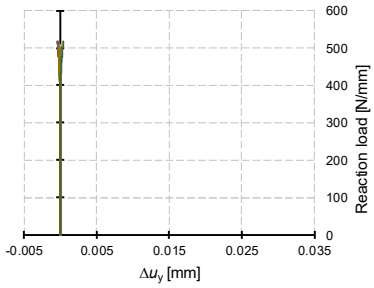
	5	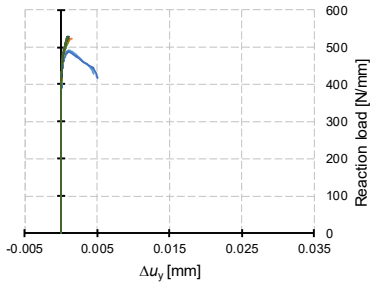

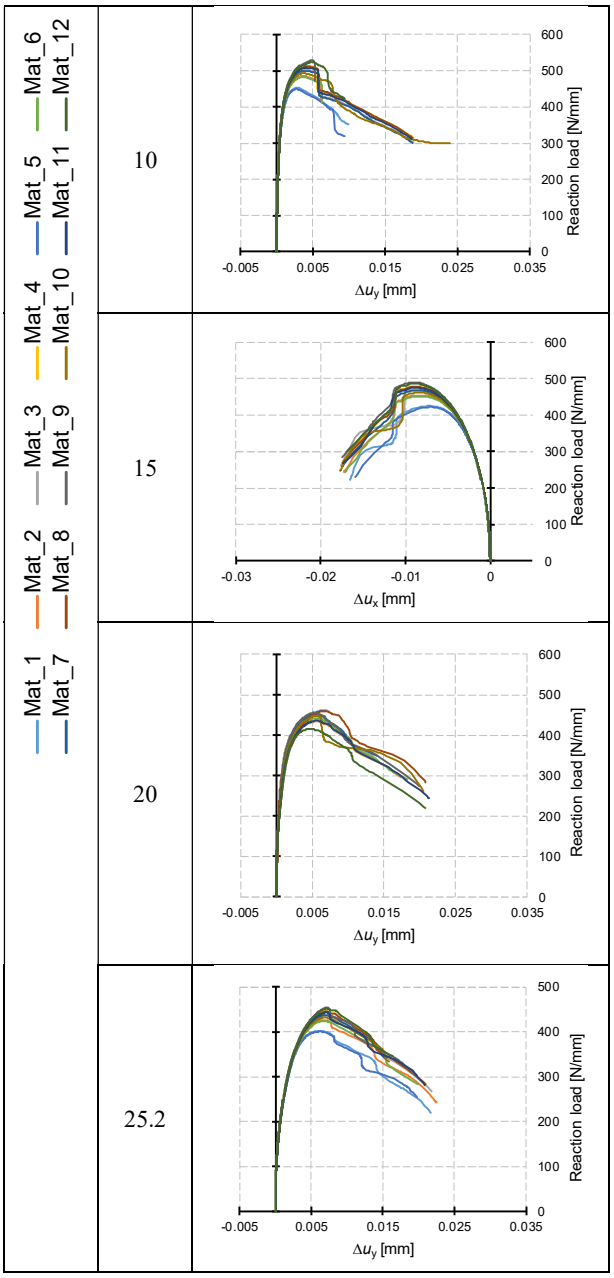
Mat_1
Mat_2
Mat_3
Mat_4
Mat_5
Mat_6
Mat_7
Mat_8
Mat_9
Mat_10
Mat_11
Mat_12
10
15
20
25.2
Reaction load [N/mm]
Δu_y [mm]
Δu_x [mm]

Appendix D. MATLAB code

D 1. Displacement Functions for ODM

```
%% Function to calculate WE fucntion for disp in mode I
%INPUT:
        %theta = angles [rad]
        %n = number of coeff for mode I
        %E = Young's Modullus
        %nu = Possion's ratio [-]
        %BC = plane stress == 1; plane strain == 0
%OUTPUT:
        %u =  displacement for mode I in the direction of X axis
function [u] = shape_mode1_u(n,theta,E,nu,BC)
    G = E/(2.0*(1.0 + nu));
    if BC == 0  %plane strain
        kappa = (3 - 4*nu);
    elseif BC == 1  %plane stress
        kappa = (3-nu)/(1+nu);
    end
    u = ((kappa + n/2 + (-1.0)^n)*cos(n/2*theta) - n/2*cos((n/2 - 2.0)*theta))/(2*G);
end
%% Function to calculate WE fucntion for disp in mode I
%INPUT:
        %theta = angles [rad]
        %n = number of coeff for mode I
        %E = Young's Modullus
        %nu = Possion's ratio [-]
        %BC = plane stress == 1; plane strain == 0
%OUTPUT:
        %v =  displacement for mode I in the direction of Y axis
function [v] = shape_mode1_v(n,theta,E,nu,BC)
    G = E/(2.0*(1.0 + nu));
    if BC == 0  %plane strain
        kappa = (3 - 4*nu);
    elseif BC == 1  %plane stress
        kappa = (3-nu)/(1+nu);
    end
    v = ((kappa - n/2 - (-1.0)^n)*sin(n/2*theta) + n/2*sin((n/2 - 2.0)*theta))/(2*G);
end
%% Function to calculate WE fucntion for disp in mode II
%INPUT:
        %theta = angles [rad]
        %m = number of coeff for mode I
        %E = Young's Modullus
        %nu = Possion's ratio [-]
        %BC = plane stress == 1; plane strain == 0
%OUTPUT:
        %u =  displacement for mode II in the direction of X axis
function [u] = shape_mode2_u(m,theta,E,nu,BC)
    G = E/(2.0*(1.0 + nu));
    if BC == 0  %plane strain
        kappa = (3 - 4*nu);
    elseif BC == 1  %plane stress
        kappa = (3-nu)/(1+nu);
    end
    u = ((-kappa - m/2 + (-1.0)^m)*sin(m/2*theta) + m/2*sin((m/2 - 2.0)*theta))/(2*G);
end
%% Function to calculate WE fucntion for disp in mode II
%INPUT:
        %theta = angles [rad]
        %m = number of coeff for mode I
        %E = Young's Modullus
        %nu = Possion's ratio [-]
        %BC = plane stress == 1; plane strain == 0
%OUTPUT:
        %v =  displacement for mode II in the direction of Y axis
function [v] = shape_mode2_v(m,theta,E,nu,BC)
    G = E/(2.0*(1.0 + nu));
    if BC == 0  %plane strain
        kappa = (3 - 4*nu);
    elseif BC == 1  %plane stress
        kappa = (3-nu)/(1+nu);
    end
    v = ((kappa - m/2 + (-1.0)^m)*cos(m/2*theta) + m/2*cos((m/2 - 2.0)*theta))/(2*G);
end
```

D 2. ODM Calculation

```
%function to evaluate coeff. of WE by ODM method proposed by Ayatollahi  2010
%INPUT:
        %theta = angles [rad]
        %r = radius [mm]
        %u,v = displacements [mm]
        %E = Young's Modullus
        %nu = Possion's ratio [-]
        %BC = plane stress == 1; plane strain == 0
        %unit = "mm" or "m" for units of SIF
        %N = number of coeff for mode I
        %M = number of coeff for mode II
%OUTPUT:
        %KI = SIF for mode I in [MPAm^1/2]
        %T = T-stress [MPa]
        %KII = SIF for mode II in [MPAm^1/2]
        %WE_coeff = values of WE without any manimulation
function [KI,T,KII,WE_coeff] = ODM_mixed_mode(theta,r,u,v,E,nu,BC,unit,N,M)
    G = E/(2.0*(1.0 + nu)); %shear modullus
    posuny = [u; v]; % Neboli [U]
    if length(r) == 1
        f0 = shape_mode1_u(0,theta,E,nu,BC).*r^(0/2);
    elseif length(r) > 1
        f0 = shape_mode1_u(0,theta,E,nu,BC).*r.^(0/2);
    end
    nuly = zeros(length(theta),1);
    if length(r) == 1
        g0 = shape_mode2_v(0,theta,E,nu,BC).*r^(0/2);
    elseif length(r) > 1
        g0 = shape_mode2_v(0,theta,E,nu,BC).*r.^(0/2);
    end
    if length(r) == 1
        f2 = shape_mode2_u(2,theta,E,nu,BC);
        g2 = shape_mode2_v(2,theta,E,nu,BC);
    elseif length(r) > 1
        f2 = shape_mode2_u(2,theta,E,nu,BC);
        g2 = shape_mode2_v(2,theta,E,nu,BC);
    end
    if length(r) == 1
        for i = 1:N
            funkce.f_modeI(:,i) = shape_mode1_u(i,theta,E,nu,BC)*r^(i/2);
            funkce.g_modeI(:,i) = shape_mode1_v(i,theta,E,nu,BC)*r^(i/2);
        end
    elseif length(r) > 1
        for i = 1:N
            funkce.f_modeI(:,i) = shape_mode1_u(i,theta,E,nu,BC)*r(i)^(i/2);
            funkce.g_modeI(:,i) = shape_mode1_v(i,theta,E,nu,BC)*r(i)^(i/2);
        end
    end
    if length(r) == 1
        for i = 1:M
            funkce.f_modeII(:,i) = shape_mode2_u(i,theta,E,nu,BC)*r^(i/2);
            funkce.g_modeII(:,i) = shape_mode2_v(i,theta,E,nu,BC)*r^(i/2);
        end
    elseif length(r) > 1
        for i = 1:M
            funkce.f_modeII(:,i) = shape_mode2_u(i,theta,E,nu,BC)*r(i)^(i/2);
            funkce.g_modeII(:,i) = shape_mode2_v(i,theta,E,nu,BC)*r(i)^(i/2);
        end
    end
    funkce.modeI = [funkce.f_modeI; funkce.g_modeI];

    funkce.modeII_f = [funkce.f_modeII(:,1), funkce.f_modeII(:,3:end)];
    funkce.modeII_g = [funkce.g_modeII(:,1), funkce.g_modeII(:,3:end)];

    funkce.modeII = [funkce.modeII_f; funkce.modeII_g];
    funkce.modeI_fo = [f0; nuly];
    funkce.modeII_g0 = [nuly; g0];

    funkce.f2_g2 = [f2; g2];
    funkce.total = [funkce.modeI, funkce.modeII, funkce.modeI_fo, funkce.modeII_g0,
funkce.f2_g2];

    WE_coeff = inv(funkce.total'*funkce.total)*funkce.total'*posuny;
```

```
    if unit == "m"
        KI = (sqrt(2*pi)*WE_coeff(1))/(sqrt(1000));
        KII = -(sqrt(2*pi)*WE_coeff(N+1))/(sqrt(1000));
    elseif unit == "mm"
        KI = (sqrt(2*pi)*WE_coeff(1));
        KII = -(sqrt(2*pi)*WE_coeff(N+1));
    end
    if N>=2
        T = 4*WE_coeff(2);
    elseif N == 1
        T = "NO T-stress value possible";
end
```

D 3. GMTS Criterion Calculation

```
% calculation of critical distance
results.KIC = 41; % in MPa*mm^1/2
results.f_t = 5.5; % MPa
r_C = [(1/(2*pi))*(results.KIC/results.f_t)^2; (1/(6*pi))*(results.KIC/results.f_t)^2;
4; 8;];
%syms theta         %defining symbolic variable theta
symbolic.theta = evalin(symengine,'`symbolic.theta`');
result=zeros(length(vstup.K_I),2)%defining variable to store MTS criterion theta_0
result1=zeros(length(vstup.K_I),2);
result2=zeros(length(vstup.K_I),2);    %defining the variable for second derivation <0
result3=zeros(length(vstup.K_I),2);    %defining the variable for second derivation <0

%MTS
results.T_MTS = zeros(length(vstup.K_I),1); %variable for second derivation <0

%GMTS
results.T_GMTS1 = zeros(length(vstup.K_I),1);%variable for second derivation <0
results.T_GMTS2 = zeros(length(vstup.K_I),1);% variable for second derivation <0

%MTS
symbolic.sdf = vstup.K_I*sin(symbolic.theta)+vstup.K_II*(3*cos(symbolic.theta)-1);
symbolic.d2=diff(symbolic.sdf,symbolic.theta); %second derivation MTS
%values of theta_0 for MTS
for i = 1:length(vstup.K_I)
    result1(i,:) = solve(symbolic.sdf(i)== 0, symbolic.theta,'Real',true);
%Solving Equation for MTS
  %d3=diff(sdf,theta); %second derivation
    symbolic.d3_0=subs(symbolic.d2,symbolic.theta,result1(i));   %sunbstituting re˘%sult
intu second derivation
    if symbolic.d3_0(i)<0
         results.T_MTS(i, 1) = max(result1(i));
    else
         results.T_MTS(i, 1) = min(result1(i));
    end
end

%GMTS for r_c(1)
symbolic.sdf1=vstup.K_I*sin(symbolic.theta)+vstup.K_II*(3*cos(symbolic.theta)-1)-
((16*vstup.T)/3)*sqrt(2*pi*r_C(1))*cos(symbolic.theta)*sin(symbolic.theta/2);

symbolic.d3=diff(symbolic.sdf1,symbolic.theta); %second derivation GMTS

symbolic.sdf2=vstup.K_I*sin(symbolic.theta)+vstup.K_II*(3*cos(symbolic.theta)-1)-
((16*vstup.T)/3)*sqrt(2*pi*r_C(2))*cos(symbolic.theta)*sin(symbolic.theta/2);

symbolic.d4=diff(symbolic.sdf2,symbolic.theta); %second derivation GMTS

%values of theta_0 for GMTS
for i = 1:length(vstup.K_I)
%GMTS plane stress or r_C(1)
    result2(i,:) = vpasolve(symbolic.sdf1(i)== 0, symbolic.theta);

%GMTS plane strain or r_C(2)
    result3(i,:) = vpasolve(symbolic.sdf2(i)== 0, symbolic.theta);
    symbolic.d3_0=subs(symbolic.d3,symbolic.theta,result2(i));%subs result into 2nd der.
    symbolic.d4=diff(symbolic.sdf2,symbolic.theta); %second derivation GMTS
    symbolic.d4_0=subs(symbolic.d3,symbolic.theta,result3(i));%subs result into 2nd der.

%GMTS plane strain or r_C(1)
    if symbolic.d3_0(i)<0
         results.T_GMTS_1(i, 1) = max(result2(i));
```

```
    else
         results.T_GMTS_1(i, 1) = min(result2(i));
    end
    %GMTS plane strain or r_C(2)
    if symbolic.d4_0(i)<0
         results.T_GMTS2(i, 1) = max(result3(i));
    else
         results.T_GMTS2(i, 1) = min(result3(i));
    end
end

%GMTS criterion - calculation of points for the resitance curve
results.K1_MTS=zeros(length(vstup.K_I),1); results.K2_MTS=zeros(length(vstup.K_I),1);
results.K1_GMTS_1=zeros(length(vstup.K_I),1);
results.K2_GMTS_1=zeros(length(vstup.K_I),1);
results.K1_GMTS_2=zeros(length(vstup.K_I),1);
results.K2_GMTS_2=zeros(length(vstup.K_I),1);

for i = 1:length(vstup.K_I) %MTS criterion - the resitance curve

results.K1_MTS(i,1)=results.KIC/((cos(results.T_MTS(i)/2)*(cos(results.T_MTS(i)/2)^2-
3/2*(vstup.K_II(i)/vstup.K_I(i))*sin(results.T_MTS(i)))));

results.K2_MTS(i,1)=results.KIC/((cos(results.T_MTS(i)/2)*((vstup.K_I(i)/vstup.K_II(i))*
cos(results.T_MTS(i)/2)^2-3/2*sin(results.T_MTS(i)))));
    %GMTS plane stress

results.K1_GMTS_1(i,1)=results.KIC/(((cos(results.T_GMTS_1(i)/2)*(cos(results.T_GMTS_1(i
)/2)^2-
3/2*(vstup.K_II(i)/vstup.K_I(i))*sin(results.T_GMTS_1(i)))+sqrt(2*pi*r_C(1))*(vstup.T(i)
/vstup.K_I(i))*sin(results.T_GMTS_1(i))^2)));
results.K2_GMTS_1(i,1)=results.KIC/(((cos(results.T_GMTS_1(i)/2)*
((vstup.K_I(i)/vstup.K_II(i))*cos(results.T_GMTS_1(i)/2)^2 -
3/2*sin(results.T_GMTS_1(i))))
+sqrt(2*pi*r_C(1))*(vstup.T(i)/vstup.K_II(i))*sin(results.T_GMTS_1(i))^2));
    %GMTS plane strain

results.K1_GMTS_2(i,1)=results.KIC/(((cos(results.T_GMTS2(i)/2)*(cos(results.T_GMTS2(i)/
2)^2-3/2*(vstup.K_II(i)/vstup.K_I(i))*sin(results.T_GMTS2(i)))
+sqrt(2*pi*r_C(2))*(vstup.T(i)/vstup.K_I(i))*sin(results.T_GMTS2(i))^2)));

results.K2_GMTS_2(i,1)=results.KIC/(((cos(results.T_GMTS2(i)/2)*((vstup.K_I(i)/vstup.K_I
I(i))*cos(results.T_GMTS2(i)/2)^2-3/2* sin(results.T_GMTS2(i))))
+sqrt(2*pi*r_C(2))*(vstup.T(i)/vstup.K_II(i))*sin(results.T_GMTS2(i))^2));
end

results.rC = r_C(1:2,1);

%Plotting the curves
figure (1)
plot(results.K1_MTS/results.KIC,results.K2_MTS/results.KIC,'K');
hold on
plot(results.K1_GMTS_1/results.KIC,results.K2_GMTS_1/results.KIC,'r--s');
plot(results.K1_GMTS_2/results.KIC,results.K2_GMTS_2/results.KIC,'b--d');
plot(results.SIF(:,1)/results.KIC,results.SIF(:,2)/results.KIC,'o')
hold off
title('Fracture resistance curve') %titulek obrzku
xlabel('K_{I}/K_{IC} [-]') %popis x-ov osy
ylabel('K_{II}/K_{IC} [-]') %popis y-ov osy
legend(['MTS r_{C} = 0'],['GMTS r_{C} = ' num2str(r_C(1))],['GMTS r_{C} = '
num2str(r_C(2))])
```